

UNIVERSITÀ
DEGLI STUDI
DI PADOVA



DIPARTIMENTO
DI INGEGNERIA
DELL'INFORMAZIONE

DIPARTIMENTO DI INGEGNERIA DELL'INFORMAZIONE

CORSO DI LAUREA MAGISTRALE IN BIOINGEGNERIA

DEVELOPMENT AND VALIDATION OF THE FINITE ELEMENT MODEL OF AN INSTRUMENTED HUMAN HEAD SURROGATE FOR IMPACT TESTS

Relatore: Prof. Nicola Petrone

Laureanda: Elisa Baldoin

Correlatori: Prof. Piero Pavan

Ing. Giuseppe Zullo

ANNO ACCADEMICO 2022 – 2023

Data di laurea 17 aprile 2023

Acknowledgments

I would like to thank all the people who supported and guided me in the realization of this work. In particular, I thank Professors Nicola Petrone and Piero Pavan for their constant support throughout all the steps of the preparation and development of my thesis.

Thanks also to Eng. Giuseppe Zullo for his presence, support and collaboration.

I would also like to thank all the PhD students and colleagues who shared these months with me, immediately making me feel like an active part of the group.

Thanks to my family for giving me the opportunity to cope with this way without ever missing their support and affection, and to my friends for being there for me.

ABSTRACT

Traumatic Brain Injury (TBI) is one of the most important reasons for brain damage, often referred to as the "silent epidemic" due to its contribution to the number of related deaths and disabilities. TBIs are among the leading causes of death and morbidity in young people, with an increasing incidence in industrialized countries also in patients over 65. Sports and road accidents are among the contexts in which traumatic events occur more frequently. Moreover, long-term disabilities resulting from brain injuries have a serious impact on the quality of life of the affected people and their families, as well as a decrease in life expectancy.

For these reasons, over the years the study of TBIs gained the increasing interest of researchers, aiming to a better knowledge of the mechanisms involved in the genesis and consequences of trauma, to reduce its negative outcomes, in particular through the development of increasingly effective protective devices like helmets.

Research in this field rely on laboratory tests to study the effects of different types of impact, using anthropometric devices (e.g. the dummies used in the crash tests) to acquire impact test data. However, these instruments are generally designed for analysis on the body as a whole, while there is need for specific instruments for analysing the effects of localized impacts on the head. In this view, the present work is part of a long-term activity conducted at the DII Department of the University of Padua which involved the design and construction of a series of prototypes of human head models equipped with different types of sensors (accelerometers, gyroscopes and pressure sensors) for the acquisition of data obtained from impact tests. Due to the complexity of the anatomical structures, it is particularly difficult to obtain a satisfactory biofidelity of the model, starting from the choice of materials. Biological tissues, in fact, have extremely peculiar physical and mechanical properties, which are very difficult to replicate with metals and polymeric materials. Also, the fabrication of the models is expensive and time-consuming, due to the prices of the materials and to the manufacturing (typically by casting or 3D printing) and assembly processes, with the insertion of the sensors as well.

For these reasons, the computer simulation of the effects of the different types of impact through a validated finite element model is of particular interest. In this way it is possible to analyse any situation without using the physical model, which would inevitably be damaged or destroyed during the most demanding tests.

The work described here concerns the realization of the finite element model of the last physical replica of a human head developed in 2022 by the DII Department, in turn built with particular attention to biofidelity in terms of biomechanical properties. The FEM model was obtained performing in parallel constitutive and geometrical analyses. Preliminarily, after an accurate

bibliographic investigation, laboratory tests were carried out for the characterization of the materials used to build the surrogates of the anatomical parts (brain, meninges, skull and skin), with the aim to identify the constitutive parameters for the subsequent modeling of their mechanical behaviour. Finally, the STL files of the parts of the physical model were suitably pre-processed using *Meshmixer* (by Autodesk) software. These were then imported into *Fusion 360* (by Autodesk) CAD design software to get the solid models for subsequent finite element analysis, performed with *Abaqus* FEA program by Dassault Systemes. To reduce the time required for the analysis, in this work it was chosen to simulate a drop test of the right half of the head surrogate, to get some preliminary information about the behaviour of the different materials when they interact, along with the analysis of the computed output data. Future developments will include the validation of the whole model.

ABSTRACT

Il trauma cranico è una delle principali cause di danno cerebrale, spesso definito anche "epidemia silenziosa" per il suo importante contributo al numero di decessi e di casi di disabilità ad esso correlati. Si tratta di una delle cause prevalenti di mortalità e morbidità nei giovani, con incidenza in aumento nei paesi industrializzati anche nei pazienti over 65; attività sportiva e incidenti stradali sono tra i contesti in cui gli eventi traumatici si verificano con maggiore frequenza. Le disabilità a lungo termine conseguenti le lesioni cerebrali hanno un grave impatto sulla qualità della vita della persona colpita e dei suoi familiari, oltre a diminuire l'aspettativa di vita.

Per questi motivi, si tratta di una patologia che nel corso degli anni ha suscitato il crescente interesse della comunità scientifica, con l'intento di conoscere meglio i meccanismi coinvolti nella genesi e nelle conseguenze del trauma per ridurne gli esiti negativi, in particolare attraverso lo studio di indumenti protettivi sempre più efficaci.

La ricerca in questo settore si avvale di test di laboratorio per studiare gli effetti dei diversi tipi di impatto, utilizzando dispositivi antropometrici per acquisire i dati delle prove di impatto; tuttavia, questi strumenti sono progettati per le analisi sul corpo nel suo complesso, mentre si rileva la necessità di strumentazioni specifiche per l'analisi degli effetti degli impatti localizzati sulla testa.

In quest'ottica, il presente lavoro si inserisce in un'attività a lungo termine condotta presso il Dipartimento DII dell'Università di Padova che ha previsto la progettazione e la realizzazione di una serie di prototipi di modelli di testa umana attrezzata con diversi tipi di sensori (accelerometri, giroscopi e sensori di pressione) per l'acquisizione dei dati ottenuti da prove di impatto. La complessità delle strutture anatomiche rende particolarmente difficile ottenere una soddisfacente biofedeltà del modello, a partire dalla scelta dei materiali: i tessuti biologici, infatti, presentano proprietà fisiche e meccaniche estremamente peculiari, difficilmente replicabili con i materiali metallici e polimerici. Inoltre, anche dopo aver individuato i materiali più idonei per realizzare i surrogati dei tessuti, la costruzione dei modelli è dispendiosa, in termini di costo dei materiali e di tempo necessario per i processi di costruzione (in genere colatura o stampa 3d) e di assemblaggio con l'inserimento dei sensori.

Per questi motivi, risulta particolarmente interessante la simulazione al computer degli effetti delle diverse tipologie di impatto mediante la modellazione agli elementi finiti. In questo modo è possibile analizzare qualsiasi situazione senza utilizzare il modello fisico, che verrebbe inevitabilmente danneggiato o distrutto durante i test più gravosi.

Il lavoro qui descritto riguarda la realizzazione del modello agli elementi finiti dell'ultima evoluzione della replica fisica di una testa umana realizzata presso il dipartimento DII

dell'Università di Padova, a sua volta costruita con particolare attenzione alla biofedeltà in termini di proprietà biomeccaniche. Per realizzare il modello FEM, sono state effettuate le necessarie analisi (costitutiva e geometrica). Preliminarmente, dopo un'accurata indagine bibliografica, sono stati effettuati test di laboratorio per la caratterizzazione meccanica dei materiali che costituiscono le parti anatomiche simulate (cervello, meningi, cranio e pelle), con lo scopo di identificarne i corrispondenti parametri costitutivi per la successiva modellazione. In seguito, i file STL delle parti del modello fisico sono stati opportunamente pre-elaborati mediante il programma Autodesk Meshmixer; successivamente, sono stati importati nel software di progettazione CAD Autodesk Fusion 360, da cui sono stati ottenuti i file da sottoporre all'analisi agli elementi finiti mediante il programma Abaqus FEA di Dassault Systemes. Per ridurre il tempo richiesto per l'analisi, in questo lavoro si è scelto di simulare una caduta libera della sola metà destra del modello, per ottenere informazioni preliminari sull'interazione dei vari materiali e sui segnali in output. Futuri sviluppi prevedono la simulazione di una caduta libera del modello complessivo e la sua validazione.

SUMMARY

ABSTRACT i

ABSTRACT iii

SUMMARY v

Chapter 1: State of the Art on human brain surrogates 1

1.1 Anatomy of human head: a brief recap 1

1.1.1 Skull 1

1.1.2 Skin: face and scalp 3

1.1.3 Brain 4

1.1.4 Protective structures of the brain: meninges and ventricular system 6

1.2 Traumatic Brain Injuries 10

1.2.1 Pathology of TBIs 10

1.2.2 Pathophysiology of TBIs 14

1.2.3 Symptoms of TBIs 15

1.2.4 Head and Brain Injury Criteria 16

1.3 Physical prototypes for impact tests 19

1.3.1 UniPD surrogates 22

Chapter 2: Constitutive analysis 29

2.1 Mechanical properties of human tissues and their surrogates 29

2.1.1 Hints on the behaviour of rubber-like materials 30

2.2 Brain simulant material 38

2.2.1 Mechanical characterization of brain simulant material 38

2.2.2 Identification of the constitutive parameters of brain simulant material 48

2.3 Subarachnoid space simulant material 71

2.3.1 Mechanical characterization of subarachnoid space simulant material 71

2.3.2 Identification of the constitutive parameters of subarachnoid space simulant material 74

2.4 Skin simulant material 75

2.4.1 Mechanical characterization of skin simulant material 75
2.4.2 Identification of the constitutive parameters of skin simulant material 80
2.5 Skull simulant material 88
2.5.1 Mechanical characterization of skull simulant material 88
2.5.2 Identification of the constitutive parameters of skull simulant material 89
2.6 Falx cerebri and tentorium cerebelli simulant material 90
2.6.1 Mechanical characterization of falx and tentorium simulant material 90
2.6.2 Identification of the constitutive parameters of falx and tentorium simulant material 91
Chapter 3: Geometrical analysis 93
3.1 STL files optimization, cleaning and repairing 93
3.1.1 Brain 93
3.1.2 Top skull, bottom skull and jaw 94
3.1.3 Skin 98
3.2 CAD models 99
3.2.1 STL files conversion in solid models 99
3.2.2 Building of missing solid models 102
Chapter 4 Finite element model of the current prototype 111
4.1 The Finite Element method 111
4.2 Some Finite Element Models of human head in literature 113
4.2.1 EEVC WG17 FE model [European enhanced vehicle safety committee, 1991] 113
4.2.2 ULP FEM of the human head, 1999 113
4.2.3 KTH Model (Kleiven, 2000) 114
4.2.4 Wayne State University (WSU) Head (Brain) Injury Model (WSUHIM, 2001) 114
4.2.5 Politecnico di Torino University FEM of the human head 115
4.2.6 University College Dublin Brain Trauma Model (UCDBTM, 2003) 115
4.2.7 HEAD-BRAIN FE Model [Masami Imawoto et al., 2007] 116
4.2.8 Yang et al. 2008 human head FE model 116

4.2.9 Harvard Medical School FEM, 2008 117
4.2.10 TNO Head FE Model, 2009 117
4.2.11 Unipd FE Model (Pavan et al. 2022) 117
4.3 Development of the finite element model of the UniPD Human Head Surrogate 119
4.3.1 Pre-processing 119
4.3.2 Processing 131
Chapter 5: Drop test simulations 133
5.1 PlatSil Gel-10 (skin simulant material) ball drop test simulation 133
5.1.1 Pre-processing 135
5.1.2 Processing 139
5.1.3 Post-processing 139
5.2 Drop test simulations of a simplified head surrogate 142
5.2.1 Preliminary simulations to optimize the mesh 142
5.2.2 Preliminary simulations from different heights 152
5.3 Drop test simulation of the right half head surrogate 160
5.3.1 Pre-processing 160
5.3.2 Processing 161
5.3.3 Post-processing 161
5.3.4 Experimental preliminary tests for model validation 165
5.4 Discussion of preliminary results and conclusions 167
REFERENCES 169

Chapter 1: State of the Art on human brain surrogates

1.1 Anatomy of human head: a brief recap

Accidental events potentially leading to traumatic injuries to the head are very frequent in the context of daily life, and in particular in some work-related situations and during sports activities. These events are responsible for a huge number of cases of death and more or less severe disability.

For these reasons, it's essential to know the anatomy of the head and the main mechanisms that determine trauma damage, as a prerequisite for improving the effectiveness of protective devices, such as helmets and protective gear in general.

In humans and higher animals, the head is the upper part of the body, connected to the trunk by the neck.

1.1.1 Skull

The bony skeleton of the head is the skull, which is made up of 22 bones, 8 cranial and 14 facial bones (fig. 1.1). It includes two main parts: the cranium and the mandible (jaw). The cranium, in turn, can be divided into two parts: the braincase and the facial skeleton.

The braincase or *neurocranium* is a robust structure that encases and protects the brain in the cranial cavity. It contains the brain with the intracranial portions of the cranial and spinal nerves, the blood vessels responsible for supplying and draining the brain, the meninges (*dura, arachnoid* and *pia mater*), and the cerebrospinal fluid (CSF). In addition, it contains the cranial segments of the respiratory and digestive systems, and special senses. The upper part of the neurocranium is also called *calvarium*. Cranial bones are frontal, parietal, sphenoid, temporal and occipital.

The facial skeleton or *viscerocranium* is composed mainly of thin bones and air-filled cavities (paranasal sinuses). Facial bones are ethmoid, lacrimal, nasal, zygomatic, maxillary, mandible and vomer. The mandible and the vomer are the only unpaired facial bones, while all the others are in pairs [Standring, 2008; Paulsen, 2019].

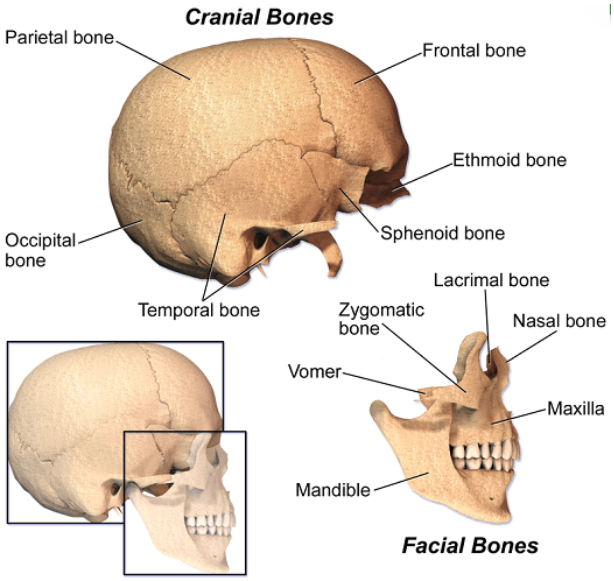


Figure 1.1 - Right lateral view of the skull bones [Knapp, 2020]

The cranium also contains the insertions of many muscles of the head and neck and the temporomandibular joint, which allows movement of the jaw.

The main function of the skull is to lodge and protect the brain (the main organ of the Central Nervous System), the brainstem, which connects the brain with the spinal cord, and the eyes orbits. It also provides an insertion for the muscles of the scalp and face, along with protecting the nerves and vessels that feed and innervate the brain, facial muscles, and skin.

In adults, all of the skull bones, except one, are locked together by fixed joints (sutures), which form a structure that is both rigid and strong. The mandible, or lower jaw, is the only moveable skull bone. The bones of the skull also include the hyoid, or lingual bone: it is a U-shaped bone located at the base of the jaw, in the front side of the neck. Hyoid is the only bone of the body that does not articulate directly with other nearby bones, and its function is to support the movement of the tongue and swallowing, as well as to provide attachment to the muscle of the floor of the mouth and tongue, larynx, epiglottis and pharynx.

From a morphological point of view, the skull is mainly formed by flat bones, consisting of two thin layers of compact bone tissue which enclose a layer of cancellous bone, reinforced by bony trabeculae (fig. 1.2); this layer may include larger gaps containing residues of hematopoietic tissue. In general, flat bones have a protective function, as they are particularly rigid and resistant.

In the cranial bones, the layers of compact tissue are known as the tables of the skull: the outer one is more thick and solid, while the inner, also termed vitreous (glass-like) table, is thin, dense, and brittle. The prevailing cancellous tissue is named diploë, and, in the nasal region, it is absorbed to form air-filled cavities (the paranasal sinuses) between the two tables.

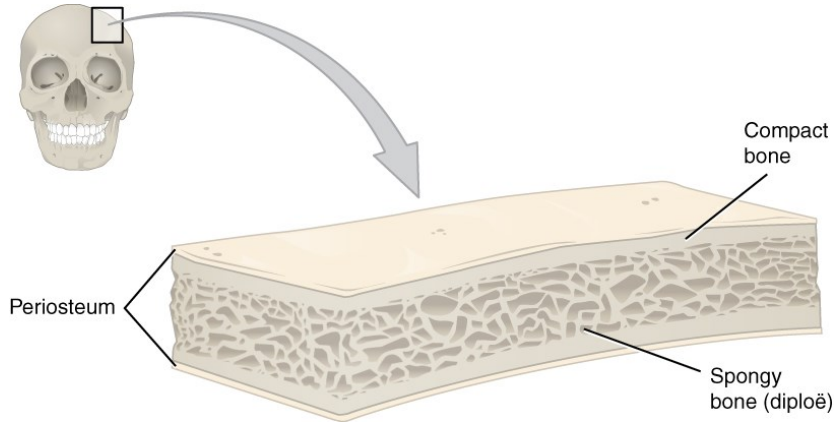


Figure 1.2 - Structure of a flat bone [Betts, 2013]

In detail, in the cranium the flat bones are occipital, parietal, frontal, nasal, lacrimal, vomer. Temporal, sphenoid, ethmoid, zygomatic, maxilla, mandible, palatine, inferior nasal concha, and hyoid belong to the irregular bones, with the same structure [Betts, 2013].

These features make the skull robust and elastic, but light at the same time; the biomechanical implications of these features will be discussed later.

1.1.2 Skin: face and scalp

The muscles of the head include two particular types: the mimic muscles, which allow changes in the facial expression, and the masticatory muscles (fig. 1.3).

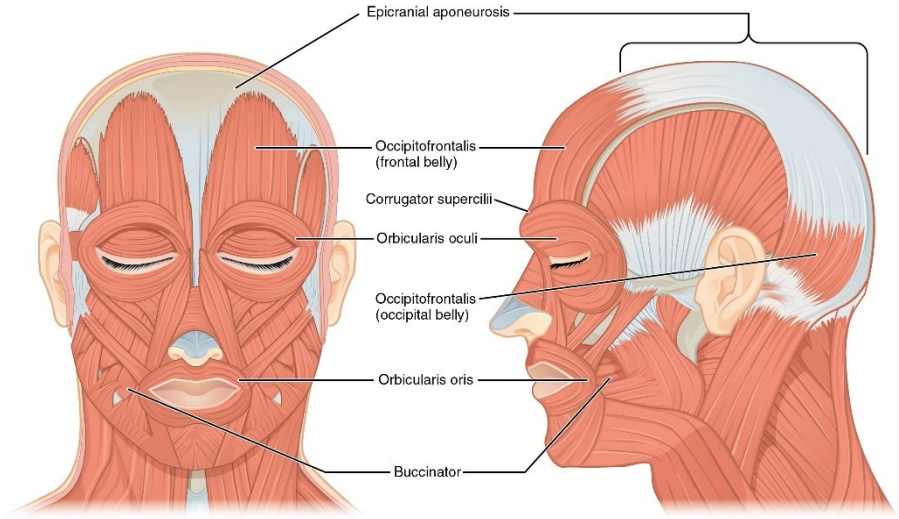


Figure 1.3 – Muscles of face [Betts, 2017 from OpenStax College]

Muscles are covered by skin, which has the primary function to protect the underlying tissues from mechanical impact, radiation, and harmful environmental factors. It also helps to regulate the internal temperature and to excrete waste products. Skins consist of multiple layers, i.e. the epidermis (the top layer), the dermis (the middle layer), and hypodermis (the deepest layer). In particular, the skin and the muscular layer which covers the upper part of the skull, i.e. the cranium, is the scalp, which refers to an anatomic region delimited anteriorly by the face, and laterally and posteriorly by the neck. It is the area where hair can grow and works as a barrier

to protect the cranium from external harms. The scalp includes five layers: the skin, a connective tissue layer, the *galea aponeurotica*, loose areolar connective tissue, and the pericranium (fig. 1.4) [Tajran, 2022].

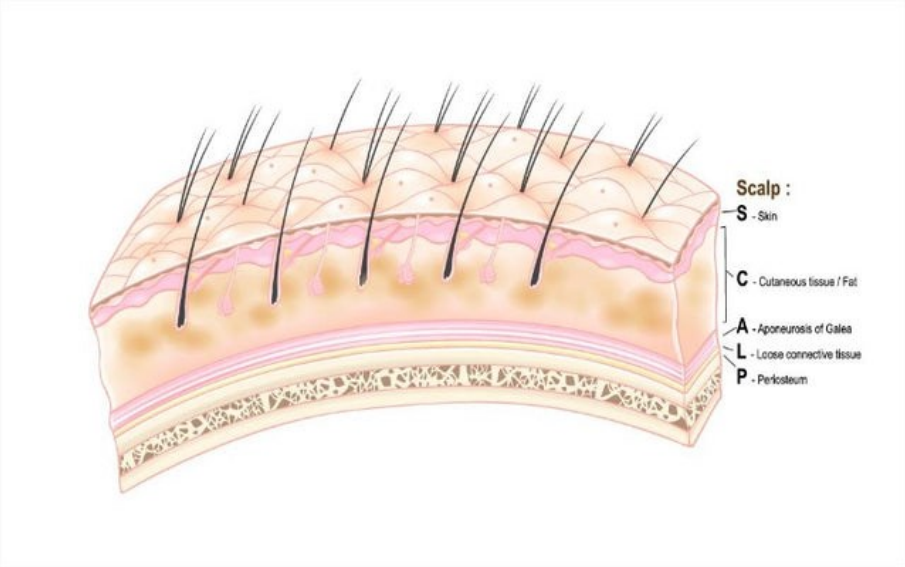


Figure 1.4 – Section of the scalp [Dandu, 2022 by Shutterstock]

1.1.3 Brain

The brain is the main organ of the Central Nervous System, responsible for all life-related activities. It controls and coordinates the functions of all other organs and systems in the body (fig. 1.5).

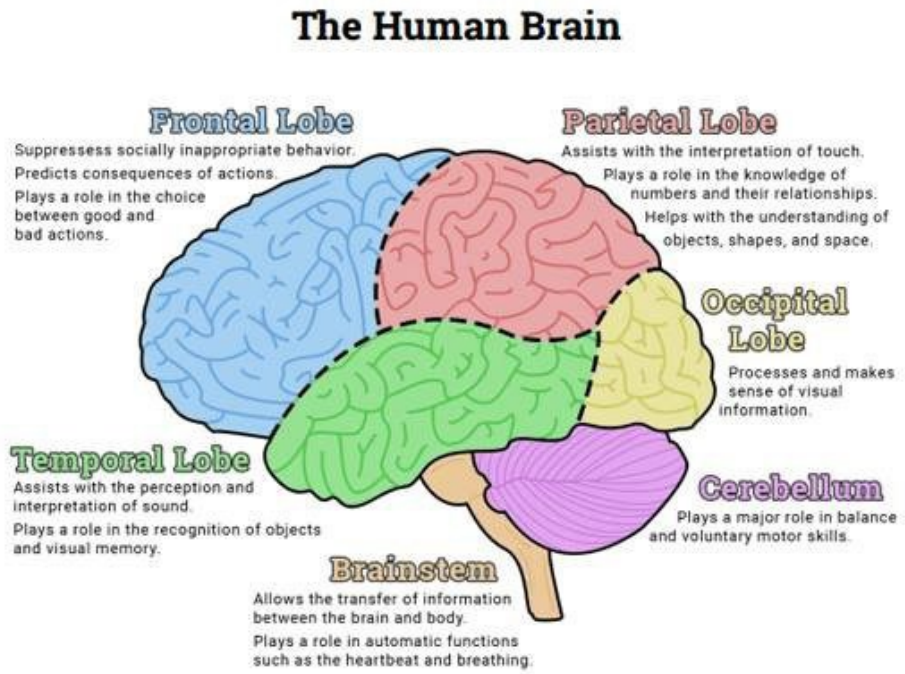


Figure 1.5 – Parts of the brain and their main functions [Therapistaid.com, 2015]

From an anatomical point of view, what is commonly referred to as the “brain” is actually a larger structure named *encephalon*, that includes the brain itself or *cerebrum*, the brain stem, and the *cerebellum*. The weight of the whole organ is on average about 1,2-1,4 kg.

Cerebrum

The *cerebrum* is the largest part of the brain. It performs extremely complex functions, such as the processing of external stimuli transmitted by the sense organs, language, movement control. Emotions, reasoning, and learning also originate here.

The cerebrum is divided into two hemispheres, right and left, connected by the *corpus callosum*, a bundle of fibers that enables the communication between the parts. Each hemisphere controls the contralateral part of the body. The functions of the two hemispheres are partially complementary: the left is associated to the abilities related to the rational sphere, such as language, writing, logical reasoning. The right hemisphere is predominantly connected to the control of emotional activities, such as creativity, intuition, spatial perception, musical competence, etc.

The outer layer of the brain, responsible for the higher functions of nervous system, is the *cerebral cortex*; it is 2-4 mm thick and contains about 70% of the total 100 billion nerve cells. It is composed of grey matter, the bodies of neurons, while the axons, extensions of the neurons that make up the white matter, are located beneath the cerebral cortex; their colour is given by the myelin coating of the nerve fibers. It is also characterized by convoluted ridges of neural tissues called "*gyri*", separated by grooves between them named "*sulci*"; this structure increases the total surface area of the brain and thus the space available for the neurons.

Deeper grooves (fissures) divide the two hemispheres into four lobes: the occipital lobe at the back of the skull, the parietal lobe (lateral), the frontal lobe (forehead), and the temporal lobe (temple). Each lobe is responsible for the control of several specific functions.

Cerebellum

The *cerebellum* is located just below the temporal and occipital lobes of the brain. Anatomically, the human cerebellum looks like an elliptical structure divided into two hemispheres (cerebellar hemispheres), weighing about 130-140 grams, and is located in the posterior cranial fossa under the cerebral hemispheres. Its cortical surface is covered with finely spaced parallel grooves, in contrast to the large irregular convolutions typical of the cerebral cortex. This is due to the structure of the cerebellar cortex, which is a thin layer of tissue, accordion-like tightly folded. The cerebellum performs tasks related to the coordination of movements, balance, the control of standing position, and the attention span. It does not start any movement because this depends on the cerebral cortex, while it helps movements to be

carried out in a smooth and controlled manner. The cerebellum doesn't deal with conscious sensation, it translates the instructions of the cortex into actions of the muscles.

Brain stem

The brain stem includes the *mesencephalon* or midbrain, the *pons*, and the *medulla oblongata*, and connects the cerebral hemispheres with the spinal cord. It controls many of the automatic functions of the body, such as breathing, heart beat regulation, digestion, thermoregulation, sleep cycle, involuntary stimuli including vomiting, sneezing, yawning, etc.

Midbrain. The midbrain (or *mesencephalon*) is a complex structure which contains neuron clusters (nuclei and colliculi), neural pathways and other components. It is involved in functions like, for example, moving the head and eyes in response to the visual and hearing reflexes.

Pons. The pons (the Latin word for "bridge") is the connection between the midbrain and the medulla. It houses the nuclei of four of the 12 cranial nerves (trigeminal, abducens, facial, vestibulocochlear), which enable a range of central activities such as tear production, chewing, eye movement, focusing vision, balance control, hearing, facial expression and sensation.

Medulla oblongata. It is the continuation of the brainstem towards the spinal cord. The medulla is essential to survival, because it regulates vital body functions, including heart rhythm, breathing, blood flow, and oxygen and carbon dioxide levels. The medulla also starts reflexive actions such as sneezing, vomiting, coughing and swallowing.

The brain stem extends to the spinal cord through a wide opening in the bottom of the skull [Hopkins, 2023].

1.1.4 Protective structures of the brain: meninges and ventricular system

Due to the vulnerability of brain tissues, there is the need for a system to protect them from events that could cause damage.

The outer surface of the brain is protected by the meninges, a series of connective tissue membranes that form a strong protective layer around the entire brain and spinal cord. Meninges are anchored to the inner surface of the cranium and to the outer surface of the brain, following the convolutions of gyri and sulci in the cerebral cortex and fitting into grooves and fissures.

The other component of the protective structure is the ventricular system with the cerebrospinal fluid (CSF), made of four open areas connected by channels. They also open into the central spinal canal and the area beneath arachnoid layer of the meninges. The ventricles produce the cerebrospinal fluid, a colourless aqueous liquid composed of organic materials such as protein, glucose and electrolytes. CSF flows in and around the ventricles, and between the meninges, surrounding and cushioning the brain; further, it provides immunological protection to the

brain, delivers nutrients, washes out waste and impurities, and also serves as a shock absorber for the brain's cortex, thereby protecting its tissue from mechanical damages.

Meninges

The meninges (fig. 1.6) protect the delicate tissues of the brain, and they are made of an external layer, hard and fibrous (the *dura mater*), and two thinner layers, the middle (arachnoid) and the deeper (*pia mater*). The dura is made of dense connective tissue, and adheres to the inner surface of the skull. The arachnoid is a thin, spider-web like membrane lying just below to the dura; it is followed by the pia, a very thin membrane that directly covers the surface of the brain [Post, 2013].

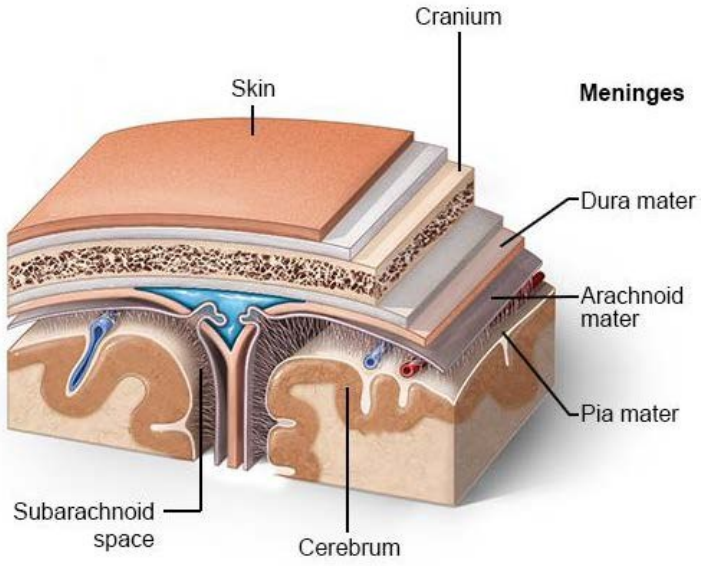


Figure 1.6 – Meninges [Post, 2013]

Dura Mater and its reflections

The dura is the outermost of the meninges. It is composed of two layers: the periosteal layer, adherent to the *calvarium*, and the meningeal layer, in contact with the brain tissue. This layered structure makes the dura thick, dense and rigid. The periosteal layer contains fibroblasts, osteoblasts, and a large amount of extracellular collagen within the intercellular space, thus making the dura particularly resistant. Periosteal and meningeal layers are virtually fused, and they separate only to form venous sinuses and dural reflections.

Dural reflections originate when two adherent meningeal layers intrude into the cranial cavity giving origin to the *septa* that divide the brain into two hemispheres. The two main dural reflections are the *falx cerebri* and the *tentorium cerebelli*.

The *falx cerebri* is so termed after its sickle-like shape; it adheres to the top of the cranium vault and hangs down into the interhemispheric fissure, dividing the right and left cerebral hemispheres.

The *tentorium cerebelli* is a "U" shaped, horizontal reflection of the meningeal dura, which runs transversely between the cerebellum and occipital lobes. The midbrain (mesencephalon) crosses the middle cranial fossa through an opening in the *falx cerebri*, the tentorial *incisura* (also denoted as tentorial notch). The front margin of the *tentorium cerebelli* is free and concave; it is fixed to the front and rear clinoid processes of the sphenoid bone, and laterally to the upper edge of the petrous temporal bone. On the rear side, *tentorium* is fixed to the periosteal dura. This attachment makes the structure fix and stiff.

Falx and *tentorium* play an important biomechanical role, which will be discussed later.

Arachnoid Mater

The arachnoid is an avascular membrane lying between the dura and the pia and plays a role in cerebrospinal fluid (CSF) metabolism via the subarachnoid space. It is generally a thin, semi-transparent membrane, with a structure made of a mesothelial layer in close contact with the dura mater, a central layer composed of cells connected by junction proteins, and a deep layer of more loosely packed cells along with an intercellular space containing many collagen fibers. Between the lower surface of the arachnoid and the pia mater there is the subarachnoid space, in which the CSF flows. In addition, typical filaments called *arachnoid trabeculae* are found in the subarachnoid space; they run from the lower surface of the arachnoid to the upper surface of the pia mater, giving rise to a spider-web like network.

Pia Mater

The *pia mater* is the deepest layer of the meninges; it consists of two sheets and follows the contours of the *sulci* and *gyri* of the brain surface. The pia structure is organized in layers: the outer layer (epipial layer), containing collagen fibers, and the inner layer (*intima pia*), with elastic and reticular fibers. Mesothelial cells of the epipial layer are connected to the arachnoid via the arachnoid trabeculae, while the intima pia adheres directly to the outer layer of neural tissue, i.e. the glial membrane. Another important function of the pia mater is forming a sheath around the blood vessels running in and out of the brain parenchyma perpendicular to the meninges, particularly those coming from the subarachnoid space. This covering creates an interstitial fluid-filled space, known as the perivascular or Virchow-Robin space, between the vessel walls and the pia.

Dural spaces

Meningeal layers are delimited by potential spaces, also called cavities, which are normally not visible, but may become clinically significant: they are epidural, subdural, and subarachnoid spaces, proceeding from the skull inner surface inwards.

The epidural space separates the periosteum of top of the cranial vault (calvarium) from the external surface of the dura (periosteal layer); blood vessels run between the inner surface of

the calvarium and the dura, therefore the epidural space becomes apparent only in pathological conditions.

The subdural space delimits the meningeal layer of the dura and the arachnoid mater. As with the epidural space, the subdural space typically exists only under pathological conditions.

The subarachnoid space is filled by the cerebrospinal fluid and lies between the arachnoid and the pia.

Ventricular system and Cerebrospinal fluid (CSF)

CSF is produced in the lateral ventricles of the brain, in the *choroid plexus*, from where it passes into the subarachnoid space via the *foramina of Luschka*. Since the subarachnoid space is continuous between the brain and spinal cord, CSF flows through the *foramen magnum* to the distal part of the spinal cord (fig. 1.7). CSF has the important function of cushioning the brain and spinal cord from shocks, as described later, as well as supplying nutrients and remove waste products. The main arteries of the brain run through the subarachnoid space as well; further, as mentioned before, arachnoid trabeculae project into subarachnoid space.

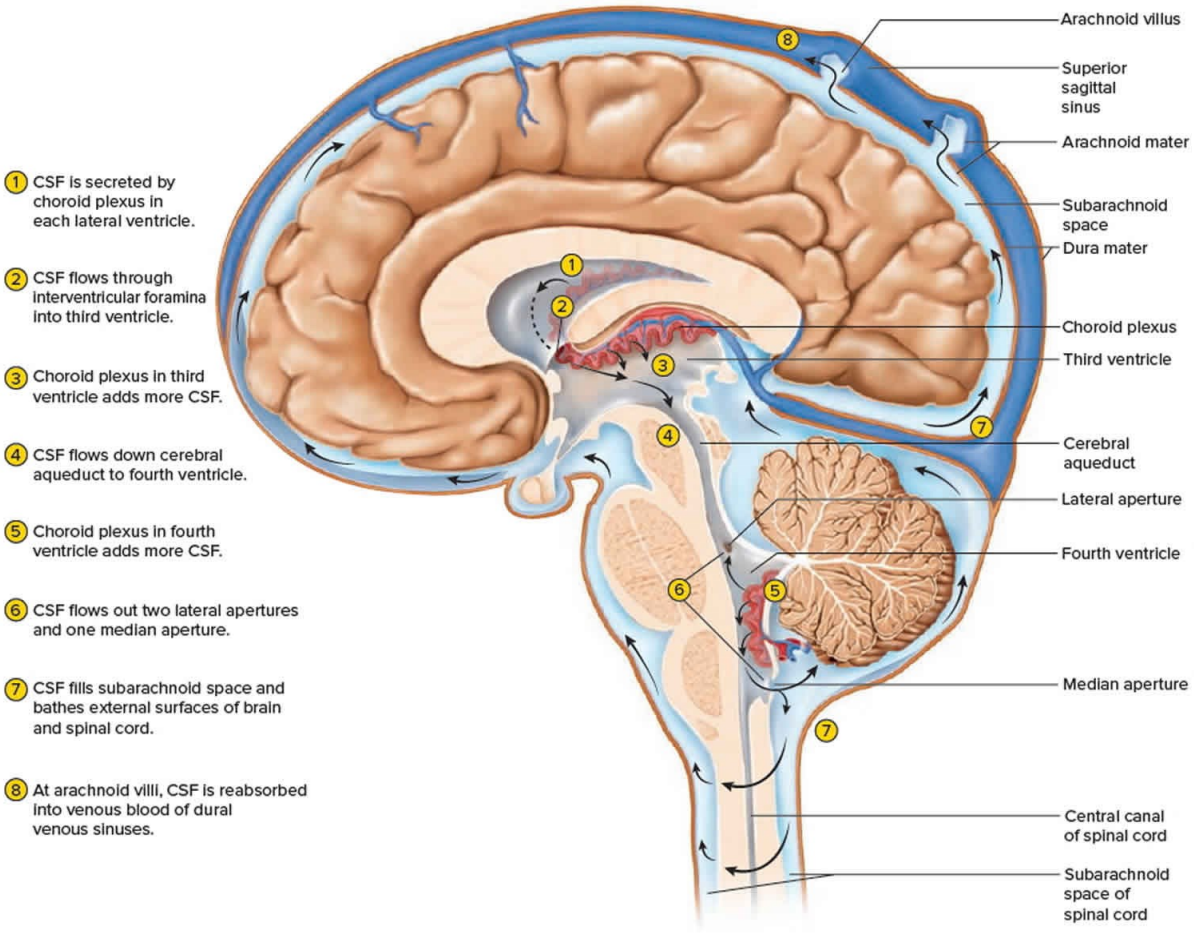


Figure 1.7 – The flow of CSF [Donatelli, 2020]

The complexity and vulnerability of the brain and its related structures, as seen in the brief summary of the anatomy of the head exposed so far, justifies concern about the consequences

deriving from impact injuries. The challenge facing researchers is the increasingly in-depth knowledge of the mechanisms underlying brain damage, with the aim of developing techniques aimed at improving both the effectiveness of treatments and the protective devices that allow to prevent and minimize the consequences of injuries.

To this end, the main types of traumatic brain injury are presented below in order to identify the best strategies to prevent and reduce the resulting damage [Vaughn, 2016; Paulsen, 2019; Ghannam JY., 2022].

1.2 Traumatic Brain Injuries

The term Traumatic Brain Injury (TBI) generally denotes a brain damage caused by an impact and/or a sudden acceleration or deceleration of the brain [*www.cliffsnotes.com*]. An international working group has established the definition: "*TBI is defined as an alteration in brain function, or other evidence of brain pathology, caused by an external force*" [Lezak, 2012].

According to studies conducted in the USA and New Zealand, 500-800 cases of head injury per 100,000 people yearly occur, while there is a lack of available data for low- and middle-income countries. Referring to Europe, about 82.000 deaths and about 2.1 million hospital discharges are estimated to be occurred in 2012 in the whole Continental Europe (population 737 million), with about 56.000 TBI-related deaths and 1,5 million hospital discharges estimated in the European Union (population 509 million) [Menon, 2010; Dewan, 2018].

Causes of TBI may include falls (particularly in older adults and children), road crashes involving motor vehicles or other transportation-related causes (e.g. bicycle crashes, collisions with pedestrians), assaults, sports activities (e.g. sports-related concussions).

TBI should never be underestimated, because the symptoms or any damage deriving from the trauma are not always immediately visible, while, in some cases they could appear several hours or even weeks after the event.

1.2.1 Pathology of TBIs

Depending on the mechanism of the accident and involved forces, structural changes in tissues may be coarse or invisible, and the severity of clinical consequences are widely variable. The mechanical events leading to a TBI may be typically closed and open injuries.

Closed injuries, generally occurring as consequences of an impact or a violent jolt of head, with rapid brain acceleration and deceleration; damage can affect the point of impact, the opposite side (countercoup), or be diffuse. Frontal and temporal lobes are particularly prone to this type of injury. Moreover, disruption of axons and/or blood vessels may occur resulting in

axonal breakup and blood leak causing contusions, intracerebral o subarachnoid hemorrage, and epidural or subdural hematomas.

Open injuries, also denoted as penetrating injuries, including penetration of skin, scalp, skull, and generally also meninges, with damage to brain tissue caused by sharp objects or bullets. Skull fractures are included in this group.

The most common consequences of TBIs are concussion, brain contusion, diffuse axonal injury, hematoma, subarachnoid haemorrhage, and skull fractures.

Concussion

Concussion, also denoted as mild traumatic brain injury or **mTBI**, is a temporary, reversible post-traumatic change in mental status, with symptoms like loss of consciousness or memory and confusion, with a duration from seconds to some minutes and, by definition, shorter than 6 hours (fig. 1.8). A temporary disability can occur with symptoms such as headache, nausea, unsteadiness, memory loss, and difficulty concentrating (post-concussion syndrome); however, generally macroscopic structural damages are not observed, and symptoms usually resolve within a few weeks. Nevertheless, it is believed that multiple concussions may lead to chronic traumatic encephalopathy, resulting in severe brain dysfunction [Mayo Clinic, 2022].

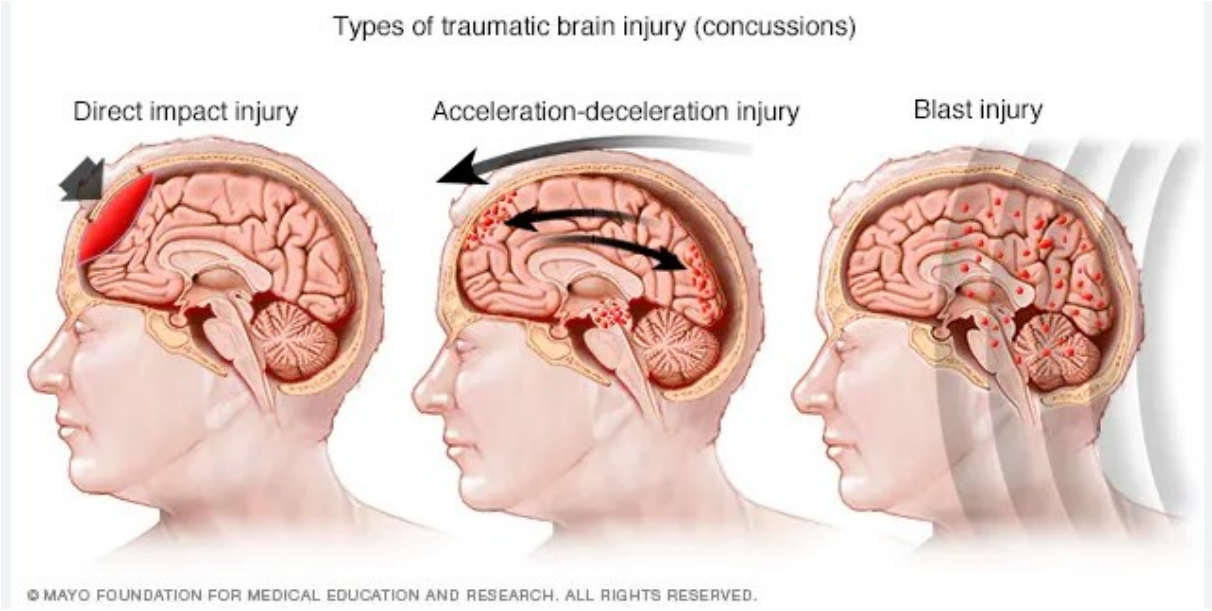


Figure 1.8 – Types of TBI [Mayo Clinic, 2022]

Brain contusions

Contusions (ecchymoses of the brain) may follow an open or closed trauma, impairing a wide range of brain functions depending on their size and location. Larger contusions can cause cerebral edema and increased intracranial pressure. Contusions may expand after the initial injury and cause neurologic decline, possibly requiring surgery.

Diffuse axonal injury

Diffuse axonal injury (DAI) occurs as a consequence of shear forces generated by rotational deceleration, causing a diffuse disruption of axonal fibers and their myelin sheaths (fig. 1.9). Sometimes DAI can result from minor head trauma. Massive structural lesions are not observed in DAI, while small petechial hemorrhages in white matter are often revealed by CT and histopathologic examination. DAI is sometimes defined as a loss of consciousness over 6 hours without specific focal lesion. Edema resulting from trauma often causes an increase in intracranial pressure, with various manifestations. DAI is typically the causal agent of Shaken Baby Syndrome (SBS) [Bray, 2018; Mayo Clinic, 2022].

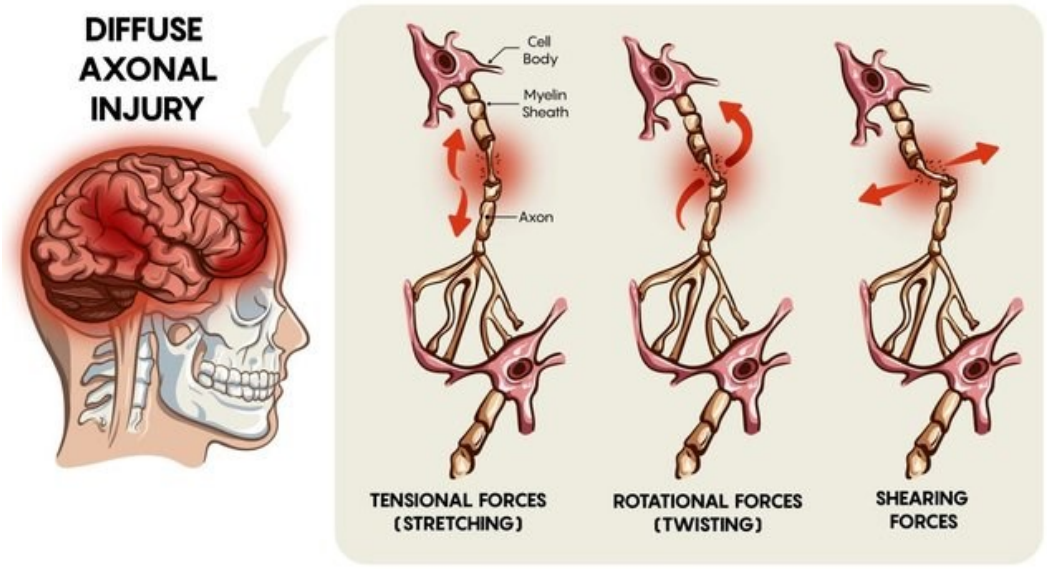


Figure 1.9 – Mechanism of DAI [Bray, 2018]

Hematomas

Hematomas (collections of blood in or around the brain) can occur following open or closed trauma (fig. 1.10). They can be subdural, epidural, or intracerebral (intraparenchymal).

Subdural hematomas are blood collections between the dura mater and the arachnoid. Acute subdural hematomas result from rupture of the cortical veins or laceration of the bridging veins between the cortex and dural sinuses. Acute subdural hematomas are frequently observed in head injuries caused by falls or road accidents, brain contusions or contralateral epidural hematoma. Hematoma can cause compression and swelling of the brain due to edema or hyperemia (increased blood flow as a result of bulge of vessels) thus increasing intracranial pressure (ICP) with possibly high mortality and morbidity. Also, a chronic subdural hematoma can arise causing worsening symptoms over several weeks after the injury. Chronic subdural hematomas are more common in alcoholics and elderly patients, especially when anticoagulant drugs are used or in cases

of brain atrophy. In chronic subdural hematoma, edema and increased intracranial pressure are not typical.

Epidural hematomas are collections of blood between the skull and dura mater and are less frequent than subdural hematomas. Epidural hematomas are large or rapidly expanding, and are usually caused by arterial bleeding, often due to the rupture of the middle meningeal artery subsequent a fracture of the temporal bone. Patients with epidural hematomas can rapidly deteriorate and die if untreated.

Intracerebral hematomas are collections of blood within the brain parenchyma resulting from the fusion of contusions after trauma events. Increased intracranial pressure, herniation, and brainstem compression may develop later, especially in the presence of lesions in the temporal lobes.

Subarachnoid haemorrhage

Subarachnoid haemorrhage or SAH is a particular event of bleeding into the subarachnoid space and is common in TBI. Blood coming from a subarachnoid hemorrhage does not collect in a discrete hematoma [Nabi, 2018].

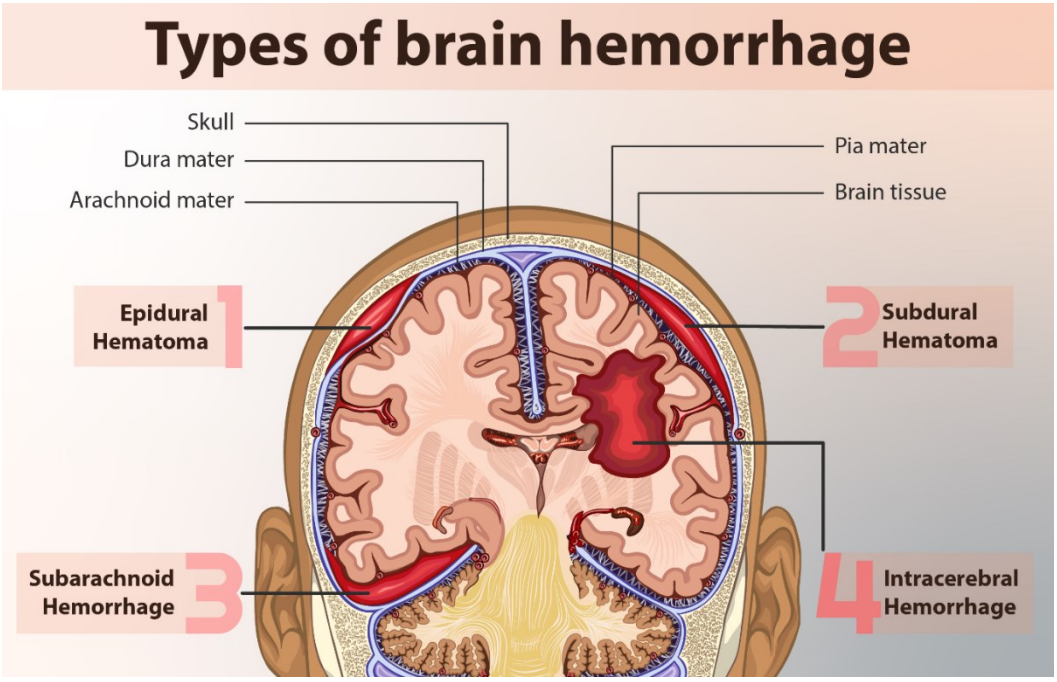


Figure 1.10 – Types of brain hemorrage [Nabi, 2018]

Skull fractures

Fractures are included in open injuries by definition; closed injuries may cause fractures as well, and these ones may be linear, depressed, or comminuted. Simple linear fractures without neurologic impairment generally do not involve high risk for brain damage, while any fracture associated with neurologic impairment increases the risk for intracranial hematomas (fig. 1.11). Skull fractures that pose special risks are:

Depressed fractures: they increase the risk of tearing the dura, with damage to the brain. Temporal bone fractures crossing the course of the middle meningeal artery may cause epidural hematoma.

Fractures crossing one of the major dural sinuses: they can cause hemorrhage and epidural or subdural venous hematomas, which can result in thromboses of damaged venous sinuses and subsequent cerebral infarction.

Fractures involving the carotid canal: they can cause carotid artery dissection.

Occipital bone and skull base bones fractures: since these bones are thick and hard, fractures in these areas indicate high-intensity impact with great increase of the risk of brain injury. When skull base fractures extend into the petrous part of the temporal bone, damage to structures in the middle and inner ear often occurs; facial, auditory, and vestibular nerve function may be impaired.

Fractures in infants: in these cases, the meninges may be trapped in a linear skull fracture of the parietal bone, and a leptomeningeal cyst with expansion of the original fracture may occur (*growth fractures*) [Bhattacharya, 2018].

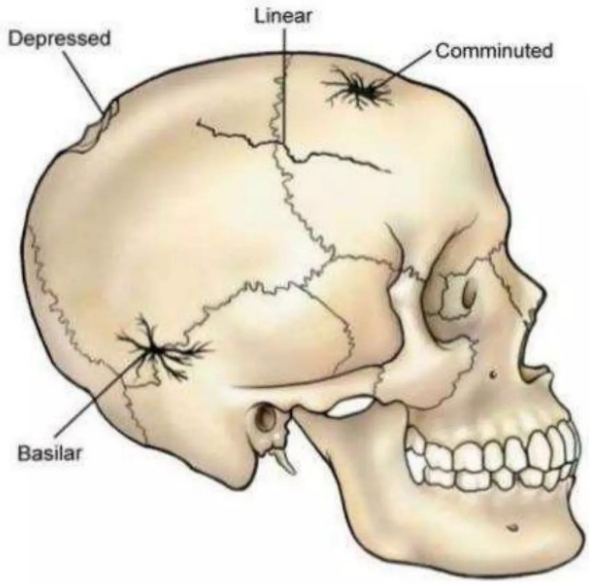


Figure 1.11 – Types of skull fractures [Bhattacharya, 2018]

1.2.2 Pathophysiology of TBIs

Traumatic damage to brain tissue can compromise its function, starting a sequence of events that cause further damage.

TBI can cause cerebral edema and decreased cerebral blood flow. The size of the cranial vault is defined by the bones of the skull and is filled by incompressible cerebrospinal fluid (CSF); the brain tissue is only minimally compressible as well. As a result, swelling in the brain due to

edema or an intracranial hematoma doesn't have any room to expand, thus causing increased intracranial pressure (ICP).

Cerebral blood flow is proportional to cerebral perfusion pressure (CPP, the difference between mean arterial pressure MAP and mean ICP). Therefore, CPP decreases as ICP increases (or MAP decreases). When cerebral perfusion pressure falls below 50 mmHg, cerebral ischemia can occur. Ischemia and edema can cause secondary damage (e.g. the release of excitatory neurotransmitters, intracellular calcium, free radicals, and cytokines), which leads to further cellular damage, edema, and further increase in ICP. Systemic complications of trauma, such as hypotension or hypoxia, can also contribute to cerebral ischemia and are often denoted as secondary brain injury.

Excessive ICP initially causes global brain dysfunction; if ICP is not relieved, brain tissue can be pushed through the tentorium or through the foramen magnum, causing cerebral herniation, with serious consequences. If ICP rises to equal the MAP, the CPP falls to zero, resulting in cerebral ischemic death by ischemia.

Lesions of the hypothalamus, subfornical organ, and nucleus of the solitary tract can lead to deep changes in cardiac and renal function. The damage affects hypothalamic-pituitary-adrenal axis, causing hemodynamic instability, hypertension, tachycardia, and inducing fluid retention in the kidney. These modifications may subsequently lead to acute kidney injury and neurogenic myocardial stress, revealing as acute systolic heart failure.

Concussive injuries in teenagers or children can lead to hyperemia and increased cerebral blood flow.

Second impact syndrome is denoted as a sudden increase in ICP, sometimes fatal, following a second traumatic event occurring before complete recovery from a previous minor head injury. It is ascribed to loss of autoregulation of cerebral blood flow, leading to vascular congestion, increased ICP, and herniation.

1.2.3 Symptoms of TBIs

First, in most patients with moderate or serious head injury, loss of consciousness occurs, generally for seconds or minutes. Some patients with minor head injury show only confusion or amnesia; this is usually retrograde (memory loss affects a period from a few seconds until a few hours before the event). Children can simply become irritable. Some patients suffer convulsions, often within the first hour or day. After these early symptoms, patients can get completely awake, or loss of consciousness and alterations of the brain function from slight confusion to the stupor and coma may occur. The duration and severity of the symptoms are approximately proportional to the gravity of the trauma but are not specific.

The Glasgow Coma Scale (GCS) is a scoring system for the first evaluation of the severity of the traumatic brain lesion. It considers eyes opening, verbal response, motor response. The lowest score (3) indicates probably lethal damage, especially if both pupils do not respond to light and no oculovestibular response is observed. The highest initial scores tend to predict better recovery. Conventionally, severity of TBI according to the Glasgow Coma Scale is defined as follows:

- 14 or 15: mild TBI
- 9-13: moderate TBI
- 3-8: serious TBI

The forecast of the severity of the traumatic brain lesion and the prognosis can be better defined considering also the CT results and other factors.

Some patients with initially moderate traumatic brain lesion and few patients with initially medium TBI lean towards worsening. In infants and small children, a Glasgow Coma Scale specifically modified is used.

Hypoxia and hypotension can decrease the score of the Glasgow Coma Scale, so the score after recovery for cardiopulmonary damage are more specific for cerebral dysfunction [Holbourn, 1943; Bilston, 2019; Mao, 2023].

1.2.4 Head and Brain Injury Criteria

To quantify the risk of injury after an impact, several Brain Injury Criteria (BIC) have been developed, analysing different types of head impacts, in particular sports and road accidents. The first BIC were developed from automotive crash tests using cadaveric specimens, thus focusing on head fractures; afterwards, brain injuries with closed head impacts gained more attention.

Initially, Head Linear Kinematics (velocity, acceleration) were chosen as indicators related to brain injuries, but later Rotational Kinematics (angular velocity, angular acceleration) were found to have a stronger correlation with brain strain. Finite element models were also introduced to simulate the effect of the application of loads equivalent to the experimental measured impact on brain behaviour. From a physiological point of view, tissue strain is often considered the key parameter to quantify brain injury.

It should be observed that the skull is a very rigid structure, which can resist to strong impacts while still protecting the brain: Holbourn found a reduction in diameter of 1 cm after the application of a force equal to 1 ton. Anyway, this is an average value, as the mechanical characteristics of the skull bones depend on the thickness of each individual bone.

The Wayne State Tolerance Curve (WSTC) is a diagram which illustrates the relationship between head acceleration, duration of acceleration and onset of concussion (fig. 1.12): values

falling above the curve exceed the tolerance level and therefore are considered as life-threatening. The WSTC indicates an inverse relation between the value of acceleration and the duration of the impact: very high acceleration can be tolerated for a very short duration, while increasing the duration of impact is likely to cause head injury for lower acceleration values.

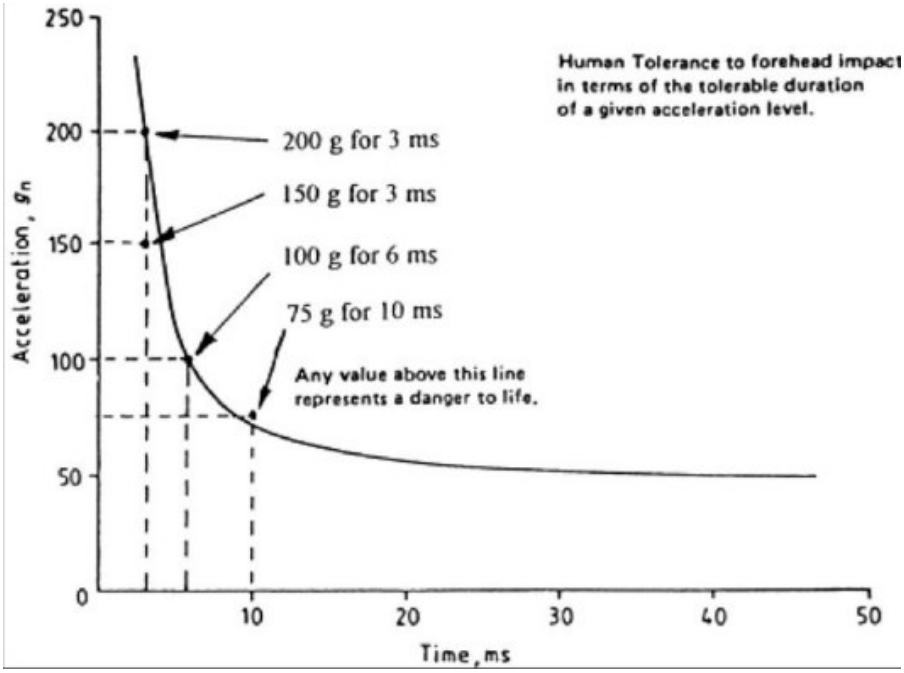


Figure 1.12 – WSTC for human tolerance to head impacts

The Head Injury Criterion (HIC), developed by Versace et al, assesses the probability of head injuries resulting from an impact. It is the most widely used injury criteria developed in the assessment of head injury risks in motor vehicle regulation. HIC value is evaluated considering the integral time of the resulting translational acceleration recorded in the head's center of mass. HIC is generally calculated as:

$$HIC = max\left\{(t_2 - t_1)\left[\frac{1}{(t_2 - t_1)}\int_{t1}^{t2} a(t)dt\right]^{2.5}\right\} \quad (1.1)$$

where:

- $a(t)$ is the resultant of the linear accelerations in g
- t_1 and t_2 are the limits of the time interval for integration

The threshold of the criterion depends on the interval time chosen. The HIC is set by the standards at the limit value of 1000 as a threshold not to be exceeded, and 15 ms is the duration of the interval to calculate the value.

Several correlations were proposed to connect the calculated HIC value to the corresponding risk of injury. For example, U.S. automotive manufacturers must comply to standards and regulations which relate the HIC and the risk of injury according to a scoring system, the AIS (Abbreviated Injury Scale) which divides the severity of the lesions into 6 levels, from minor to lethal (fig. 1.13).

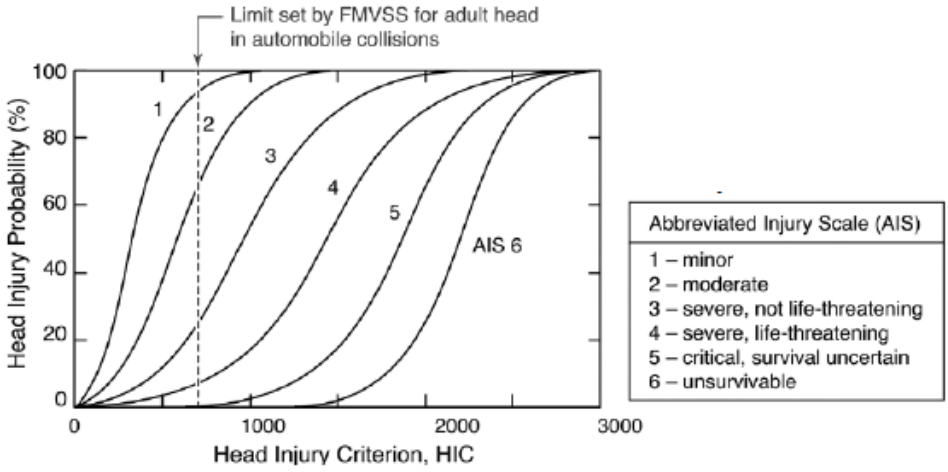


Figure 1.13 – Limits to HIC in road collisions

Anyway, the only HIC, although widely used, is not a comprehensive predictor for all the head injuries, since it considers linear acceleration, but neglects the rotational movements occurring during the impact. In fact, most traumatic head injuries are caused by non-linear impacts, which impose a rotational motion, thus eliciting forces that twist or shear the brain inside the cranium. Linear and rotational acceleration injuries often occur together, but the damages they cause are quite different: while linear acceleration is often underlying focal brain injuries, rotational acceleration more commonly implicates both focal and diffuse brain injuries [Holburn, 1943]. Focal injuries due to linear impact generally result in contusion, laceration, and intracranial haemorrhage, while diffuse damage mainly induced by acceleration/deceleration usually results in diffuse axonal injury or brain swelling. The consequences of head injuries vary significantly as a result of the type of impact received. To this purpose, in addition to HIC, Takhounts et al. along with the NHTSA (National Highway Traffic Safety Administration) developed the Brain Injury Criterion (BrIC) based on head rotational velocity for a more complete evaluation of TBI risk.

The assessment of BrIC needs to record the angular velocities ωx, ωy, and ωz:

$$BrIC = \sqrt{\left(\frac{\omega_x}{\omega_{xC}}\right)^2 + \left(\frac{\omega_y}{\omega_{yC}}\right)^2 + \left(\frac{\omega_z}{\omega_{zC}}\right)^2} \tag{1.2}$$

where:

- ω_i is the maximum angular velocity about ith axis (i = x, y, z)

- ω_{xC}, ω_{yC}, and ω_{zC} are critical values, corresponding to 66,25 rad·s^{-1}, 56,45 rad·s^{-1} and 42,87 rad·s^{-1}

The highest value that BrIC can assume is 1 and it corresponds to a probability of 50% of AIS 4 (severe, life threatening). Since BrIC introduces an effect of angular velocity on brain damage, it allows a better assessment of the risk of head injury [Versace, 1971; Takhounts, 2013].

PRA (Peak Rotational Acceleration) was identified as strongly related to injury severity, with a value which should not exceed 10000 rad·s^{-2}. Specifically, multiple studies identified a correlation between increasing magnitude of rotational acceleration and increasing injury severity [Abel, 1978; Margulies, 1992].

The finite element modeling technique, which will be discussed later, allows the measurement of some parameters that can be used for brain damage estimation. These are for example Maximum Principal Strain (MPS), Cumulative Strain Damage Measure (CSDM), Dilatational Damage Measure (DDM), and Relative Motion Damage Measure (RMDM).

The maximum principal strain (MPS) is a widely used indicator for mild TBI [Zhan et al., 2020].

The Cumulative Strain Damage Measure (CSDM) is used as a predictor of diffuse axonal injury event; it expresses the fraction of brain volume exceeding a certain strain threshold.

The Dilatational Damage Measure (DDM) is a cumulative indicator for localized injury or contusion; it is defined as the fraction of brain volume exceeding a defined pressure threshold.

The Relative Motion Damage Measure (RMDM) is a non-cumulative time-dependent measure to predict subdural hematomas risk [Takhounts, 2008].

The above considerations have important implications in the field of protective devices. Indeed, helmets are relatively effective in absorbing linear impacts, but not so effective in impacts involving rotation of the head. In these cases, the helmet grips the head dragging it into rotation in the direction of the force generated by the impact [SHP – Safety and Health Practitioner, 2023]. Only recently, manufacturers have been designing helmets keeping this aspect in mind. In this regard, the forthcoming ECE 22.06 standard for testing motorbike helmets involves an oblique impact test on a steel anvil covered with P80 abrasive paper inclined at 45°, at a speed of 8 m/s. The pass criteria are:

- PRA<10400 rad·s^{-2}
- BrIC <0.78

1.3 Physical prototypes for impact tests

As mentioned before, there is a strong need to investigate about the biomechanical response of brain tissue related to traumatic events.

Experiments on human tissues are very difficult to carry out, both for ethical reasons and because brain samples taken from cadavers must be used immediately, as cold storage alters their mechanical properties. Experiments on animal tissue are also only partially representative, since the mechanical properties of animal brains are quite different from human ones.

Moreover, the experimental literature references about the mechanical properties of brain tissue show a very large variability; this is due to many factors, including heterogeneity, anisotropy, age dependence, post-mortem time and others. Differences in test protocols also influence the measured properties, so that it is very challenging to achieve comparable and repeatable results with this methodology.

What above mentioned explains the wide use of lab testing with the aid of surrogates or dummies to simulate the effects of different types of impact, using anthropometric devices (ATD) to acquire the test data. Two well-known examples are the Hybrid III 50th Percentile and the THOR (Test device for Human Occupant Restraint) ATD (fig. 1.14), developed by Humanetics in collaboration with the National Highway Traffic Safety Administration (NHTSA) and the biomechanics committees of the Society of Automotive Engineers (SAE). These dummies are commonly used in automotive to assess the severity of injuries resulting from a road accident.

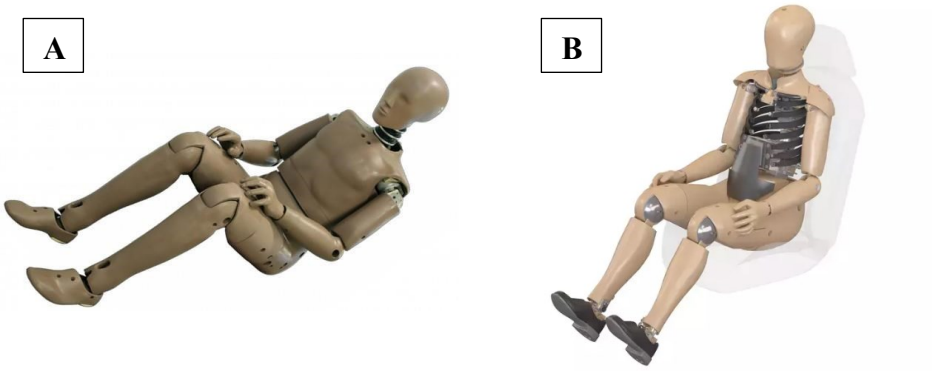


Figure 1.14 – (A) Hybrid III 50th Percentile and (B) THOR ATDs [Humanethics]

However, accurate testing on specific body parts like the head require specific instruments for analysing the effects of localized impacts on the head, while the general-purpose instrumented dummies are generally designed for analysis on the body as a whole. For example, the head of Hybrid III 50th Percentile (fig. 1.15 A) is a hollow aluminium body without any simulants for the brain; it's wrapped with a silicone rubber layer to mimic the external soft tissue. Instruments located in the head of dummies like Hybrid III or THOR are typically only triaxial accelerometers in the CoM. However, the data collected are focused on the kinematics of the head, not considering the brain. Another example of rigid headform is the EN960 (1.15 B), which consists of a hollow aluminum or magnesium skull, with an accelerometer at the CoM. NOCSAE (fig. 1.15 C) is a more biofidelic headform which consists of a nylon skull covered

with a urethane layer simulating the external soft tissue along with a gelatine mass representing the brain; it is instrumented with triaxial accelerometers at the CoM.

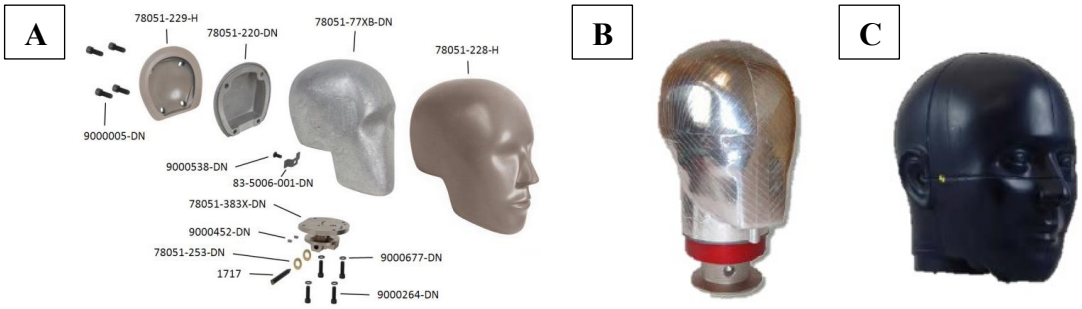


Figure 1.15 – (A) Head of Hybrid III ATD, (B) EN960 headform, (C) NOCSAE headform

More advanced headforms have been developed including brain simulants.

In 2014, Freitas et al. used an advanced human head surrogate for investigations on blast effects on military helmets (fig. 1.16). This headform is made of a re-hydrated human cranium and gels to reproduce the soft tissues like the skin (5–7 mm Perma-gel layer), the dura (0.5 mm silicone membrane), and the brain (Perma-gel with iron). This headform is equipped with 4 pressure sensors in the brain to measure intracranial pressure, 12 strain rosettes to detect cranial strain, and a triaxial accelerometer placed at the hard palate to acquire skull and helmet acceleration.



Figure 1.16 - Freitas et al. headform from human skull [Freitas et al., 2014]

In 2017, Miyazaki et al. introduced a modular and destructible headform (fig. 1.17) for the assessment of baseball and hockey impacts. It is composed by a 3D printed skull equipped with accelerometers, a gel brain with markers for video capture, and water [Petrone et al., 2018].



Figure 1.17 - Miyazaki et al. headform [Miyazaki et al., 2017]

The work here reported aims to contribute to improve the biofidelity of human head surrogates. The experimental activity carried out is part of a long-term project, also in collaboration with Mid Sweden University, aiming to design and build a biofidelic replica of a human head,

equipped with different types of sensors (accelerometers, gyroscopes and pressure sensors) for the acquisition of data obtained from impact tests. The development of the project lead to build several prototypes with progressive improving levels of biofidelity, as described later.

With particular reference to the aspect of biofidelity, it should be stated that, due to the complexity of the anatomical structures and to the characteristics of biological tissues, it is particularly difficult to obtain a satisfactory biofidelity of the model. The first issue relates to the choice of materials: biological tissues, in fact, have very peculiar physical and mechanical properties, along with the way the different tissues interact in the living body, which are quite difficult to replicate using metals and polymeric materials. Also, the fabrication of the models is expensive and time-consuming, due to the prices of the materials, the costs of the production (typically by casting or additive manufacturing), and the assembly processes, with the insertion of the sensors as well.

For these reasons, the computer simulation of the effects of the different types of impact through finite element modeling is a very useful tool. In this way, once the model is validated, it is possible to analyse any loading condition without using the physical headform, which would unavoidably be damaged or destroyed during the most demanding tests. This allows to optimize development timing, reduces the amount of materials, and permits to proceed with laboratory experiments after having excluded the solutions that have not proved to be adequate during the simulations.

1.3.1 UniPD surrogates

The main characteristics of the previous prototypes of Instrumented Human Head Surrogate (IHHS) are briefly summarized. Simulants for soft tissues are described by the manufacturer (Polytek Development Corp, USA) as follows:

PlatSil® Gels are 1A:1B (by weight or volume) platinum cured silicone systems that can be used as mold rubbers, to create prosthetic appliances, and for life casting. Polytek offers an array of accessory products that can be used independently or in concert to increase working time, accelerate cure time, thicken the mix for brushing/layering, thin the mix for easier pouring, or soften or harden the rubber. Smith's Theatrical Prosthetic Deadener and PlatSil® Deadener LV can be added to soften and eliminate the snappy, synthetic look and feel of ordinary silicone rubbers. "Deadened" PlatSil Gels can be made to look, feel and move like living tissue. Unlike silicone fluid, Deadener does not leach from the cured rubber/appliance, so bonding and use are far easier.

IHHS 1.0 (2018)

The material chosen to surrogate skin was PlatSil Gel-25 1A:1B. The skull was made with ABSplus-P430 (acrylonitrile butadiene styrene thermoplastic), 3D printed with FDM technology and assembled with a sawtooth suture (fig. 1.18 A) to ensure a firm connection between the top and bottom parts of the model. The skull was fitted with sensors placed outside (3 triaxial accelerometers and 2 biaxial gyroscopes) and inside (10 pressure sensors - Solid State Pressure Sensor STD Series). CSF was simulated with siliconic oil SilOil M4.165/220.10 (Huber). The meninges were manufactured using a 7 mm thick silicone coated Nylon Denier 31 (Dura mater) and nonwoven polyester (arachnoid trabeculae). The brain was made with silicone rubber PlatSil Gel-10 1A:1B (fig. 1.18 B), embedding during the casting 8 triaxial accelerometers (ADXL377, Analog Devices, +/- 200g) (fig. 1.18 C) and 2 biaxial gyroscopes (LPY4150AL and LPR4150AL) manufactured by STMicroelectronics [Carraro, 2018; Petrone et al., 2019].

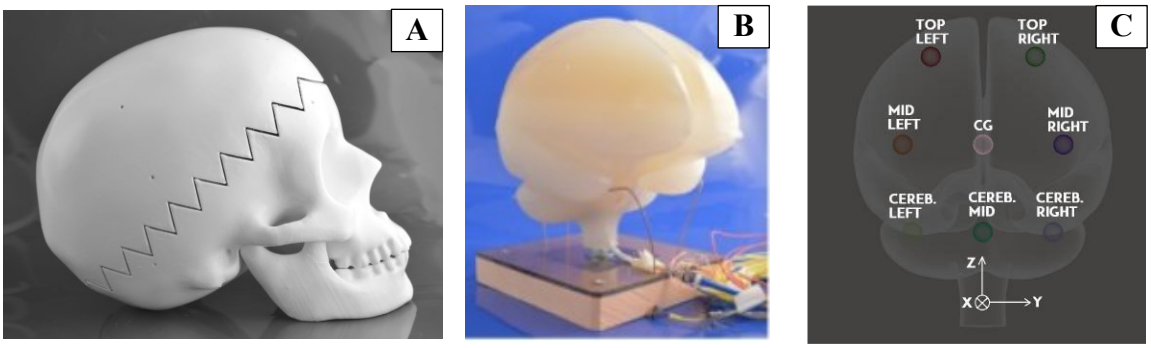


Figure 1.18 – Some details of IHHS 2018: (A) sawtooth suture of the skull, (B) brain, (C) triaxial accelerometers [Carraro, 2018; Petrone et al., 2019]

IHHS 2.0 (2019)

The model was downscaled by 10% to allow to fit a helmet for further testing. Respect to the previous unit, the material used for the skin was PlatSil Gel-10 1A:1B (fig. 1.19 A). Skull was made with Polyamide PA2200, 3D printed with SLS, AM technology (fig. 1.19 B). Casco Rubber Fix was used to connect low and top parts of the skull surrogate, that was not reopenable. The sensors placed outside the skull were 1 triaxial accelerometer and 2 biaxial gyroscopes, while inside the skull 10 pressure sensors - MS5401-AM Miniature SMD Pressure Sensor Surface mount, with a full-scale range of 1 bar were fitted. CSF was simulated with synthetic motor oil Q8 Formula Ultra V 0W-20; for the meninges a thin layer of Silicone Glue Contractive Adhesive S9 Super was sprayed on the skull to mimic the Dura mater, along with 3 mm thick nonwoven fabric placed only in some spots (SAS). Brain tissue was surrogated with PlatSil Gel-OO20 1A:1B (fig. 1.19 C). The sensor equipment was updated with 7 triaxial accelerometers (ADXL377 3-Axis accelerometer, manufactured by Analog Devices Inc) (fig.

1.19 D) and 2 biaxial gyroscopes (LPY4150AL and LPR4150AL) by STMicroelectronics [Uriati, 2019].

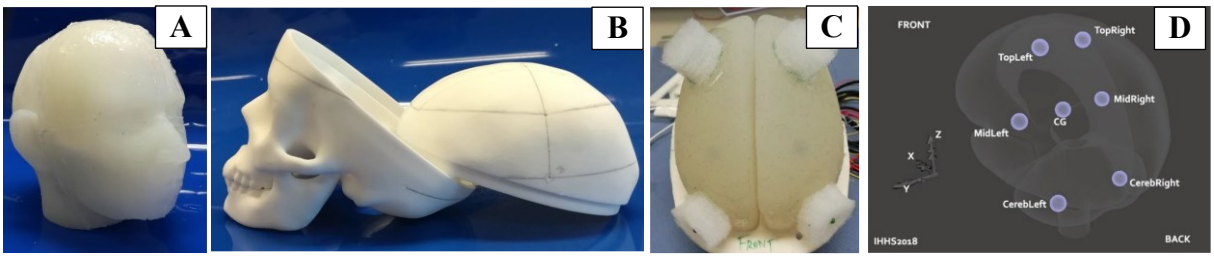


Figure 1.19 – Some details of IHHS 2019: (A) skin, (B) skull, (C) brain and meninges, (D) triaxial accelerometers [Uriati, 2019]

IHHS 2020

Skin was made with the same PlatSil Gel-10 1A:1B (fig. 1.20 A), while the skull was 3D printed with Polyamide PA12. A triaxial accelerometer was placed externally and 4 pressure sensors were fitted inside. CSF simulant was distilled water, which is more biofidelic than oil, which is lighter and more viscous than CSF. To realize the meninges, a 6 mm thick nonwoven polyester (fig. 1.20 B) was wrapped all around the brain with a thin layer of PlatSil Gel-OO30 1A:1B:2D. Brain was cast in silicone rubber PlatSil Gel-OO30 1A:1B:2D (fig. 1.20 C), with 2 triaxial accelerometers ADXL377 (Contento's cube) embedded (fig. 1.20 D). Brain Multi Axial Sensorized Cube (MASC) in PlatSil Gel-OO30 1A:1B:2D with inside 4 triaxial accelerometers (ADXL377 3-axis ±200g), 2 biaxial gyroscopes at the origin (LPR4150AL and LPY4150AL) and 3 uniaxial pressure sensors in the center of gravity of BMASC (MS5401-AM (1bar) 240 mV) was proposed for a future prototype (fig. 1.20 E) [Faggin, 2020; Silvestroni, 2020].

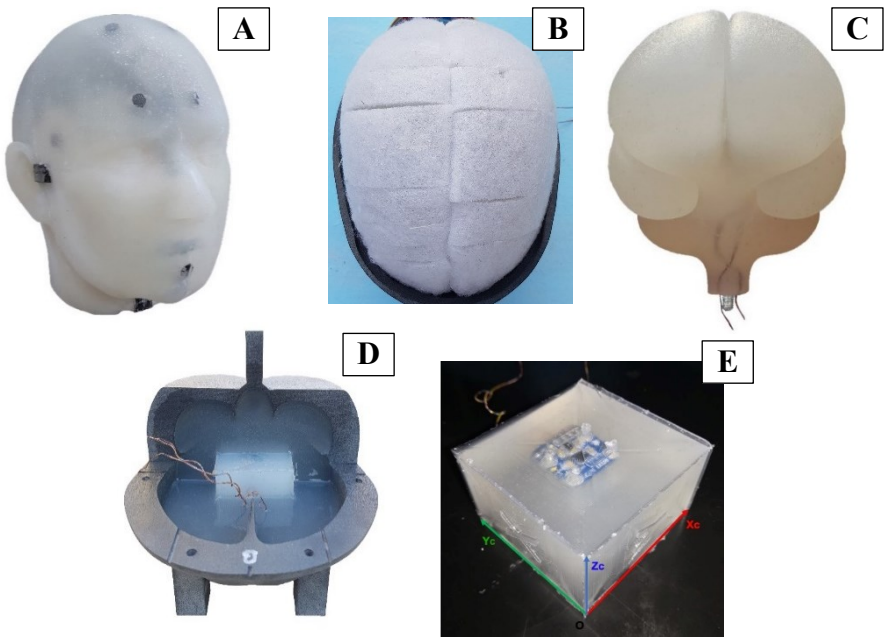


Figure 1.20 – Some details of IHHS 2020: (A) skin, (B) meninges, (C) brain, (D) Contento's cube, (E) BMASC [Faggin, 2020; Silvestroni, 2020]

IHHS 2021

Simulant material for skin, skull and CSF were unchanged. With respect to the previous model, the modifications relate to the sensors, with an external triaxial accelerometer in the front of the skull and 4 internal pressure sensors on both halves of the skull. Meninges have been fabricated using a 6 mm thick nonwoven polyester applied with a thin layer of PlatSil Gel-OO30 1A:1B:2D (fig. 1.21 A). To simulate brain, silicone rubber PlatSil Gel-OO 1A:1B:1D was chosen. A MAPS (Multi-Axial Stress Sensor) was installed to detect stresses inside the silicone rubber, composed of a triad of orthogonal pressure sensors p1, p2, p3 plus three auxiliary pressure sensors p4, p5, p6 placed at their bisectors. Moreover, 2 triaxial accelerometers and 1 triaxial gyroscope were embedded (fig. 1.21 B) [Zullo et al., 2021].

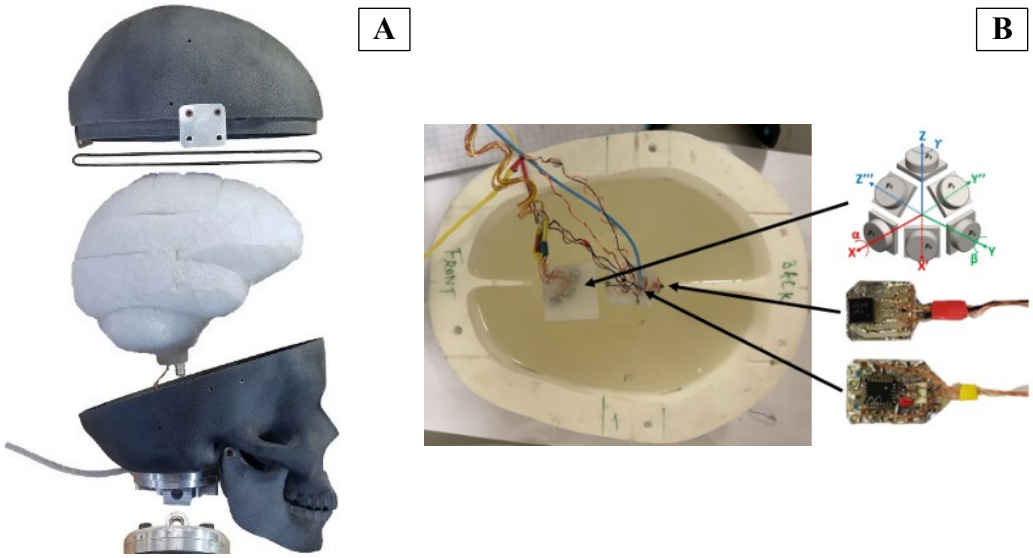


Figure 1.21 – Some details of IHHS 2021: (A) skull and meninges, (B) MAPS, triaxial accelerometers and gyroscope [Zullo et al., 2021]

Current prototype (IHHS 2022)

Simulant material for skin (fig. 1.22 A), skull (1.22 B), CSF, and brain (fig. 1.22 C) were unchanged. The coupling of the two parts of the skull was improved by a triangular indentation (fig. 1.22 D). The arachnoid trabeculae were surrogated in open-cell polymer foam 30 PPI (pores per inch) (fig. 1.22 E). Falx cerebri and tentorium cerebelli were designed in CAD and 3D printed in thermoplastic polyurethane (TPU Shore 95A) using SLS technique (fig. 1.22 F/G/H). Further refinements were made to improve force transmission, the assembly, and the sensor equipment. In detail, 10 metric screws M3 and brass inserts were added to allow a solid and removable closure. A DTS 6DX PRO-A triaxial accelerometer (500 g) and gyrometer (8000 dps) was positioned under the mouth floor of the skull (fig. 1.23 A). Moreover, 12 MS5407 piezoresistive pressure sensors (700 kPa) were all mounted on the upper half of the internal skull to measure CSF pressure (fig. 1.23 B). A MAPS (700 kPa), an ADXL 377 triaxial

accelerometer (200 g), and a LPR+LPY triaxial gyrometer (2000 dps) were all placed in brain COM (fig. 1.23 C).

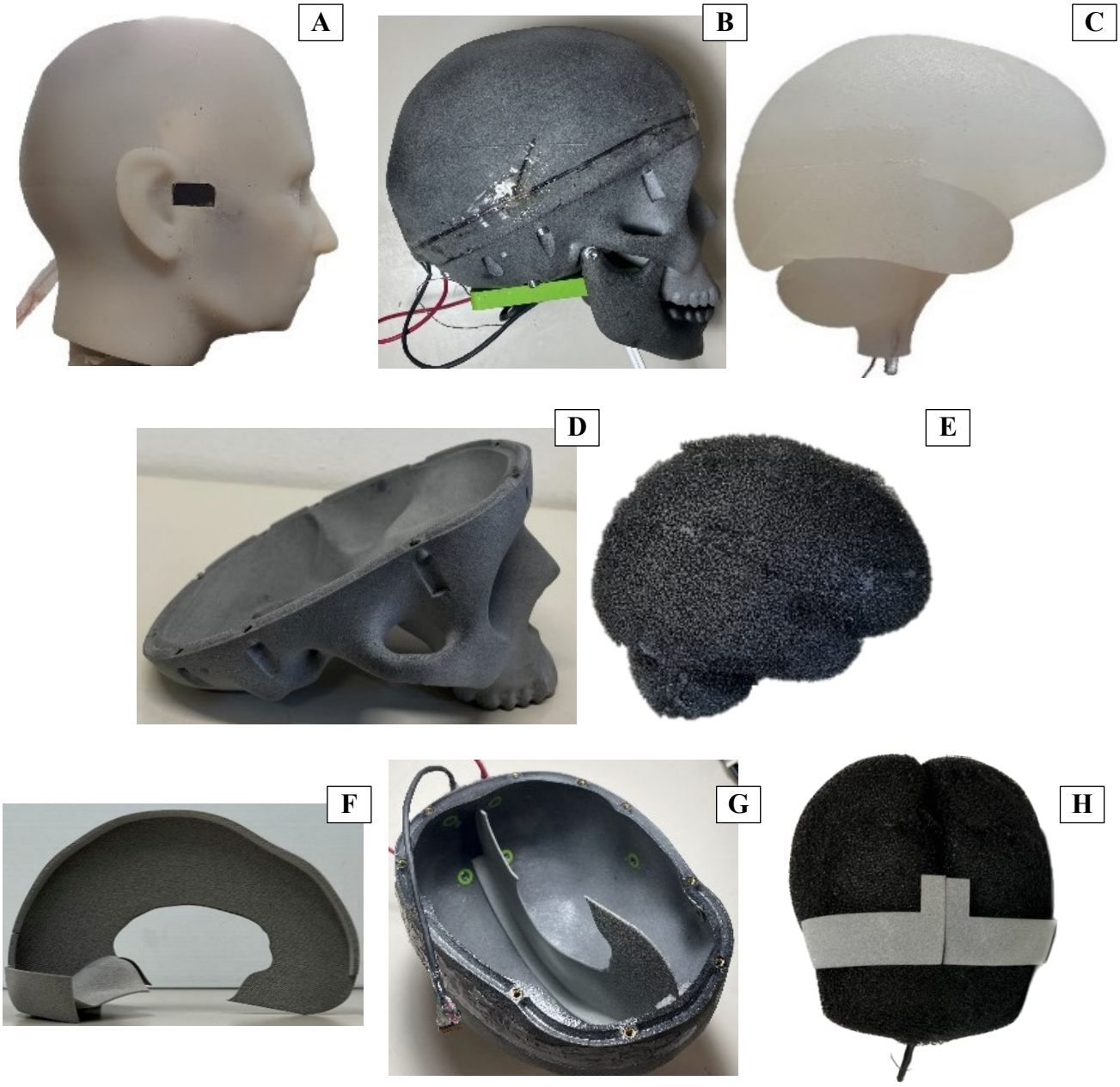


Figure 1.22 – Details of the current prototype components: (A) skin, (B) top skull, bottom skull-jaw, (C) brain, (D) triangular indentation for skull closure, (E) arachnoid trabeculae, (F) falx-tentorium, (G) falx glued to the top skull, (H) tentorium placed between brain occipital lobes and cerebellum

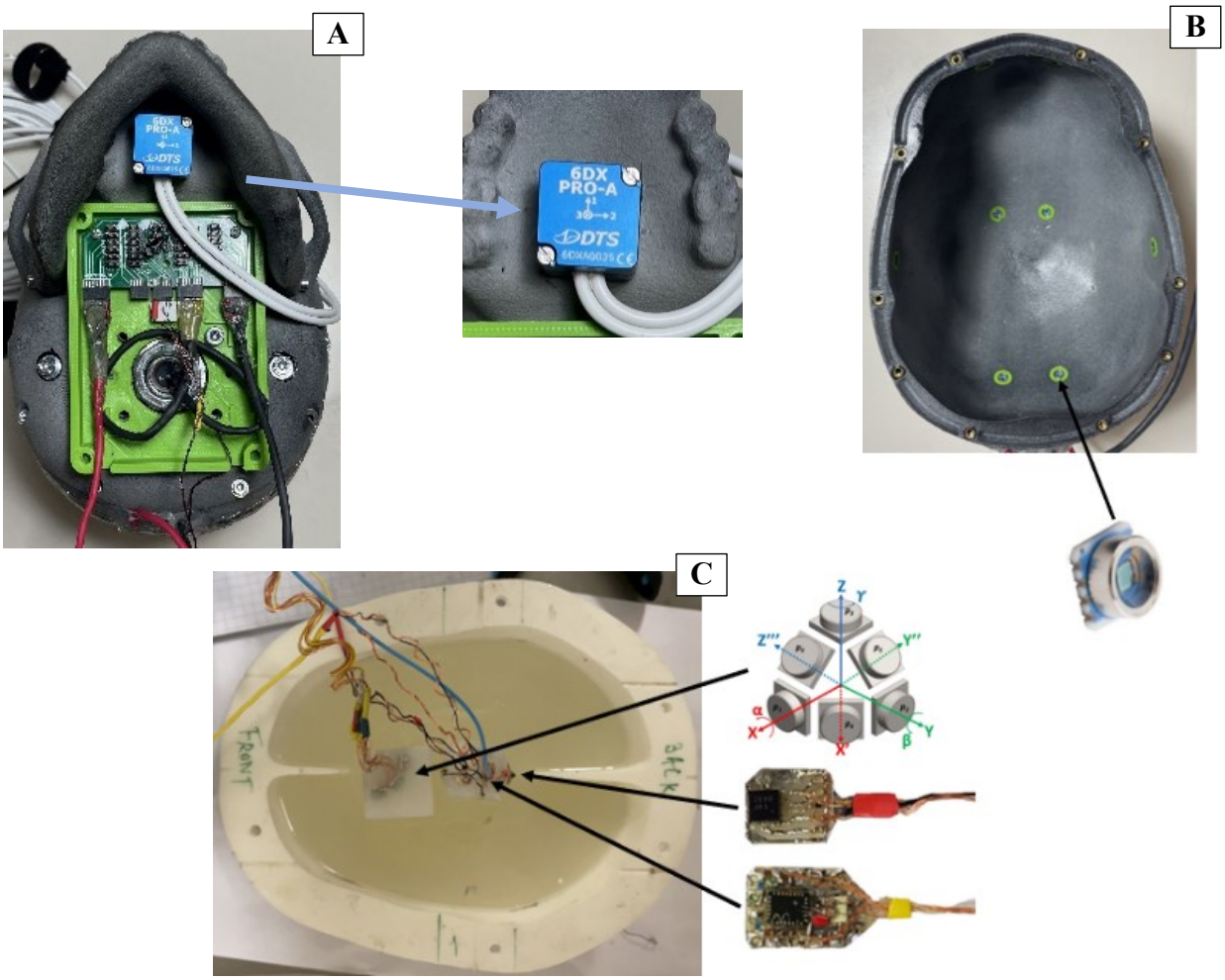


Figure 1.23 – Details of the current prototype sensors: (A) DTS 6DX PRO-A, (B) MS5407 piezoresistive pressure sensors, (C) MAPS, ADXL 377 triaxial accelerometer and LPR+LPY gyroscope

Table 1.1 summarizes the materials used for the IHHS versions.

	2018	**2019**	**2020**	**2021**	**current**
Brain	PlatSil Gel-10 1A:1B	PlatSil Gel-OO20 1A:1B	PlatSil Gel-OO30 1A:1B:2D	PlatSil Gel-OO 1A:1B:1D	PlatSil Gel-OO 1A:1B:1D
Arachnoid trabeculae	Nonwoven polyester	3 mm thick nonwoven fabric (spots)	6 mm thick nonwoven polyester	6 mm thick nonwoven polyester	Open-cell polymer foam 30 PPI
Falx and Tentorium	-	-	-	-	TPU
Cerebrospinal fluid	SilOil M4.165/220.10	Synthetic motor oil	Distilled water	Distilled water	Distilled water
Skull	ABSplus-P430 styrene thermoplastic	Polyamide PA2200	Polyamide PA12	Polyamide PA12	Polyamide PA12
Skin	PlatSil Gel-25 1A:1B	PlatSil Gel-10 1A:1B	PlatSil Gel-10 1A:1B	PlatSil Gel-10 1A:1B	PlatSil Gel-10 1A:1B

Table 1.1 – Materials used for UniPD prototypes

The objective of this project is the development of a finite element model of the latest evolution of the instrumented surrogate of the human head; to do this, a constitutive and a geometric analysis are required.

The constitutive analysis involves the mechanical characterisation of the materials which compose the parts of the object to be modeled, and the identification of the corresponding constitutive parameters.

The geometric analysis consists of CAD drawing of the accurate solid model of the prototype. In the case of modelling anatomical structures, images from diagnostic investigations (MRI/CT) are segmented to obtain files in STL[1] format for 3D printing. These files are then processed and converted into solid models for FE analysis by importing them into the appropriate software, in this case Abaqus FEA by Dassault Systèmes.

The following chapters describe the entire process in detail.

[1] STL (STereo Lithography interface format, or an acronym for 'Standard Triangulation Language' or alternatively 'Standard Tassellation Language') is a file format, binary or ASCII, created for CAD stereolithography software, widely used in rapid prototyping. The 3D geometry is described by a mesh of triangles, each of which contains dimensional information: the more complex the surface, the more numerous the triangles. In addition, each triangle contains the definition of the normal, a line exiting the triangle and perpendicular to it, which describes the direction of the inside and outside of the object.
Unlike other CAD formats, the object is not 'solid', but is formed only by the outer surface or 'skin'. The STL format, unlike CAD formats, is independent of the modelling mode or the mathematical definition of the constituent surfaces: the STL format, in fact, saves, for each triangle, only the co-ordinates of the 3 vertices in space (co-ordinates x, y, z) and the direction of the normal. This leads to a series of problems, due to the approximation of curved lines with broken straight lines, which must be resolved by appropriate processing on the mesh. [http://www.weerg.com/it/guide/file-formato-stl]

Chapter 2: Constitutive analysis

2.1 Mechanical properties of human tissues and their surrogates

In general, biological soft tissues exhibit an anisotropic behaviour, due to their non-homogeneous microstructure and to the arrangement of their fibers, which show preferred directions. The tensile response of soft tissues is nonlinear, and they may endure large deformations. Soft tissues show viscoelastic behaviour, depending on the structure of their collagen-based extra cellular matrix, which contains proteoglycans providing a viscous sliding between collagen fibrils.

The mechanical properties of brain tissue are heterogeneous and anisotropic, and show both time-independent hyperelasticity and time-dependent viscoelasticity. With a shear modulus of the order of 1 kPa, brain results to be made of the softest tissue in the human body (fig. 2.1). It also deforms noticeably under the effect of gravity, and this may have consequences on the experiment results. Further, brain tissue is very fragile, especially when subjected to large deformations. It was found that a tensile strain about approximately 18% is the threshold limit before the tear of the axons enclosed in the white matter [Budday et al., 2020].

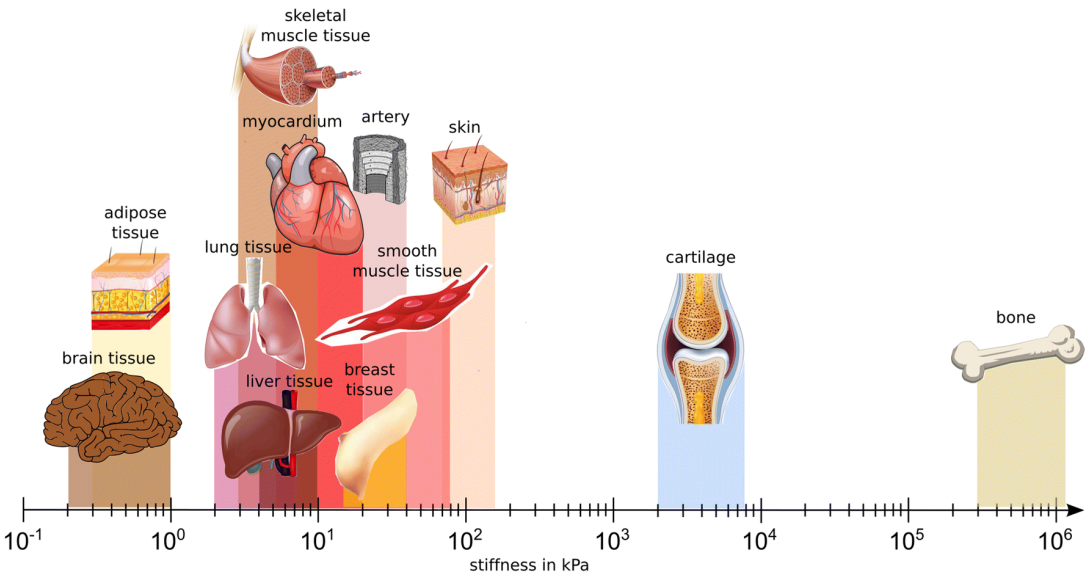


Figure 2.1 – Shear stiffness of human tissues [Budday et al., 2020]

The main challenge in this research field is the choice of materials suitable to simulate the mechanical behaviour of biological tissues. Typically, very low hardness silicone rubbers are used to simulate brain tissue and skin. As for the skin and the underlying tissue, the most used materials are silicone rubbers of the type used in the cinema for making masks. For brain substitutes, very fluid two-component gels are used, which in any case are often harder than biological tissue.

Bone tissue is difficult to simulate due to its sandwich structure which gives it its peculiar properties of resistance, lightness and flexibility; the best compromise is generally represented by polymers (e.g. polyamide).

2.1.1 Hints on the behaviour of rubber-like materials

Rubber-like materials exhibit a viscoelastic behaviour, showing both elastic and viscous properties while strain subjected. Viscoelastic materials are characterized by time-dependent mechanical properties; thus, the mechanical response of a material point results to be strongly influenced by time.

As observed while performing a uniaxial tensile test, their stiffness depends on the time during which the load is applied, resulting in a different effective Young modulus E as a function of the strain rate $\dot{\varepsilon}$. Moreover, load-unload test shows that load and unload stress-strain curves don't overlap, and the area enclosed by the two curves (hysteresis area) represents the dissipated energy. In fact, when a viscoelastic material is subjected to a time-dependent strain mechanism, some energy is dissipated in the relative sliding among the subcomponents of the microstructure.

Creep test, stress relaxation test and Dynamic Mechanical Analysis (DMA) can be performed to characterize the mechanical behaviour of a viscoelastic material.

A creep test consists of imposing a protracting constant stress in an almost zero loading time, with a resulting strain that increases with time. Conversely, stress relaxation consists of imposing a protracting constant strain in an almost zero loading time with a resulting stress decreasing with time.

In particular, the characterization of the viscoelastic behaviour of polymers like rubbers can be performed with the Dynamic Mechanical Analysis (DMA). This method allows to study the mechanical response of a viscoelastic material at different loading frequencies under dynamic perturbations. This procedure consists of imposing an oscillatory (generally sinusoidal) strain to the specimen. Strain and stress equations can be written as follows:

$$\varepsilon(t) = \varepsilon_0 \sin(\omega t) \tag{2.1}$$

$$\sigma(t) = \sigma_0 \sin(\omega t + \delta) \tag{2.2}$$

where ε_0 and σ_0 represent strain and stress amplitude respectively, ω is the angular frequency and δ denotes stress and strain phase lag (phase angle). The stress and strain curves are in phase in an ideal elastic material (fig. 2.2 A), while an ideal viscous material is characterized by a 90° phase angle (fig. 2.2 C). Polymers (like rubbers) show both viscous and elastic behaviour, resulting in a $0° < \delta < 90°$ phase lag between the stress and the strain curves [Meyers and Chawla, 1999; Paar, 2023], as shown in fig. 2.2 B.

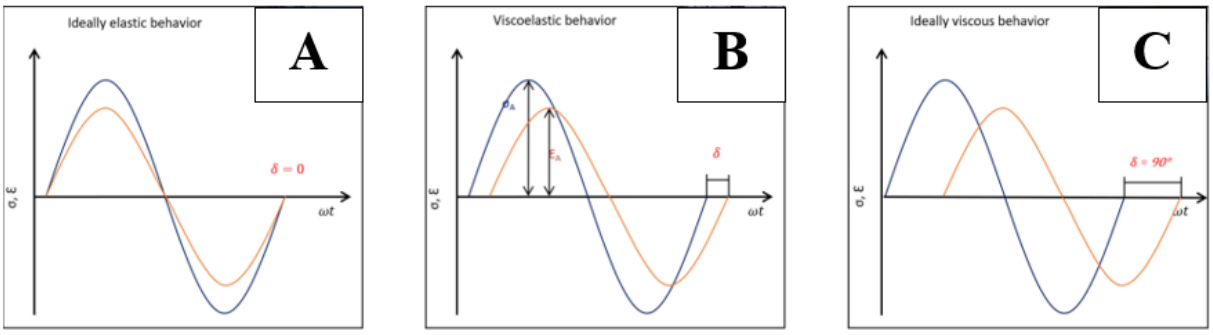


Figure 2.2 – Stress-strain relationship and phase angle behaviour for: (A) ideally elastic material, (B) viscoelastic material, (C) ideally viscous material [Paar, 2023]

The energy stored is quantified by the tensile storage modulus, while the tensile loss modulus assesses the energy lost in heat. These two moduli can be determined developing the (2.2) as follows:

$$\sigma(t) = \sigma_0 \cos(\delta) \sin(\omega t) + \sigma_0 \sin(\delta) \cos(\omega t) \tag{2.3}$$

$$\sigma(t) = \frac{\sigma_0}{\varepsilon_0} \varepsilon_0 \cos(\delta) \sin(\omega t) + \frac{\sigma_0}{\varepsilon_0} \varepsilon_0 \sin(\delta) \cos(\omega t) \tag{2.4}$$

The ratio $\frac{\sigma_0}{\varepsilon_0} = E^* = E' + iE''$ is called complex tensile modulus and it is the sum vector of the tensile storage modulus $E'$and the tensile loss modulus E'', as shown in fig. 2.3.

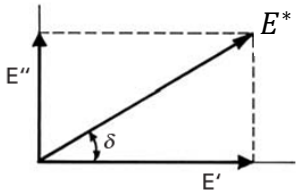


Figure 2.3 – Complex tensile modulus [Meyers and Chawla, 1999]

The stress equation (2.4) can be written as follows:

$$\sigma(t) = E^* \cos(\delta)\, \varepsilon_0 \sin(\omega t) + E^* \sin(\delta)\, \varepsilon_0 \cos(\omega t) \tag{2.5}$$

$$\sigma(t) = E' \varepsilon_0 \sin(\omega t) + E'' \varepsilon_0 \cos(\omega t) \tag{2.6}$$

Finally, the tensile storage and loss moduli can be written as:

$$E' = E^* \cos(\delta) \tag{2.7}$$

$$E'' = E^* \sin(\delta) \tag{2.8}$$

The hysteresis area during a loading/unloading cycle depends on the loss modulus E'':

$$W = \pi E'' {\varepsilon_0}^2 \tag{2.9}$$

Therefore, tensile loss and storage moduli can be determined by the expressions:

$$E'' = \frac{W}{\pi {\varepsilon_0}^2} \tag{2.10}$$

$$E' = \sqrt{(E^*)^2 - (E'')^2} = \sqrt{\left(\frac{\sigma_0}{\varepsilon_0}\right)^2 - \left(\frac{W}{\pi {\varepsilon_0}^2}\right)^2} \tag{2.11}$$

Analogously, the shear loss modulus G'', measure of the energy lost in heat, and the shear storage modulus G', measure of the stored energy, can be written as follows:

$$G'' = G\sin(\delta) = \frac{W}{\pi {\gamma_0}^2} \tag{2.12}$$

$$G' = G\cos(\delta) = \sqrt{(G^*)^2 - (G'')^2} \tag{2.13}$$

where γ_0 is the strain amplitude, $G^* = G' + iG''$ is the complex shear modulus, and δ is the phase shift.

The loss tangent, defined as the ratio between loss and stored energy, is defined as follows [Meyers and Chawla, 1999]:

$$\tan(\delta) = \frac{G''}{G'} = \frac{E''}{E'} \tag{2.14}$$

Rubber-like materials are made of macromolecular chains entangled in an ideal three-dimensional network, where entanglements or cross-links join polymer branches with more or less close connections [Steinmann et al., 2012].

Deformation of these materials can develop according to two strain mechanisms. The instantaneous strain mechanism is the dilation of the chemical bonds along the macromolecular chain itself and it takes no time to develop. The time-dependent strain mechanism involves the uncoiling of the chain-like macromolecules by breaking the physical (entanglements) and chemical (cross-links) links which connect the polymer branches, and this takes time to develop. If the load is applied at low strain rate ($\dot{\varepsilon} \to 0$), the macromolecular chains have time to uncoil and therefore oppose low resistance to deformation; when all the inter-chain bonds have been loosened, further deformation requires the dilation of the chemical bonds between the atoms along the chains, and the stiffness of the material increases rapidly. This representation describes an ideal scenario of simultaneous uncoiling of the whole chains with following chemical bonds dilation along the chains themselves. Conversely, when the sample is deformed suddenly ($\dot{\varepsilon} \to \infty$) the uncoiling of the macromolecular chains cannot develop and the chemical bonds dilate immediately. Considering an actual scenario, the uncoiling does not occur simultaneously for all the macromolecular chains. Hence, the stress-strain curve behaviour is represented in fig. 2.4.

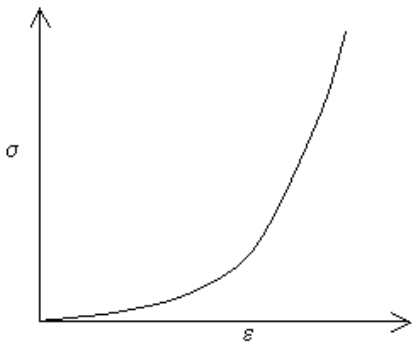


Figure 2.4 – Stress-strain curve of rubber-like materials

A viscoelastic constitutive model can be used to describe this behaviour. Viscoelastic models involve springs and dashpots arranged in series or in parallel.

In case of tensile stress, spring and dashpot constitutive models are defined as follows:

$$\sigma = E\varepsilon \tag{2.15}$$

$$\sigma = \eta \frac{d\varepsilon}{dt} \tag{2.16}$$

where:

- σ is the tensile stress
- E is the Young modulus
- ε is the tensile strain
- η is dashpot viscosity
- $\frac{d\varepsilon}{dt} = \dot{\varepsilon}$ is the strain rate

In case of shearing stress, spring and dashpot constitutive models are defined as follows [Tapia-Romero et al., 2020]:

$$\tau = G\gamma \tag{2.17}$$

$$\tau = \eta \frac{d\gamma}{dt} \tag{2.18}$$

where:

- τ is the shear stress
- G is the shear modulus
- γ is the shear strain
- η is dashpot viscosity
- $\frac{d\gamma}{dt} = \dot{\gamma}$ is the strain rate

Generalized Maxwell model (also called Maxwell-Wiechert model) is suitable to interpret the observed phenomenological behaviour of polymers from creep, stress relaxation, uniaxial tensile and loading-unloading tests. It consists of a set of K parallel Maxwell elements (spring and dashpot arranged in series) and an additional linear elastic spring in parallel. In the case of a simple shear test under strain control, the total stress τ consists of the sum of the equilibrium and non-equilibrium stresses, respectively expressed by the linear elastic spring and the K Maxwell elements, as shown in fig. 2.5 [Wiechert, 1889-1893].

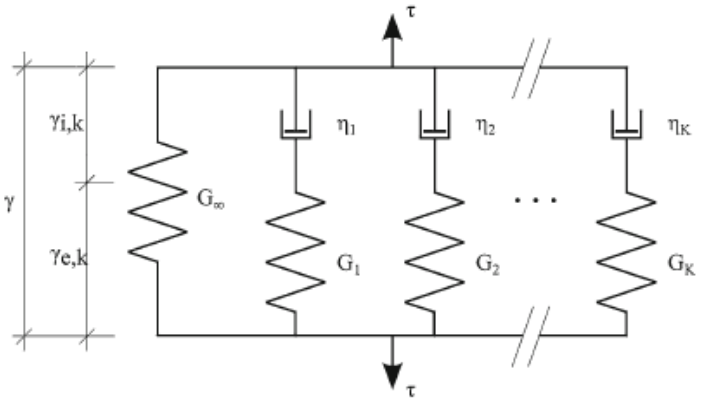


Figure 2.5 – Generalized Maxwell model

Each Maxwell branch gives a contribute to the whole model relaxation modulus as follows:

$$G_i(t) = G_i e^{-t/\tau_i} \tag{2.19}$$

where G_i and τ_i respectively represent the spring constant and the relaxation time of the i^{ih} element, where τ_i is function of that element dashpot viscosity η_i as:

$$\tau_i = \eta_i / G_i \tag{2.20}$$

The whole model relaxation modulus $G(t)$ is described as the sum of the spring contribute G_∞ and $G_i(t)$ contributes, obtaining the Prony series of the material:

$$G(t) = G_\infty + \sum_{i=1}^{K} G_i e^{-t/\tau_i} \tag{2.21}$$

where G_i, τ_i and G_∞ are named as Prony-parameters [Tapia-Romero et al., 2020]. Each Maxwell element has an initial stiffness G_i and it relaxes exponentially taking the corresponding time τ_i. Hence, this model allows for relaxation to happen in a set of times. When $t \to \infty$, after all Maxwell elements have relaxed, the stiffness is given by the supplementary linear elastic spring (G_∞). When $t \to 0$, the instantaneous shear relaxation modulus is defined as:

$$G_0 = G_\infty + \sum_{i=1}^{K} G_i \tag{2.22}$$

Fourier transform links the time dependent relaxation properties defined by (2.21) to the complex modulus G^* as follows:

$$G^*(\omega) = G_\infty + \sum_{i=1}^{K} G_i \frac{\omega^2 {\tau_i}^2}{1+\omega^2 {\tau_i}^2} + i \sum_{i=1}^{K} G_i \frac{\omega \tau_i}{1+\omega^2 {\tau_i}^2} \tag{2.23}$$

where ω is the angular frequency, the real part represents the Storage modulus $\Re(G^*) = G'(\omega)$, and the imaginary part is called Loss modulus $\Im(G^*) = G''(\omega)$.

Normalized Prony parameters g_i are defined as:

$$g_i = {G_i}/{G_0} \tag{2.24}$$

Thus, in frequency domain, the equation (2.23) can be written as:

$$G^*(\omega) = G_0 \left(1 - \sum_{i=1}^{K} g_i + \sum_{i=1}^{K} g_i \frac{\omega^2 {\tau_i}^2}{1+\omega^2 {\tau_i}^2} + i \sum_{i=1}^{K} g_i \frac{\omega \tau_i}{1+\omega^2 {\tau_i}^2}\right) \tag{2.25}$$

Equations (2.24) and (2.25) define rubber-like materials viscoelastic properties in ABAQUS CAE software.

The generalized Maxwell model describes the linear viscoelastic behaviour of polymeric materials subjected to small strains. In the large strain domain, polymers are also characterized by a nonlinear stress-strain response, defined by a hyperelastic model [Kraus et al., 2017].

In continuum mechanics, an infinite number of material points compose a material body. As shown in fig. 2.6, considering a material body in its undeformed B^0 and deformed B^t configurations, the material point $\boldsymbol{X}$ occupies the position $\boldsymbol{x}$ at instant t.

$$B^t = \boldsymbol{e}(B^0, t) \tag{2.26}$$

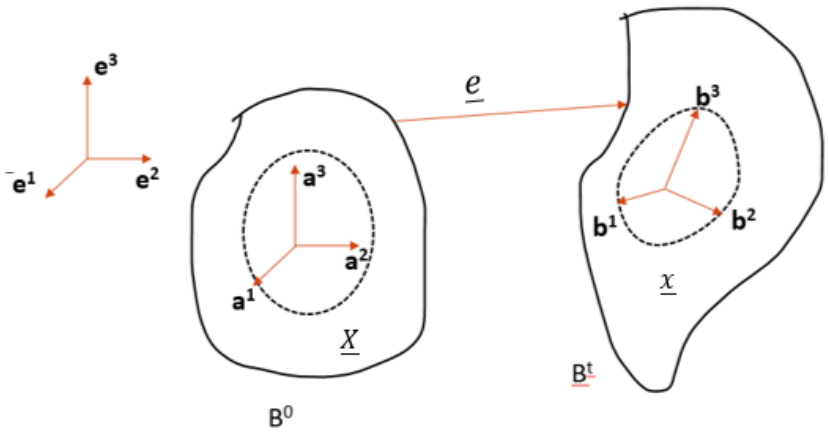


Figure 2.6 – Material body undeformed and deformed configurations

The motion function $\boldsymbol{e}$ correlates the undeformed configuration of the body to the region occupied by the body at the current instant t:

$$\boldsymbol{x} = \boldsymbol{e}(\boldsymbol{X}, t) = \boldsymbol{x}(\boldsymbol{X}, t) \tag{2.27}$$

The deformation gradient $\boldsymbol{F}$ describes the variability of the motion function within the material point:

$$\boldsymbol{F} = \frac{\partial \boldsymbol{e}}{\partial \boldsymbol{X}} = \frac{\partial \boldsymbol{x}}{\partial \boldsymbol{X}} \tag{2.28}$$

$$F_{ij} = \frac{\partial x_i}{\partial X_j} \tag{2.29}$$

The Cauchy-Green right deformation tensor $\boldsymbol{C}$ is defined as $\boldsymbol{C} = \boldsymbol{F}^T\boldsymbol{F}$. Terms on $\boldsymbol{C}$ diagonal (C_{ii}) describe the dilations or contractions the material point undergoes along ith direction. Terms outside $\boldsymbol{C}$ diagonal (C_{ij}) can be related to angular slides.

The Cauchy stress tensor $\boldsymbol{\sigma}$ describes stresses that are actually exchanged within the body:

$$\boldsymbol{\sigma} = J^{-1}\boldsymbol{P}\boldsymbol{F}^T \tag{2.30}$$

where:

- $J = \det(\boldsymbol{F})$
- $\boldsymbol{P}$ is the 1st Piola-Kirchhoff stress tensor (nominal stress tensor) and it describes the forces that are exchanged within the body in the deformed configuration with respect to elements of undeformed area

The 2nd Piola-Kirchhoff stress tensor $\boldsymbol{S}$ doesn't have a physical meaning, but it's useful because of its symmetry and it's defined as:

$$\boldsymbol{S} = \boldsymbol{F}^{-1}\boldsymbol{P} \tag{2.31}$$

$$\boldsymbol{S}(\boldsymbol{C}, \boldsymbol{\alpha^j}) = 2\frac{\partial \psi}{\partial \boldsymbol{C}} \tag{2.32}$$

where Helmholtz free energy ψ is the part of the work spent to deform the material point that's reversibly stored. Helmholtz free energy depends on the Cauchy-Green right deformation tensor $\boldsymbol{C}$ and on the internal variables $\boldsymbol{\alpha^j}$, which describe the evolution of the material point (strain history):

$$\psi = \psi(\boldsymbol{C}(\boldsymbol{X}, t), \boldsymbol{\alpha^j}(\boldsymbol{X}, t)) \tag{2.33}$$

A hyperelastic material is characterized by a non-linear stress-strain relationship and it's based on not dissipative deformation mechanisms. Therefore:

- a hyperelastic material elastically responds even when subjected to large deformations, which are fully recoverable
- Helmholtz free energy ψ is only function of the current deformative state
- Helmholtz free energy ψ is a potential of the deformative state

Hence, for a hyperelastic material, the constitutive equations (2.32) and (2.33) can be defined as follows:

$$\begin{cases} \psi = \psi(\boldsymbol{C}) = W(C) & (2.34) \\ S = 2\dfrac{\partial W(\boldsymbol{C})}{\partial \boldsymbol{C}} & (2.35) \end{cases}$$

where W is the strain energy density function [Carniel, 2020]. For rubber-like materials, which typically show a decoupled response when subjected to volumetric and deviatoric deformations, (2.34) can be decomposed as follows [Steinmann et al., 2012]:

$$\psi(\boldsymbol{C}) = \psi_{vol}(J) + \psi_{iso}(\overline{\boldsymbol{C}}) \tag{2.36}$$

where:

- $\psi_{vol}(J)$ is the volumetric part (shape is preserved)
- $\psi_{iso}(\overline{\boldsymbol{C}})$ is the isocoric part (volume is preserved)

Considering an isotropic material, W can be expressed in terms of λ_1, λ_2, and λ_3 (three principal stretches) or I_1, I_2, and I_3 (three strain invariants) [Steinmann et al., 2012; Kraus et al., 2017; Bien-aimé et al., 2020] where:

$$I_1 = \sum_{i=1}^{3} {\lambda_i}^2 \tag{2.37}$$

$$I_2 = \sum_{i,j=1}^{3} (\lambda_i \lambda_j)^2 \; with \; i \neq j \tag{2.38}$$

$$I_3 = \prod_{i=1}^{3} {\lambda_i}^2 \tag{2.39}$$

Since rubber-like materials are uncompressible, $I_3 = 1$.

Neo-Hookean and Ogden are some of the strain energy potential forms available in ABAQUS (software used for numerical analysis).

The strain energy potential in the Neo-Hookean constitutive model is defined as:

$$W = C_{10}(\overline{I_1} - 3) + \frac{1}{D_1}(J^{el} - 1)^2 \tag{2.40}$$

In the expression:

- C_{10} and D_1 are temperature-dependent material parameters
- $\overline{I_1}$ is the first deviatoric strain invariant → $\overline{I_1} = {\bar{\lambda}_1}^2 + {\bar{\lambda}_2}^2 + {\bar{\lambda}_3}^2$ with $\bar{\lambda}_i$ deviatoric stretches ($i = 1,2,3$)
- $\overline{I_2}$ is the second deviatoric strain invariant → $\overline{I_2} = {\bar{\lambda}_1}^{(-2)} + {\bar{\lambda}_2}^{(-2)} + {\bar{\lambda}_3}^{(-2)}$ with deviatoric stretches ($i = 1,2,3$)
- J^{el} is the elastic volume ratio

The initial shear modulus μ_0 is defined as:

$$\mu_0 = 2C_{10} \tag{2.41}$$

The initial bulk modulus K_0 is defined as:

$$K_0 = \frac{2}{D_1} \tag{2.42}$$

In 1971, Ogden proposed a strain energy function for elastic isotropic rubberlike solids:

$$\mathrm{W} = \sum_{i=1}^{N} \frac{2\mu_i}{{\alpha_i}^2}\left(\bar{\lambda}_1^{\alpha_i} + \bar{\lambda}_2^{\alpha_i} + \bar{\lambda}_3^{\alpha_i} - 3\right) + \sum_{i=1}^{N} \frac{1}{D_1}(J^{el} - 1)^{2i} \tag{2.43}$$

In the expression:

- μ_i, α_i, and D_1 are temperature-dependent material parameters → in particular, α_i are positive or negative real numbers that describe how quickly stiffness evolves with strain
- $\bar{\lambda}_i = J^{-\frac{1}{3}}\lambda_i$ are the deviatoric stretches ($i = 1,2,3$), with λ_i principal stretches
- J^{el} is the elastic volume ratio
- N expresses the number of terms considered for the model

The initial shear modulus μ_0 is defined as:

$$\mu_0 = \sum_{i=1}^{N} \mu_i = \frac{1}{2}\sum_{i=1}^{N} \alpha_i \mu_i \tag{2.44}$$

The initial bulk modulus K_0 is defined as:

$$K_0 = \frac{2}{D_1} \tag{2.45}$$

Poisson's ratio can be expressed as function of the initial shear modulus μ_0 and the initial bulk modulus K_0 as follows:

$$\nu = \frac{3K_0/\mu_0 - 2}{6K_0/\mu_0 + 2} \tag{2.46}$$

Equations (2.44), (2.45), and (2.46) define rubber-like materials hyperelastic properties in ABAQUS CAE software [Abaqus documentation].

2.2 Brain simulant material

2.2.1 Mechanical characterization of brain simulant material

Brain tissue can be considered as a soft material with both hyperelastic and viscoelastic behaviour. Hyperelasticity enables the brain tissue to undergo large, but recoverable, deformation under severe external loadings. The viscoelastic nature of brain tissue helps to dissipate the deformation energy, which is beneficial for example to reduce the damage probability of Traumatic Brain Injuries.

2.2.1.1 Dynamic mechanical analysis (DMA)

In 1969, Fallenstein et al. used the Dynamic Mechanical Apparatus to perform DMA on human brain specimens and find the tissue shear storage and loss moduli (G' and G'') and the phase lag (δ). The samples were subjected to a sinusoidal shear strain (7% - 24% strain interval) at 9-10 Hz [Fallenstein et al., 1969]. Fallenstein et al. results are shown in table 2.1.

Material	Year	Strain ε []	Frequency f [Hz]	Shear Storage modulus G' [kPa]	Shear Loss modulus G'' [kPa]	Shear Phase angle δs [rad]
Human brain	1969 (Fallenstein et al.)	0,07-0,24	9-10	1,1-0,6	0,6-0,35	0,50-0,38

Table 2.1 – DMA results on human brain specimen

In 2020/2021, DMA was performed at the University of Padua on samples made of PlatSil Gel-OO30 1A:1B:2D. This silicone rubber was chosen as brain simulant material of a physical head prototype by A. L. Silvestroni and G. Zullo. A 50x50x30 mm specimen was cyclically subjected to 10%, 20%, 30% and 40% strain levels in tension, compression and shear at different frequencies for the number of cycles indicated in the table 2.2 [Silvestroni, 2020].

Strain ε [%]	Displacement u [mm]
10	3
20	6
30	9
40	12

Frequency f [Hz]	Number of cycles n []
0,2	15
0,5	15
1	20
2	25
5	35
7	50

Table 2.2 – DMA Unipd protocol [Silvestroni, 2020]

The use of PlatSil Deadener LV to soften the silicone rubber is discouraged by the manufacturer with PlatSil-Gel OO-30 [Polytek Deadener & Hardener for PlatSil Gels Technical Bulletin]. PlatSil Gel-OO hardness is stated to be equivalent to PlatSil Gel-OO30 (shore OO30), but in this case deadener is allowed. PlatSil Gel-OO 1A:1B:1D was chosen as simulant brain material of the current physical head prototype. As reported on the deadener technical bulletin, PlatSil Gel-OO shore hardness should reach OOO45 with mixing ratio 1A:1B:1D, while PlatSil Gel-25 1A:1B:2D shore hardness should be about OOO10. Human brain hardness is about 4,5 ± 1,5 in the shore OO scale (corresponding to shore OOO20-OOO30) [Tejo-Otero, 2022], which is intermediate between PlatSil Gel-25 1A:1B:2D and PlatSil Gel-OO 1A:1B:1D tabulated shore hardness (fig. 2.7), therefore it was chosen to test both of them.

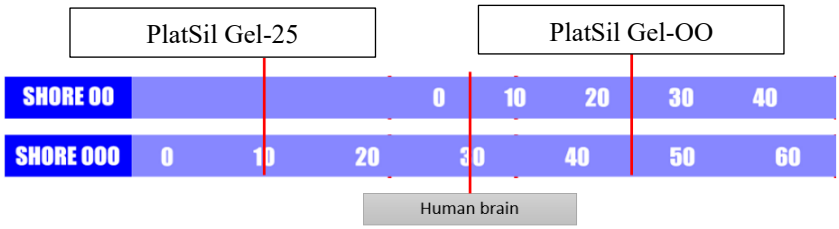


Figure 2.7 – Shore hardness of human brain and surrogates tested

DMA was performed to assess shear storage modulus, shear loss modulus and shear phase angle of the gels and compare findings with Fallenstein results. To evaluate also differences with respect to previous results on PlatSil Gel-OO30 1A:1B:2D (Silvestroni, 2020), it was chosen to adopt the same protocol and perform also compressive and tensile cyclic tests.

Three 50x50x30 mm samples were prepared using:

- PlatSil Gel-OO30 1A:1B:2D (material of the previous prototype)
- PlatSil Gel-OO 1A:1B:1D (material of the current prototype)
- PlatSil Gel-25 1A:1B:2D (material eventually proposed for a future prototype)

For PlatSil Gel-OO30 1A:1B:2D only 10% and 20% tension and compression strain levels were cyclically imposed to compare results with the previous Silvestroni analysis. For the other two silicone gels, 10%, 20%, 30% and 40% strain levels were cyclically imposed in tension, compression and shear with relative displacement u at different frequencies f for n cycles, as shown in table 2.2. A testing machine MTS 858 Mini Bionix II was used to evaluate time, displacement u and force F imposed on the samples performing tests in displacement control. An example of the tensile, compressive and shear cyclic tests is shown in fig. 2.8.

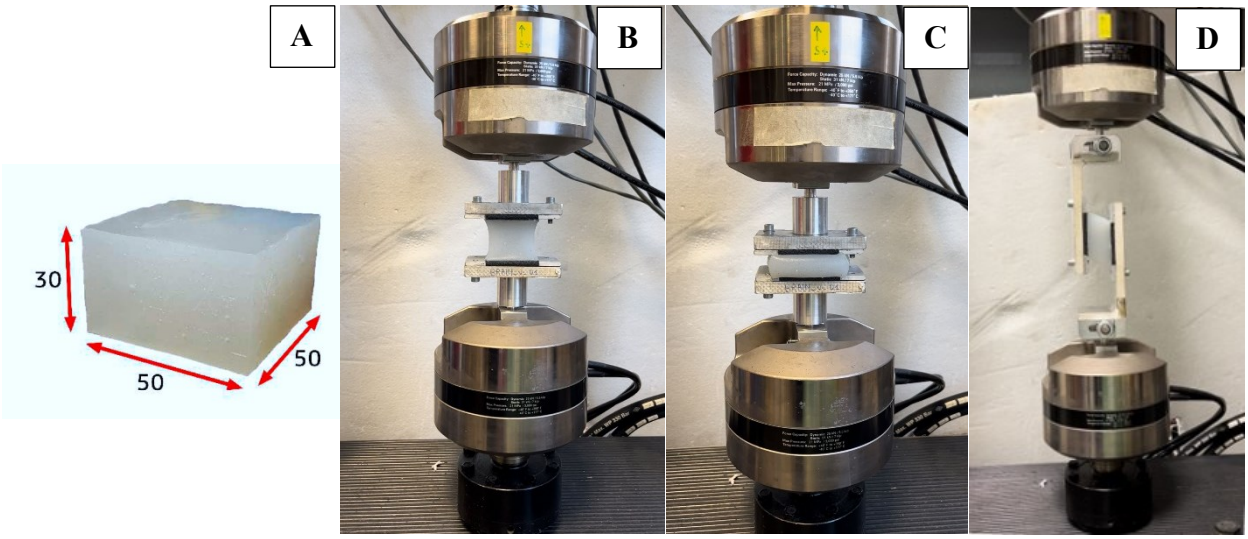


Figure 2.8 – PlatSil Gel-OO 1A:1B:1D specimen (A) and experimental set-up for (B) tensile, (C) compressive, and (D) shear DMA

In particular, considering the cyclic compressive test (same procedure for tensile and shear tests), the detailed testing protocol is described below.

The samples were first subjected to 10% compressive strain level (imposed displacement of -3 mm) at 0,2 Hz cycle frequency for 15 cycles, at 0,5 Hz cycle frequency for other 15 cycles, at 1 Hz cycle frequency for other 20 cycles and so on, as reported in table 2.2, till the last 50 cycles with a cycle frequency of 7 Hz. Then, the same procedure was applied imposing a displacement of -6 mm (20% compressive strain), -9 mm (30% compressive strain), and -12 mm (40% compressive strain). Time, displacement and force results were then elaborated using MATLAB R2022b software. Engineering (nominal) strain ε and stress σ were computed as

$$\varepsilon = \frac{u}{L_0} \tag{2.47}$$

$$\sigma = \frac{F}{A_0} \tag{2.48}$$

where:

- u is the displacement measured as machine output
- $L_0 = 30\ mm$ is the initial height of the sample
- F is the force applied on the sample (machine output)
- $A_0 = 50 \cdot 50 = 2500\ mm^2$ is the initial cross section area of the sample

Engineering stress-strain curves were pre-processed to smooth noisy data using MATLAB R2022b *Signal Analyzer* app. Storage moduli, loss moduli and phase angles were calculated with the (2.10), (2.11), (2.12) and (2.13). Literature, previous and current results at 7 Hz are shown in tables 2.3, 2.4, and 2.5.

Material	Year	Brain Surrogate ID	Strain ε []	Tensile storage modulus Et' [kPa]	Tensile loss modulus Et'' [kPa]	Tensile phase angle δt [rad]
PlatSil Gel-OO30 1A:1B:2D	2020 (Silvestroni)	BS_01_20	0,1	100,62	29,93	0,29
			0,2	88,71	27,19	0,30
			0,3	78,71	24,65	0,30
			0,4	70,83	22,29	0,30
PlatSil Gel-OO30 1A:1B:2D	2021 (Zullo)	BS_01_21	0,1	122,84	36,83	0,29
			0,2	104,79	32,16	0,30
			0,3	89,93	28,07	0,30
			0,4	81,11	25,24	0,30
PlatSil Gel-OO30 1A:1B:2D	2022 (current)	BS_01_22	0,1	115,39	34,89	0,29
			0,2	102,23	30,84	0,29
PlatSil Gel-OO 1A:1B:1D	2022 (current)	BS_02_22	0,1	89,49	32,38	0,35
			0,2	78,96	27,86	0,34
			0,3	77,58	29,14	0,36
			0,4	69,91	26,02	0,36
PlatSil Gel-25 1A:1B:2D	2022 (current)	BS_03_22	0,1	46,42	36,82	0,67
			0,2	40,08	31,96	0,67
			0,3	34,56	27,93	0,68
			0,4	31,29	24,64	0,67

Table 2.3 – Comparison of previous (BS_01_20, BS_01_21) and current (BS_01_22, BS_02_22, BS_03_22) tensile storage moduli, loss moduli, and phase angles results

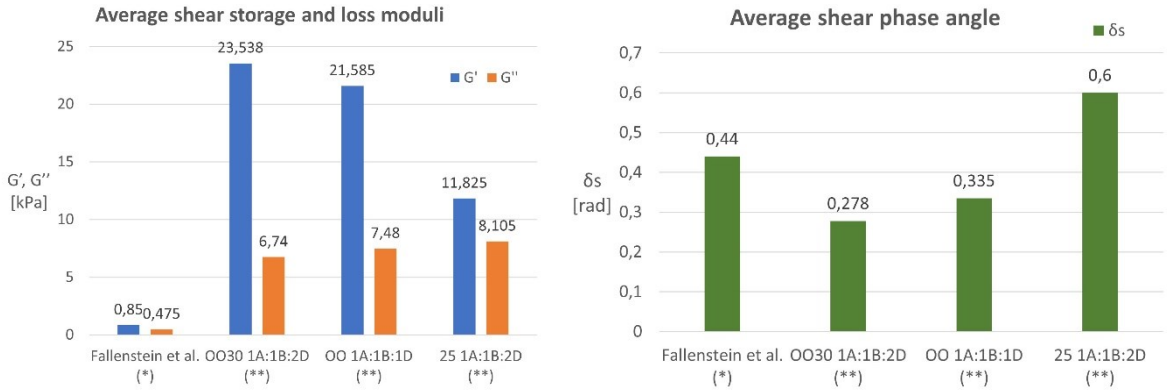
Material	Year	Brain Surrogate ID	Strain ε []	Compressive storage modulus Ec' [kPa]	Compressive loss modulus Ec'' [kPa]	Compressive phase angle δc [rad]
PlatSil Gel-OO30 1A:1B:2D	2020 (Silvestroni)	BS_01_20	0,1	129,71	38,76	0,29
			0,2	140,15	41,89	0,29
			0,3	151,86	46,66	0,30
			0,4	170,77	53,65	0,30
PlatSil Gel-OO30 1A:1B:2D	2021 (Zullo)	BS_01_21	0,1	161,17	49,73	0,30
			0,2	174,42	55,49	0,31
			0,3	198,03	62,96	0,31
			0,4	252,14	75,71	0,29
PlatSil Gel-OO30 1A:1B:2D	2022 (current)	BS_01_22	0,1	149,94	44,74	0,29
			0,2	161,93	49,69	0,30
PlatSil Gel-OO 1A:1B:1D	2022 (current)	BS_02_22	0,1	115,26	41,76	0,35
			0,2	126,30	46,75	0,35
			0,3	164,09	63,34	0,37
			0,4	206,40	77,26	0,36
PlatSil Gel-25 1A:1B:2D	2022 (current)	BS_03_22	0,1	58,99	46,43	0,67
			0,2	62,25	50,98	0,69
			0,3	66,76	55,84	0,70
			0,4	78,92	64,36	0,68

Table 2.4 - Comparison of previous (BS_01_20, BS_01_21) and current (BS_01_22, BS_02_22, BS_03_22) compressive storage moduli, loss moduli, and phase angles results

Material	Year	Brain Surrogate ID	Strain ε []	Frequency f [Hz]	Shear storage modulus G' [kPa]	Shear loss modulus G'' [kPa]	Shear phase angle δs [rad]
Human brain	1969 (Fallenstein et al.)	-	0,24-0,07	9-10	0,6-1,1	0,35-0,6	0,38-0,50
PlatSil Gel-OO30 1A:1B:2D	2020 (Silvestroni)	BS_01_20	0,1	7	24,60	6,74	0,27
			0,2		22,47	6,57	0,28
			0,3		22,93	6,58	0,28
			0,4		23,53	6,33	0,26
PlatSil Gel-OO30 1A:1B:2D	2021 (Zullo)	BS_01_21	0,1	7	24,33	7,04	0,28
			0,2		22,75	6,61	0,28
			0,3		22,07	6,52	0,29
			0,4		19,46	6,18	0,31
PlatSil Gel-OO30 1A:1B:2D	2022 (current)	BS_01_22	0,1	7	-	-	-
			0,2				
PlatSil Gel-OO 1A:1B:1D	2022 (current)	BS_02_22	0,1	7	21,69	7,55	0,34
			0,2		21,48	7,41	0,33
			0,3		20,50	7,21	0,34
			0,4		20,04	7,15	0,34
PlatSil Gel-25 1A:1B:2D	2022 (current)	BS_03_22	0,1	7	12,45	8,19	0,58
			0,2		11,20	8,02	0,62
			0,3		9,64	7,76	0,67
			0,4		10,03	7,60	0,65

Table 2.5 - Comparison of literature (Fallenstein et al.), previous (BS_01_20, BS_01_21) and current (BS_01_22, BS_02_22, BS_03_22) shear storage moduli, loss moduli, and phase angles results

Fallenstein performed DMA imposing a sinusoidal 7%-24% shear strain with a cycle frequency of 9-10 Hz. Thus, the average shear storage modulus, loss modulus and phase angles obtained from Unipd analyses at 7 Hz cycle frequency in the 10%-20% strain range were compared with Fallenstein's average results. In particular, as shown in fig. 2.9, the average PlatSil Gel-OO 1A:1B:1D shear storage modulus is a bit lower than the PlatSil Gel-OO30 1A:1B:2D average one, but it's still too high with respect to Fallenstein's findings. PlatSil Gel-25 1A:1B:2D average shear storage modulus is about half the value of the current simulant material and the previous prototype silicone rubber, suggesting that it could be a better choice for a future prototype. Nevertheless, its value results to be still too high with respect to Fallenstein.



(*) cycle frequency f = 9 – 10 Hz, strain range 7% - 24%

(**) cycle frequency f = 7 Hz, strain range 10% - 20%

Figure 2.9 – Shear DMA results on brain simulants vs. literature (Fallenstein et al.) findings

2.2.1.2 Quasi-static tests

In 1997, Miller and Chinzei performed uniaxial compression tests on swine brain tissue in large strain domain. Cylindrical specimens were axially compressed at 30% engineering strain level at three loading velocities, corresponding to the three strain rates of about 0,64 s^{-1}, 0,0064 s^{-1}, and $0{,}64 \cdot 10^{-5}$ s^{-1} [Miller and Chinzei, 1997]. The experimental set-up is shown in fig. 2.10.

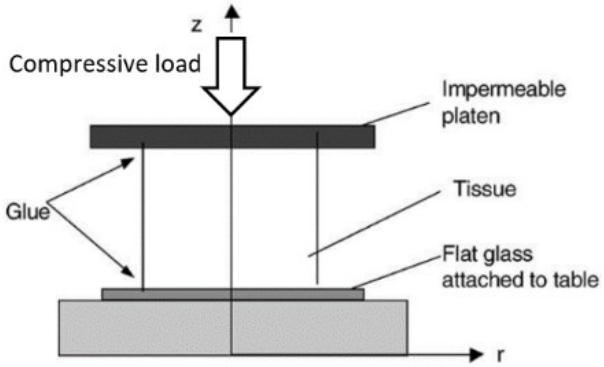


Figure 2.10 – Set-up of Miller and Chinzei uniaxial compression test [Miller and Chinzei, 1997]

The non-linear relationships between engineering stress (absolute value) and true strain in the three scenarios are shown in fig. 2.11 A,B,C.

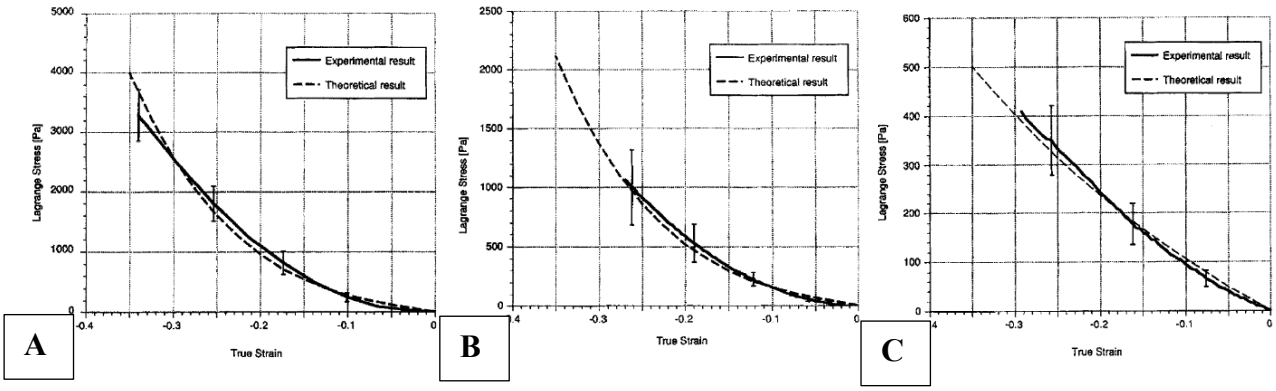


Figure 2.11 – Engineering stress – true strain curves from literature for a uniaxial compressive test at strain rate of: (A) 0,64 s^{-1}, (B) 0,0064 s^{-1}, (C) 0,64·10^{-5} s^{-1} [Miller and Chinzei, 1997]

In 2002, Miller and Chinzei performed uniaxial tensile tests on swine brain tissue in large strain domain. Cylindrical specimens were axially imposed a 20% engineering tensile strain level at two loading velocities, corresponding to the two strain rates of about 0,64 s^{-1} and 0,0064 s^{-1} [Miller and Chinzei, 2002]. The experimental set-up is shown in fig. 2.12.

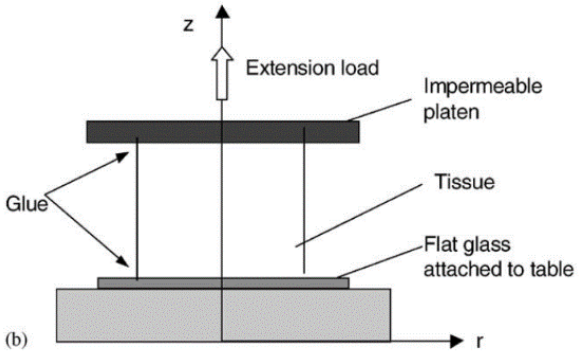


Figure 2.12 – Set-up of Miller and Chinzei uniaxial tension test [Miller and Chinzei, 2002]

The non-linear relationships between engineering stress and stretch along loading direction in the two scenarios are shown in fig. 2.13.

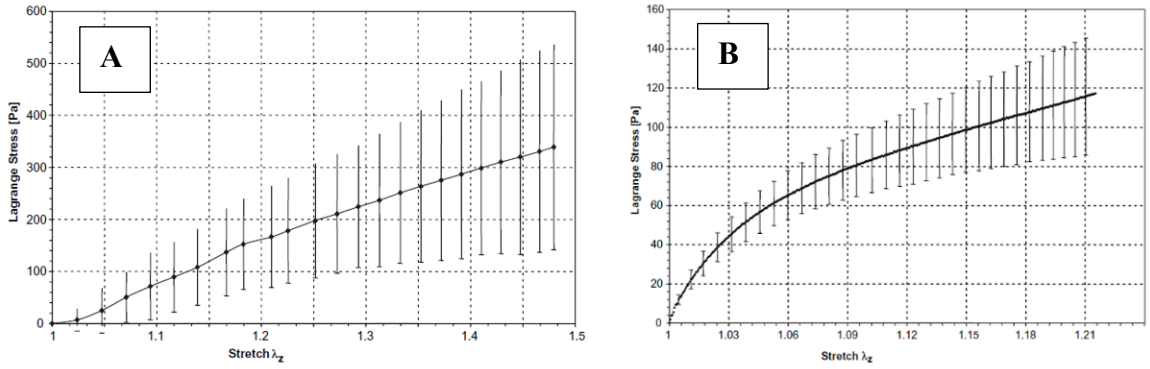


Figure 2.13 – Engineering stress – stretch curves from literature for a uniaxial tensile test at strain rate of: (A) 0,64 s^{-1}, (B) 0,0064 s^{-1} [Miller and Chinzei, 2002]

In both compressive and tensile tests, the stress-strain response resulted to be highly dependent on the strain rate, exhibiting an increase of the stiffness with the loading velocity. Moreover, it was observed that swine brain tissue was significantly softer in extension with respect to the compression [Miller and Chinzei, 1997] [Miller and Chinzei, 2002].

To characterize the stress-strain relationship of the silicone rubbers under investigation in the current work, uniaxial compressive, tensile, and shear quasi-static tests were performed using MTS 858 Mini Bionix II (same testing layout as in fig. 2.8). A 40% strain level was imposed on 50x50x30 mm specimens made of PlatSil Gel-OO 1A:1B:1D and PlatSil Gel-25 1A:1B:2D (with the only exception for the 50% compressive strain level imposed only to the PlatSil Gel-OO 1A:1B:1D sample). The samples were deformed with a loading velocity of 0,1 $mm \cdot s^{-1}$, corresponding to a strain rate of 0,0033 s^{-1}.

Data were processed with MATLAB 2022b to remove the noise.

The resulting engineering stress-strain curves for PlatSil Gel-OO 1A:1B:1D and PlatSil Gel-25 1A:1B:2D are shown in fig. 2.14 A/C/E and fig. 2.14 B/D/F respectively.

The current work results were compared to literature using the expression:

$$\varepsilon_t = \ln(\lambda) = ln(1 + \varepsilon) \tag{2.49}$$

where ε_t is the true strain, λ is the stretch ratio, and ε is the engineering strain (ε is positive in tensile test and negative in compression test).

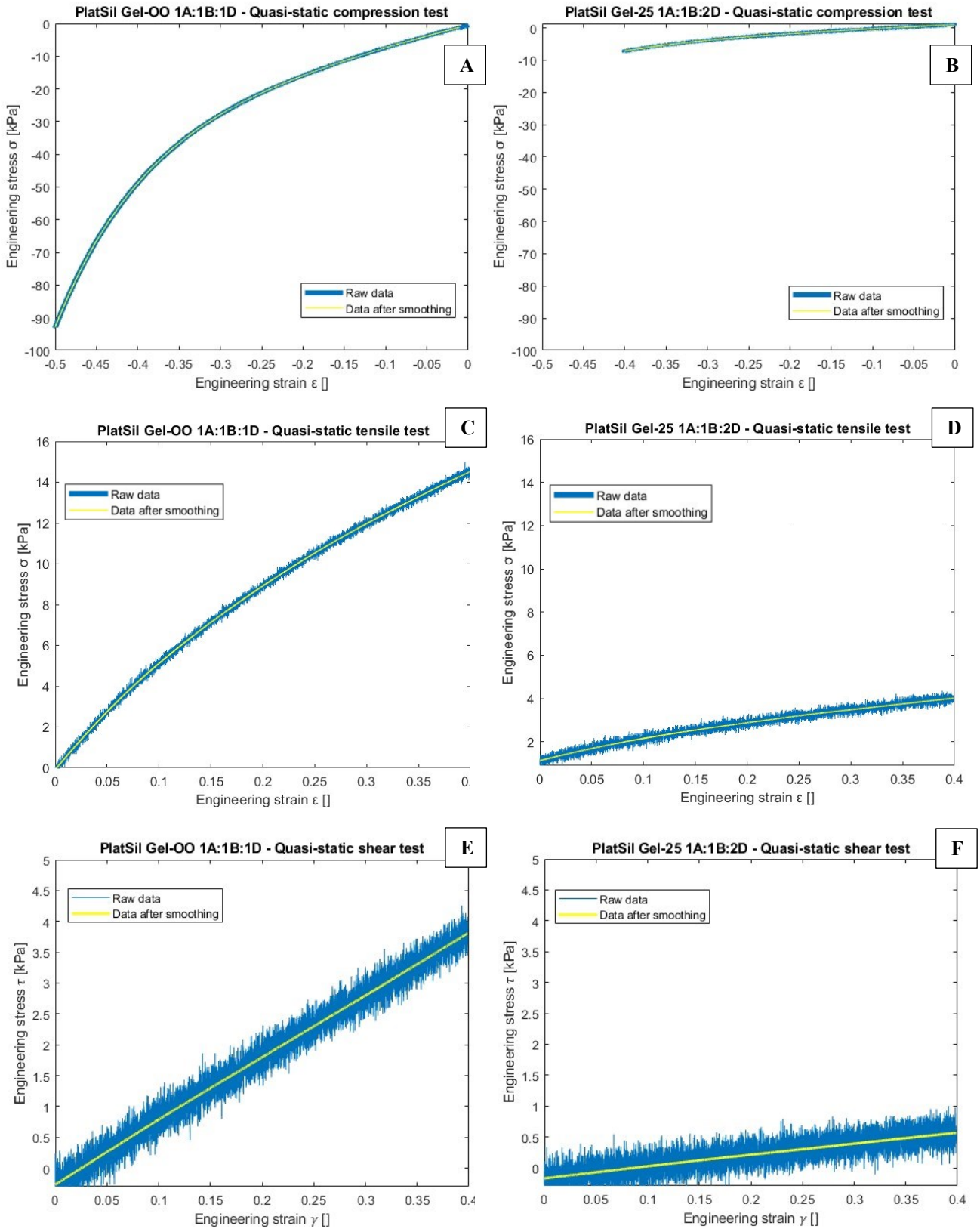


Figure 2.14 – Resulting engineering stress-strain curves from: quasi-static compression tests [(A) PlatSil Gel OO 1A:1B:1D, (B) PlatSil Gel 25 1A:1B:2D], quasi-static tensile tests [(C) PlatSil Gel OO 1A:1B:1D, (D) PlatSil Gel-25 1A:1B:2D], quasi-static shear tests [(E) PlatSil Gel OO 1A:1B:1D, (F) PlatSil Gel 25 1A:1B:2D]

For the compressive test, the absolute values of engineering stress obtained for 10%, 20%, and 30% engineering strain levels for silicone rubbers were compared with Miller and Chinzei results at the strain rate of 0,0064 s^{-1} (fig. 2.15).

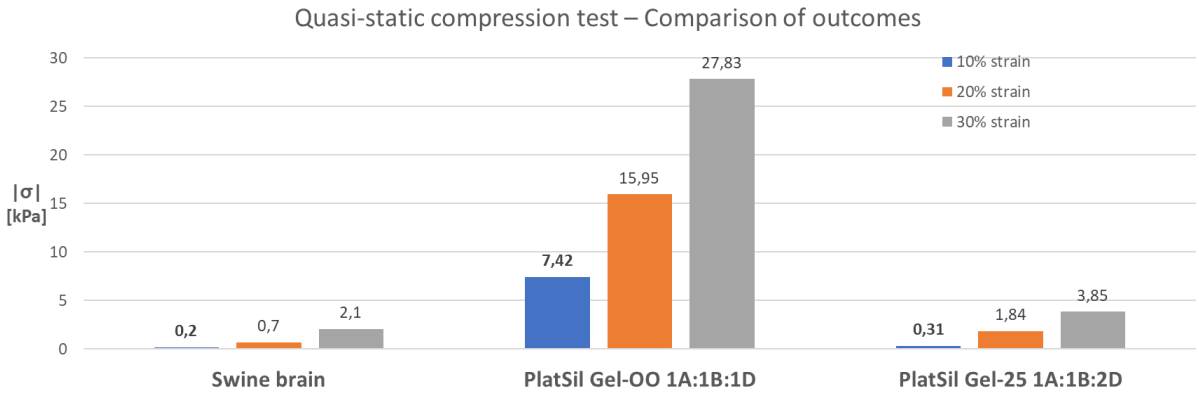


Figure 2.15 – Comparison of Unipd silicone rubbers with literature (Miller and Chinzei, 1997) absolute value of the engineering stress for quasi-static compression tests at 10%, 20%, and 30% engineering strain levels

For the tensile test, the engineering stress obtained for 10% and 20% engineering strain levels for silicone rubbers were compared with Miller and Chinzei results at the strain rate of 0,0064 s^{-1} (fig. 2.16).

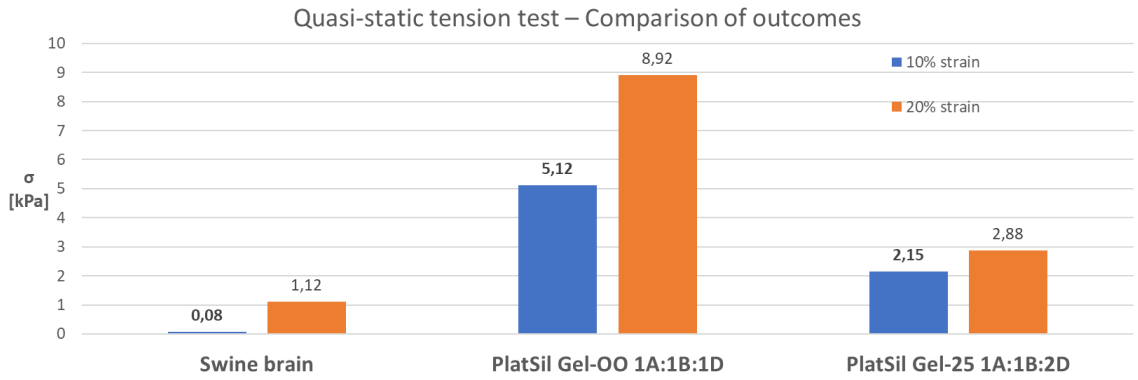


Figure 2.16 - Comparison of Unipd silicone rubbers with literature (Miller and Chinzei, 2002) engineering stress for quasi-static tension tests at 10% and 20% engineering strain levels

As evinced by the histograms, PlatSil Gel-25 1A:1B:2D results are closer to literature with respect to PlatSil Gel-OO 1A:1B:1D. As supposed analysing DMA results, PlatSil Gel-25 1A:1B:2D silicone rubber appears to be a better brain simulant material for a future head prototype with respect to the current PlatSil Gel-OO 1A:1B:1D. Despite this, PlatSil Gel-OO 1A:1B:1D was easy to manipulate and cast, while Platsil Gel-25 1A:1B:2D was sticky.

2.2.2 Identification of the constitutive parameters of brain simulant material

PlatSil Gel-OO 1A:1B:1D hyperelastic and viscoelastic constitutive parameters have been identified based on the mechanical characterization. Then, numerical simulations of the experimental tests were carried out to enhance the reliability of the parameters.

2.2.2.1 Hyperelastic constitutive parameters

At first, hyperelastic behaviour was defined by fitting experimental test data in ABAQUS. Quasi-static uniaxial compressive and tensile engineering (nominal) stress-strain data obtained by the mechanical characterization were inserted as test data (fig. 2.17 A). ABAQUS was asked to identify Ogden constitutive parameters with Poisson's ratio $\nu = 0.49$ and N ranging from 1 to 6 (fig. 2.17 B and C). Viscoelastic behavior (fig. 2.17 D) was defined as described later (see fig. 2.46). *Evaluate* option was used to identify the constitutive parameters of the six investigated Ogden models.

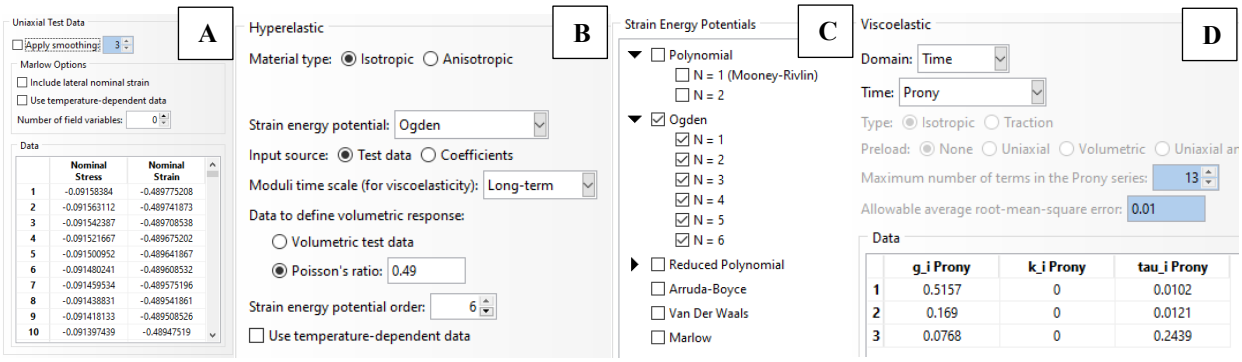


Figure 2.17 – Definition of hyperelastic and viscoelastic behaviour to use the Evaluate option: (A) quasi-static compressive and tensile Uniaxial Test Data obtained from the mechanical characterization, (B) Poisson's ratio, (C) Ogden Strain Energy Potentials chosen to be applied to the data, (D) viscoelastic constitutive parameters

Ogden strain energy function with N=1 (fig. 2.18 A) and N=5 (fig. 2.18 B) resulted the only cases in which stability was satisfied for all strains.

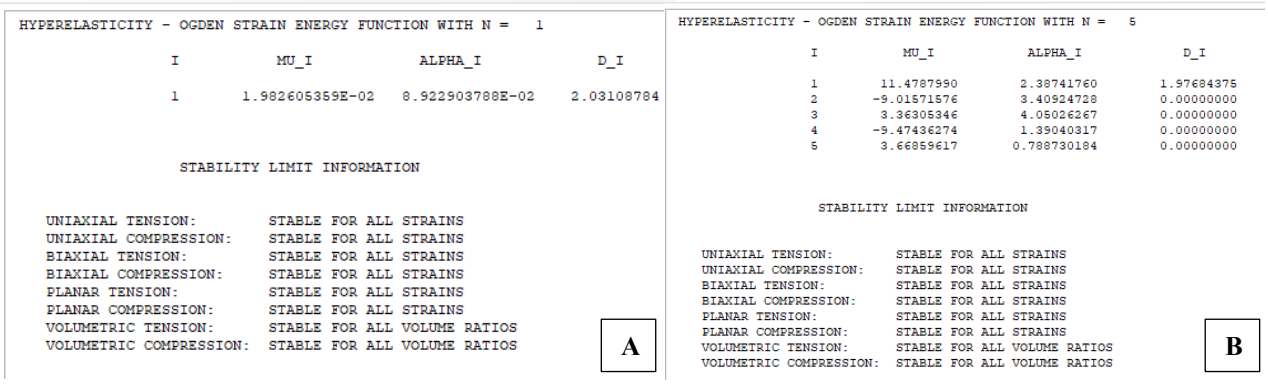


Figure 2.18 – Hyperelastic constitutive parameters resulting from Evaluate option for Ogden strain energy function with: (A) N=1, (B) N=5

In order to identify the best Ogden strain energy function, it was chosen to simulate the performed quasi-static uniaxial compressive, tensile and shear tests using ABAQUS. The aim

was to evaluate the reaction force vs displacement output in the two cases (N=1 and N=5) and to choose the one that was able to best fit the experimental force-displacement curves.

Therefore, a first 50x50x30 mm brain surrogate sample was created in ABAQUS as a *Part* and it was assigned the *Section* made of the *Material* (fig. 2.19) defined by:

- hyperelastic constitutive parameters (*Evaluate* output for N=1)
- viscoelastic Prony series parameters (identified as described later – see fig. 2.46)

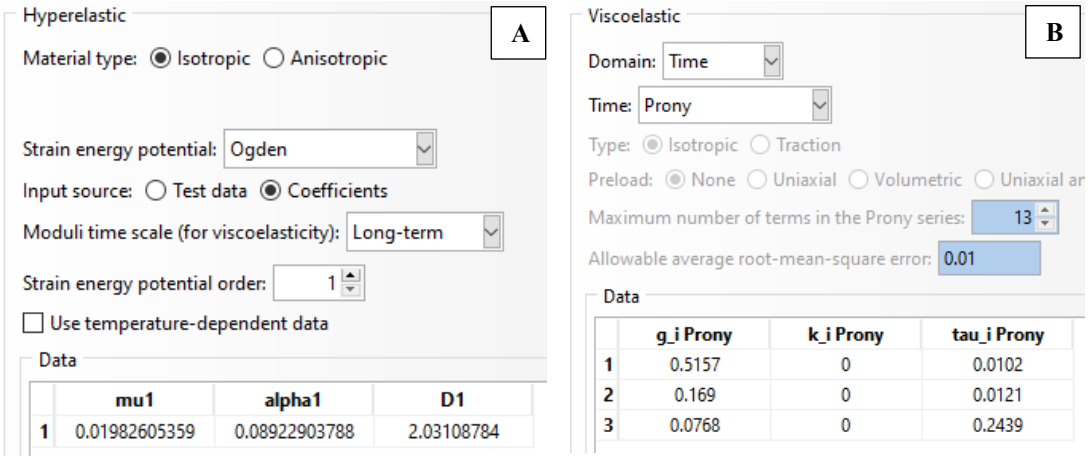


Figure 2.19 – PlatSil Gel-OO 1A:1B:1D hyperelastic and viscoelastic behaviour: (A) Ogden hyperelastic constitutive parameters resulting from Evaluate option with N=1, (B) viscoelastic Prony series parameters

A 90x50x4 mm plate was created as a *Part* and it was assigned the *Section* made of the *Material* (aluminium) defined by the elastic parameters in fig. 2.20.

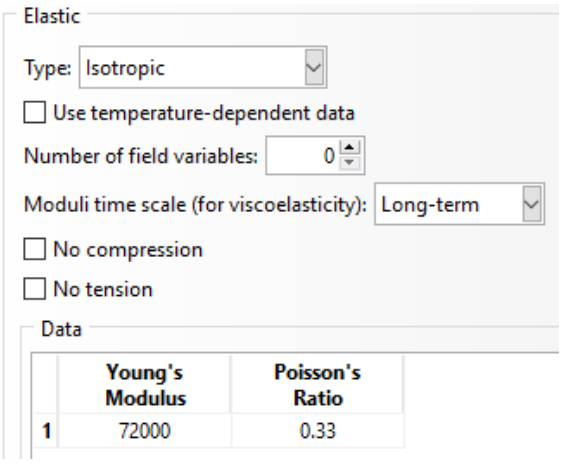


Figure 2.20 – Aluminium elastic parameters

Two plate *Instances* and the silicone rubber *Instance* were then created (*Assembly* → *Instances*) and the sample was positioned among the two aluminium plates (fig. 2.21 A). The lower plate was fixed (*BCs* → Symmetry/Antisymmetry/Encastre → ENCASTRE) and the upper plate was subjected to a displacement of -15 mm along z axis (*BCs* → Displacement/Rotation → U3=-15) in 150 s (*Step* → Time period=150) to simulate a quasi-static compression test at the same strain rate of 0.1 mm/s (0.0033/s) imposed in the laboratory test (fig. 2.21 B). A Tie *Constraint* was imposed to simulate the silicone sample upper and lower faces gluing to the plates and an

Interaction with Normal Behavior "Hard" Contact was assigned to avoid the interpenetration of the lateral faces of the sample with the plates (fig. 2.21 C). The instances were then meshed (fig. 2.21 D).

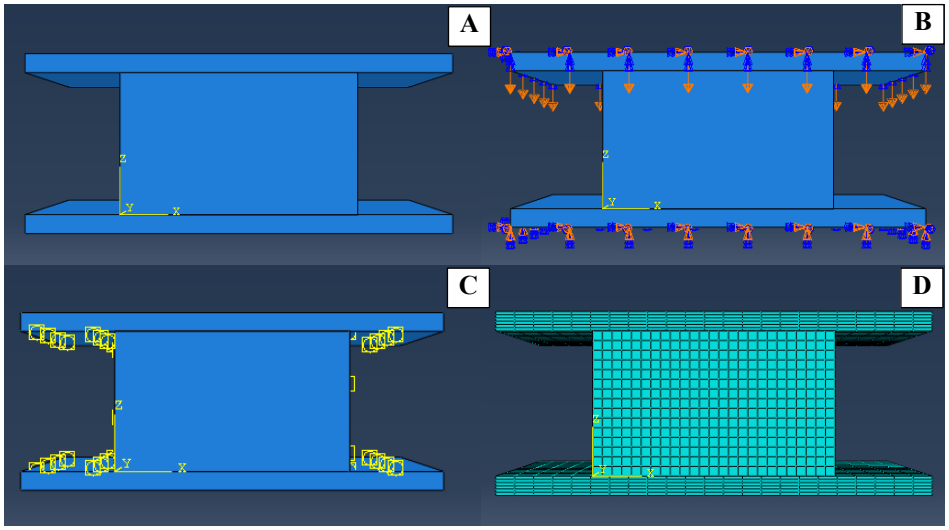


Figure 2.21 – PlatSil Gel-OO 1A:1B:1D quasi-static compression test simulation: (A) Assembly, (B) BCs, (C) Constraints and Interactions, (D) Mesh

The reaction force RF3 and the displacement U3 along z axis were then computed and saved. The model was then copied and the hyperelastic constitutive parameters were changed (fig. 2.22) to define the Ogden constitutive model with N=5 as determined by the *Evaluate* output.

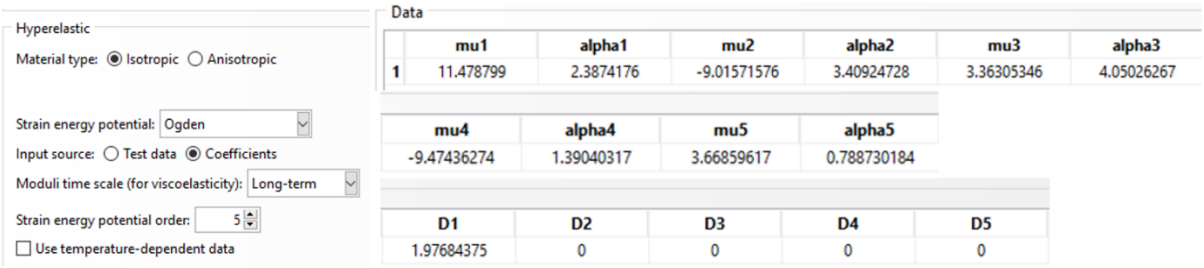


Figure 2.22 – PlatSil Gel-OO 1A:1B:1D Ogden hyperelastic constitutive parameters resulting from Evaluate option with N=5

The reaction force RF3 and the displacement U3 along z axis were saved to compare the RF3-U3 curve to the experimental and the first model ones (fig. 2.23). Despite an initial common slope, it can be noticed that the Ogden constitutive model with 5 terms isn't suitable to fit the experimental curve, because the stiffness remarkably increases after a nominal strain of about 30%. On the other hand, the sample defined by the Ogden constitutive model with 1 term exhibits a more similar behaviour with respect to experimental curve.

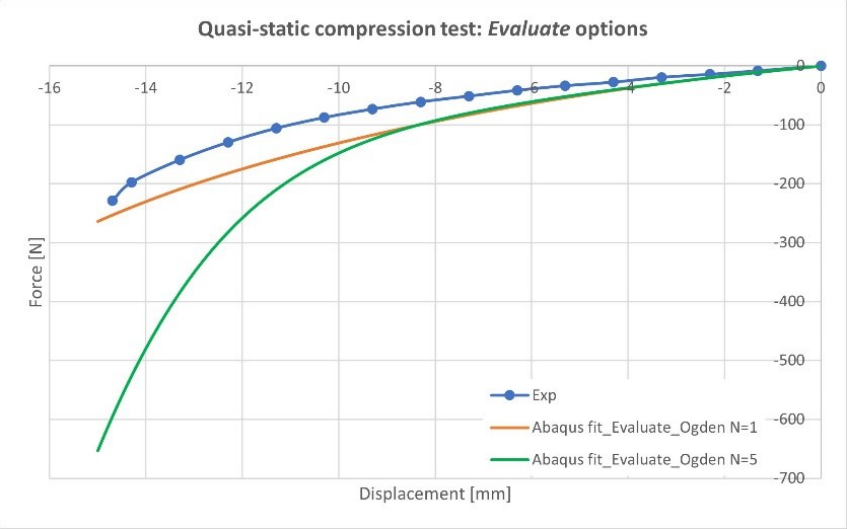


Figure 2.23 – Abaqus results for Ogden strain energy function with N=1 and N=5: fit of RF3-U3 curve output with the experimental force-displacement curve for quasi-static compression test simulation

Hence, quasi-static tensile and simple shear tests were simulated only for the first model, where the silicone rubber hyperelastic behaviour was defined by the Ogden constitutive model with N=1. To do this, the model was copied, and the upper plate was subjected to a displacement of 12 mm along z axis (*BCs* → Displacement/Rotation → U3=12) in 120 s (*Step* → Time period=120) to simulate a quasi-static tensile test at the same strain rate of 0.1 mm/s (0.0033/s) imposed in the laboratory test. Then, the model was copied, and the upper plate was subjected to a displacement of 12 mm along x axis (*BCs* → Displacement/Rotation → U1=12) in 120 s (*Step* → Time period=120) to simulate a quasi-static simple shear test at the same strain rate of 0.1 mm/s (0.0033/s) imposed in the laboratory test. In both cases, the *Interaction* defined in the compression test simulation was deleted. The *Constraints* and *BCs* are shown in fig. 2.24.

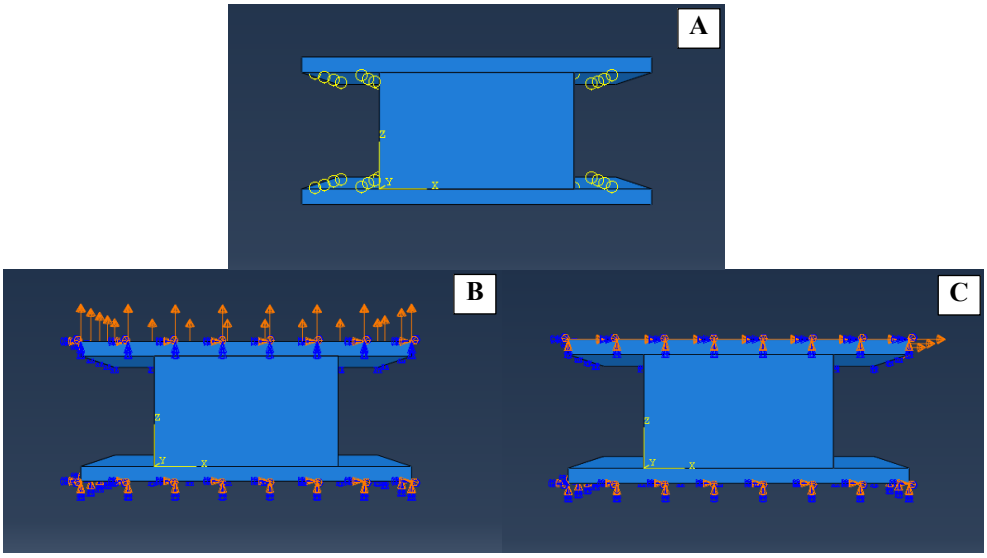


Figure 2.24 - (A) Constraints for PlatSil Gel-OO 1A:1B:1D quasi-static tensile and shear test simulations, (B) BCs for PlatSil Gel-OO 1A:1B:1D quasi-static tensile test simulation, (C) BCs for PlatSil Gel-OO 1A:1B:1D quasi-static shear test simulation

Figures 2.25 and 2.26 show the comparison of the experimental force-displacement curve with respect to Abaqus RF3 vs U3 fit for the tensile test and Abaqus RF1 vs U1 fit for the simple shear test.

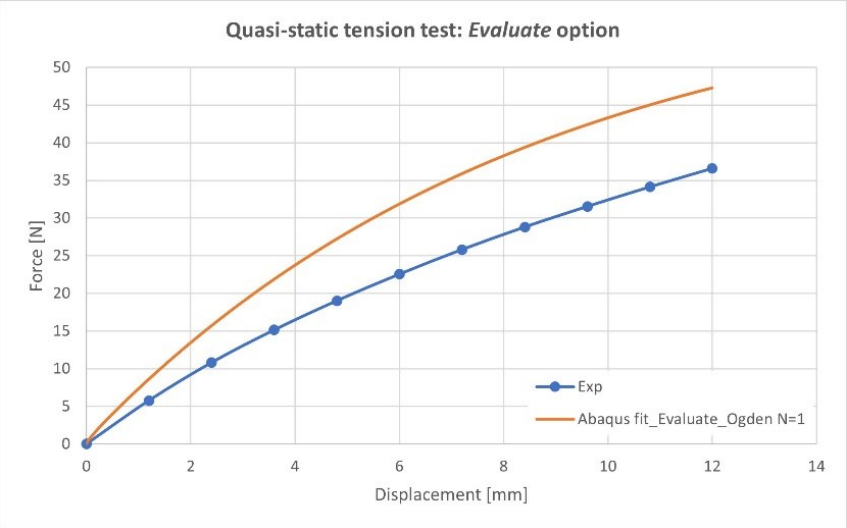


Figure 2.25 – Abaqus results for Ogden strain energy function with N=1: fit of RF3-U3 curve output with the experimental force-displacement curve for quasi-static tension test simulation

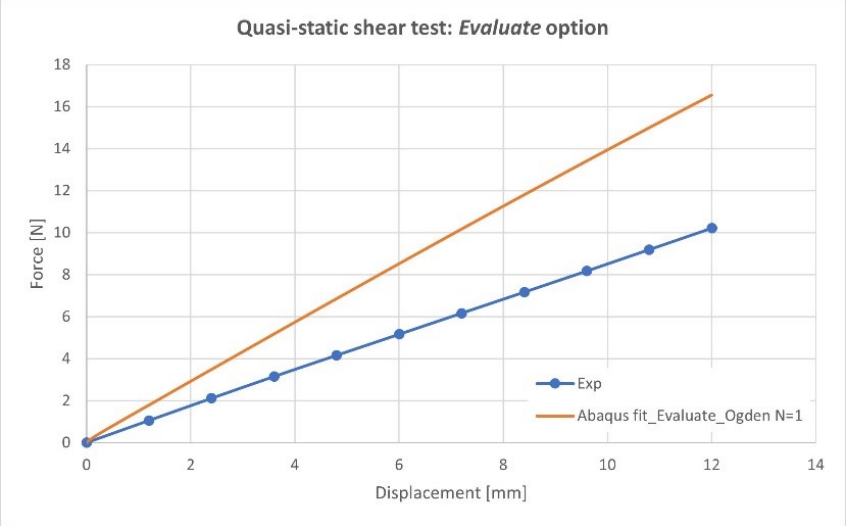


Figure 2.26 – Abaqus results for Ogden strain energy function with N=1: fit of RF1-U1 curve output with the experimental force-displacement curve for quasi-static shear test simulation

These force-displacement comparisons evinced that the *Evaluate* output parameters were not suitable to interpret the experimental response. In particular, since brain shear strain is an important parameter to study TBIs effects, it was chosen to modify these Ogden parameters to find a set that could allow the Abaqus output RF1 vs U1 curve to behave in a more similar way with respect to the shear experimental curve. Therefore, a new Ogden model with N=1 was initially proposed to define PlatSil Gel-OO 1A:1B:1D hyperelastic bahaviour.

The initial shear modulus $\mu_0 = 0.0101\ MPa$ was quantified as the slope of the experimental engineering stress-strain curve in fig. 2.14 E. The formula (2.44) was used to identify α_1 value as follows:

$$\mu_0 = \sum_{i=1}^{N=1} \mu_i = \mu_1 \tag{2.50}$$

$$\mu_0 = \frac{1}{2}\sum_{i=1}^{N=1} \alpha_i \mu_i = \frac{1}{2}\alpha_1 \mu_1 \tag{2.51}$$

Hence, $\alpha_1 = 2$.

The Poisson's ratio was set to 0,49 and the equation (2.46) was used to identify the initial bulk modulus K_0 as follows:

$$K_0 = -\frac{2}{3} \cdot 0.0101 \cdot \frac{0{,}49\ + 1}{2 \cdot 0{,}49\ - 1} MPa = 0.501633\ MPa \tag{2.52}$$

Therefore, equation (2.45) was used to identify D_1 as:

$$D_1 = \frac{2}{0.501633}\ MPa^{-1} = 3.986976\ MPa^{-1} \tag{2.53}$$

Experimental quasi-static compressive, tensile and shear tests were then simulated as described before, with the only difference in the hyperelastic behaviour definition. In fact, these was described via *Coefficients* instead of *Test data*, as shown in fig. 2.27.

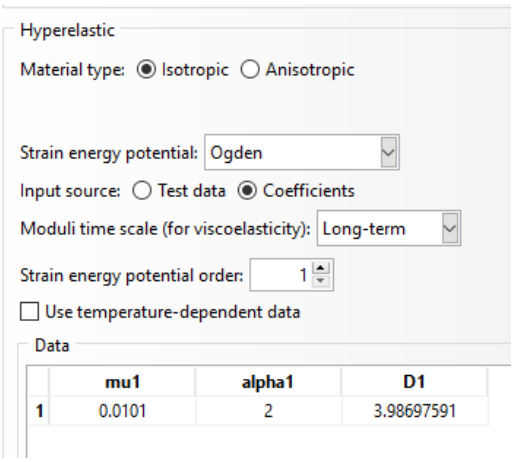


Figure 2.27 – First proposal: PlatSil Gel-OO 1A:1B:1D new Ogden hyperelastic constitutive parameters (Coefficients)

For the compressive and the tensile tests, the reaction force RF3 and the displacement U3 along z axis were computed and saved, as well as RF1 and U1 along x axis for the shear test. Figures 2.28 and 2.29 show the comparison of experimental data with respect to the corresponding old model results (Ogden parameters as *Evaluate* output with N=1) and to this first proposal results.

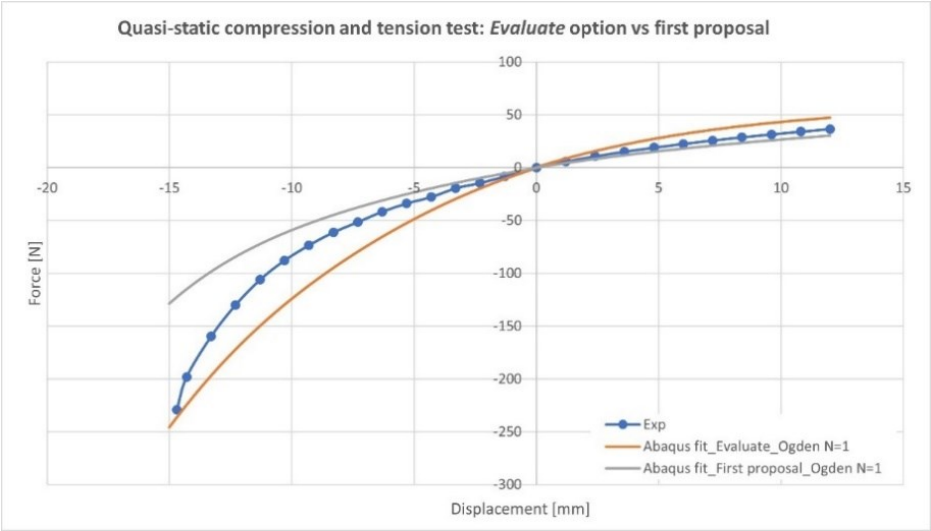


Figure 2.28 – Abaqus results for hyperelastic behaviour defined by Evaluate coefficients (N=1) vs first proposal: fit of RF3-U3 curve output with the experimental force-displacement curve for quasi-static compression and tension test simulation

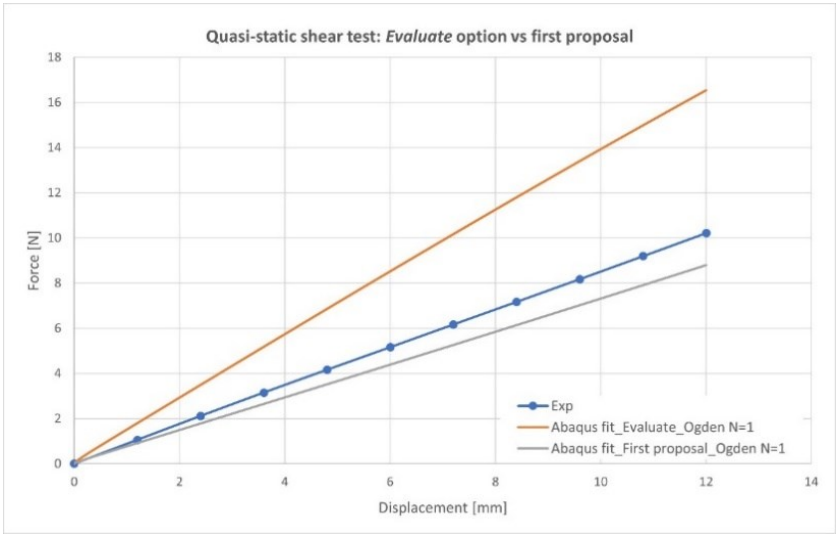


Figure 2.29 - Abaqus results for hyperelastic behaviour defined by Evaluate coefficients (N=1) vs first proposal: fit of RF1-U1 curve output with the experimental force-displacement curve for quasi-static simple shear test simulation

As evinced by the curves, the last Ogden constitutive parameters result to be suitable for fitting the experimental data until about 10% strain level in compression (-3 mm), 30% strain level in tension (9 mm), and 5% in shear (1.5 mm). This model improves the suitability of the fit with respect to the previous one, but it was chosen to propose a second set of Ogden constitutive parameters to try enhancing the fit aptness. For this reason, a new Ogden model with N=1 was proposed to define PlatSil Gel-OO 1A:1B:1D hyperelastic behaviour. It was chosen to first modify the initial shear modulus from $\mu_0 = 0.0101\ MPa$ to $\mu_0 = 0.013\ MPa$. The Poisson's ratio was set to 0,49 and the (2.46) was used to identify the initial bulk modulus K_0 as follows:

$$K_0 = -\frac{2}{3} \cdot 0.013 \cdot \frac{0.49 + 1}{2 \cdot 0.49 - 1} MPa = 0.645667\ MPa \tag{2.54}$$

Therefore, equation (2.44) was used to identify D_1 as:

$$D_1 = \frac{2}{0.501633}\ MPa^{-1} = 3.097574\ MPa^{-1} \tag{2.55}$$

Experimental quasi-static compressive, tensile and shear tests were then simulated as described before, with the only difference in the hyperelastic behaviour definition (fig. 2.30).

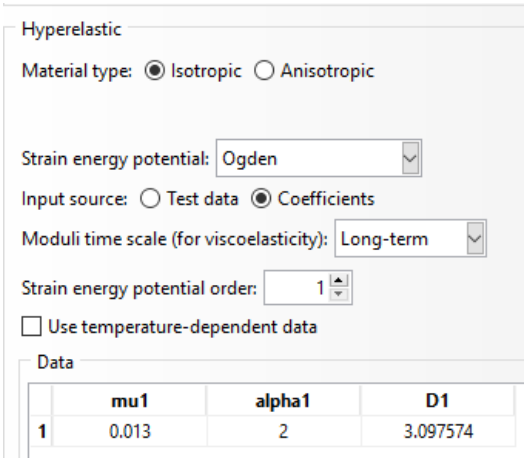


Figure 2.30 – Second proposal: PlatSil Gel-OO 1A:1B:1D new Ogden hyperelastic constitutive parameters (Coefficients)

As for the previous post-processing, for the compressive and the tensile tests, the reaction force RF3 and the displacement U3 along z axis were computed and saved, as well as RF1 and U1 along x axis for the shear test. Figures 2.31 and 2.32 show the comparison of experimental data with respect to the corresponding old model (Ogden parameters as *Evaluate* output with N=1), the first proposal and this second proposal results.

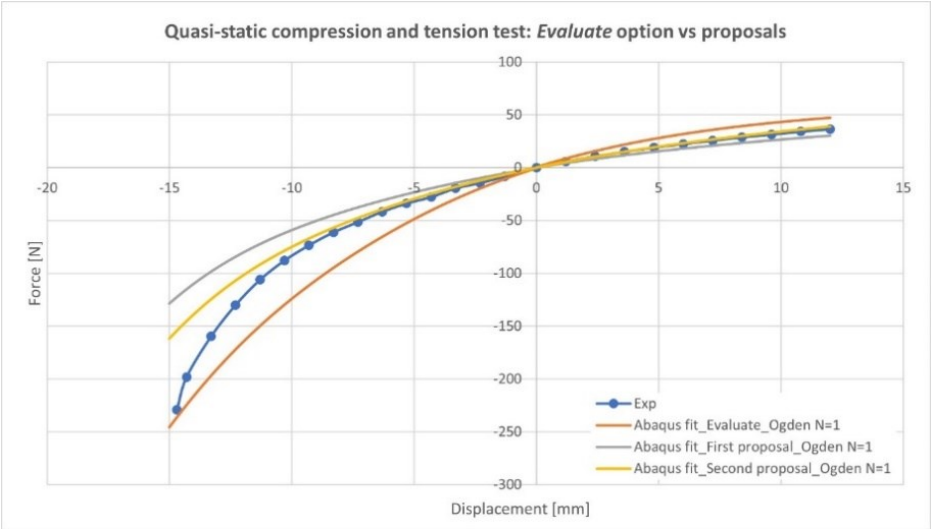


Figure 2.31 - Abaqus results for hyperelastic behaviour defined by Evaluate coefficients (N=1) vs first proposal vs second proposal: fit of RF3-U3 curve output with the experimental force-displacement curve for quasi-static compression and tension test simulation

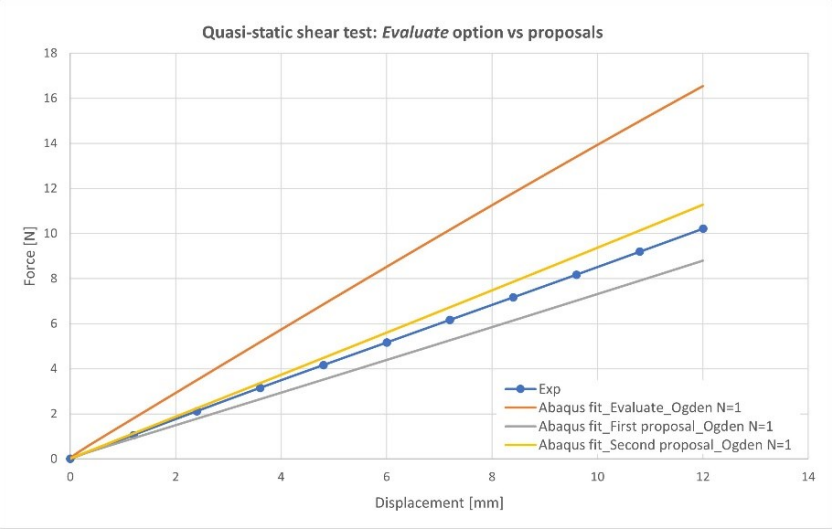


Figure 2.32 - Abaqus results for hyperelastic behaviour defined by Evaluate coefficients (N=1) vs first proposal vs second proposal: fit of RF1-U1 curve output with the experimental force-displacement curve for quasi-static simple shear test simulation

As evinced by the force-displacement curves, the second proposal results to be suitable for fitting the experimental data until about 30% strain level in compression (-9 mm), 40% strain level in tension (12 mm), and 20% strain level in shear (6 mm). This model improves the fit with respect to the previous ones, so the hyperelastic behaviour of the brain simulant material was described with the parameters shown in fig. 2.30. Figure 2.33 shows the experimental and numerical deformed specimen in tension, compression and shear quasi-static tests for the chosen set of parameters.

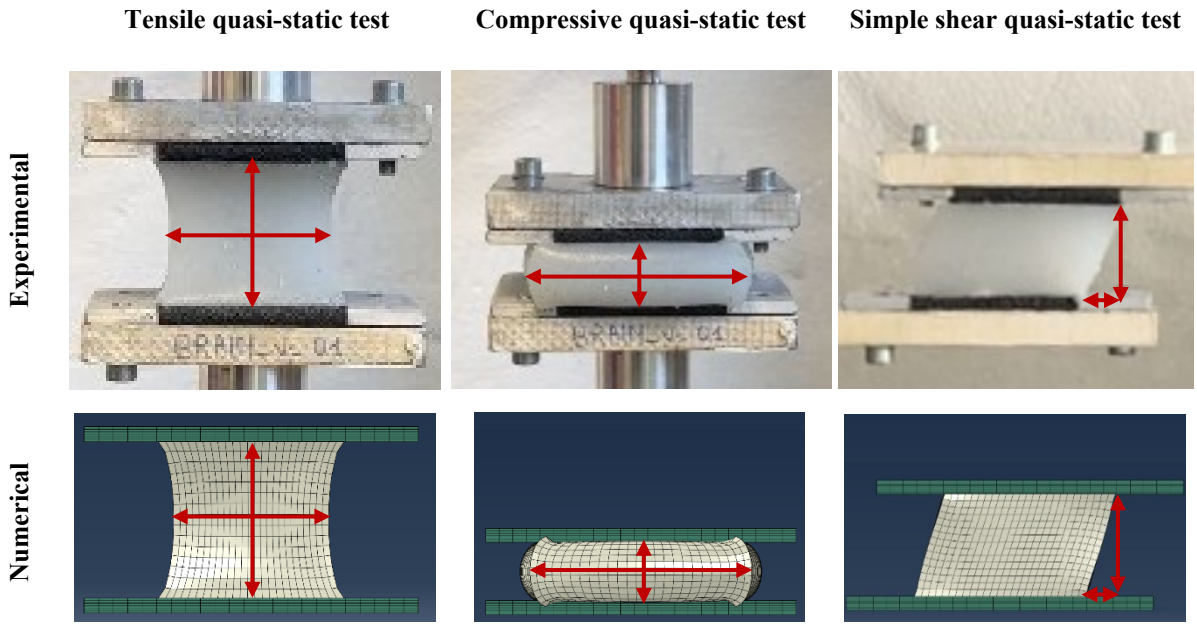


Figure 2.33 – Comparison of experimental vs numerical deformed shape of the specimen in quasi-static tests

As shown by the arrows in fig. 2.33, the final height and the lateral deformation of the specimen in tensile and compressive tests and the displacement in the simple shear test are well reproduced by the numerical simulation.

2.2.2.2 Viscoelastic constitutive parameters

MATLAB *Curve Fitter* app was used to identify Prony series parameters to describe the viscoelastic behaviour of PlatSil Gel-OO 1A:1B:1D in ABAQUS. After an interpolation, frequencies f $[Hz]$ ranging from 0,2 to 7 Hz were reported in x-axis, while shear storage moduli G' [MPa] computed for each frequency f were reported in y-axis. As first attempt, data were fitted using as *Custom Equation* $\Re(G^*)$ with $\omega = 2\pi f$ and $K = 2$:

$$G'(f) = G_\infty + \sum_{i=1}^{K} G_i \frac{(2\pi f)^2 {\tau_i}^2}{1 + (2\pi f)^2 {\tau_i}^2} = G_\infty + \frac{G_1 (2\pi f)^2 {\tau_1}^2}{1 + (2\pi f)^2 {\tau_1}^2} + \frac{G_2 (2\pi f)^2 {\tau_2}^2}{1 + (2\pi f)^2 {\tau_2}^2} \quad (2.56)$$

Data obtained by experimental tests (DMA) and their approximation are shown in fig. 2.34.

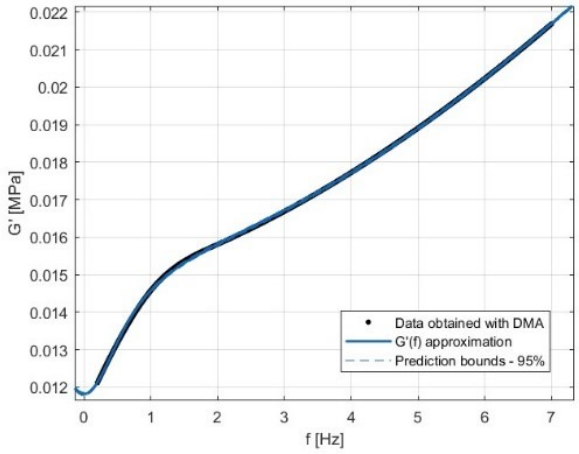


Figure 2.34 – G' approximation resulting from MATLAB Curve Fitter app

The unknown values in the (2.56) computed by *Curve Fitter* app are shown in table 2.6.

G_∞ $[MPa]$	G_1 $[MPa]$	τ_1 $[s]$	G_2 $[MPa]$	τ_2 $[s]$
0,01182	0,003823	0,2347	0,2347	0,009026

Table 2.6 – Prony series with two terms computed by MATLAB Curve Fitter app

Thus, using (2.24), Prony series parameters can be written in the dimensionless form (table 2.7).

g_1 []	τ_1 $[s]$	g_2 []	τ_2 $[s]$
0,0633	0,2347	0,7411	0,009026

Table 2.7 – Dimensionless form of Prony series parameters

In order to verify the reliability of this set of viscoelastic parameters, it was chosen to simulate the experimental tensile, compressive and shear DMA using ABAQUS. To optimize the analyses duration, it was chosen only to simulate:

- 3 cycles out of the 15 imposed at 0.2 Hz frequency
- 6 cycles out of the 25 imposed at 2 Hz frequency
- 10 cycles out of the 35 imposed at 5 Hz frequency
- 10 cycles out of the 50 imposed at 7 Hz frequency

Each of these four analyses was run for 10%, 20%, 30% and 40% strain levels imposed in tension, compression, and shear, for a total of 48 analyses.

The aim was to plot the reaction force vs displacement output and examine the last cycle fitting with the experimental force-displacement mean cycle. Therefore, a 50x50x30 mm brain surrogate sample was created as a *Part* in ABAQUS and it was assigned the *Section* made of the *Material* (fig. 2.35) defined by:

- hyperelastic constitutive parameters (second, and last, proposal described before)
- viscoelastic Prony series parameters (obtained by *Curve Fitter* app)

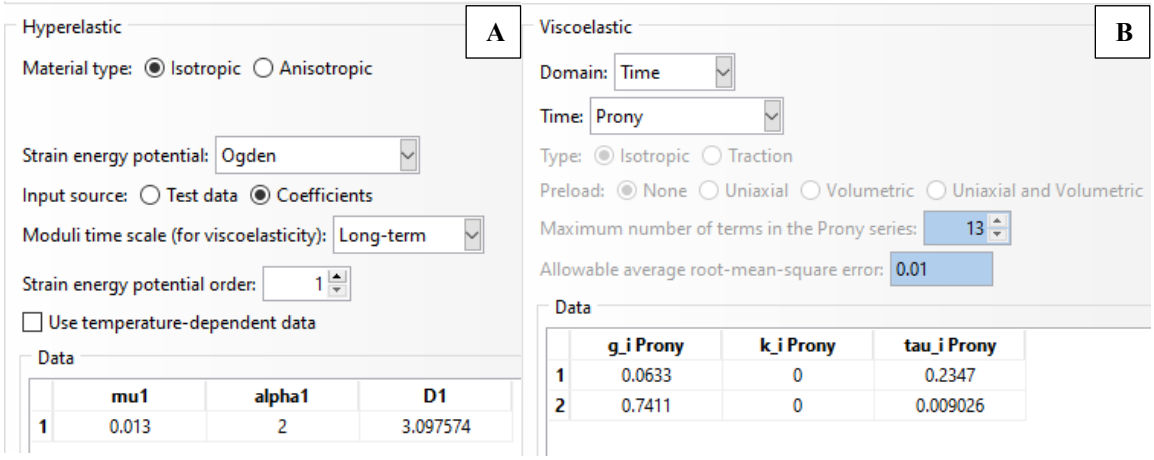


Figure 2.35 – PlatSil Gel-OO 1A:1B:1D hyperelastic and viscoelastic behaviour: (A) Ogden hyperelastic constitutive parameters resulting from the second proposal described above, (B) dimensionless form of the viscoelastic Prony series parameters (2 terms) computed by MATLAB Curve Fitter app

A 90x50x4 mm plate was created as a *Part* and it was assigned the *Section* made of the *Material* (aluminium) defined by the elastic parameters shown in fig. 2.36.

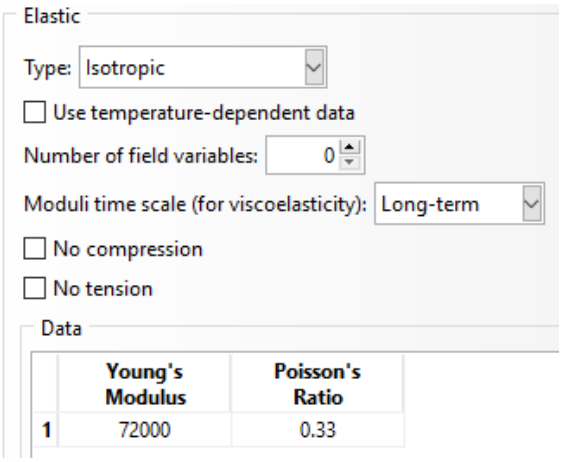


Figure 2.36 – Aluminium elastic parameters

As for the quasi-static tests, two plate *Instances* and the silicone rubber *Instance* were then created (*Assembly* → *Instances*) and the sample was positioned among the two aluminium plates. A Tie *Constraint* was imposed to simulate the silicone sample gluing to the plates and the lower plate was fixed (*BCs* → Symmetry/Antisymmetry/Encastre → ENCASTRE).

The detailed procedure described below refers to the tensile DMA simulation with an imposed 10% strain level at 0.2 Hz frequency.

At first, the upper plate was subjected to a displacement of 1.5 mm (half of the total displacement of 3 mm) along z axis (*BCs* → Displacement/Rotation → U3 = 1.5) in 0.5 s (*Step* → Visco → Time period = 0.5). A second Visco *Step* with a Time period of 15.25 s was created to simulate:

- the first 0.25 s, during which the displacement was kept constant at 1.5 mm
- the following 3 sinusoidal cycles, each of period $T = \frac{1}{f} = \frac{1}{0.2} s = 5\ s$, during which the sample displacement ranged from 0 to 3 mm with a sinusoidal *Amplitude* of Circular frequency $\omega = 2\pi f = 2\pi \cdot 0.2\ \frac{\text{rad}}{\text{s}} = 1.256\ \frac{\text{rad}}{\text{s}}$

The reaction force RF3 and the displacement U3 along z axis were computed and saved.

For the imposed 20%, 30%, and 40% tensile strain level at 0.2 Hz frequency, U3 was respectively assigned the value of 3 mm, 4.5 mm, and 6 mm. Fig. 2.37 shows the displacement vs time plots related to the four tensile strain levels at 0.2 Hz.

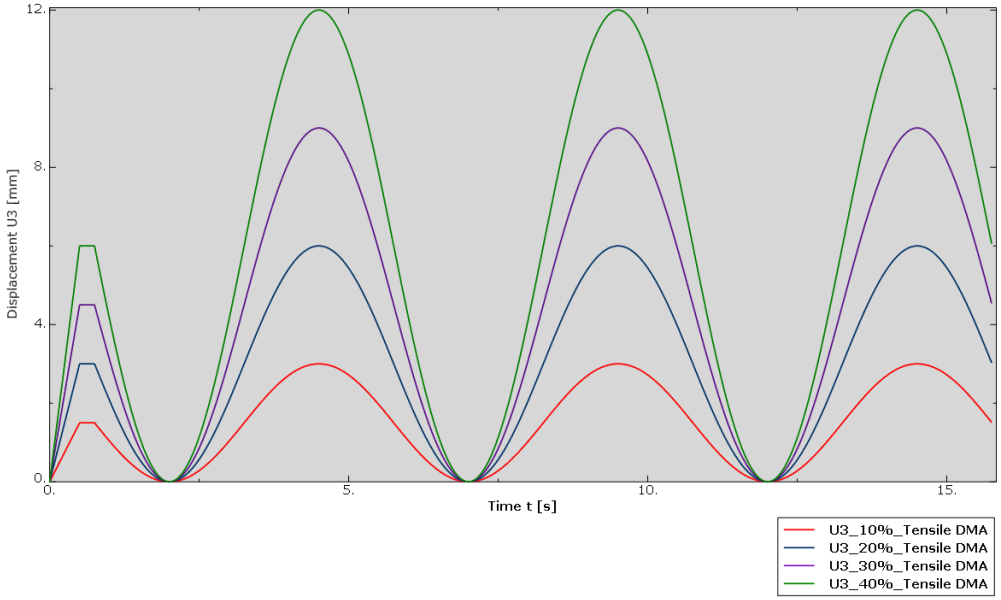


Figure 2.37 – Displacement imposed (10%, 20%, 30%, and 40% strain level) in tensile DMA simulations

The same procedure was followed to simulate the tensile DMA at 2 Hz frequency, 5 Hz frequency, and 7 Hz frequency, with the only differences in:

- *Amplitude* Circular frequency definition:
  - $f = 2\ Hz \rightarrow \omega = 2\pi f = 2\pi \cdot 2\ \frac{\text{rad}}{\text{s}} = 12.56\ \frac{\text{rad}}{\text{s}}$
  - $f = 5\ Hz \rightarrow \omega = 2\pi f = 2\pi \cdot 5\ \frac{\text{rad}}{\text{s}} = 31.4\ \frac{\text{rad}}{\text{s}}$
  - $f = 7\ Hz \rightarrow \omega = 2\pi f = 2\pi \cdot 7\ \frac{\text{rad}}{\text{s}} = 43.96\ \frac{\text{rad}}{\text{s}}$
- Time period definition in the second *Step*:

- $f = 2\ Hz$ → Time period = 3.25 to simulate the 0.25 s of constant displacement and the next 6 sinusoidal cycles, each of period $T = \frac{1}{f} = \frac{1}{5} s = 0.5\ s$
- $f = 5\ Hz$ → Time period = 2.25 to simulate the 0.25 s of constant displacement and the next 10 sinusoidal cycles, each of period $T = \frac{1}{f} = \frac{1}{5} s = 0.2\ s$
- $f = 7\ Hz$ → Time period = 1.679 to simulate the 0.25 s of constant displacement and the next 10 sinusoidal cycles, each of period $T = \frac{1}{f} = \frac{1}{7} s \approx 0.1429\ s$

Figures 2.38, 2.39, and 2.40 show the imposed displacement for the tensile DMA at 2 Hz, 5 Hz, and 7 Hz frequency respectively for the tests at 10% strain level.

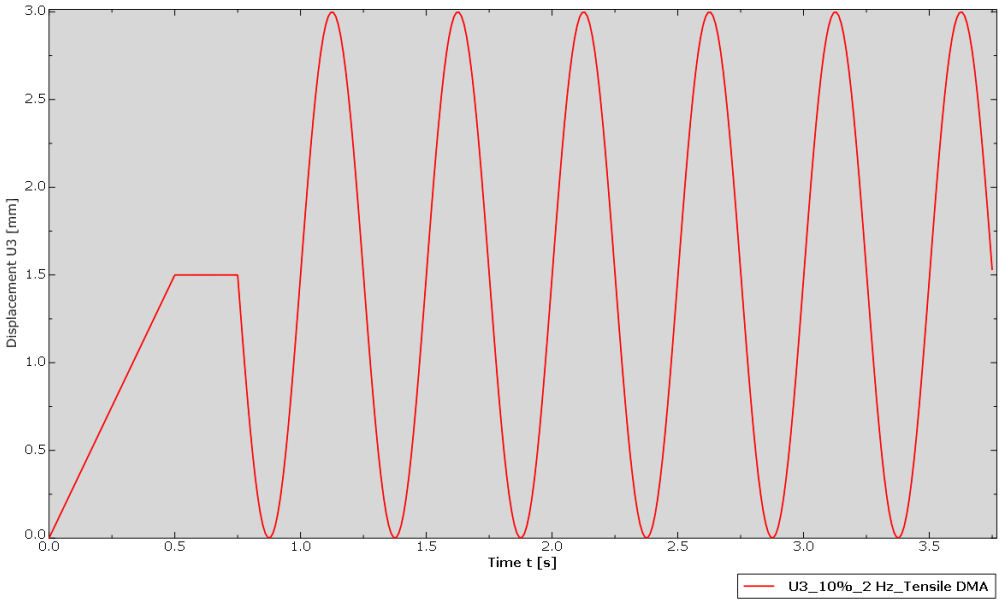


Figure 2.38 – Displacement imposed (10% strain level) in tensile DMA simulation at 2 Hz

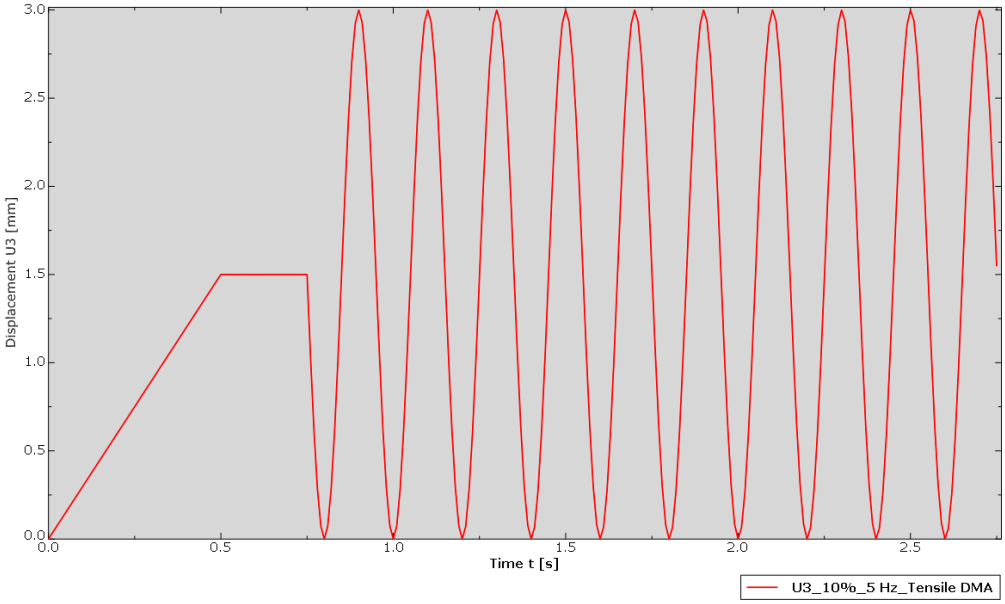


Figure 2.39 - Displacement imposed (10% strain level) in tensile DMA simulation at 5 Hz

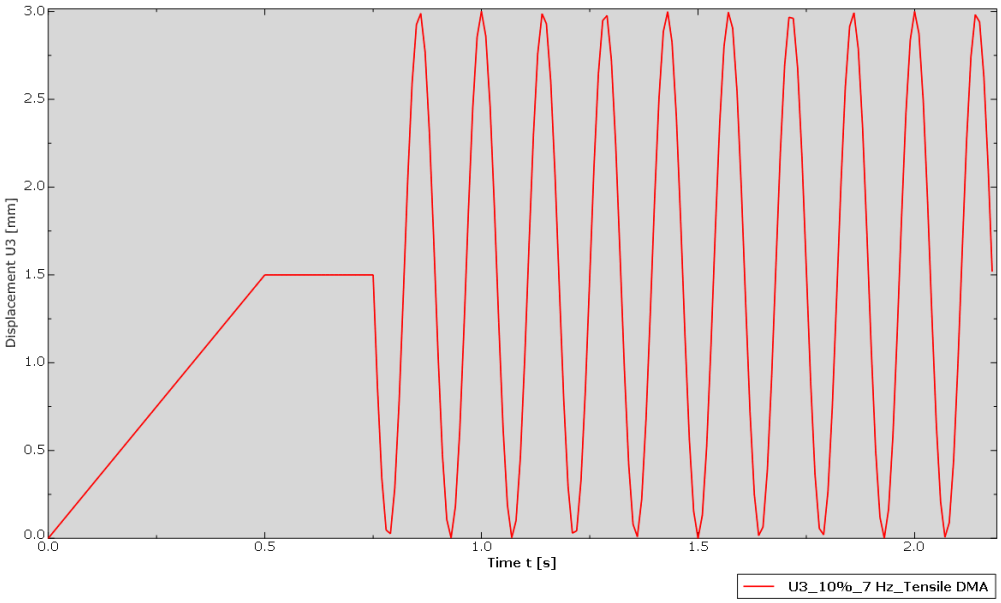


Figure 2.40 - Displacement imposed (10% strain level) in tensile DMA simulation at 7 Hz

Analogously, compressive and shear DMA at 10%, 20%, 30% and 40% imposed strain levels at 0.2 Hz, 2 Hz, 5 Hz and 7 Hz frequency were simulated. Reaction forces and displacements along z axis for the compression test (RF3 vs U3) and along x axis for the shear test (RF1 vs U1) were computed and saved.

Fig. 2.41 shows force-displacement experimental curves and Abaqus RF3-U3 output for the tensile DMA at low frequencies (0.2 Hz and 2 Hz). As observed, the simulate sample behaves in a similar way with respect to the physical specimen tested, in particular until 20% strain level, when RMSE value is <1, indicative of a good fit of the simulated curve with the experimental one. A better fit is observed in all cases in the central areas of the loading and unloading curves, with a more pronounced deviation at reversals in the direction of force application, i.e. at the end of the curves.

Fig. 2.42 shows force-displacement experimental curves and Abaqus RF3-U3 output for the compressive DMA at low frequencies (0.2 Hz and 2 Hz). As observed, the simulate sample behaves in a similar way with respect to the physical specimen tested until 20% strain level. For compressive strain levels higher than 20% the simulate curves begin to deviate from the experimental ones more than observed in the tensile case. In particular, the simulated curve remains close to the experimental one approximately in the first half, while a greater deviation is observed as the displacement increases. At higher strains (30% and 40%), RMSE around 15 is observed, which compares with maximum force values (dependent variable) of 70 and 140 N respectively.

Fig. 2.43 shows force-displacement experimental curves and Abaqus RF1-U1 output for the simple shear DMA at low frequencies (0.2 Hz and 2 Hz). As observed, the simulated sample behaves in a similar way with respect to the physical specimen tested at 0.2 Hz for all the strain levels. For shear strain levels imposed at 2 Hz frequency, the loading curve accurately fits the experimental one, while the hysteresis area resulting by the model appears slightly higher with respect to the one experimentally estimated. The good fit to acquired data at low frequencies is confirmed by the RSME, e. g. equal to 0.35 and 0.65 for the shear DMA analysis at 20% strain-0.2 Hz and 30% strain-2 Hz frequency respectively.

Tensile DMA simulations at low frequencies

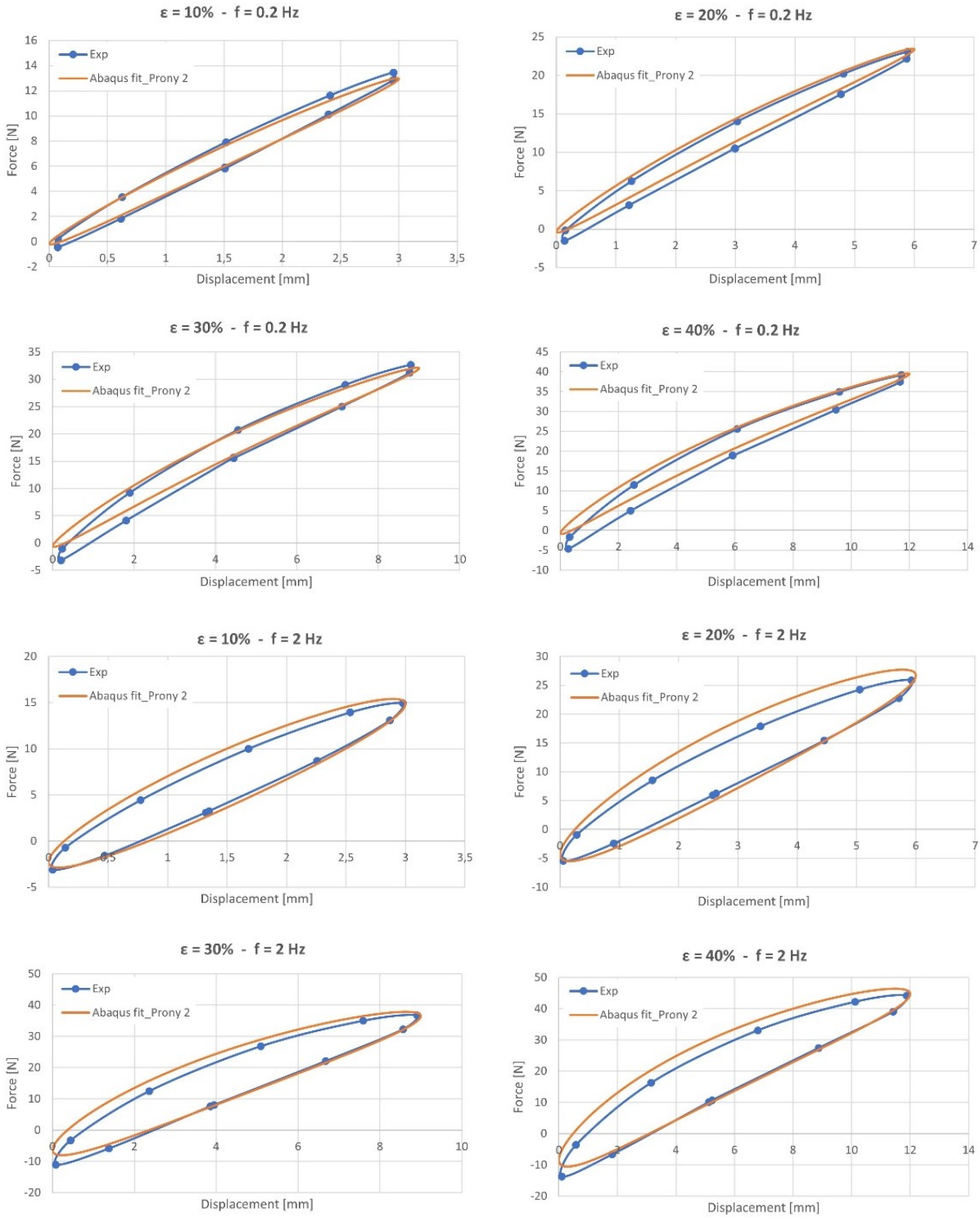


Figure 2.41 – Force-displacement experimental curves and Abaqus RF3-U3 output for the tensile DMA simulation at 10%, 20%, 30%, and 40% strain levels at low frequencies (0.2 Hz and 2 Hz); viscoelastic behaviour was defined by the Prony series with two terms computed by Curve Fitter app

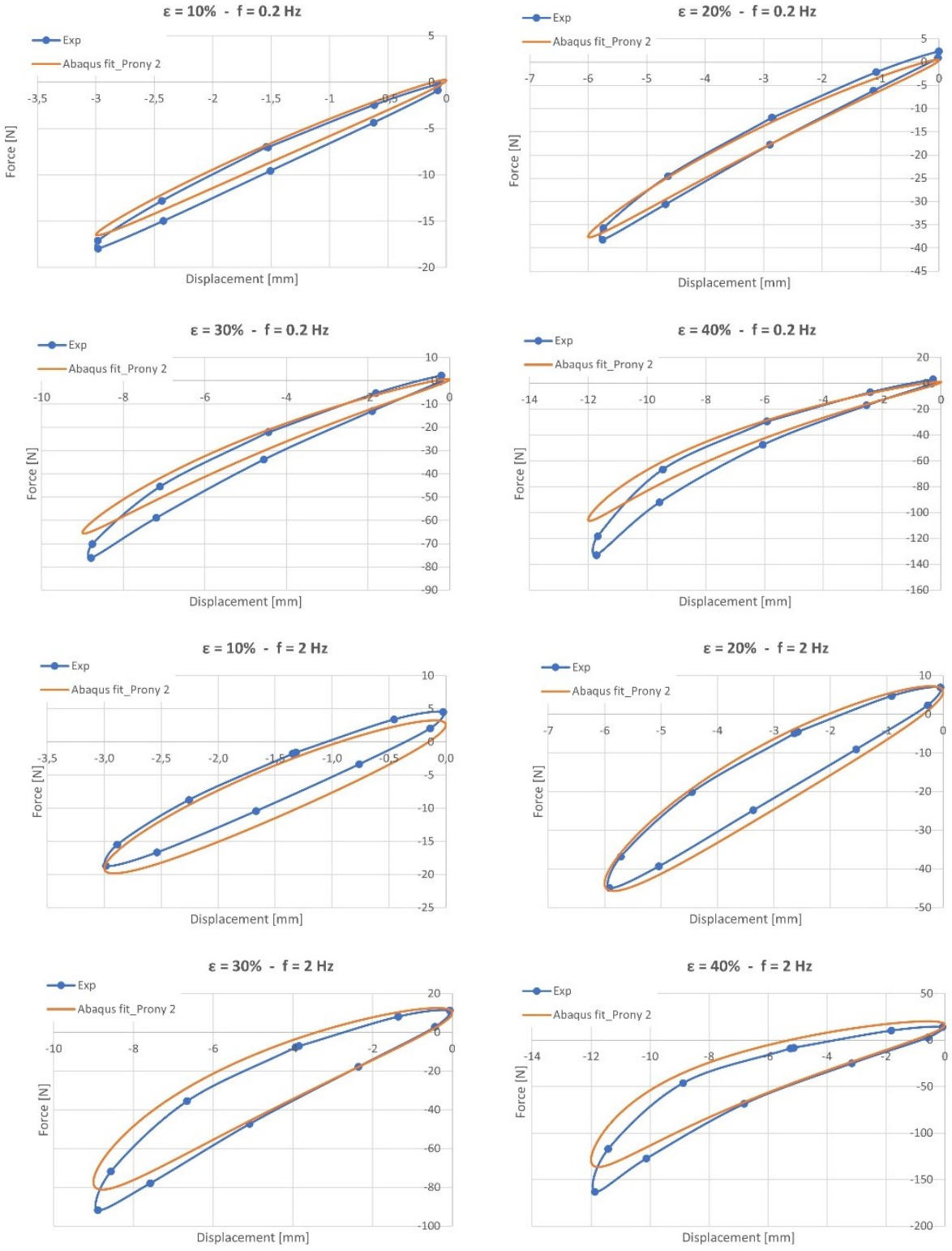


Figure 2.42 - Force-displacement experimental curves and Abaqus RF3-U3 output for the compressive DMA simulation at 10%, 20%, 30%, and 40% strain levels at low frequencies (0.2 Hz and 2 Hz); viscoelastic behaviour was defined by the Prony series with two terms computed by Curve Fitter app

Simple shear DMA simulations at low frequencies

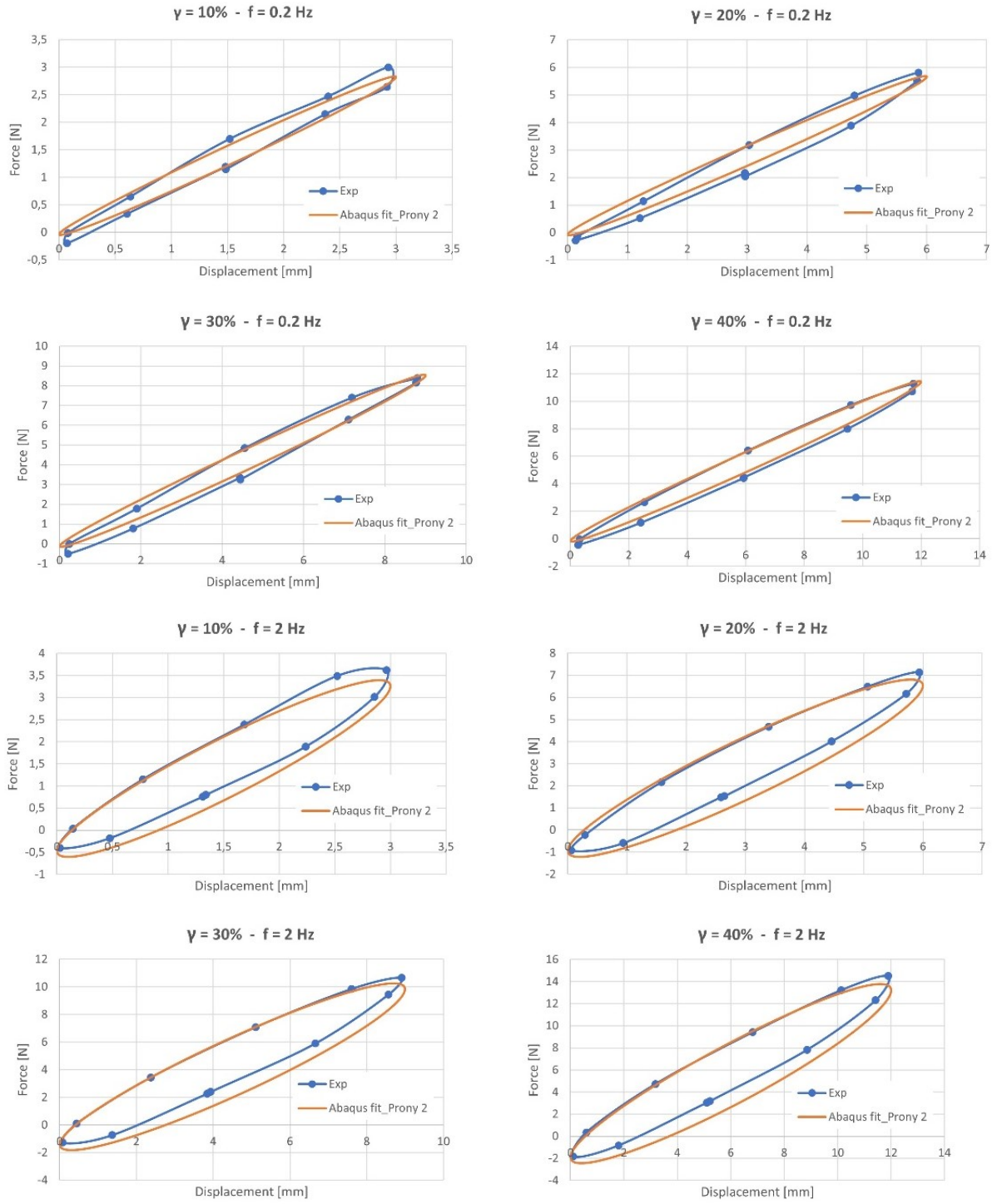


Figure 2.43 - Force-displacement experimental curves and Abaqus RF1-U1 output for the simple shear DMA simulation at 10%, 20%, 30%, and 40% strain levels at low frequencies (0.2 Hz and 2 Hz); viscoelastic behaviour was defined by the Prony series with two terms computed by Curve Fitter app

At high frequencies (5 and 7 Hz) the simulated hysteresis area was found to be significantly higher than the one obtained experimentally for all strain levels in tension, compression and shear. Therefore, Matlab *Curve Fitter* app was used to fit the experimental storage modulus in function of frequencies, as described for the Prony series with 2 terms used for the simulations above, to find the Prony series with 3, 4, 5 and 6 terms. As shown in fig. 2.44, all the obtained sets of parameters accurately fit the experimental data.

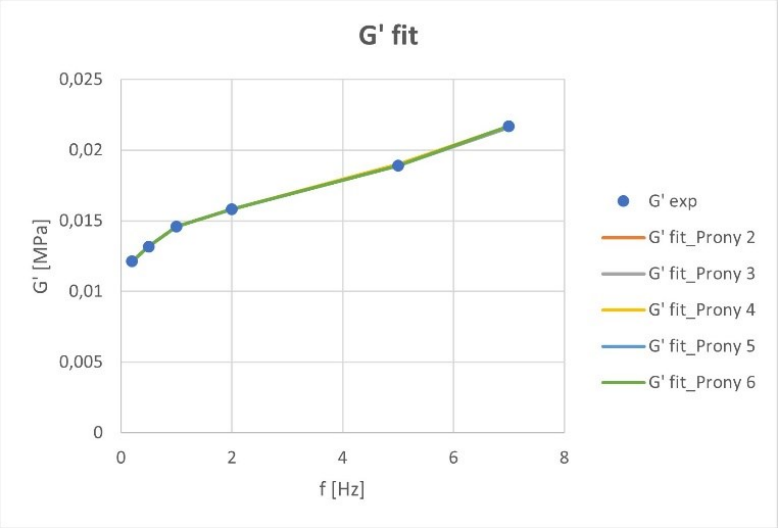


Figure 2.44 – Fit of G' for Prony series with 2, 3, 4, 5, and 6 terms computed by MATLAB Curve Fitter app

The parameters obtained were then used to estimate the loss moduli as function of frequencies using the equation $\Im(G^*) = G''(\omega)$. The aim was to choose the Prony series which allowed the estimated loss modulus curve to be closest to the experimental one. As evinced by fig. 2.45, for low frequencies the Prony series with 2, 3, 4 and 5 terms accurately fit the experimental loss modulus behaviour. For high frequencies, the Prony series with 3 terms was found to be the best choice among the possible sets.

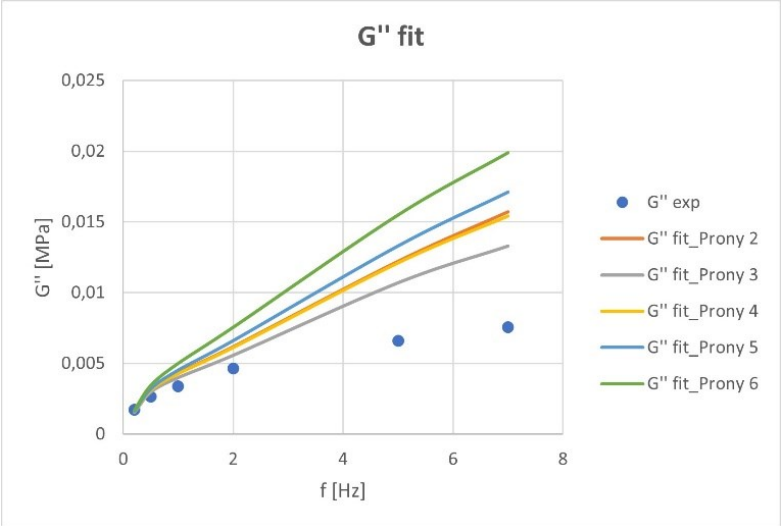
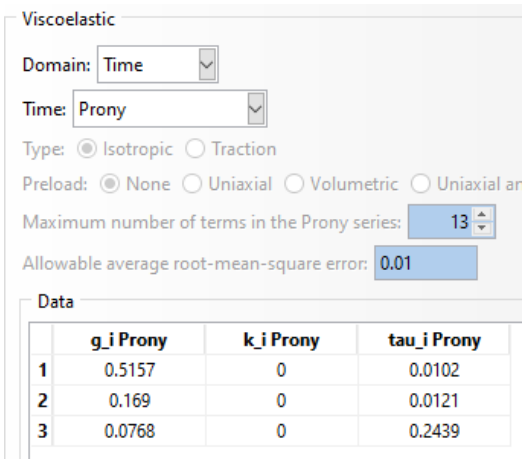


Figure 2.45 - Fit of G'' for Prony series with 2, 3, 4, 5, and 6 terms computed by MATLAB Curve Fitter app

Therefore, it was chosen to simulate again the tensile, compressive and shear DMA at 5 and 7 Hz frequencies at 10%, 20%, 30% and 40% strain levels with the viscoelastic behaviour described by the Prony series parameters with 3 terms (fig. 2.46).



	g_i Prony	k_i Prony	tau_i Prony
1	0.5157	0	0.0102
2	0.169	0	0.0121
3	0.0768	0	0.2439

Figure 2.46 – New viscoelastic behaviour definition: Prony series parameters with 3 terms

Figures 2.47, 2.48, and 2.49 show force-displacement experimental curves and Abaqus output for the tensile, compressive, and simple shear DMA at high frequencies (5 Hz and 7 Hz) with the viscoelastic behaviour described by the Prony series with 2 and 3 terms. As observed for all the strain levels, the hysteresis areas slightly decrease in case of Prony series with 3 terms. This is also confirmed by RMSE values, which clearly decrease for the curves plotted with this parameter set (e.g. RMSE drops from 0.65 to 0.34 in the shear test at 40% strain at 7 Hz). Even if the experimental curves still show a lower hysteresis area, this set of parameters allows to enhance the suitability of the DMA fit compared to the previous one. Hence, this new proposal (fig. 2.46) was chosen to describe the viscoelastic behaviour of the brain simulant material.

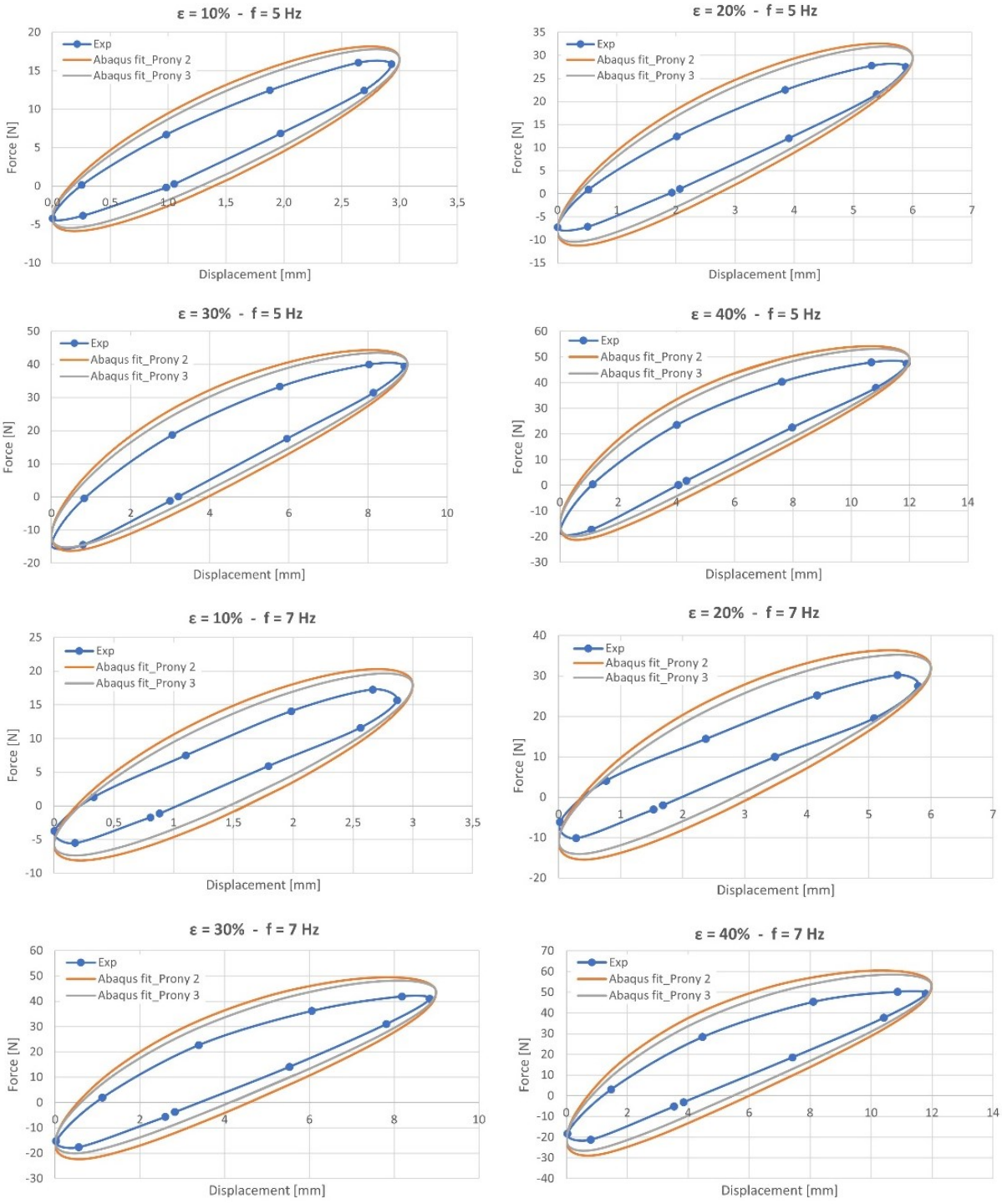


Figure 2.47 - Force-displacement experimental curves and Abaqus RF3-U3 output for the tensile DMA simulation at 10%, 20%, 30%, and 40% strain levels at low frequencies (0.2 Hz and 2 Hz); viscoelastic behaviour was defined by the Prony series with two and three terms computed by Curve Fitter app

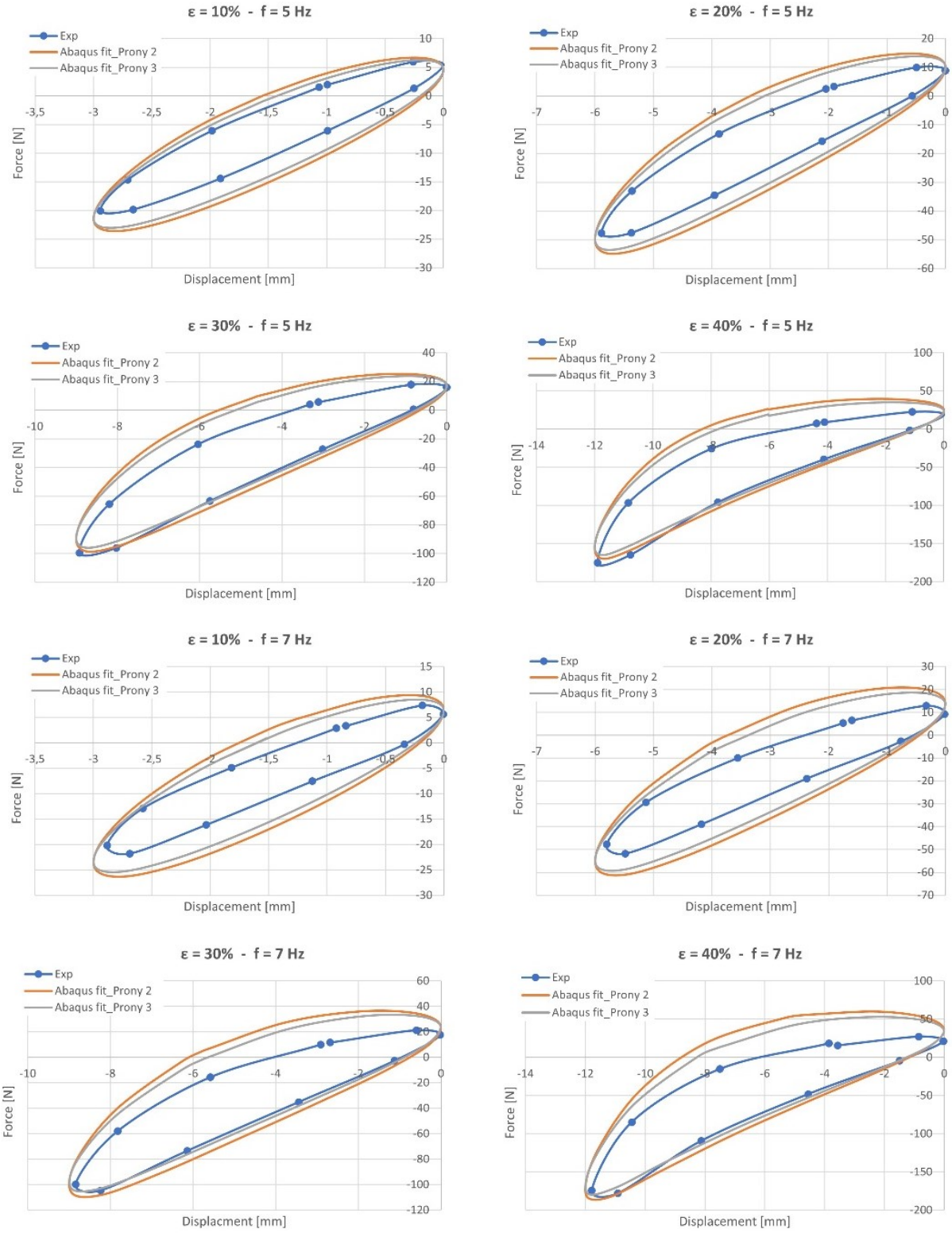


Figure 2.48 - Force-displacement experimental curves and Abaqus RF3-U3 output for the compressive DMA simulation at 10%, 20%, 30%, and 40% strain levels at low frequencies (0.2 Hz and 2 Hz); viscoelastic behaviour was defined by the Prony series with two and three terms computed by Curve Fitter app

Simple shear DMA simulations at high frequencies

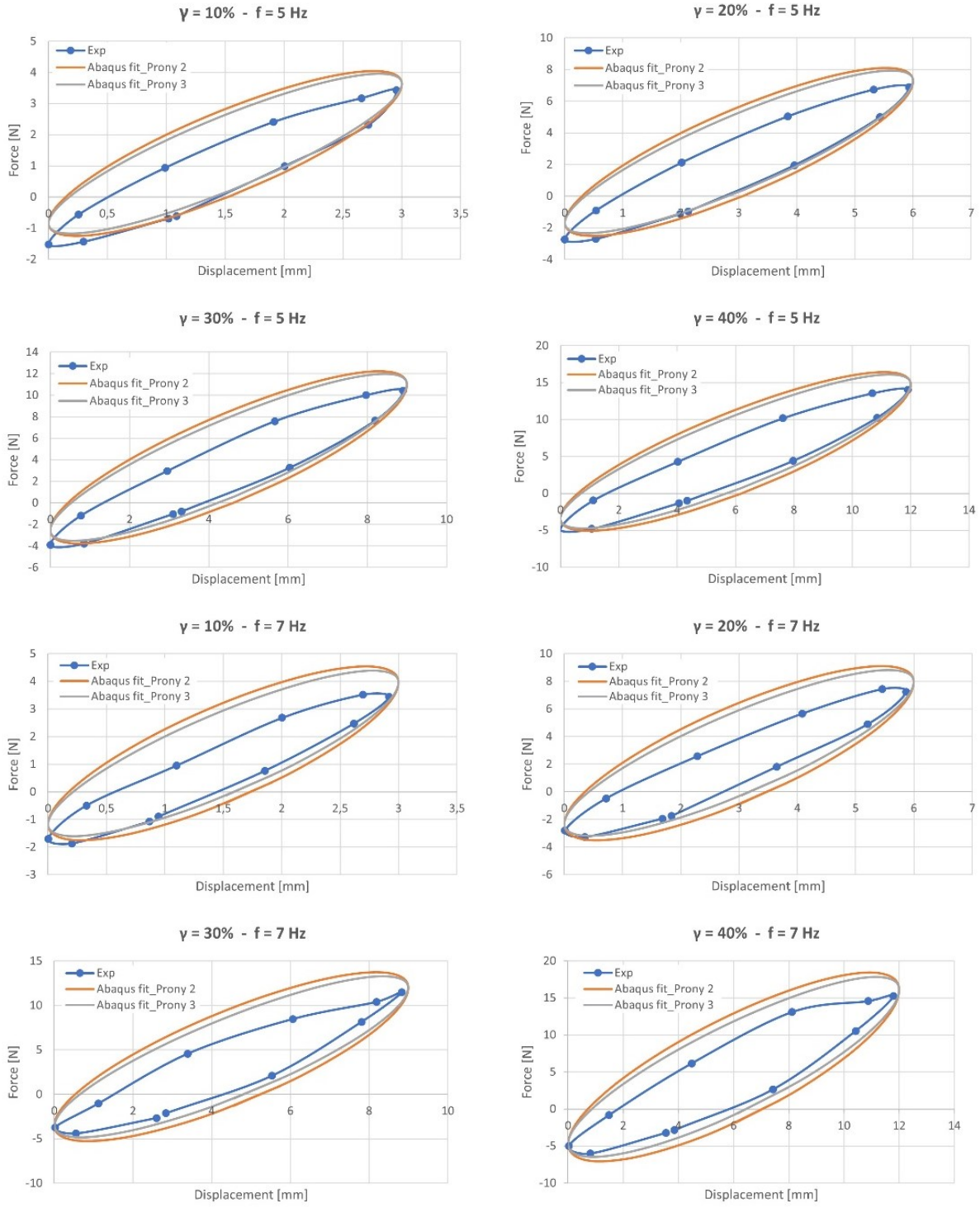


Figure 2.49 - Force-displacement experimental curves and Abaqus RF1-U1 output for the simple shear DMA simulation at 10%, 20%, 30%, and 40% strain levels at low frequencies (0.2 Hz and 2 Hz); viscoelastic behaviour was defined by the Prony series with two and three terms computed by Curve Fitter app

Figures 2.30 and 2.46 are here recalled in fig. 2.50 for a brief recap on the identified hyperelastic and viscoelastic constitutive parameters.

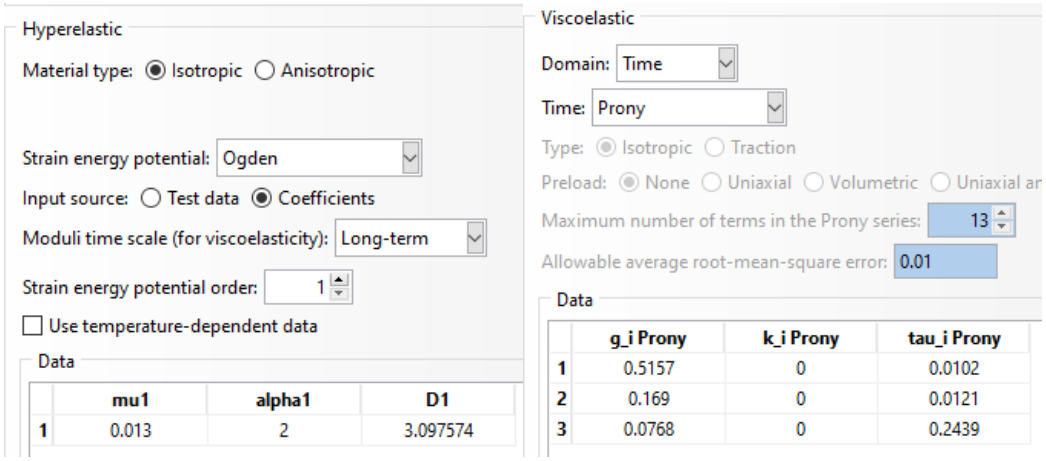


Figure 2.50 – Identified hyperelastic and viscoelastic constitutive parameters for brain simulant material

On the basis of the constitutive analysis performed, it was chosen to model the PlatSil Gel-OO 1A:1B:1D (brain simulant material) with a one-term Ogden model and a Prony series with 3 terms.

2.3 Subarachnoid space simulant material

2.3.1 Mechanical characterization of subarachnoid space simulant material

As a consequence of a direct or indirect impact, the pia-arachnoid complex (PAC) partially mediates the transfer of kinetic energy, thus contributing to reduce deformation to the brain. In particular, the subarachnoid space (SAS) behaves as a damper thanks to solid/fluid interactions among arachnoid trabeculae and cerebrospinal fluid. The cerebrospinal fluid helps keeping brain shape and position while moving. The arachnoid trabeculae play a passive role absorbing the shock when they buckle if subjected also to a very low compressive load. Moreover, tensile and shear loading are actively supported by these collagen-based rods, that limit the skull-brain relative motion. When a compression of SAS occurs, trabeculae contribute to absorb the load by developing hydraulic resistance, in conjunction to the CSF pressure, without any transfer of load to the brain. In case of tensile loads, the damping effect is ensured by the combination of the tethering effect exerted by the trabeculae and the hydraulic resistance of CSF [Jin et al., 2006-2014; Ghaffari et al., 2014; Saboori and Sadegh, 2011-2014; Benko et al., 2021].

Human arachnoid trabeculae elastic modulus reported in literature ranges from a value of about 1-1,5 kPa (Saboori and Sadegh) to $21{,}5 \cdot 10^3$ kPa (Zhang et al).

In 2006 Jin et al. performed in-plane tensile, normal traction and shear tests on bovine PAC samples under different strain rates (0,22 s^{-1}, 1,0 s^{-1}, 9,2 s^{-1}, 49 s^{-1}). As shown in table 2.8, it was observed that the elastic moduli obtained in the normal traction and shear tests were much lower than those obtained for the in-plane tensile tests. This is due, in the first two cases, to the

resistance that just the arachnoid trabeculae oppose to the relative movement between the skull and the brain [Jin et al., 2006-2013]. The experimental set-up is shown in fig. 2.51. Elastic modulus in normal traction tests is intermediate with respect to Saboori and Sadegh (1-1,5 kPa) and Zhang et al. ($21{,}5 \cdot 10^3$ kPa) results.

	Normal traction test	Shear test	In-plane tensile test
Elastic modulus	61-148 kPa	11-22 kPa	6-40 MPa

Table 2.8 – Elastic moduli of bovine PAC [Jin et al., 2013]

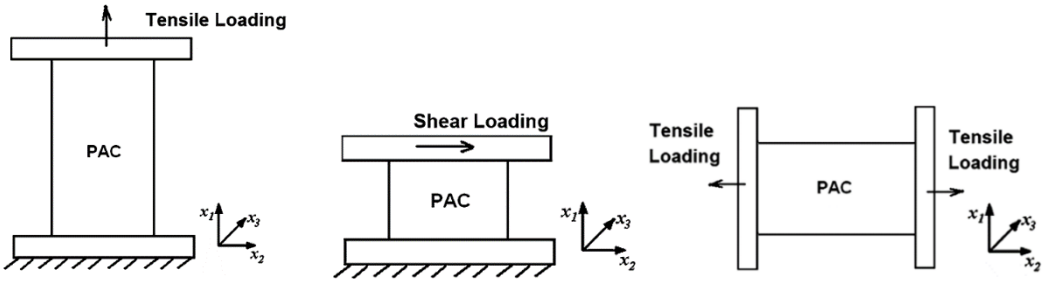


Figure 2.51 – Set-up of loading tests. Left to right: normal traction, shear, and in-plane tensile tests on Bovine PAC [Jin et al., 2013]

In 2021, Benko et al. performed a normal traction test via fluid pressurization on human cadaver PAC samples. The average normal traction modulus was quantified in 12,6 ± 4,8 kPa, that's between the value proposed by Saboori and Sadegh in their modelling approach (1 kPa) and measured by Jin et al. on bovine PAC specimens (61-148 kPa) [Benko et al., 2021].

To characterize the stress-strain relationship of the open-cell polymer foams under investigation in the current work, uniaxial compressive and normal traction quasi-static tests were performed using MTS 858 Mini Bionix II. A 40% strain level was imposed in compression and normal traction on 50x50x5 mm specimens made of 20 PPI (pores per inch) and 30 PPI polyurethane open-cell foams. The experimental set-up is shown in fig. 2.52.

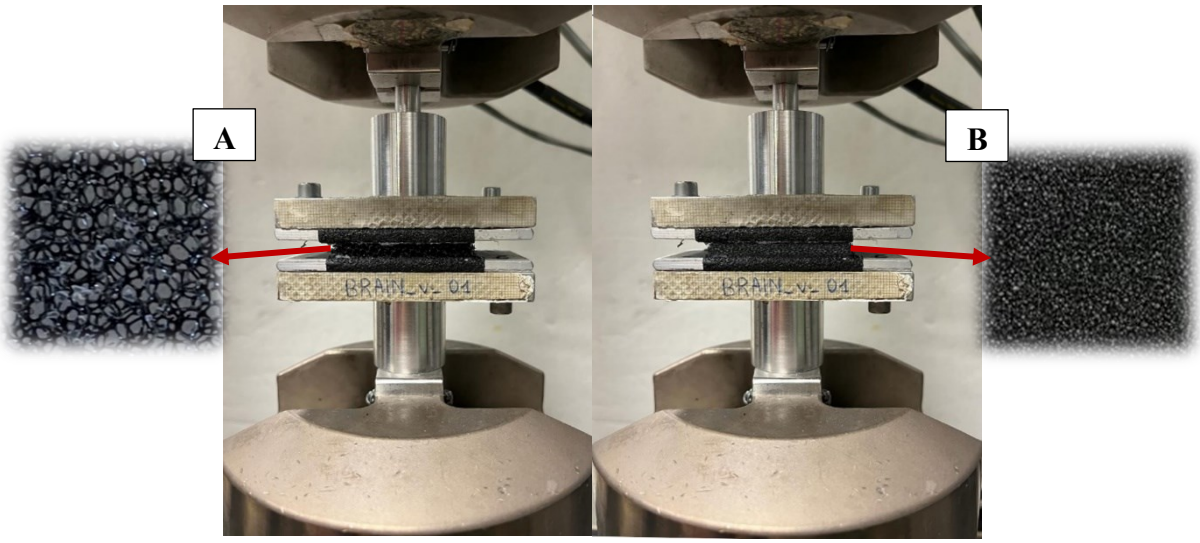


Figure 2.52 – Experimental set-up for quasi-static tests on (A) 20 PPI and (B) 30 PPI open-cell polymer foams

The samples were deformed with a loading velocity of 0,05 mm/s, corresponding to a strain rate of 0,01 s^{-1}. Data were processed using MATLAB R2022b software to remove the noise. The resulting engineering stress-strain curves are shown in fig. 2.53 A/C and 2.53 B/D for the 20 PPI and 30 PPI open-cell polymer foams respectively.

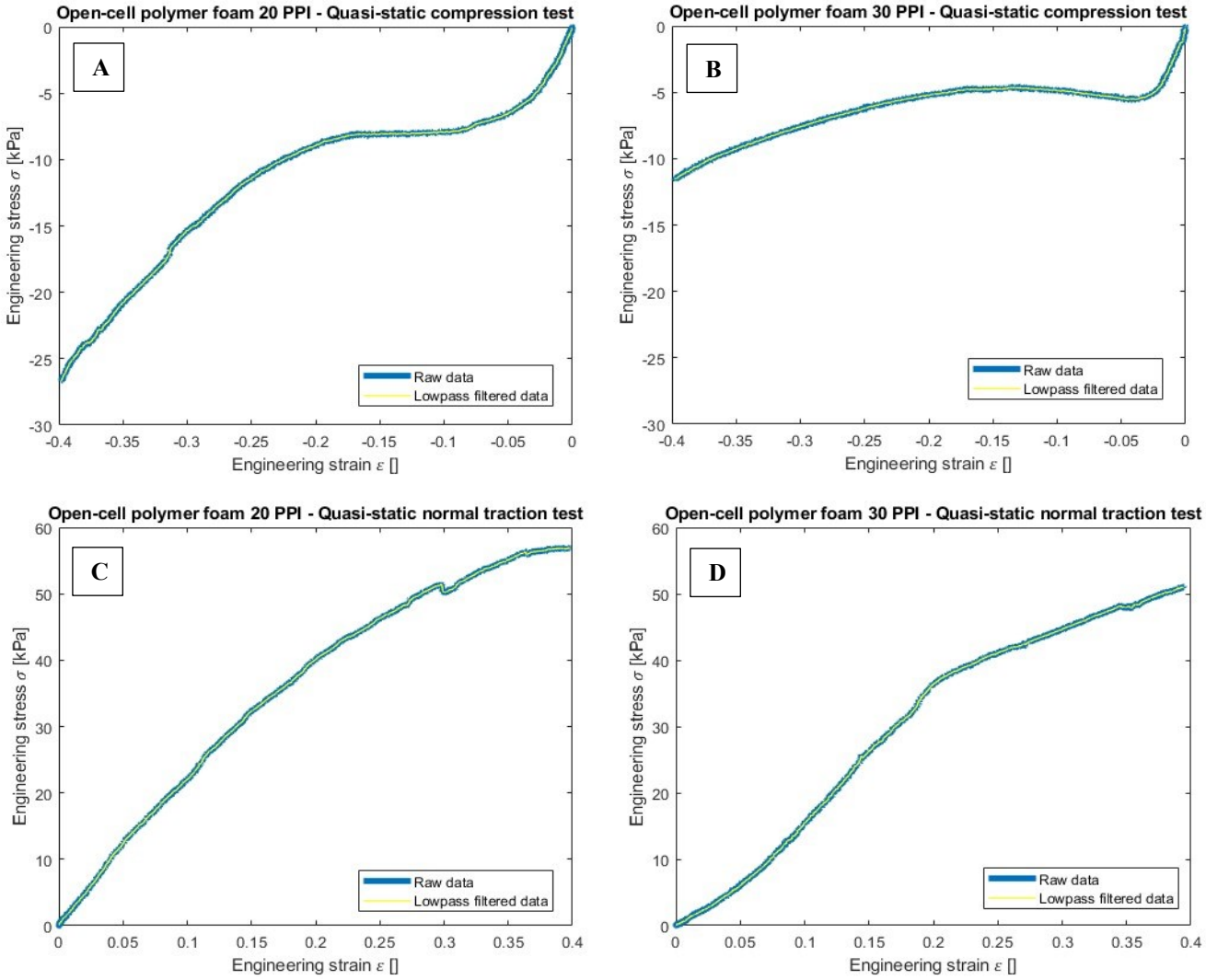


Figure 2.53 – Resulting engineering stress-strain curves from: quasi-static compression tests [(A) 20 PPI, (B) 30 PPI open-cell polymer foam], quasi-static normal traction tests [(C) 20 PPI, (D) 30 PPI open-cell polymer foam]

During compression, as consequence of the cell wall bending, the two foams firstly exhibit a linear elastic stress-strain response. Then, buckling phenomena leads to a plateau at almost constant stress. Last, the stress rapidly increases due to cell walls densification [Abaqus documentation]. These foams could play a passive role in the physical prototype absorbing the shock when they buckle.

During normal traction, cell wall bending leads to linear elastic stress-strain relationship at small strains. Then, for elastomeric foams, there would be an increase of stiffness due to walls alignment [Abaqus documentation]. During the experimental test, the foam started detaching

from the plates, so this stiffness increase is not observable. However, the elastic normal traction moduli were quantified as:

- E = 228,2 kPa for 20 PPI open-cell polyurethane foam
- E = 107,4 kPa for 30 PPI open-cell polyurethane foam

30 PPI open-cell foam resulted to be closer, but still too high, to Jin et al. 61 kPa with respect to 20 PPI open-cell foam. Despite the excessive stiffness compared to Saboori and Sadegh, Benko et al. and Jin et al. tests, in the current head prototype it was chosen to simulate arachnoid trabeculae with the 30 PPI open-cell foam. For now, this was accepted because the foam was not glued to the skull surrogate, with the aim to evaluate merely its contribute to absorb compressive loads by developing hydraulic resistance in conjunction to the distilled water (CSF simulant material) pressure.

Distilled water that simulates CSF is incompressible and it's characterized by a bulk modulus of 2200 MPa.

2.3.2 Identification of the constitutive parameters of subarachnoid space simulant material

2.3.2.1 Hyperelastic constitutive parameters

As stated before (par. 1.3.1), in the physical head prototype the 5 mm thick open-cell polymer foam was wrapped around the brain surrogate. The remained cavity in between brain and skull surrogates was filled with the distilled water. In several studies involving the development of a FEM model [Zhang et al., 2001; Kleiven and Hardy, 2002; Takhounts et al., 2008], the complex structure of the subarachnoid space has been modelled as a soft solid with water bulk modulus and a modest shear modulus [Saboori and Sadegh, 2011]. According to this, since the space between the brain and skull surrogates is occupied simultaneously by both simulant materials, it was chosen to realize a single solid 3D body with hyperelastic behaviour described by a Neo-Hookean model. It has been assigned:

- a very low shear modulus, equal to 1/10 of the shear modulus of PlatSil Gel-OO 1A:1B:1D which simulates the brain:

$$\mu_0 = \frac{\mu_{0\ PlatSil\ Gel-OO1D}}{10} = \frac{0{,}013}{10} MPa = 0{,}0013\ MPa \tag{2.57}$$

- water bulk modulus:

$$K_0 = 2200\ MPa \tag{2.58}$$

To do this, the constitutive parameters of the Neo-Hookean model have been identified using (2.41) and (2.42) as follows:

$$C_{10} = \frac{\mu_0}{2} = \frac{0{,}0013}{2}\ MPa = 0{,}00065\ MPa \tag{2.59}$$

$$D_1 = \frac{2}{K_0} = \frac{2}{2200} MPa^{-1} = 0{,}00091\ MPa^{-1} \tag{2.60}$$

The resulting Poisson's ratio was verified using the formula (2.46) to ensure the incompressibility of the solid due to the presence of distilled water:

$$\nu = \frac{3 \cdot 2200 / 0{,}0013 - 2}{6 \cdot 2200 / 0{,}0013 + 2} = 0{,}4999997 \tag{2.61}$$

2.4 Skin simulant material

2.4.1 Mechanical characterization of skin simulant material

Human skin exhibits both viscoelastic and hyperelastic properties, showing a strong dependence on strain-rate. This allows for energy dissipation under exterior loads [Dall'Aqua et al., 2020]. Skin surrogate in the physical prototype is made of silicone rubber.

2.4.1.1 Dynamic mechanical analysis (DMA)

In 2020/2021, DMA was performed at the University of Padua on samples made of PlatSil Gel-10 1A:1B. This silicone rubber was chosen as skin simulant material of a physical head prototype by A. L. Silvestroni and G. Zullo. MTS 858 Mini Bionix II was used to characterize this silicone rubber. As described for the brain surrogate silicone rubber mechanical characterization, a 50x50x30 mm specimen was cyclically subjected to 10%, 20%, 30% and 40% strain levels in tension, compression and shear at different frequencies for the number of cycles indicated in table 2.9 [Silvestroni, 2020].

Strain ε [%]	Displacement u [mm]
10	3
20	6
30	9
40	12

Frequency f [Hz]	Number of cycles n []
0,2	15
0,5	15
1	20
2	25
5	30
7	45

Table 2.9 - DMA Unipd protocol [Silvestroni, 2020]

In literature, human skin hardness is stated to be in the range of shore A 20-75 [Jammes et al., 2017; Periyasamy, Anand, and Ammini, 2012], so it was chosen to perform DMA on PlatSil Gel-25 50x50x30 mm sample (fig. 2.54 A). To compare results with previous ones, it was followed the same protocol described above. As reported for brain simulant materials, MTS 858 Mini Bionix II was used to evaluate time, displacement u and force F imposed on the PlatSil Gel-25 sample performing tests in displacement control. Unfortunately, the machine didn't allow to perform 40% cyclic compressive test. Moreover, imposing the 10% tensile level on

the sample, it detached form the grabs (fig. 2.54 B). Hence, it were performed only 10%, 20% and 30% cyclic compressive tests (fig. 2.54 C).

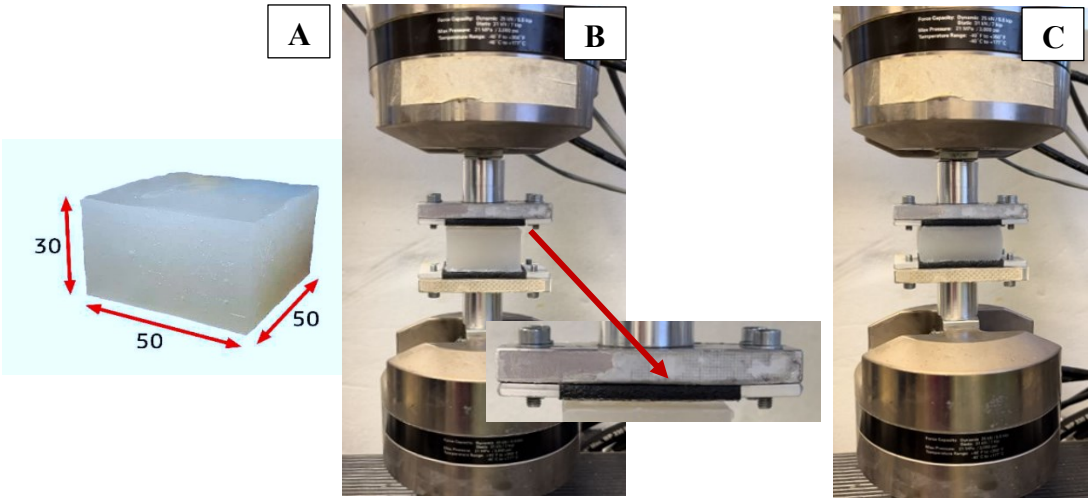


Figure 2.54 - PlatSil Gel-25 specimen (A) and experimental set-up for (B) tensile DMA (with the sample detachment from the grabs) and (C) compressive DMA

Time, displacement and force results were then elaborated using MATLAB R2022b software. As described above for brain simulant materials, machine results were divided on various sets on the basis of both imposed strain level and cycle frequency. The first and the two last cycles of each set were discarded to avoid analysis of data collected while passing from a cycle frequency acquisition to the following one. Engineering stress-strain curves were pre-processed to smooth noisy data using MATLAB R2022b *Signal Analyzer* app. PlatSil Gel-25 storage moduli, loss moduli and phase angles were calculated with the (2.10), (2.11), (2.12) and (2.13). Previous PlatSil Gel-10 and current PlatSil Gel-25 results at 7 Hz are shown in tables 2.10, 2.11, and 2.12.

Material	Year	Skin Surrogate ID	Strain ε []	Compressive storage modulus Ec' [kPa]	Compressive loss modulus Ec'' [kPa]	Compressive phase angle δc [rad]
PlatSil Gel-10 1A:1B	2020 (Silvestroni, Zullo)	SS_01_20	0,1 0,2 0,3 0,4	287,94 313,98 338,01 385,43	38,44 45,05 50,31 60,79	0,13 0,14 0,15 0,16
PlatSil Gel-25 1A:1B	2022 (current)	SS_02_22	0,1 0,2 0,3 0,4	990,27 1155,41 1293,64 -	74,48 88,81 97,50 -	0,08 0,08 0,08 -

Table 2.10 - Comparison of previous (SS_01_20) and current (SS_02_22) compressive storage moduli, loss moduli, and phase angles results

Material	Year	Skin Surrogate ID	Strain ε []	Tensile storage modulus Et' [kPa]	Tensile loss modulus Et'' [kPa]	Tensile phase angle δt [rad]
PlatSil Gel-10 1A:1B	2020 (Silvestroni, Zullo)	SS_01_20	0,1	215,25	27,23	0,13
			0,2	187,10	24,52	0,13
			0,3	164,46	25,32	0,15
			0,4	149,81	23,63	0,16

Table 2.11 – Previous (SS_01_20) tensile storage moduli, loss moduli, and phase angles results

Material	Year	Skin Surrogate ID	Strain ε []	Shear storage modulus G' [kPa]	Shear loss modulus G'' [kPa]	Shear phase angle δs [rad]
PlatSil Gel-10 1A:1B	2020 (Silvestroni, Zullo)	SS_01_20	0,1	49,75	5,45	0,11
			0,2	47,20	5,23	0,11
			0,3	46,44	5,12	0,11
			0,4	46,56	4,95	0,11

Table 2.12 - Previous (SS_01_20) shear storage moduli, loss moduli, and phase angles results

As evinced by table 2.10, for SS_01_20 and SS_02_22:

- the compressive storage moduli differ by 113.8527% on average
- the compressive loss moduli differ by 64.3557% on average
- the compressive phase angles differ by 54.3447% on average

2.4.1.2 Quasi-static tests

In 2020, Dall'Aqua et al. performed quasi-static compression tests on porcine skin, because of its comparable physiological and histological properties with respect to human scalp. A compressive strain was imposed on porcine scalp samples with strain rates of 0.1 s^{-1}, 0.025 s^{-1}, and 0.00625 s^{-1}, revealing an increase of strain rate dependency after 15% compressive true strain (fig. 2.55) [Dall'Aqua et al., 2020].

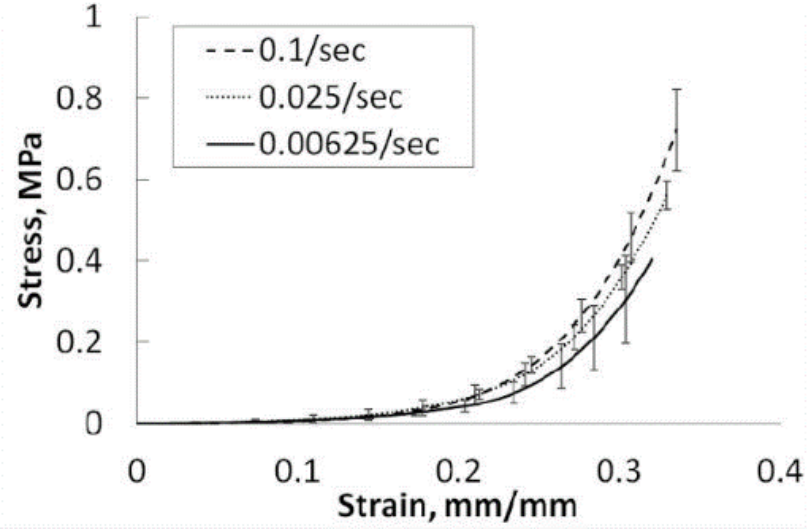


Figure 2.55 – True stress-strain curves from literature for a uniaxial compressive test on porcine skin at strain rate of 0.1 s^{-1}, 0.025 s^{-1}, and 0.00625 s^{-1} [Dall'Aqua et al., 2020]

To characterize the stress-strain relationship of the two silicone rubbers under investigation in the current work, uniaxial compressive, tensile, and shear quasi-static tests were performed using MTS 858 Mini Bionix II. A 40% strain level was imposed on 50x50x30 mm specimens made of PlatSil Gel-10 and PlatSil Gel-25. As assessed for DMA, PlatSil Gel-25 was only characterized under uniaxial compressive test, because the sample detached from the grabs when subjected to a tensile strain. Fig. 2.56 shows the experimental set-up for PlatSil Gel-10.

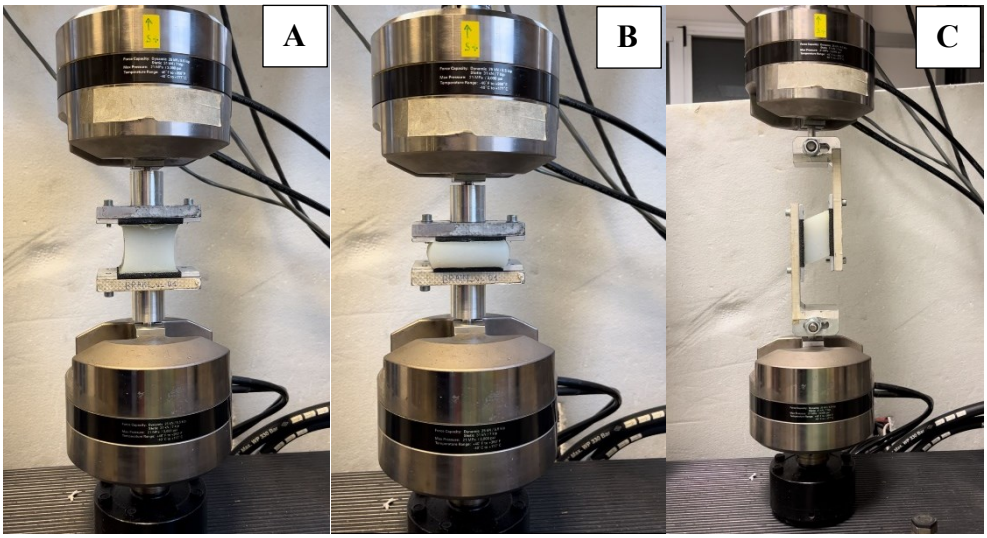


Figure 2.56 – Experimental set-up for (A) tensile, (B) compressive, and (C) shear DMA on PlatSil Gel-10 specimens

The specimens were deformed with a loading velocity of 0,1 mm/s, corresponding to a strain rate of 0,0033 s^{-1}. Data were processed with MATLAB 2022b to remove the noise.

The resulting engineering stress-strain curves are shown in fig. 2.57 A/C/D and 2.57 B for PlatSil Gel-10 and PlatSil Gel-25 respectively.

To compare the results with literature, compressive engineering stress-strain curves $\sigma - \varepsilon$ were converted to true stress-strain curves $\sigma_t - \varepsilon_t$ using the (2.62) and (2.63) to obtain positive values along both axes:

$$\varepsilon_t = -ln(1 - |\varepsilon|) \tag{2.62}$$

$$\sigma_t = |\sigma|(1 - |\varepsilon|) \tag{2.63}$$

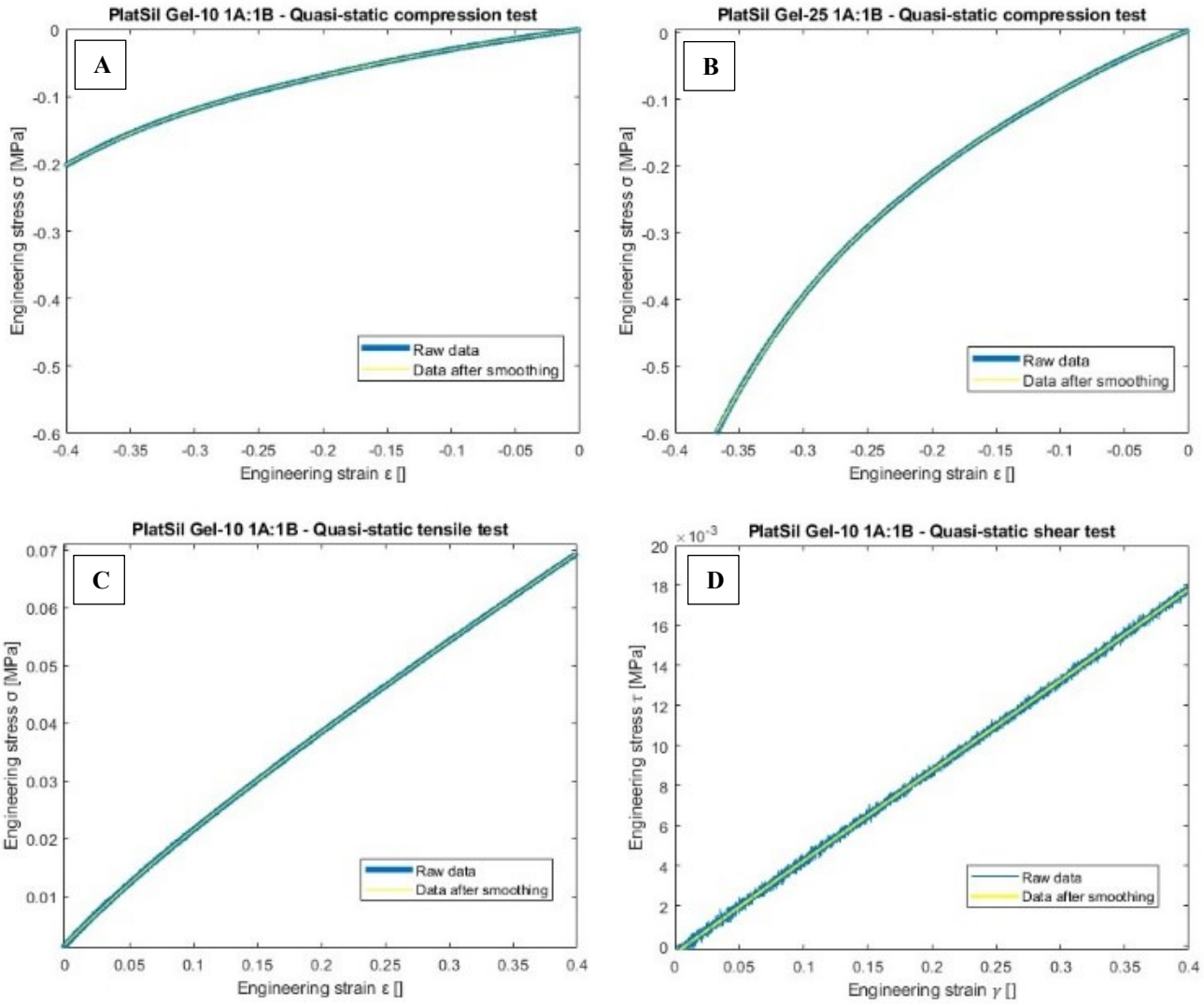


Figure 2.57 - Resulting engineering stress-strain curves from: quasi-static compression tests [(A) PlatSil Gel-10, (B) PlatSil Gel-25], quasi-static tensile test [(C) PlatSil Gel-10], quasi-static shear test [(D) PlatSil Gel-10]

Fig. 2.58 shows the comparison of experimental results (strain rate of 0,0033 s^{-1}) with literature data by Dall'Aqua at the strain rate of 0,00625 s^{-1}.

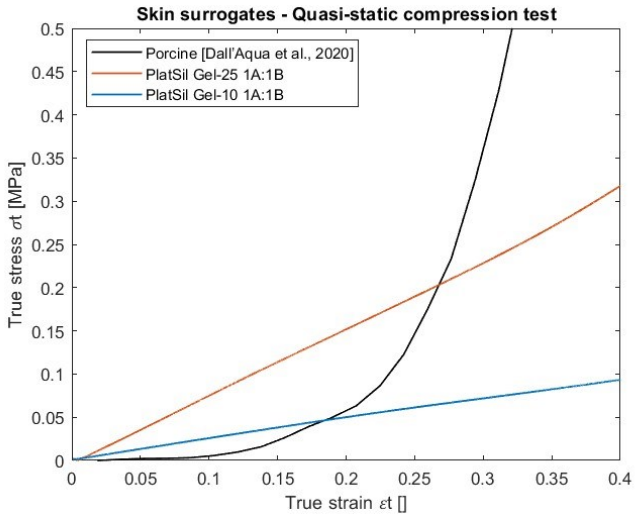


Figure 2.58 - Comparison of true stress-strain curves for quasi-static compressive tests related to Unipd silicone rubbers (strain rate of 0,0033 s^{-1}) and literature (Dall'Aqua et al., 2020, strain rate of 0,00625 s^{-1}

PlatSil Gel-10 true stress-strain curve was found to be a good approximation of human scalp data up to 20% true strain, while PlatSil Gel-25 exhibits too high stiffness with respect to literature data.

2.4.2 Identification of the constitutive parameters of skin simulant material

2.4.2.1 Viscoelastic constitutive parameters

MATLAB *Curve Fitter App* was used to identify PlatSil Gel-10 Prony series parameters to describe the current skin simulant material viscoelastic behaviour in ABAQUS. After an interpolation, frequencies f $[Hz]$ ranging from 0,2 to 7 Hz were reported in x-axis, while shear storage moduli G' [MPa] computed at 10% strain level for each frequency f were reported in y-axis. Data were fitted using as *Custom Equation* $\Re(G^*)$ with $\omega = 2\pi f$ and it was chosen to immediately test the 6 different scenarios with K ranging from 1 to 6. The parameters obtained were then used to estimate the loss moduli as function of frequencies using the equation $\Im(G^*) = G''(\omega)$. The aim was to choose the Prony series which allowed the estimated storage and loss modulus curves to be closest to the experimental ones. Data obtained by experimental tests (DMA) and their approximation are shown in fig. 2.59.

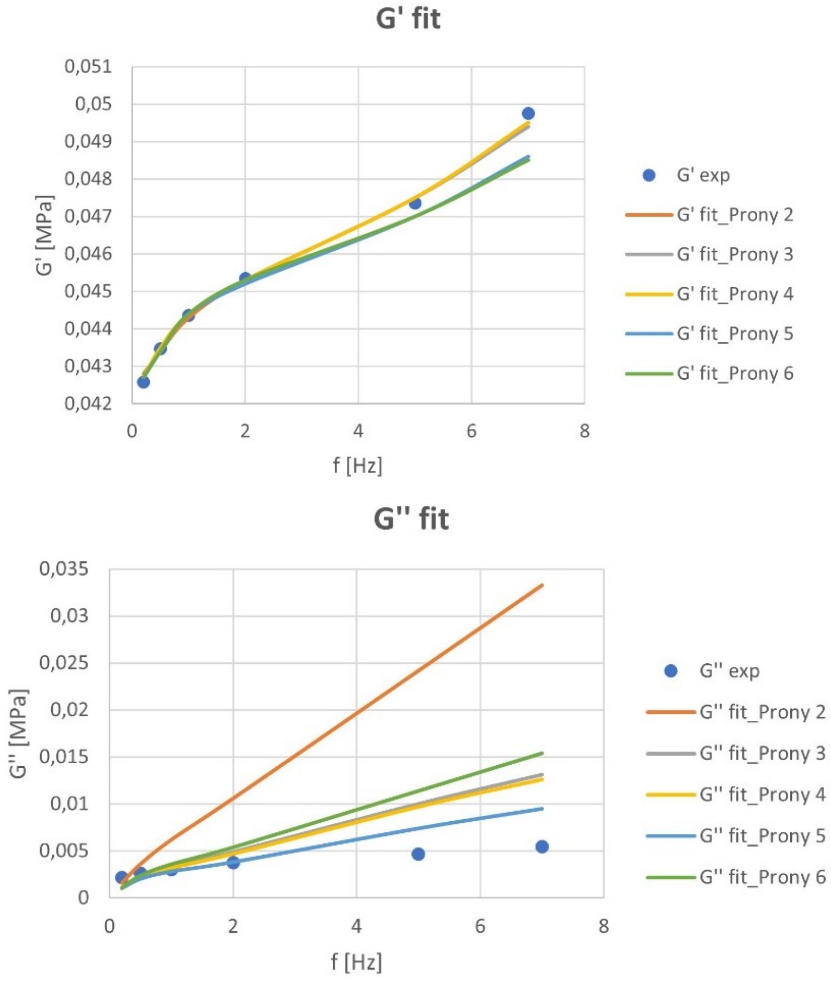


Figure 2.59 – Fit of G' and G'' for Prony series with 2, 3, 4, 5, and 6 terms computed by MATLAB Curve Fitter app

As evinced by fig. 2.59, for high frequencies the Prony series with 5 and 6 terms don't fit the experimental storage modulus behaviour. Hence, among the remaining options, Prony series with 4 terms was selected because of its closer fit of loss modulus curve to the experimental data points. Thus, Prony series parameters computed with (2.24) are shown in table 2.13.

g_i []	τ_i [s]
0,1466	0,009282
0,1284	0,002248
0,228	0,008001
0,0295	0,2328

Table 2.13 – Dimensionless form of the Prony series with 4 terms

2.4.2.2 Hyperelastic constitutive parameters

Initially, PlatSil Gel-10 1A:1B hyperelastic behaviour was defined by fitting experimental test data in ABAQUS. Quasi-static uniaxial compressive and tensile engineering (nominal) stress-strain data obtained by the mechanical characterization were inserted as test data (fig. 2.60 A). ABAQUS was asked to identify Ogden constitutive parameters with Poisson's ratio ν = 0.49 and N=1 (fig. 2.60 B and C). Viscoelastic behaviour (fig. 2.60 D) was defined by the Prony series with 4 terms obtained before (see table 2.13).

Evaluate option was used to identify the constitutive parameters of the investigated Ogden model. As evinced by fig. 2.61, the stability was satisfied for all strains.

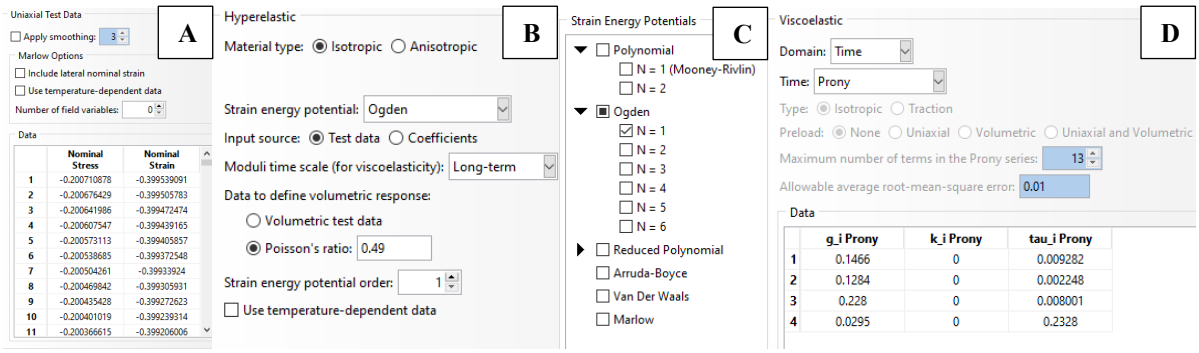


Figure 2.60 – Definition of hyperelastic and viscoelastic behaviour to use the Evaluate option: (A) quasi-static compressive and tensile Uniaxial Test Data obtained from the mechanical characterization, (B) Poisson's ratio, (C) Ogden Strain Energy Potential chosen to be applied to the data, (D) viscoelastic constitutive parameters

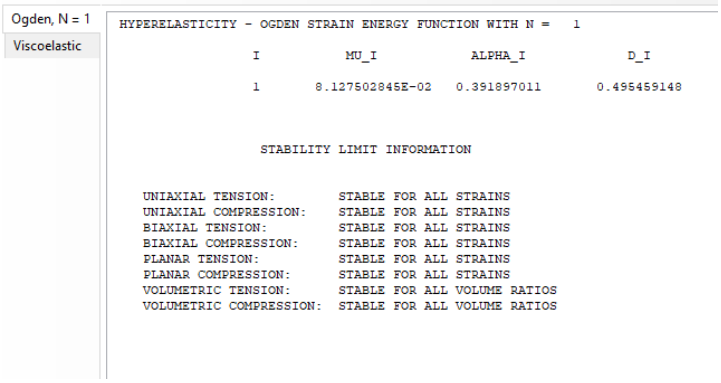


Figure 2.61 Hyperelastic constitutive parameters resulting from Evaluate option for Ogden strain energy function with N=1

In order to verify the suitability of the Ogden strain energy function to interpret the experimental quasi-static tests performed to characterize the material, it was chosen to simulate quasi-static uniaxial compressive, tensile and shear tests using ABAQUS.

The implemented procedure was the same described for the identification of brain surrogate material parameters, with the only difference in the rubber *Material* definition (fig. 2.62). Moreover, since the imposed strain was of 40%, for the compression test the imposed displacement was set to 12 mm instead of 15 mm.

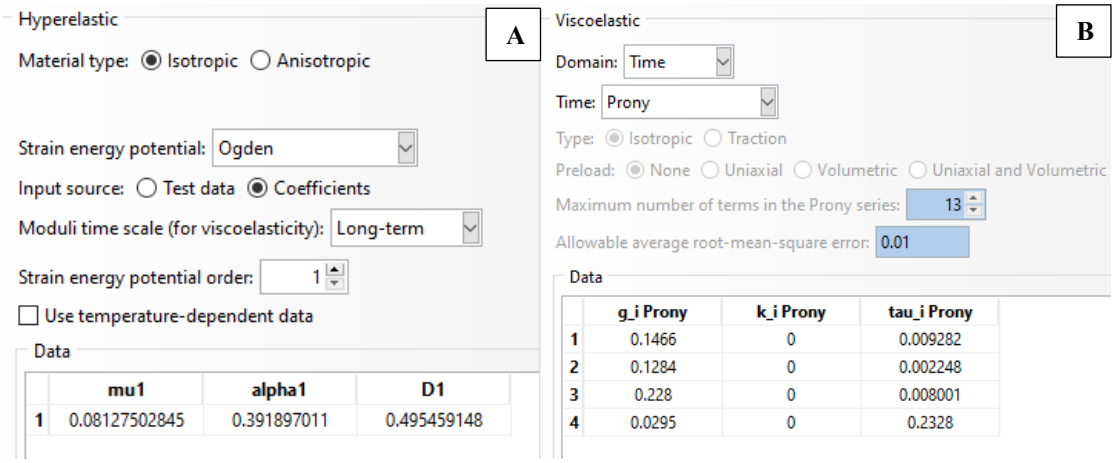


Figure 2.62 – PlatSil Gel-10 1A:1B hyperelastic and viscoelastic behaviour: (A) Ogden hyperelastic constitutive parameters resulting from Evaluate option, (B) viscoelastic Prony series with 4 terms

Figures 2.63 and 2.64 show the comparison of the experimental force-displacement curve with respect to Abaqus RF3 vs U3 fit for the compression and tensile test and Abaqus RF1 vs U1 fit for the simple shear test.

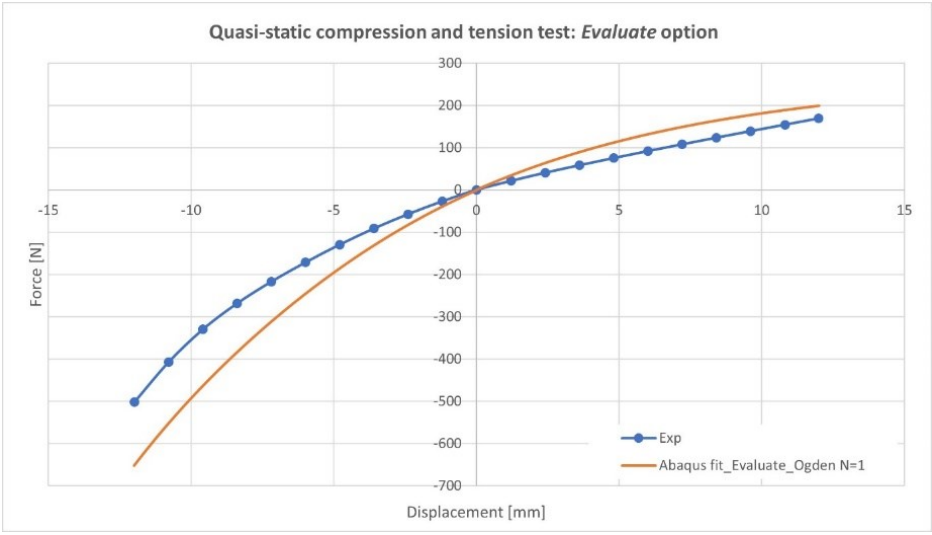


Figure 2.63 - Experimental force-displacement curve with respect to Abaqus RF3-U3 curve output for quasi-static compression and tensile test simulation

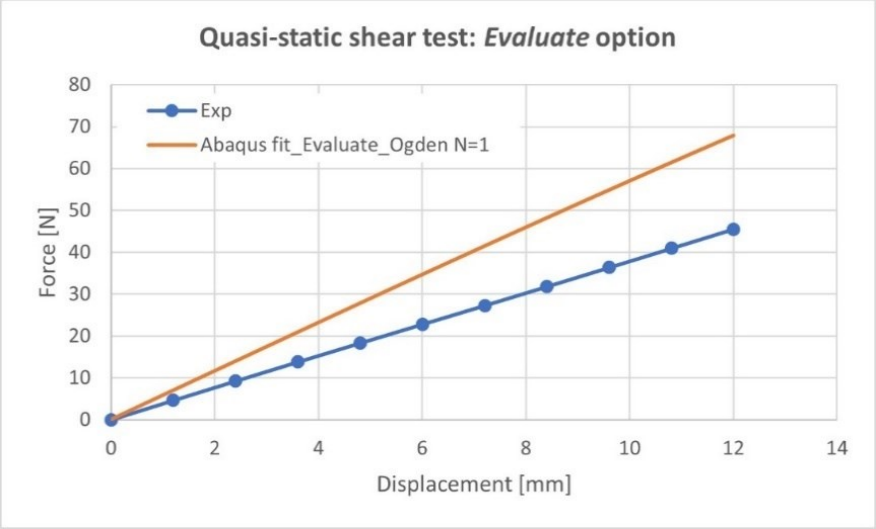


Figure 2.64 - Experimental force-displacement curve with respect to Abaqus RF1-U1 curve output for quasi-static shear test simulation

These force-displacement comparisons evinced that the *Evaluate* output parameters were not suitable to interpret the experimental response. As for the brain surrogate material, it was chosen to modify to these Ogden parameters to find a set that could allow the Abaqus output curves to behave in a more similar way with respect to the experimental ones. Therefore, a new Ogden model, always with N=1, was initially proposed to define PlatSil Gel-10 1A:1B hyperelastic bahaviour.

The initial shear modulus $\mu_0 = 0.045335\ MPa$ was quantified as the slope of the experimental engineering stress-strain curve.

The (2.44) was used to identify α_1 value as follows:

$$\mu_0 = \sum_{i=1}^{N=1} \mu_i = \mu_1 \tag{2.64}$$

$$\mu_0 = \frac{1}{2}\sum_{i=1}^{N=1} \alpha_i \mu_i = \frac{1}{2}\alpha_1 \mu_1 \tag{2.65}$$

Hence, $\alpha_1 = 2$.

The Poisson's ratio was set to 0,49 and the (2.46) was used to identify the initial bulk modulus K_0 as follows:

$$K_0 = -\frac{2}{3} \cdot 0.045335 \cdot \frac{0{,}49\ +1}{2 \cdot 0{,}49\ -1} MPa = 2.251652\ MPa \tag{2.66}$$

Therefore, (2.45) was used to identify D_1 as:

$$D_1 = \frac{2}{2.251652}\ MPa^{-1} = 0.888237\ MPa^{-1} \tag{2.67}$$

Quasi-static compressive, tensile and shear tests performed in the laboratory were then simulated again, with the only difference in the hyperelastic behaviour definition. In fact, these was described via *Coefficients* instead of *Test data*, as shown in fig. 2.65.

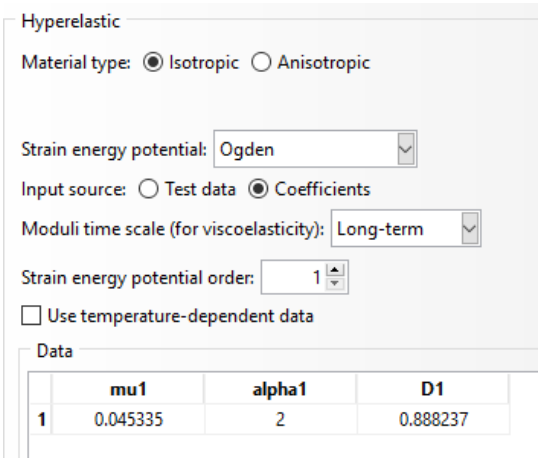


Figure 2.65 – First proposal: PlatSil Gel-10 1A:1B new Ogden hyperelastic constitutive parameters (Coefficients)

For the compressive and the tensile deformation modes, the reaction force RF3 and the displacement U3 along z axis were computed and saved. For the shear test, the reaction force RF1 and the displacement U1 along x axis were computed and saved.

Figures 2.66 and 2.67 show the comparison of experimental data with respect to the corresponding old model results (Ogden parameters as *Evaluate* output) and to this first proposal results.

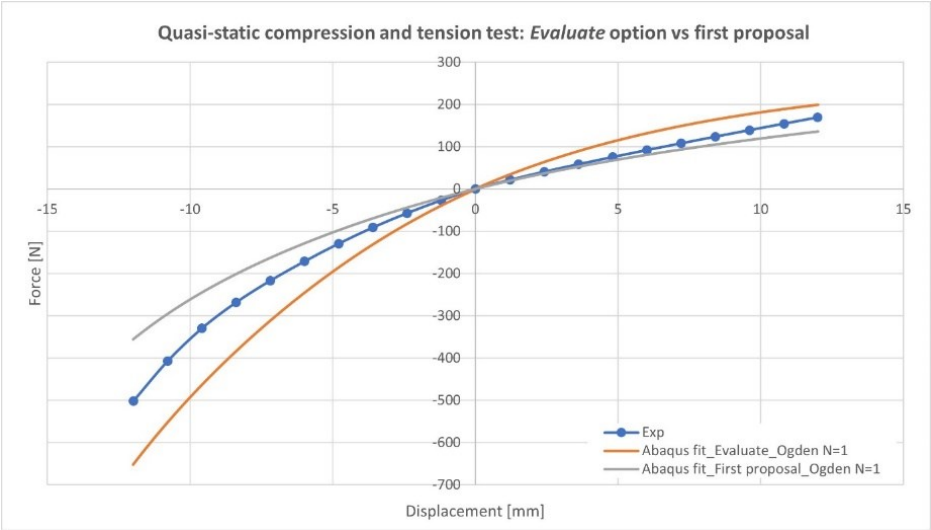


Figure 2.66 - Abaqus results for hyperelastic behaviour defined by Evaluate coefficients vs first proposal: fit of RF3-U3 curve output with the experimental force-displacement curve for quasi-static compression and tension test simulation

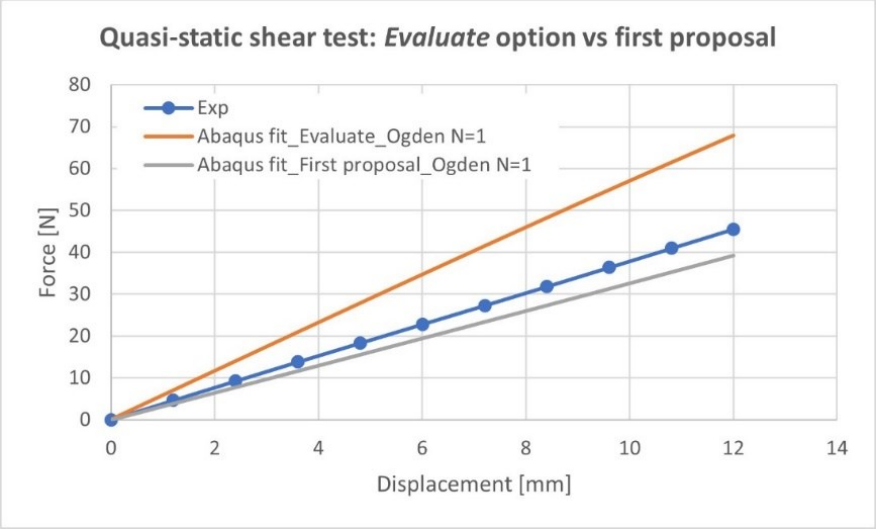


Figure 2.67 – Abaqus results for hyperelastic behaviour defined by Evaluate coefficients vs first proposal: fit of RF1-U1 curve output with the experimental force-displacement curve for quasi-static simple shear test simulation

As evinced by the force-displacement curves, the last Ogden constitutive parameters resulted to be suitable for fitting the experimental data until about 10% strain level in compression, 20% strain level in tension, and 10% in shear. This model improved the fit aptness with respect to the previous one. Despite this, since the skin surrogate behaviour under compressive loads must be considered in impact tests, it was chosen to modify these Ogden parameters to find a set that could allow the Abaqus output RF3 vs U3 curve to behave in a more similar way with respect to the compressive experimental curve. For this reason, a new Ogden model with N=1 was proposed to define PlatSil Gel-10 1A:1B hyperelastic behaviour.

It was chosen to start modifying the initial shear modulus from $\mu_0 = 0.045335\ MPa$ to $\mu_0 = 0.06\ MPa$.

The Poisson's ratio was set to 0,49 and the equation (2.46) was used to identify the initial bulk modulus K_0 as follows:

$$K_0 = -\frac{2}{3} \cdot 0.06 \cdot \frac{0{,}49\ +1}{2 \cdot 0{,}49\ -1} MPa = 2.98\ MPa \tag{2.68}$$

Therefore, equation (2.55) was used to identify D_1 as:

$$D_1 = \frac{2}{2.98}\ MPa^{-1} = 0.671141\ MPa^{-1} \tag{2.69}$$

Quasi-static compressive, tensile and shear tests performed in the laboratory were then simulated again, with the only difference in the hyperelastic behaviour definition (fig. 2.68).

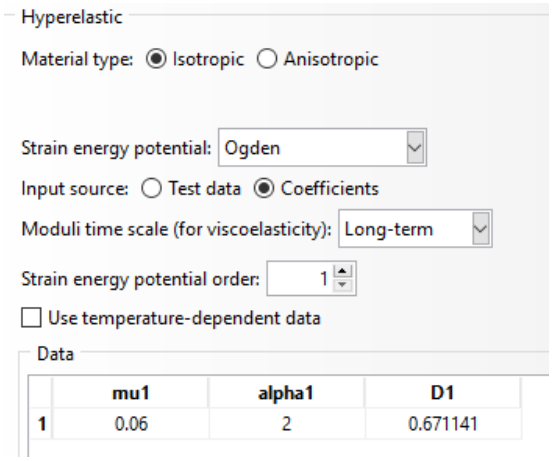


Figure 2.68 – Second proposal: PlatSil Gel-10 1A:1B new Ogden hyperelastic constitutive parameters (Coefficients)

As for the previous post-processing, for the compressive and the tensile tests, the reaction force RF3 and the displacement U3 along z axis were computed and saved. For the shear test, the reaction force RF1 and the displacement U1 along x axis were computed and saved.

Figures 2.69 and 2.70 show the comparison of experimental data with respect to the corresponding old model (Ogden parameters as *Evaluate* output), to the first proposal and to this second proposal results.

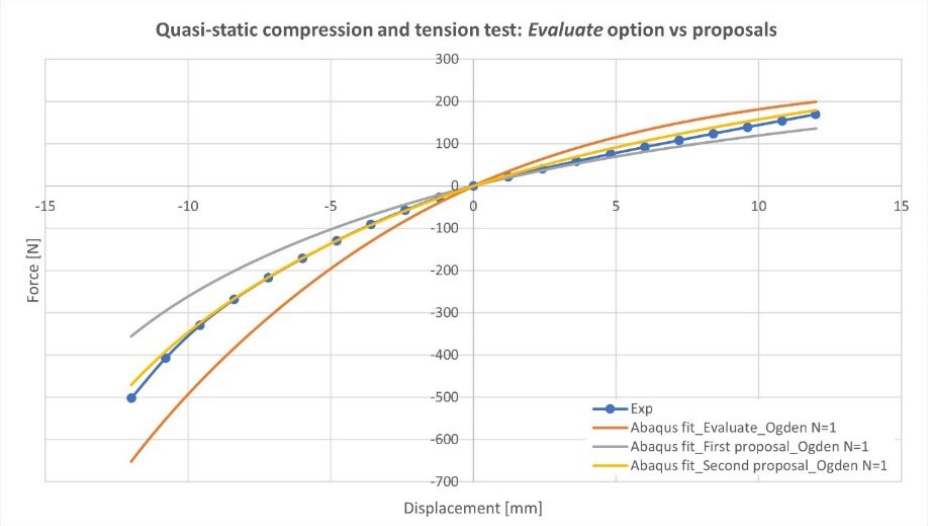


Figure 2.69 - Abaqus results for hyperelastic behaviour defined by Evaluate coefficients vs first proposal vs second proposal: fit of RF3-U3 curve output with the experimental force-displacement curve for quasi-static compression and tension test simulation

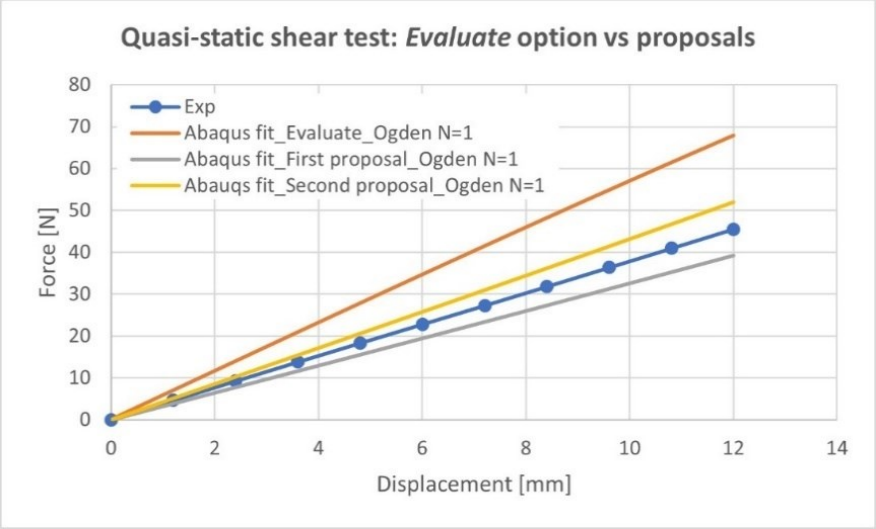


Figure 2.70 - Abaqus results for hyperelastic behaviour defined by Evaluate coefficients vs first proposal vs second proposal: fit of RF1-U1 curve output with the experimental force-displacement curve for quasi-static shear test simulation

As evinced by the force-displacement curves, the second proposal resulted to be suitable for fitting the experimental data until about 40% strain level in compression, 40% strain level in tension, and 15% strain level in shear. This model improved the aptness of the fit with respect to the previous ones, so the hyperelastic behaviour of the skin simulant material was described with the parameters shown in fig. 2.68. Figure 2.71 shows the experimental and numerical deformed specimen in tension, compression and shear quasi-static tests for the chosen set of parameters.

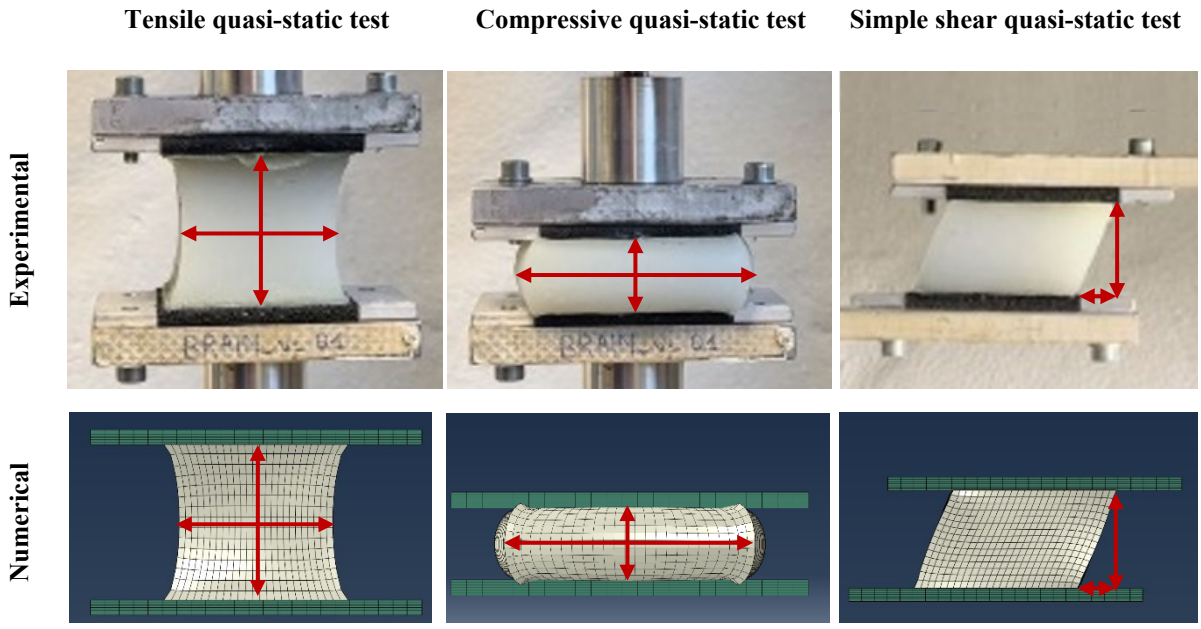


Figure 2.71 – Comparison of experimental vs numerical deformed shape of the specimen in quasi-static tests

As shown by the arrows in fig. 2.71, the final height and the lateral deformation of the specimen in tensile and compressive tests and the displacement in the simple shear test are well reproduced by the numerical simulation.

Figures 2.68 and 2.60 D are here recalled in fig. 2.72 for a brief recap on the identified hyperelastic and viscoelastic constitutive parameters.

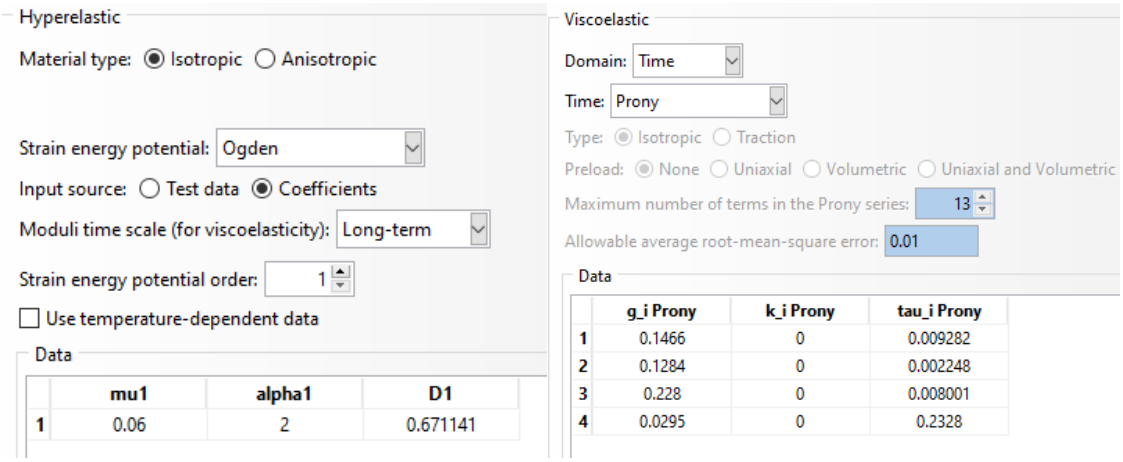


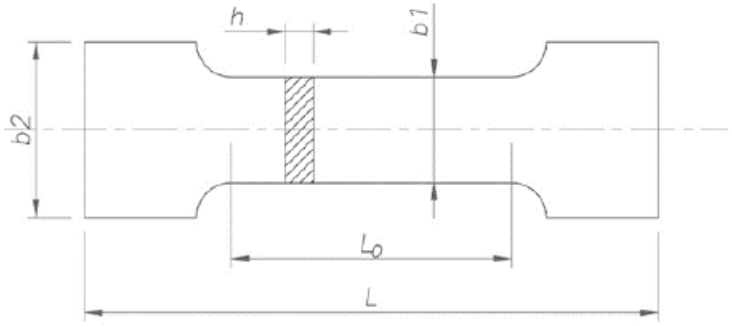
Figure 2.72 – Identified hyperelastic and viscoelastic constitutive parameters for skin simulant material

On the basis of the constitutive analysis performed, it was chosen to model the PlatSil Gel-10 (skin simulant material) with a one-term Ogden model and a Prony series with 4 terms.

2.5 Skull simulant material

2.5.1 Mechanical characterization of skull simulant material

In 2020, polyamide PA12 was mechanically characterized by Faggin and Silvestroni in their Master thesis works. They performed uniaxial tensile tests on six dog-bone shape specimens following the standard BS EN ISO 527-1: 1996 (fig. 2.73) [Faggin, 2020; Silvestroni, 2020].



Overall length	L = 82 mm
Gauge length	L_0 = 40 mm
Thickness	h = 4 mm
Narrow portion width	b_1 = 15 mm
Overall width	b_2 = 25 mm

Figure 2.73 - Dog-bone shape specimens according to BS EN ISO 527-1: 1996

The six specimens exhibited brittle failure when subjected to tensile strain, as indicated by the engineering stress-strain curves in fig. 2.74. The average Young modulus (E), the average ultimate tensile strength (UTS), and the average failure engineering strain (ε^f) are reported in table 2.14.

Average Young modulus E [MPa]	Average ultimate tensile strength UTS [MPa]	Average engineering failure strain ε^f [%]
1127,07 ± 0,05	40 ± 2	10,96 ± 5

Table 2.14 - Young modulus, ultimate tensile strength (UTS), and average failure engineering strain [Faggin, 2020; Silvestroni, 2020]

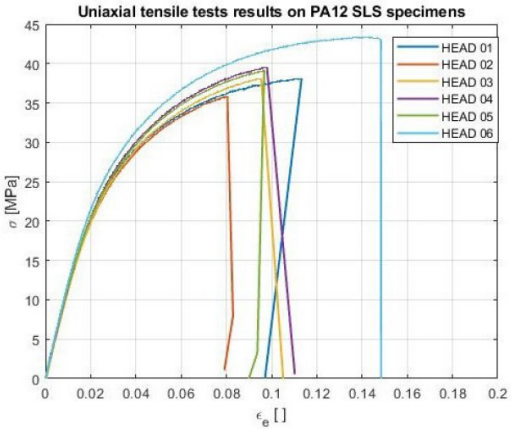


Figure 2.74 - Engineering stress-strain curves from quasi-static uniaxial tensile tests on 6 specimens [Faggin, 2020; Silvestroni, 2020]

2.5.2 Identification of the constitutive parameters of skull simulant material

Polyamide PA12 was modelled as an elastic-plastic material in ABAQUS.

5.5.2.1 Elastic constitutive parameters

Elastic behaviour (*ELASTIC option in Abaqus) was defined by the Young modulus E = 1127,07 MPa and the Poisson's ratio ν = 0,41.

5.5.2.2 Plastic constitutive parameters

The post-yield behaviour (*PLASTIC option in Abaqus) was described by the true stress as function of the true plastic strain (data pairs). The first couple of data computes the first yield stress and the initial true plastic strain, that's always zero. Then, a series of data pairs can be used to connect the first yield to the failure data pairs [Abaqus documentation]. For simplicity, it was chosen to directly define the failure true stress – true plastic strain data pair. As detailed in the formulas below, to define the plastic behaviour:

- engineering first yield stress σ^y was converted to true initial yield stress ${\sigma_t}^y$:

$$ {\sigma_t}^y = \sigma^y(1 + \varepsilon^y) \tag{2.70} $$

  where ε^y is the engineering first yield strain

- engineering failure stress σ^f was converted to failure stress ${\sigma_t}^f$:

$$ {\sigma_t}^f = \sigma^f(1 + \varepsilon^f) \tag{2.71} $$

  where ε^f is the engineering failure strain

- engineering failure strain ε^f was converted to true failure strain ${\varepsilon_t}^f$:

$$ {\varepsilon_t}^f = \ln(1 + \varepsilon^f) \tag{2.72} $$

Thus, the true initial yield stress ${\sigma_t}^y$ was defined as:

$$ {\sigma_t}^y = \sigma^y(1 + \varepsilon^y) = 20 \cdot (1 + 0{,}02)\, MPa = 20{,}4\, MPa \tag{2.73} $$

The true initial plastic strain ${\varepsilon_t}^{pl,y}$ was defined as:

$$ {\varepsilon_t}^{pl,y} = 0 \tag{2.74} $$

The true failure stress ${\sigma_t}^f$ was defined as:

$$ {\sigma_t}^f = \sigma^f(1+\varepsilon^f) = 40 \cdot (1+0{,}1096)\ MPa = 44{,}384\ MPa \tag{2.75} $$

The true failure plastic strain ${\varepsilon_t}^{pl,f}$ was computed subtracting the true elastic strain ${\varepsilon_t}^{el}$ from the true failure strain ${\varepsilon_t}^f$ as follows:

$$ {\varepsilon_t}^{pl,f} = {\varepsilon_t}^f - {\varepsilon_t}^{el} $$
$$ {\varepsilon_t}^{pl,f} = \ln(1+\varepsilon^f) - {{\sigma_t}^f}/{E} = \ln(1+0{,}1096) - {44{,}384}/{1127{,}07} = 0{,}0646 \tag{2.76} $$

2.6 Falx cerebri and tentorium cerebelli simulant material

2.6.1 Mechanical characterization of falx and tentorium simulant material

The falx has an important role in reducing the brain strain during coronal rotation and preventing the brain motion inside the skull cavity [Golman et al., 2014]. In 1981, van Noort et al. subjected human dura mater samples to uniaxial tensile load. Ho et al. extracted the elastic modulus of 31.5 MPa from van Noort et al. stress-strain curve and used it to define the linear properties of a falx cerebri finite element model (fig. 2.75) [Ho et al., 2017].

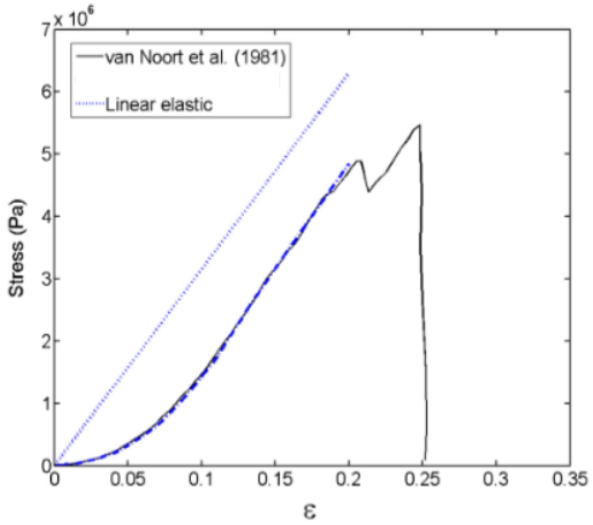
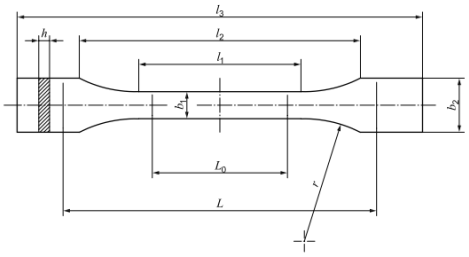


Figure 2.75 – Uniaxial tensile test results on human dura mater [Ho et al., 2017]

Golman et al. performed uniaxial tensile tests on falx cerebri and tentorium cerebelli of six post mortem human subjects, measuring a mean elastic modulus of 36 MPa [Golman et al., 2014]. In the current work it was chosen to simulate the falx cerebri and the tentorium cerebelli using TPU, since it has an elastic modulus similar to the literature ones of 31,5-36 MPa.

Dog-bone specimens were prepared according to BS EN ISO 527-2:2012, as shown in fig. 2.76 for specimen type 1A.



Dimensions in millimetres

	Specimen type	1A	1B
l_3	Overall length[a]	170	≥150
l_1	Length of narrow parallel-sided portion	80 ± 2	60,0 ± 0,5
r	Radius	24 ± 1	60 ± 0,5
l_2	Distance between broad parallel-sided portions [b]	109,3 ± 3,2	108 ± 1,6
b_2	Width at ends	20,0 ± 0,2	
b_1	Width at narrow portion	10,0 ± 0,2	
h	Preferred thickness	4,0 ± 0,2	
L_0	Gauge length (preferred)	75,0 ± 0,5	50,0 ± 0,5
	Gauge length (acceptable if required for quality control or when specified)	50,0 ± 0,5	
L	Initial distance between grips	115 ± 1	115 ± 1

[a] The recommended overall length of 170 mm of the type 1A is consistent with ISO 294-1 and ISO 10724-1. For some materials, the length of the tabs may need to be extended (e.g. l_3 = 200 mm) to prevent breakage or slippage in the jaws of the testing machine.

[b] $l_2 = l_1 + [4r(b_2 - b_1) - (b_2 - b_1)^2]^{1/2}$, resulting from l_1, r, b_1 and b_2, but within the indicated tolerances.

Figure 2.76 - Dog-bone shape specimens according to BS EN ISO 527-2:2012

Uniaxial tensile tests are planned to characterize the material.

2.6.2 Identification of the constitutive parameters of falx and tentorium simulant material

2.6.2.1 Elastic constitutive parameters

Since mechanical characterization wasn't performed due to lack of time, data from manufacturer were used to identify the elastic constitutive parameters shown in table 2.15.

Young modulus E [MPa]	Poisson's ratio ν []
26	0.48

Table 2.15 – TPU elastic constitutive parameters

Tables 2.16, 2.17, 2.18, 2.19, and 2.20 summarize the constitutive parameters identified above to define the mechanical behaviour of the simulant materials composing brain, subarachnoid space, skin, skull, and falx-tentorium surrogates.

Brain simulant material constitutive parameters

Hyperelasticity (1-term Ogden model)	$\mu_1\ [MPa]$	$\alpha_1\ []$	$D_1\ [MPa^{-1}]$
	0.013	2	3.097574
Viscoelasticity (Prony series with 3 terms)	$g_i\ []\ with\ i = 1,2,3$		$\tau_i\ [s]\ with\ i = 1,2,3$
	0.5157		0.0102
	0.169		0.0121
	0.0768		0.2439

Table 2.16 - Brain simulant material (PlatSil Gel-OO 1A:1B:1D) constitutive parameters

Subarachnoid space simulant material constitutive parameters

Hyperelasticity (Neo-Hookean model)	$C_{10}\ [MPa]$	$D_1\ [MPa^{-1}]$
	0.00065	0.00091

Table 2.17 – Subarachnoid space simulant material (30 PPI open-cell foam + distilled water) constitutive parameters

Skin simulant material constitutive parameters

Hyperelasticity (1-term Ogden model)	$\mu_1\ [MPa]$	$\alpha_1\ []$	$D_1\ [MPa^{-1}]$
	0.06	2	0.671141
Viscoelasticity (Prony series with 4 terms)	$g_i\ []\ with\ i = 1,2,3,4$		$\tau_i\ [s]\ with\ i = 1,2,3,4$
	0.1466		0.009282
	0.1284		0.002248
	0.228		0.008001
	0.0295		0.2328

Table 2.18 - Skin simulant material (PlatSil Gel-10 1A:1B) constitutive parameters

Skull simulant material constitutive parameters

Elasticity	Young's modulus [MPa]	Poisson's ratio []
	1127.07	0.41
Plasticity	Yield stress [MPa]	Plastic strain []
	20.4	0
	44.384	0.0646

Table 2.19 - Skull simulant material (Polyamide PA12) constitutive parameters

Falx-tentorium simulant material constitutive parameters

Elasticity	Young's modulus [MPa]	Poisson's ratio []
	26	0.48

Table 2.20 – Falx-tentorium simulant material (TPU) constitutive parameters

The constitutive parameters above identified were then used to define the mechanical behaviour of the materials composing the parts of the numerical model. The geometry of the model is the object of the next chapter.

Chapter 3: Geometrical analysis

To create the numerical model, the first step was the processing of the STL format files used for 3D printing the components of the prototype (brain, skull and skin mold). These triangulated surfaces, obtained from MRI/CT diagnostic images, needed to be properly treated in order to derive the solid models for subsequent finite element analysis. For this purpose, surface optimization, cleaning and repair steps were required using specific programs (Meshmixer by Autodesk and MeshLab by ISTI-CNR). The STL files of the brain, skull and skin mold thus processed were converted into the corresponding solid models using Autodesk's Fusion 360 software, with which the solid models of the subarachnoid space, falx, tentorium, flange and screws were also created.

3.1 STL files optimization, cleaning and repairing

3.1.1 Brain

Brain STL model was imported in Autodesk Meshmixer (fig. 3.1) to prepare the file for the subsequent processes of 3D solid model creation and finite element analysis.

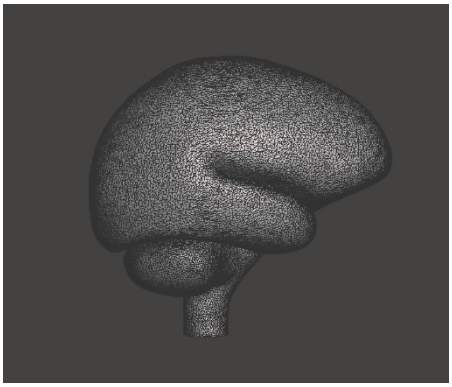


Figure 3.1 – STL file of brain imported in Meshmixer

Select tool (*Select* → *Edit* → *Discard*) was used to identify brain mesh defects to discard (fig. 3.2).

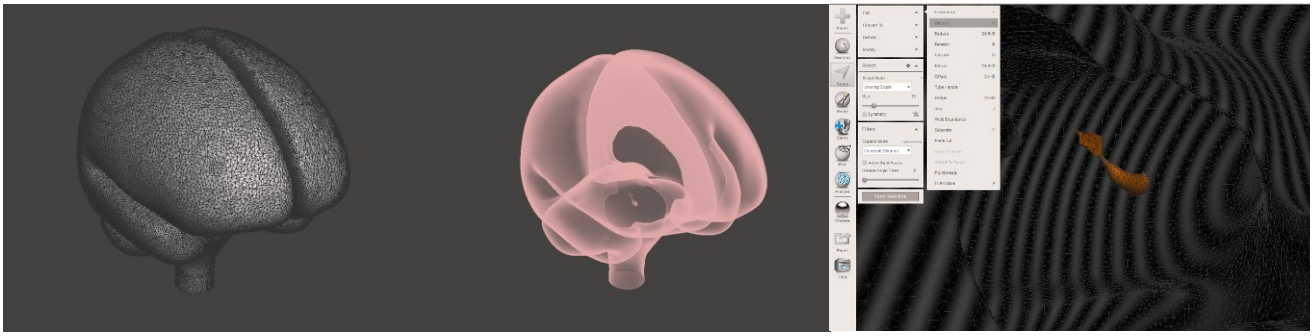


Figure 3.2 – Selection of specific parts of the brain mesh to repair defects

3.1.2 Top skull, bottom skull and jaw

STL models of top skull, bottom skull and jaw were imported in Meshmixer (fig. 3.3).

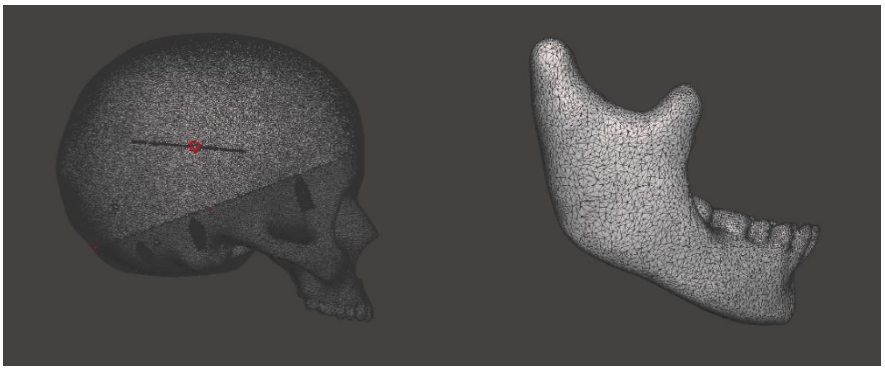


Figure 3.3 – STL files of top skull, bottom skull, and jaw imported in Meshmixer

Select tool was used to identify top and bottom skull areas to discard (*Select* → *Edit* → *Discard*), i.e. cavities for pressure sensors (fig. 3.4 A) and holes for their wires (fig. 3.4 B), cavities of screws (fig. 3.4 C) and coupling triangular indentation between top and bottom skull (fig. 3.4 D), and cavities of screws for bottom skull-neck connection (fig. 3.4 E).

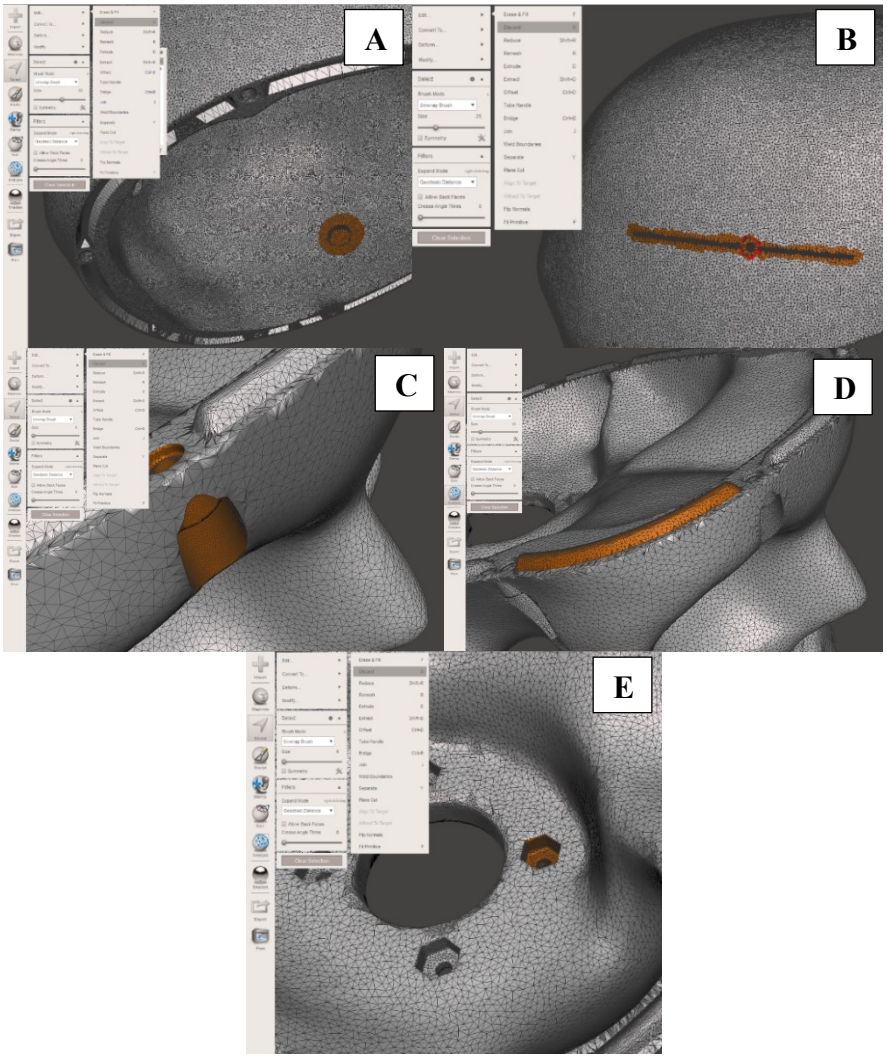


Figure 3.4 – Example of selection of specific parts of top and bottom meshes: (A) cavities for pressure sensors, (B) holes for wires, (C) cavities of screws for top-bottom skull connection, (D) triangular indentation, (E) cavities for bottom skull-neck connection

Inspector tool (*Analysis* → *Inspector*) was used to fill holes created after *Discard* operation (fig. 3.5):

- *Smooth Fill* mode to fill holes and cavities for pressure sensors (fig. 3.5 A), their wires (fig. 3.5 B), and holes for top-bottom skull connection screws (fig. 3.5 C)
- *Flat* Fill mode to fill cavities for bottom skull-neck connection screws (fig. 3.5 D) and connections between top and bottom skull (fig.3.5 E)

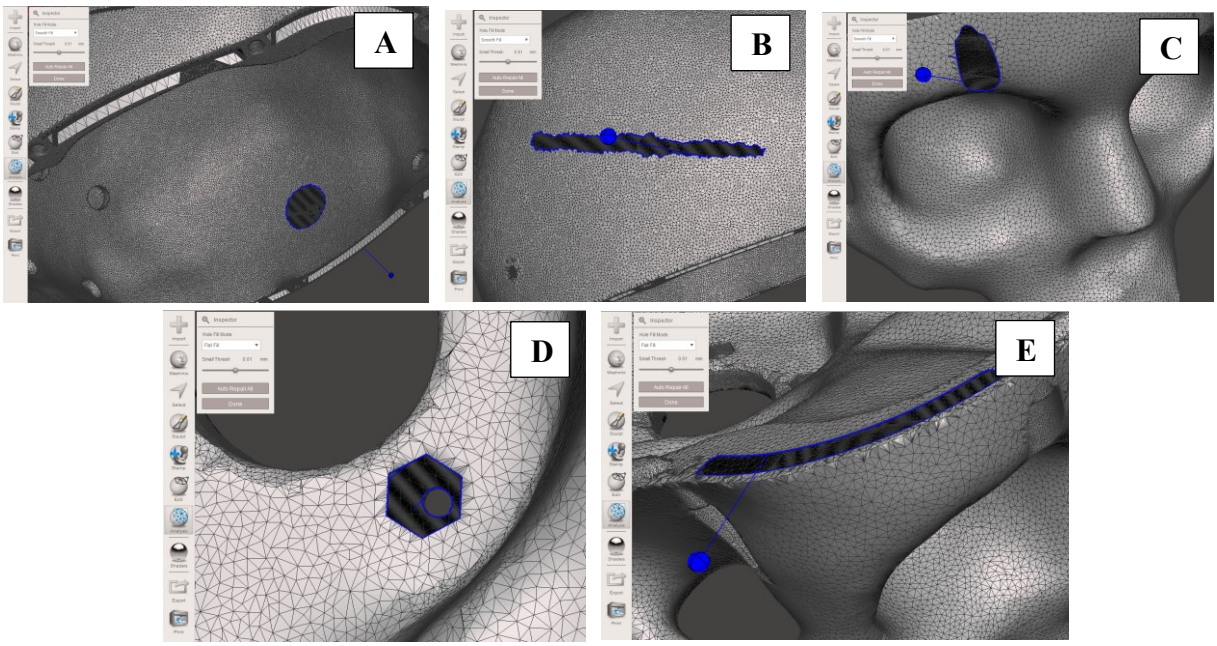


Figure 3.5 – Holes and cavities filling after removal of unnecessary parts of the mesh to repair defects and to simplify the mesh in view of the subsequent processes: (A) cavities for pressure sensors, (B) holes for wires, (C) holes for top-bottom skull connection screws, (D) cavities for bottom skull-neck connection screws, (E) top-bottom skull connections

Meshes were then reduced (*Select* → *Edit* → *Reduce*) in some areas (fig. 3.6) to simplify the following conversion in solids using Fusion 360 software.

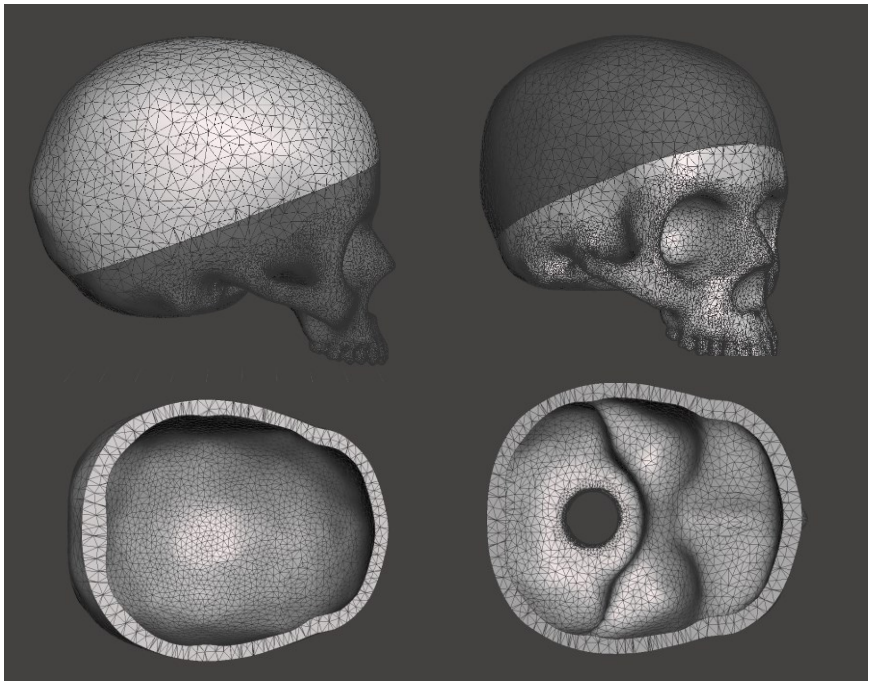


Figure 3.6 – Reduction of some areas of the mesh to optimize the elements size

As shown in fig 3.7, the conversion of top and bottom skull meshes (fig. 3.7 A) in two solids delimited by T-splines surfaces in Fusion 360 (fig. 3.7 B) would have smoothed the edges at the interfaces. The mismatch (fig. 3.7 C) would have not allowed a correct coupling between top and bottom skull, leading to an incorrect skull sealing. Therefore, it was chosen to obtain the STL model of the whole skull, to be later converted in a unique solid model using Fusion 360.

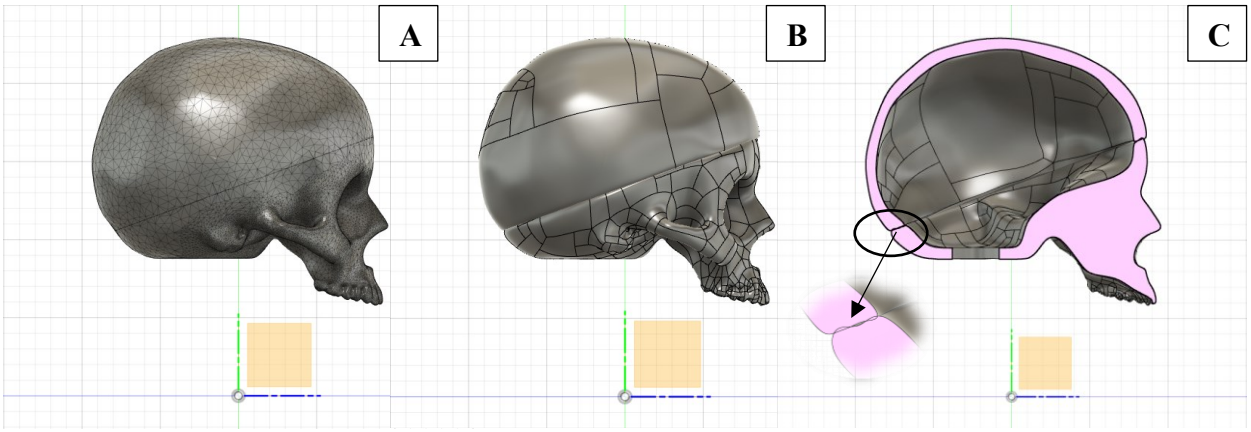


Figure 3.7 – Imperfect top-bottom skull coupling (B and C) due to smoothing of the edges after conversion in solid of the individual parts of the model (A)

Before proceeding with the implementation of the whole skull STL model, the position of the division plane between the two parts of the skull was saved. This was required because it was necessary to divide the whole solid skull into solid top skull and solid bottom skull, preserving the coupling at the interface.

Select tool (*Select* → *Edit* → *Discard*) was used to identify interfaces of top and bottom skull to be discarded (fig. 3.8).

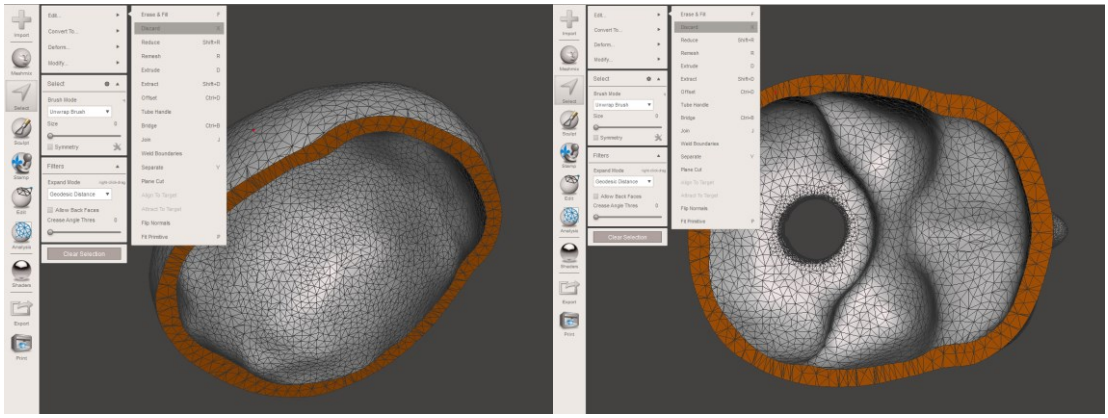


Figure 3.8 – Selection of top-bottom skull interfaces

The boolean union (*Edit* → *Boolean Union*) aborted, so it was chosen to group the two meshes (*Edit* → *Combine*); this was required to work a unique STL file, with the aim to modify mesh elements in the joining area to get a uniform triangulated shell (fig. 3.9). Therefore, operations

like *Select → Edit → Bridge/Discard*, *Analysis → Inspector*, and *Select → Edit → Remesh* were needed.

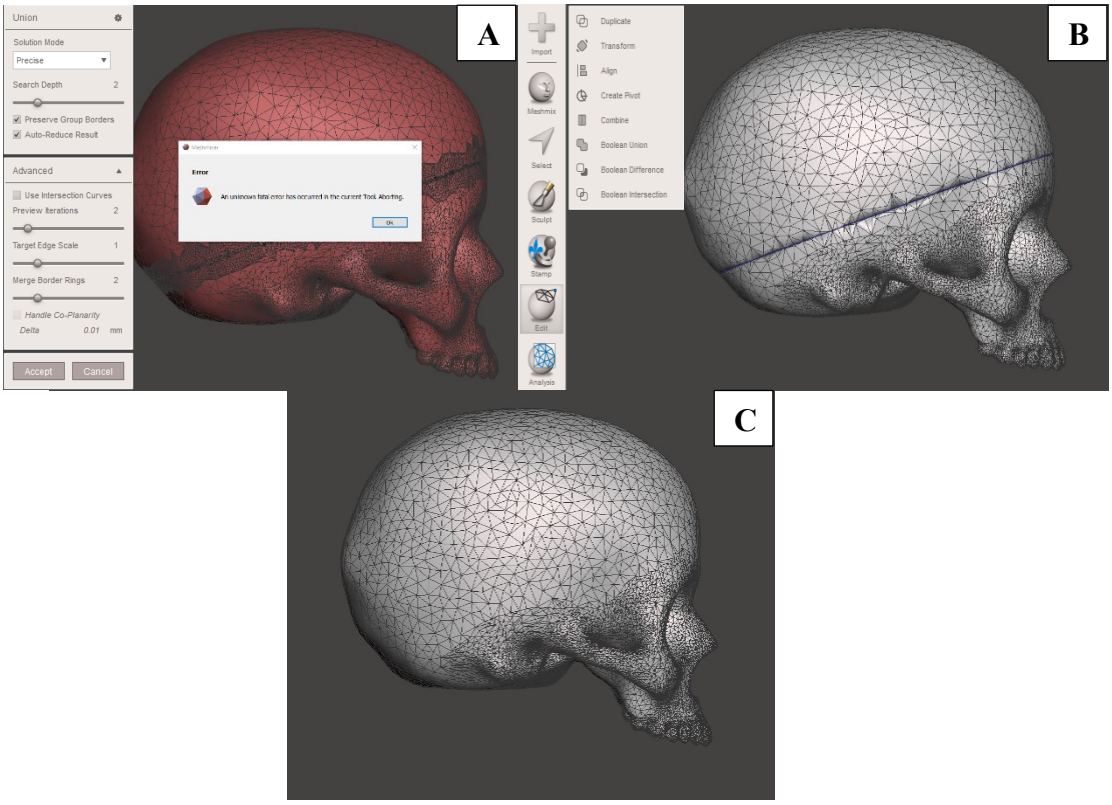


Figure 3.9 – (A) Abort of Boolean Union, (B) combination of the two parts of the skull, (C) whole skull mesh

Jaw mesh was reduced (*Select → Edit → Reduce*) in some areas (fig. 3.10) to simplify the following conversion in solid.

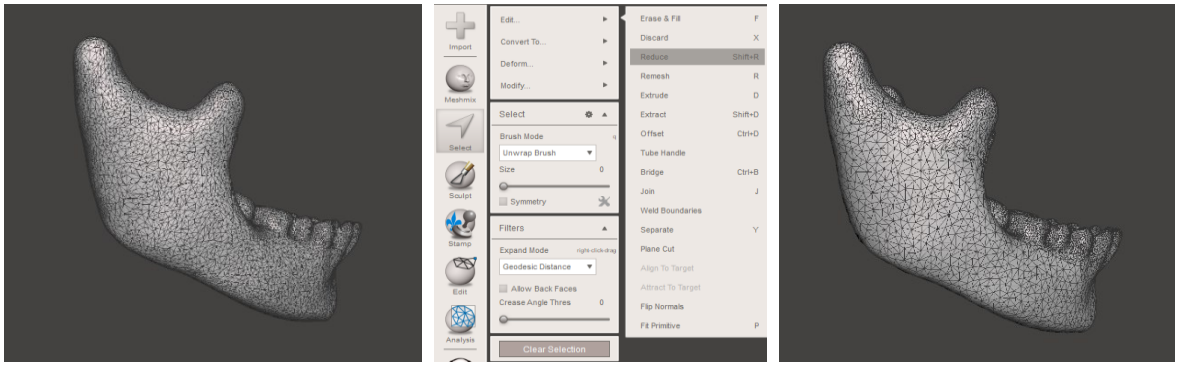


Figure 3.10 – Reduction of the jaw mesh to reduce the number of elements

To simplify constraints and interactions in Abaqus, since the focus of the study doesn't involve the temporomandibular joint, jaw mesh was connected (*Edit → Combine*) to the whole skull triangulated surface (fig. 3.11) and tools like *Select → Edit → Extrude/Discard/Tube Handle* and *Analysis → Inspector* were needed to generate a uniform mesh in the joining areas.

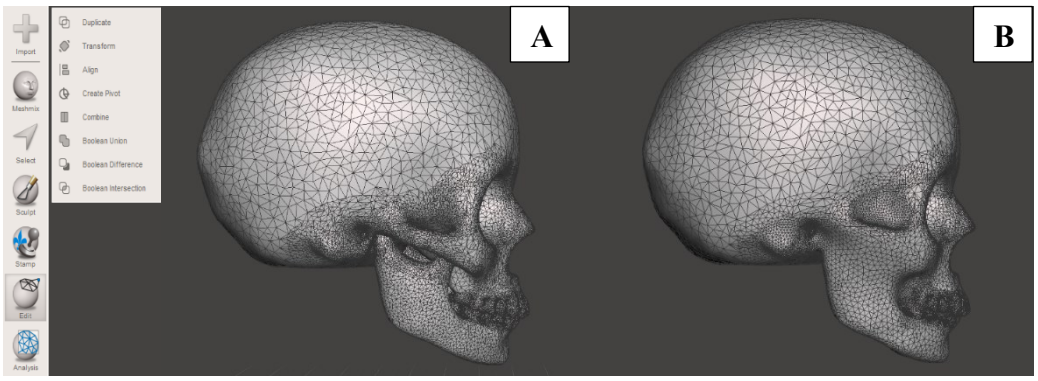


Figure 3.11 – Combine of skull and jaw (A) and resulting unique mesh (B)

3.1.3 Skin

The STL model of the skin was built starting from the eight internal shells of the external skin moulds STL files imported in Meshmixer (fig. 3.12).

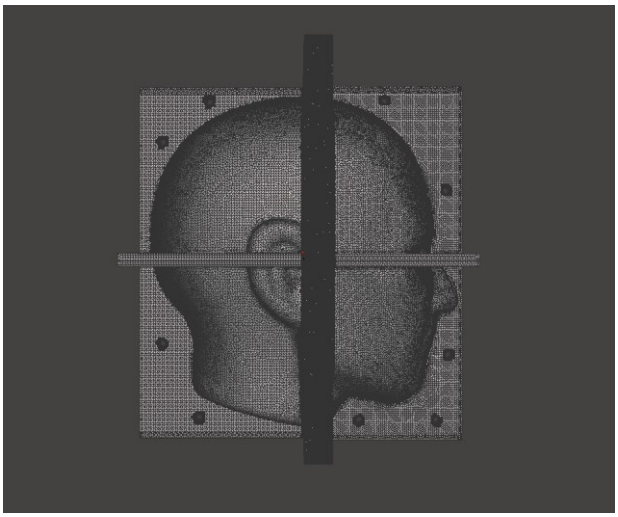


Figure 3.12 – STL file of the external moulds used to cast the skin of the head surrogate

Select tool (*Select* → *Edit* → *Discard*) was applied to select moulds areas to be discarded (fig. 3.13); internal shells obtained in this way were then combined (*Edit* → *Combine*) to work on a unique STL model.

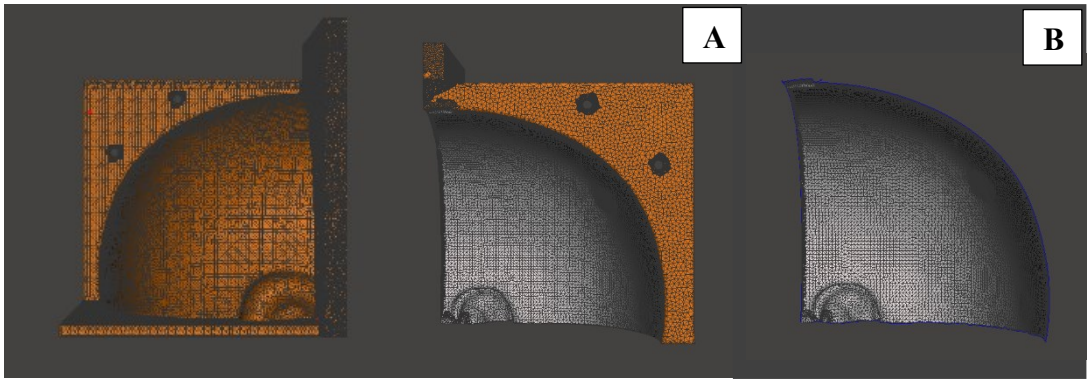


Figure 3.13 – Discard of the non-necessary areas of the mould (A) and 1 internal shell out of 8 (B)

Internal shells were connected thanks to operations like *Select* → *Edit* → *Bridge/Discard* and *Analysis* → *Inspector*. Since the whole shell obtained was oriented inwards, the command *Select* → *Edit* → *Flip Normals* was applied to get the final external skin model (fig. 3.14).

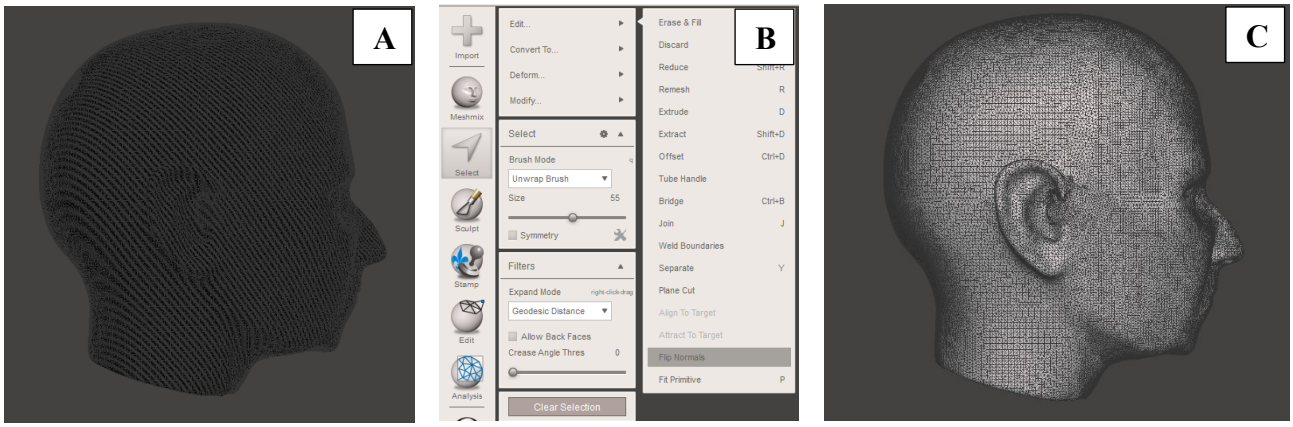


Figure 3.14 – Inversion of the orientation of the normals (B) to get the positive model (C) from the negative mould (A)

Brain, whole skull and skin models were then exported as STL files and imported in MeshLab software (example in fig. 3.15) for cleaning and repairing operations. For this purpose, filters like *Remove Duplicate Faces*, *Remove Duplicate Vertices*, *Repair non Manifold Edges*, and *Select Self Intersecting Faces* were applied.

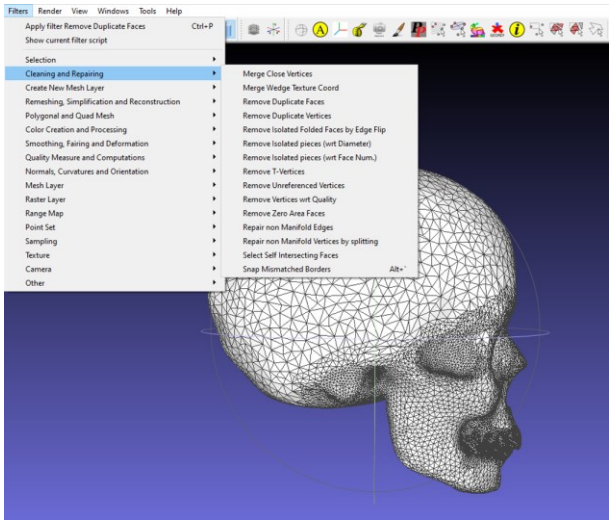


Figure 3.15 – Cleaning and repairing of the mesh in MeshLab

3.2 CAD models

3.2.1 STL files conversion in solid models

Optimized models of the head anatomical districts were then imported into Fusion 360 software to obtain the solid models to be imported in Abaqus as *Parts*. In the following figures the reference system was retained from the original STL files, with yz sagittal plane, where z is the sagittal axis and y is the longitudinal axis. The origin lays on the neck base.

3.2.1.1 Brain

Brain STL file was converted (*MESH → MODIFY → Convert Mesh*) into a solid model delimited by T-splines surfaces (fig. 3.16).

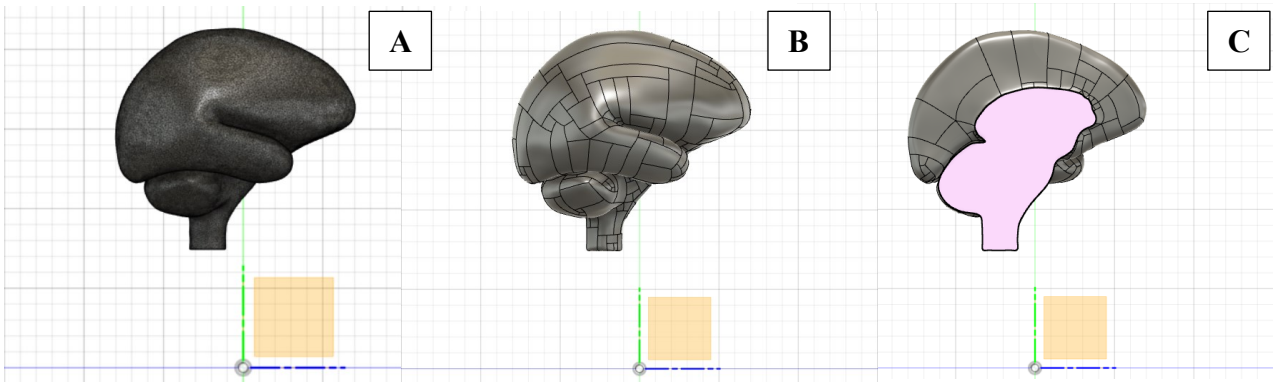


Figure 3.16 – Import and conversion of the STL file into solid model: (A) STL file, (B) solid model, (C) sagittal section of the solid model

3.2.1.2 Top skull, bottom skull, and jaw

The whole skull STL file was converted (*MESH → MODIFY → Convert mesh*) into a solid model delimited by T-splines surfaces (fig. 3.17).

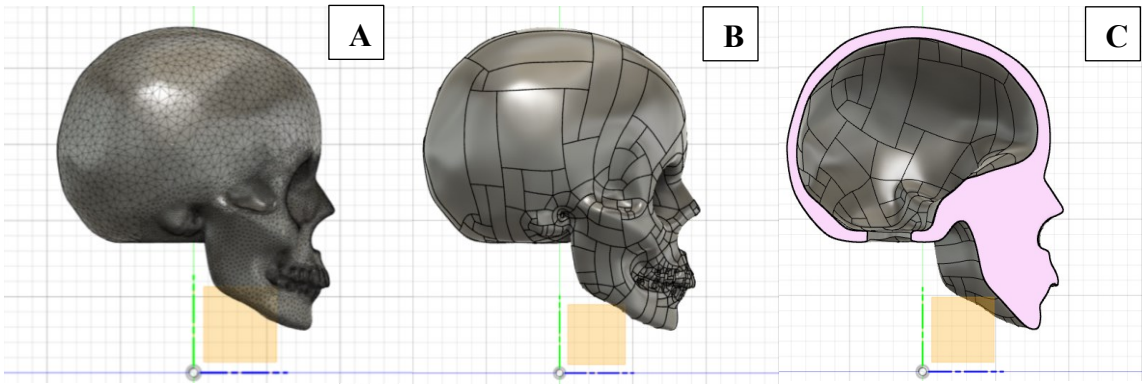


Figure 3.17 – Import and conversion of the whole skull mesh into T-spline delimited solid: (A) STL file, (B) solid model, (C) sagittal section of the solid model

The position of the division plane at the interfaces of the STL models of top and bottom skull saved before was used to create the same plane in Fusion 360 (*SOLID → CONSTRUCT*). This was required to divide the whole skull solid model (*SOLID → MODIFY → Split Body*) into top skull and bottom skull-jaw solid models (fig. 3.18).

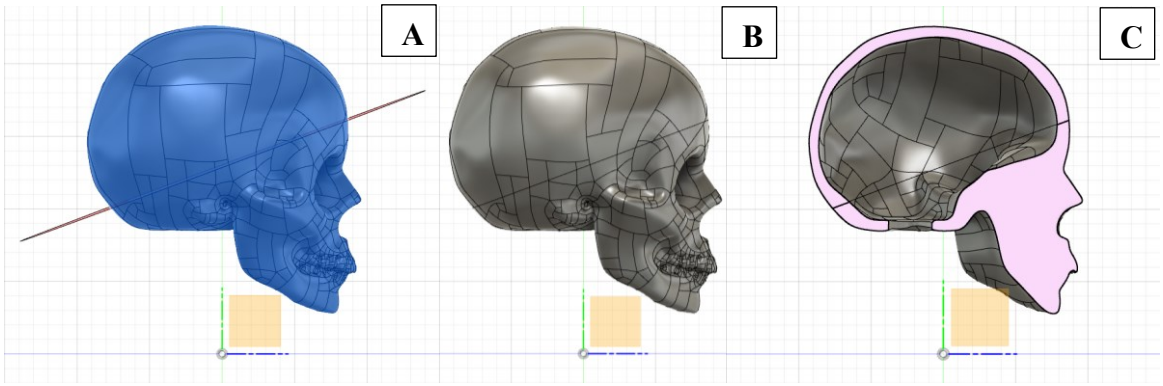


Figure 3.18 - Division of the whole model (A) into top and bottom parts (B) to retain the characteristics of the physical model to be submitted to FE analysis; (C) sagittal section

3.2.1.3 Skin

External skin STL file was converted (*MESH → MODIFY → Convert Mesh*) into a solid model delimited by T-splines surfaces (fig. 3.19).

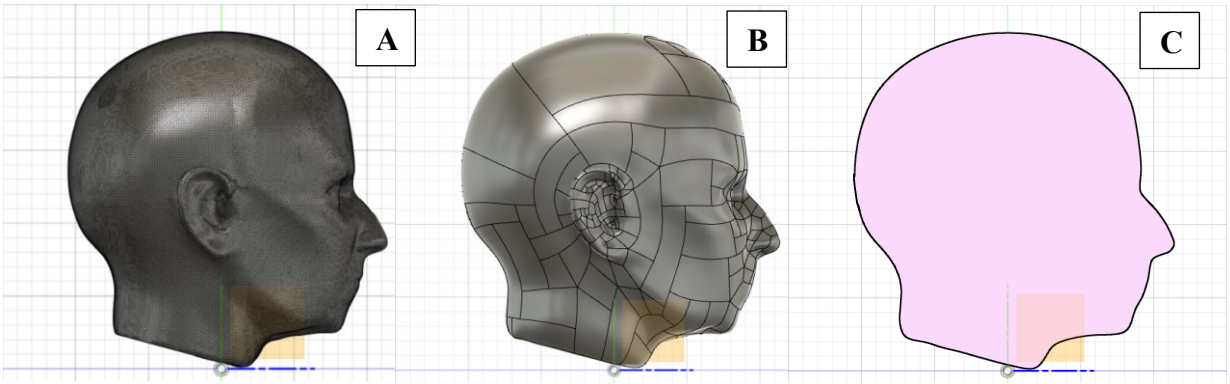


Figure 3.19 – (A) Imported mesh, (B) solid model, (C) section of the solid model of the skin

The final solid model of the skin was then obtained thanks to Boolean operations (*SOLID → MODIFY → Combine*). As shown in fig. 3.20, at first original skin model was cut with whole skull and brain models (fig. 3.20 A) and a cylinder (fig. 3.20 B), thus also obtaining the solid model of the region occupied by arachnoid trabeculae, cerebrospinal fluid, falx and tentorium (see par. 1.1.4).

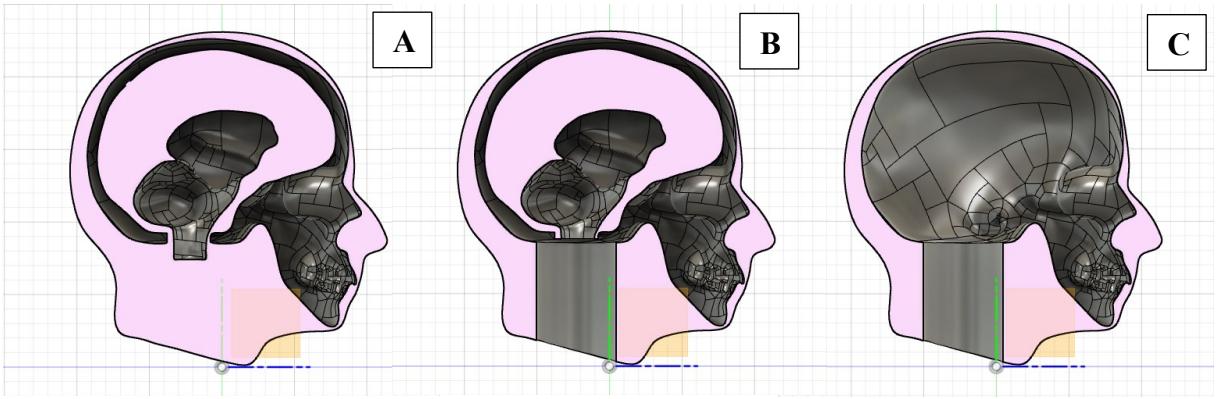


Figure 3.20 –Boolean operations to obtain a first model of skin and internal regions of the cranium: (A) whole solid, (B) the cylinder to simulate the cavity for the neck, (C) section of the skin after the removal of the solid model of the region occupied by arachnoid trabeculae, cerebrospinal fluid, falx and tentorium

Then, the model in fig. 3.20 C was cut with a bigger cylinder and divided (*SOLID → MODIFY → Split Body*) with the surface shown in fig. 3.21.

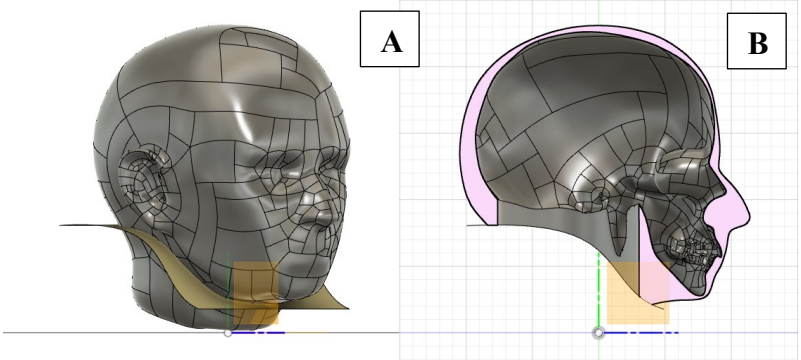


Figure 3.21 – Refinement of the bottom part of the model: (A) cutting surface, (B) section of the model after cut

The remaining part (fig. 3.21 B) was divided with three other surfaces (fig. 3.22 A/B) to remove the areas of the cranial orbits and the zone occupied by tissues under the jaw. Edges obtained after the cut with the bigger cylinder and the division under the jaw zone were then rounded (*SOLID → MODIFY → Fillet*) to get the final skin model shown in fig. 3.22 C.

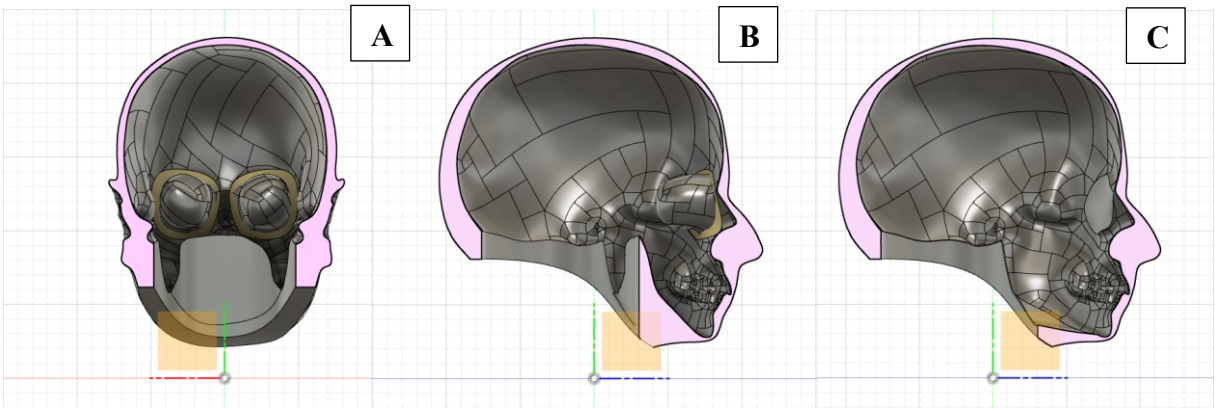


Figure 3.22 – Final refinement (A and B) and lateral section (C) of the final skin model

3.2.2 Building of missing solid models

The solid models of arachnoid trabeculae-cerebrospinal fluid and falx cerebri-tentorium were built starting from brain, whole skull, and original external skin solid models.

As described above, the solid model of the region occupied by arachnoid trabeculae, cerebrospinal fluid, falx and tentorium was built thanks to Boolean operations (*SOLID → MODIFY → Combine*). In fact, as shown in fig. 3.23 A, the original skin model was cut with whole skull and brain models, and a cylinder. Starting from this model (fig. 3.23 B/C), denoted as full meninges model in the next paragraphs, arachnoid trabeculae-cerebrospinal fluid and falx-tentorium models were then built as described below.

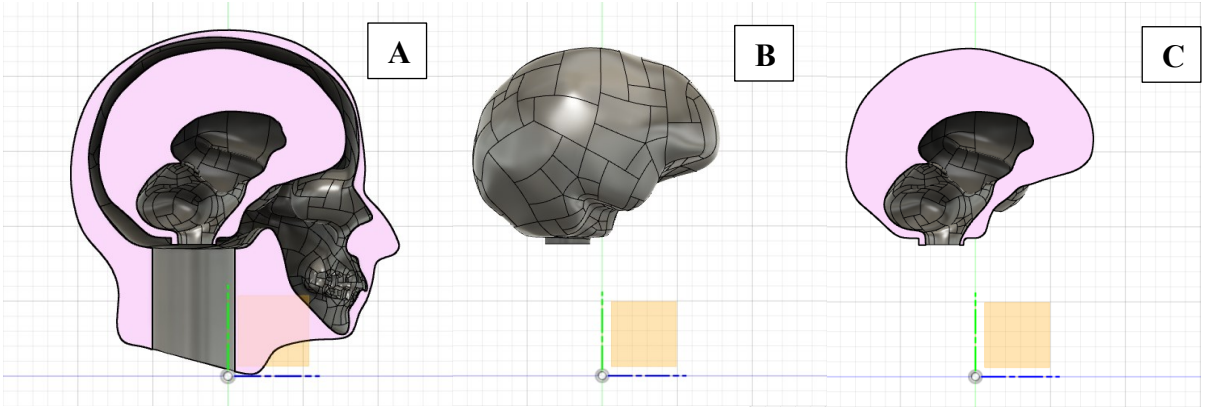


Figure 3.23 – Building of the solid model of the full meninges: (A) original skin model cut with skull, brain, and cylinder models, (B) full meninges model, (C) section of the full meninges model

3.2.2.1 Falx cerebri-Tentorium cerebelli

Falx solid model was built thanks to Boolean operations (*SOLID → MODIFY → Combine*). As shown in fig. 3.24 A, the model was obtained intersecting the full meninges model with a 1 mm thick parallelepiped and cutting it to get the falx cerebri shape (fig. 3.24 B).

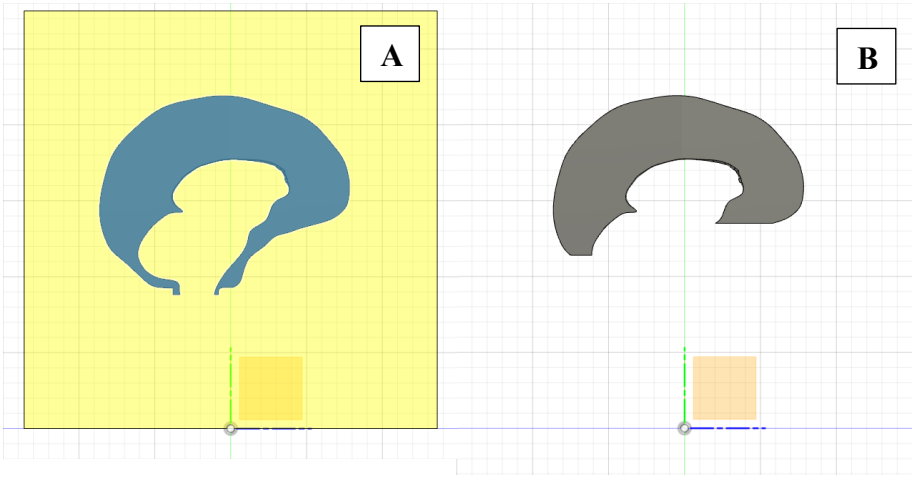


Figure 3.24 – Construction of the falx model: (A) Boolean intersection with a solid parallelepiped, (B) the resulting model of the falx

In order to allow a proper gluing of the physical falx to the skull, it was chosen to add a band of about 1 mm thickness on both sides of the falx. This band was built thanks to Boolean operations (*SOLID → MODIFY → Combine*), starting from the intersection of the full meninges model with a 20 mm width parallelepiped (fig. 3.25 A). The obtained solid was then refined to get the proper shape (fig. 3.25 B).

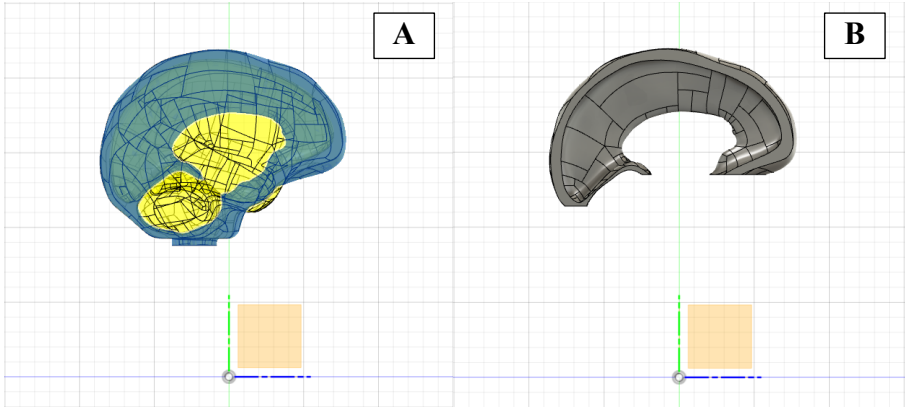


Figure 3.25 – First step of the construction of the connection band of the falx with the internal surface of the skull: (A) intersection in the central region of the model of the meninges, (B) refined part

The solid was then cut with the 1 mm thick parallelepiped (used to get the falx model built before) and two other solids drawn to leave only bands of about 1 mm thickness, as shown in fig. 3.26 A. The two bands obtained were then divided (*SOLID → MODIFY → Split Body*) with the planes shown in figures 3.26 B/C, to limit the gluing zone to the top skull only.

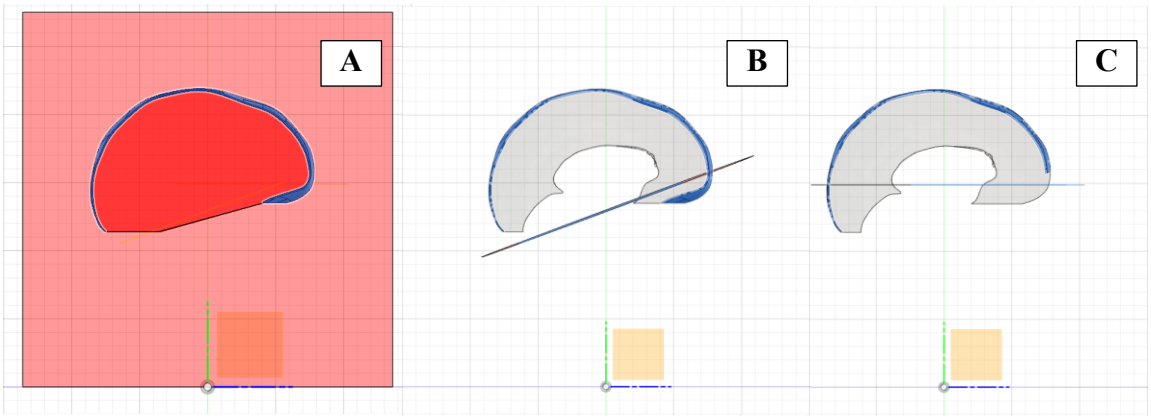


Figure 3.26 - Second step of the construction of the connection band of the falx with the internal surface of the skull: (A) cut of the exceeding material to leave only the 1 mm thick profile on the two sides of the falx, (B-C) cut to match the profile of the internal vault of the top skull only

The two final bands (fig. 3.27 A) were then unified with the falx to get the final falx model (fig. 3.27 B/C).

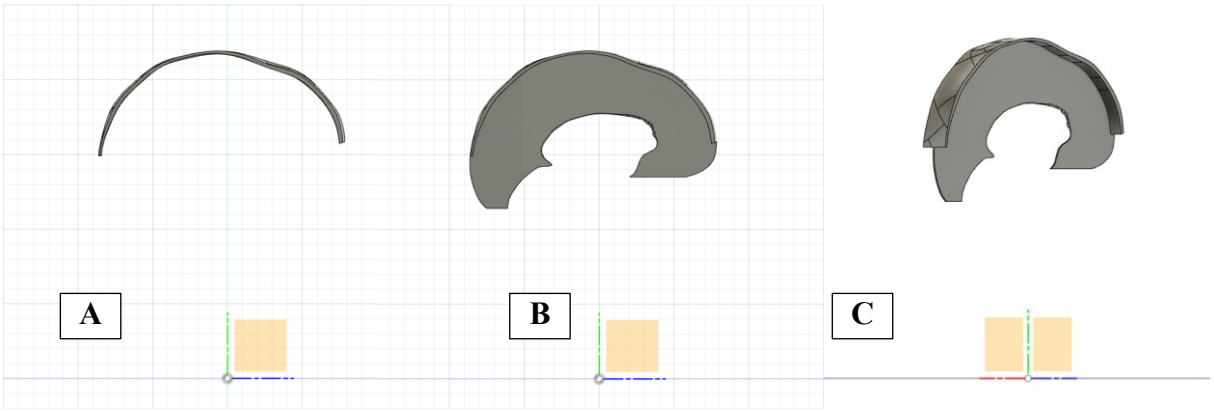


Figure 3.27 – Assembly of the connection bands (A) to the falx (B) to obtain the final falx model (C)

Tentorium model was built using the *Loft* tool (*SURFACE* → *CREATE* → *Loft*). This tool creates a transitional shape between sketch *profiles*. One or more profiles named *rails* can be used as guides to follow the desired shape in the transition between profiles [Fusion 360 documentation]. The same procedure (here described for the right side) was adopted to draw left and right parts of the whole tentorium model, to be attached to the falx.

A part of the right side of the full meninges model (fig. 3.28 A) was divided into three solids to identify four section planes and draw planar sketches (fig. 3.28 B). The four splines drawn were then used as *Profiles* in the *Loft* tool tab. A 3D sketch (fig. 3.28 C) was then created to draw seven splines acting as *Rails* in the *Loft* tool tab.

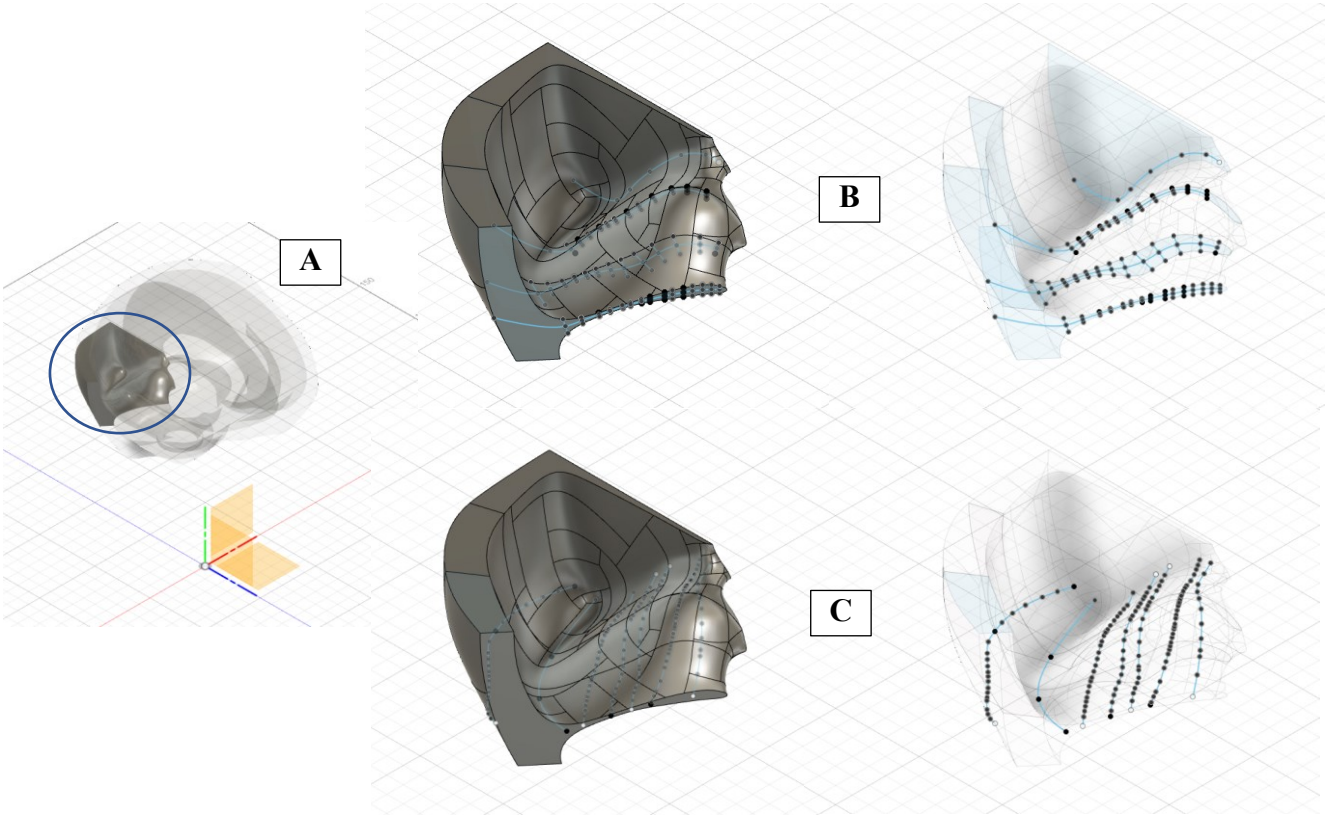


Figure 3.28 – The part of the model (A) used to draw the Profiles (B) and Rails (C) for the construction of the tentorium model

The obtained surface (fig. 3.29 A) was then symmetrically thickened (fig. 3.29 B) to obtain the 1 mm thick solid model of the right part of the tentorium.

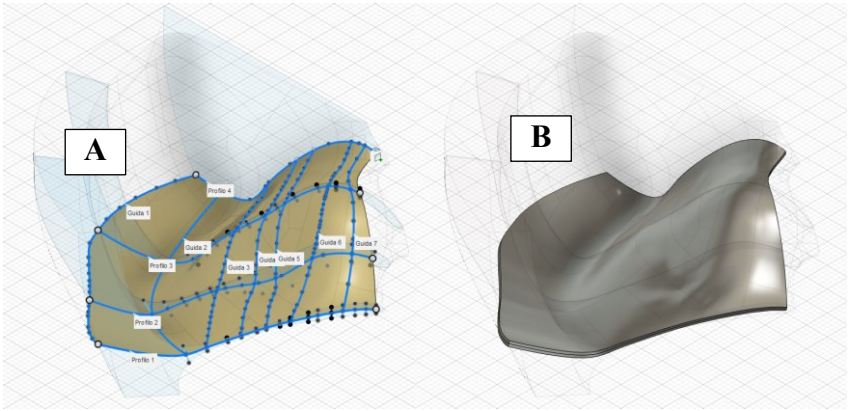


Figure 3.29 – Loft surface (A) before and (B) after thickening

A 1 mm thick band was then built along the rear profile to allow a proper gluing to the physical skull. To prevent any mismatch between touching surfaces during the subsequent FE analysis, it was needed to ensure in the model the perfect adherence of the band to the internal surface of the skull. To this purpose, it was chosen to create a loft surface (*SURFACE* → *CREATE* → *Loft*) at 1 mm distance inwards with respect to the external rear surface of the full meninges model (fig. 3.30 A) to be used as dividing surface to extract the 1 mm tick band. To do this, several splines were drawn on the external surface of the model (fig. 3.30 B) and then translated

1 mm inwards to act as *Rails* (fig. 3.30 C) in the *Loft* tool. Five splines were then drawn (fig. 3.30 D) and translated 1 mm inwards to act as *Profiles* (fig. 3.30 E) in the *Loft* tool.

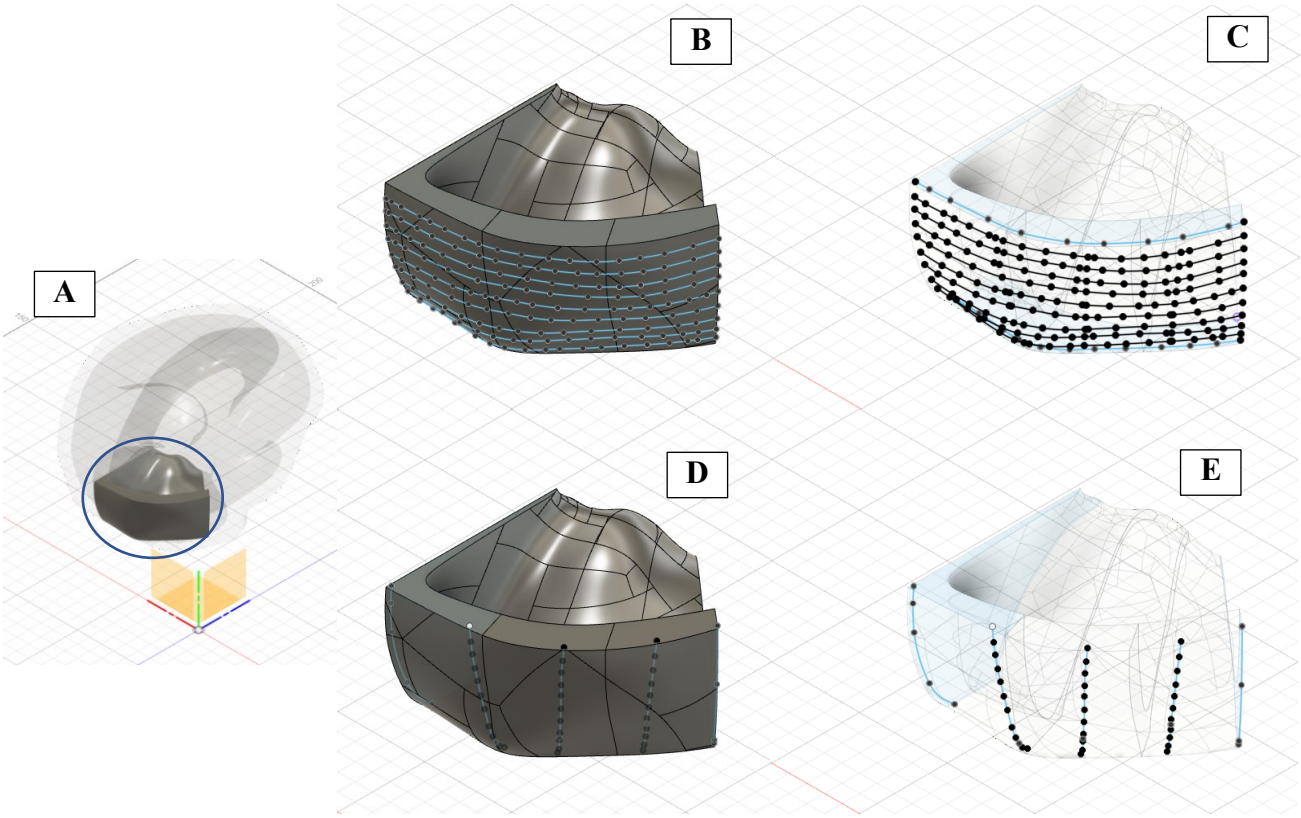


Figure 3.30 – (A) Part of the full meninges region used to draw the Rails (B → C) and Profiles (D → E) to generate the Loft for the construction of the tentorium band model

The loft surface (fig. 3.31 A) was used to divide (*SOLID → MODIFY → Split Body*) the model and get the 1 mm band as mentioned before. The band was further refined (fig. 3.31 B) for the assembly with the falx model. The right band was then unified with the right tentorium obtained before getting the final right tentorium model (fig. 3.31 C).

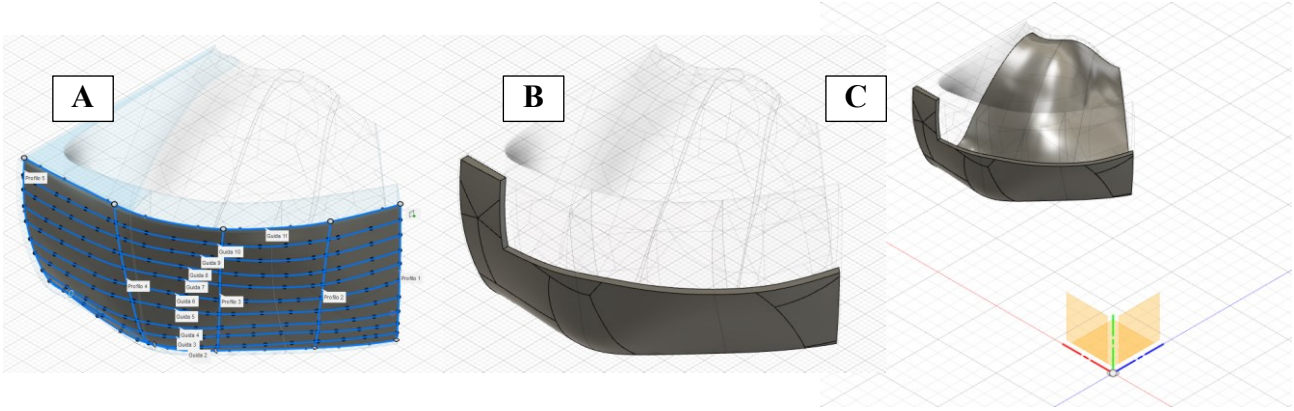


Figure 3.31 – (A) Right tentorium loft surface, (B) band, and (C) final right tentorium model

The same procedure was adopted for the left side of the full meninges and the final left tentorium model is shown in fig. 3.32.

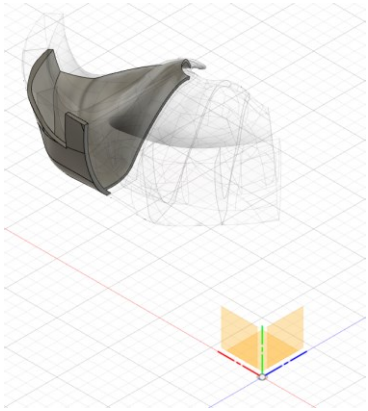


Figure 3.32 – Left tentorium model

Final falx, right tentorium and left tentorium models are represented in fig. 3.33.

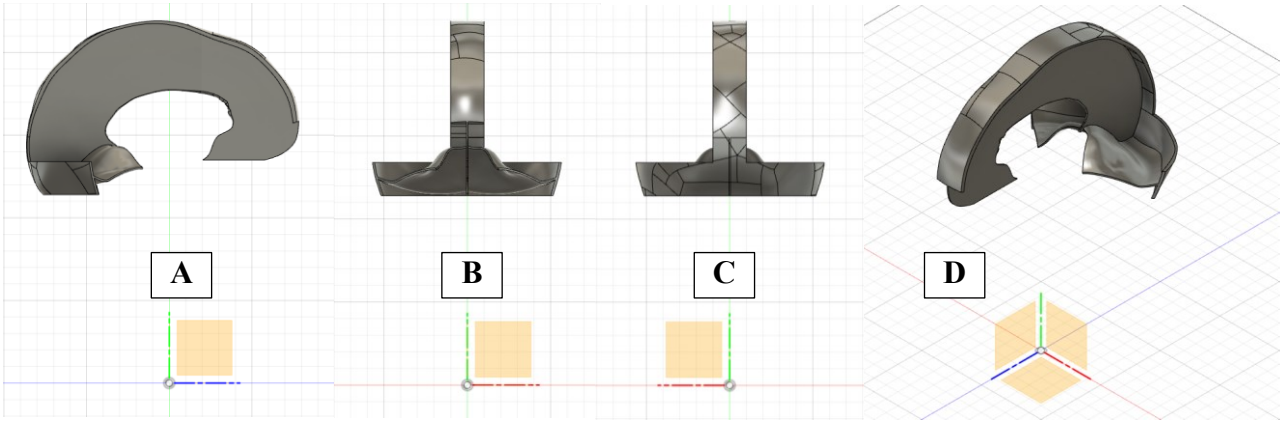


Figure 3.33 – Views of the assembly of falx, left and right tentorium: (A) lateral, (B) front, (C) rear, and (D) isometric views

Falx, right tentorium and left tentorium solid models were then exported as STL files to be 3D printed in thermoplastic polyurethane (TPU) with SLS technology. For FE analysis purposes, the three solid models were then unified (SOLID → MODIFY → Combine) to create the final Falx-Tentorium model.

3.2.2.2 Arachnoid trabeculae-Cerebrospinal fluid

The solid model of the region occupied by arachnoid trabeculae and cerebrospinal fluid surrogates was built using Boolean operations (*SOLID → MODIFY → Combine*) and refined thanks to divisions with proper surfaces (SOLID → MODIFY → Split Body). The full meninges model was initially cut with Falx-Tentorium model (fig. 3.34 A), obtaining the solid shown in fig. 3.34 B/C/D/E/F in different perspectives.

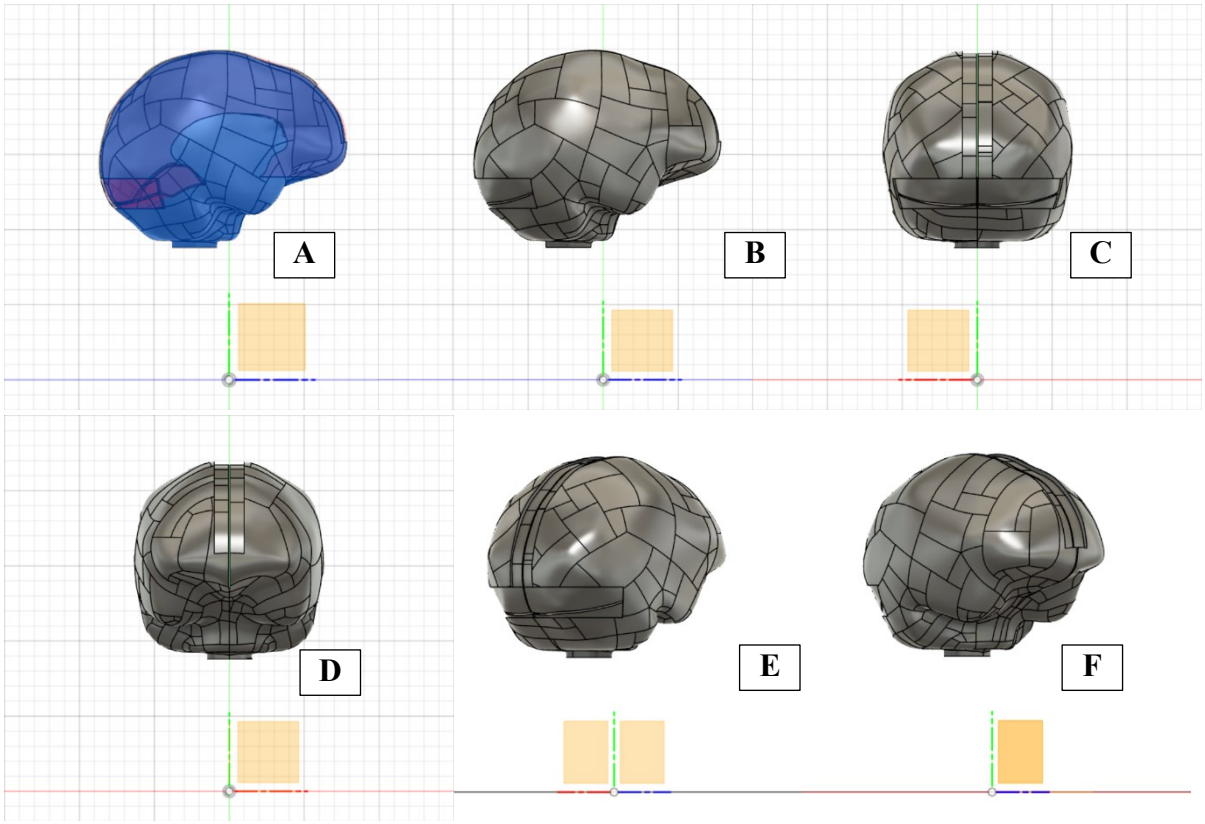


Figure 3.34 – (A) Cut of the full meninges model with Falx-Tentorium and views of the solid model of the space occupied by the arachnoid trabeculae and CSF: (B) lateral view, (C) rear view, (D) front view, (E) rear-lateral view, (F) front-lateral view

The tentorium model was realized with a thickness of 1 mm, as required by the 3D printing technique as minimum thickness value. As a consequence, the analysis of the solid model resulting from the boolean cut with Falx-Tentorium shown in fig. 3.34 evidenced that the thickness in some of the areas surrounding the tentorium was less than 0,5 mm. This would have caused issues in Abaqus solid meshing procedure, therefore the solid parts of the model surrounding the tentorium were discarded. According to this point, in the physical model the open-cell polymer foam simulating the arachnoid trabeculae was not placed between brain occipital lobes and cerebellum. The modeling of the final arachnoid trabeculae-cerebrospinal fluid involved the division of the obtained solid with properly drawn surfaces. The discarded areas are shown in fig. 3.35 A (right side) and fig. 3.35 B (left side) from different perspectives.

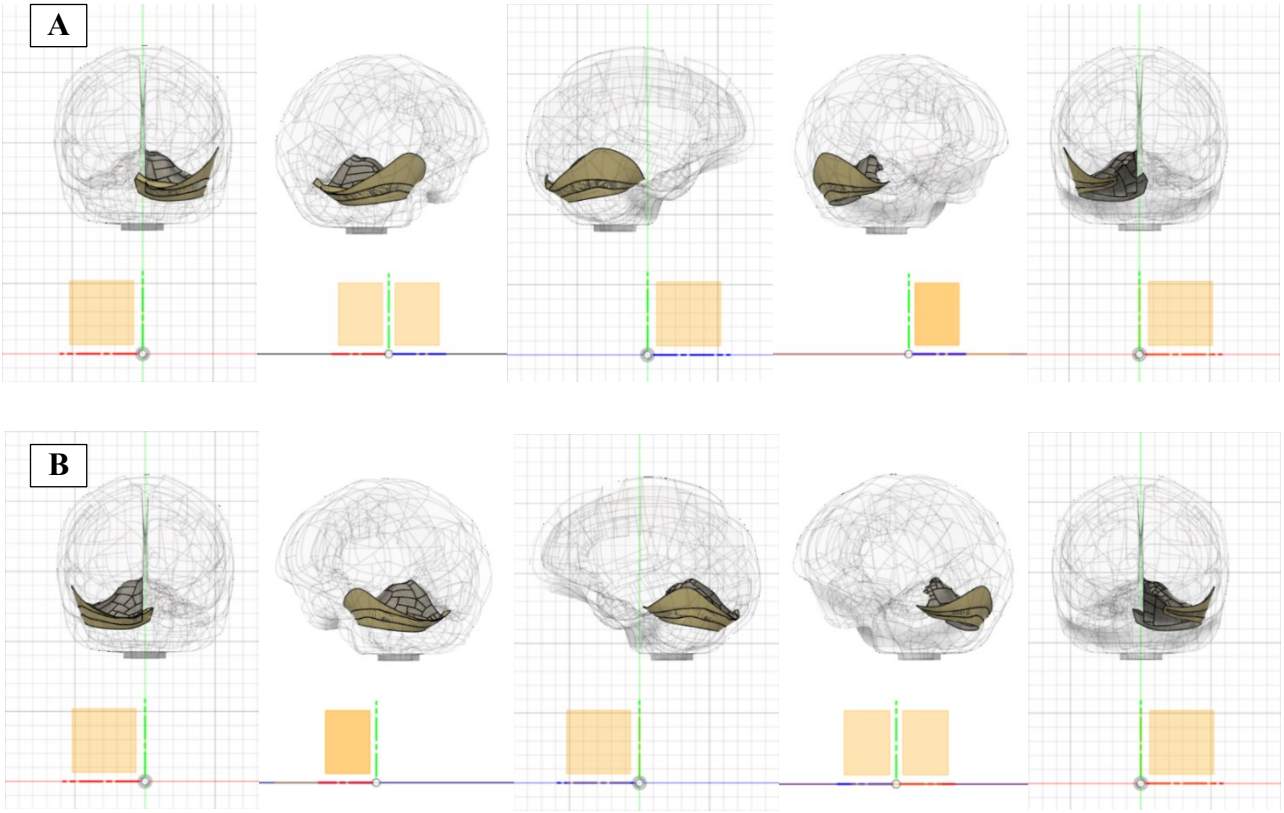


Figure 3.35 – Right (A) and left (B) discarded areas

The final model was divided in right (fig. 3.36 A) and left (fig. 3.36 B) parts to simplify the selection of the surfaces for constraints definition in Abaqus.

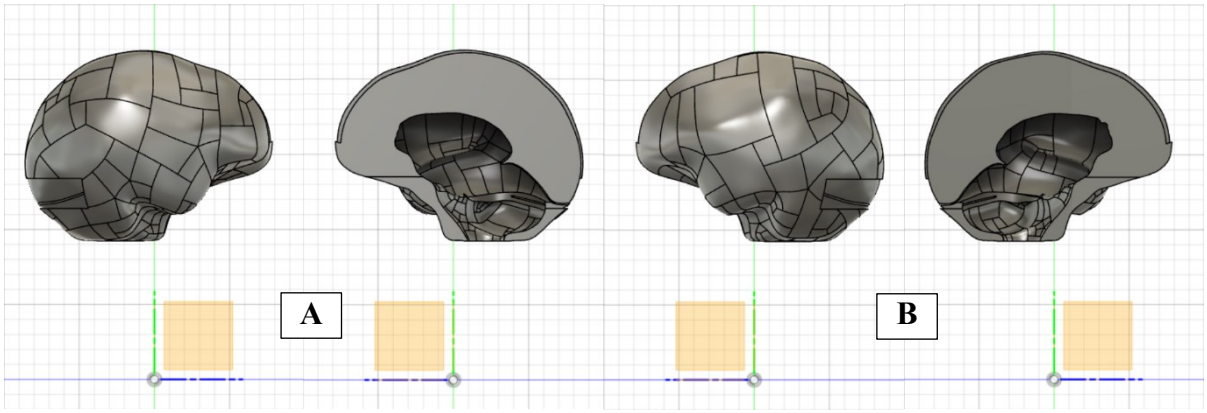


Figure 3.36 – Right (A) and left (B) parts of the arachnoid trabeculae-CSF model

3.2.2.3 Flange and screws

In the physical model, a flange was positioned in contact with the bottom skull-jaw surrogate to interact with the threaded bolt representing the brain stem. Some refinements were made on the CAD model to ensure a perfect coupling also in Abaqus simulation. For simplicity, the four flange screws were drawn as grub screws. Flange and flange grub screws are shown in fig. 3.37.

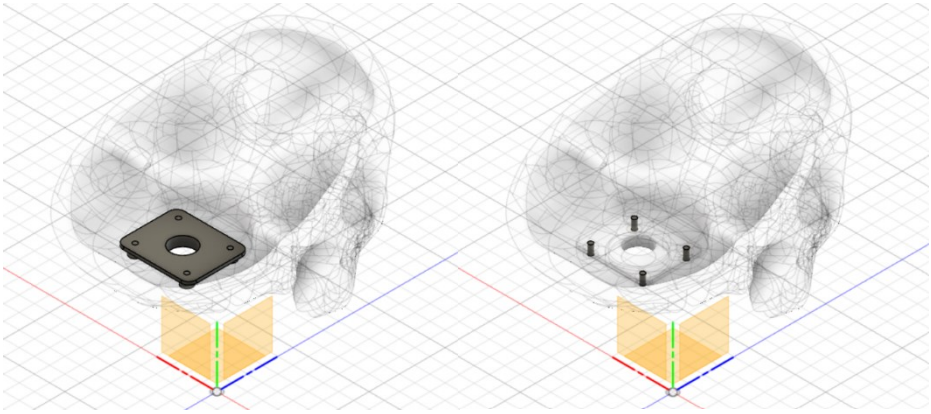


Figure 3.37 – Flange and grub screws for head-neck connection

To model top-bottom skull interaction, since the focus of the study involves anatomical parts surrogates mechanical behaviour, the 10 screws were modeled as grub screws for simplicity. These were then placed along top-bottom skull interface with the correct position and orientation as shown in fig. 3.38.

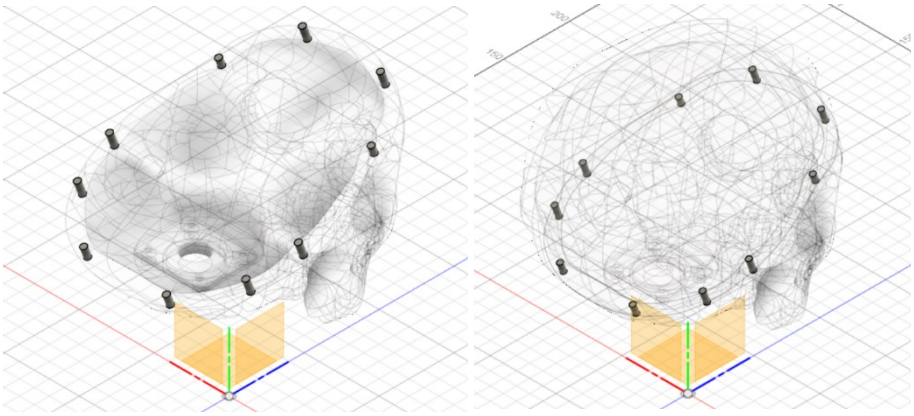


Figure 3.38 – Model of the grub screws to connect the two parts of the skull

The solid models of the components were finally exported as .SAT files to be imported in Abaqus as *Parts* for the subsequent analyses.

Chapter 4 Finite element model of the current prototype

4.1 The Finite Element method

Finite element analysis (FEA) is a widely used method which allows to predict and analyse the behaviour of an object under different physical conditions using calculations, models and simulations. It permits to optimize the components of a complex structure during the design phase, thus allowing to reduce the number of physical prototypes to build and the number of experiments. The softwares for FEA were created in the 1970s, with very popular programs such as Abaqus and Ansys. FEA is used in several design environments such as structural static analysis, thermal engineering, vibrations analysis, design of anti-seismic structures.

FEA is based on the finite element method (FEM), a numerical technique that subdivides the complex object under testing into a finite number of subdomains, called finite elements, interconnected at points denoted as nodes. This method allows to solve engineering problems described by partial differential equations (PDEs), providing an approximate solution. The analysis is performed by creating a mesh, made of a number of small elements which form the shape of the structure. Calculations are performed on every single element to provide the final result for the full structure.

In particular, considering a single element, the displacement field $\boldsymbol{s}$ within that subdomain can be expressed as:

$$\boldsymbol{s}(x,y,z) = N_e(x,y,z)\boldsymbol{s_e} = N_e(x,y,z)\begin{bmatrix} u_1 \\ v_1 \\ w_1 \\ \cdots \\ u_n \\ v_n \\ w_n \end{bmatrix} \tag{4.1}$$

where:

- x, y, and z are the coordinates of a single point inside that element
- N_e is the shape function matrix of the element *e*
- $\boldsymbol{s_e}$ is the vector of nodal displacements, which can be written as function of its components (*n* represents the number of nodes which identify the finite element *e*)

The shape functions allow to determine an approximate solution (continuous displacement field $\boldsymbol{s}(x,y,z)$) on the basis of the exact computed nodal displacement components according to the (4.1). Hence, the vector of strain components $\boldsymbol{\varepsilon}$ can be determined as function of the displacement vector $\boldsymbol{s}$ as follows:

$$\boldsymbol{\varepsilon} = \begin{pmatrix} \partial/\partial x & 0 & 0 \\ 0 & \partial/\partial y & 0 \\ 0 & 0 & \partial/\partial z \\ 0 & \partial/\partial z & \partial/\partial y \\ \partial/\partial z & 0 & \partial/\partial x \\ \partial/\partial y & \partial/\partial x & 0 \end{pmatrix} \boldsymbol{s}(x,y,z) = L\boldsymbol{s}(x,y,z) = LN_e(x,y,z)\boldsymbol{s_e} = B_e(x,y,z)\boldsymbol{s_e} \quad (5.2)$$

where:

- L is a partial derivative operator
- $B_e(x,y,z) = LN_e(x,y,z)$

Thus, the vector of stress components $\boldsymbol{\sigma}$ can be determined as function of the vector of strain components $\boldsymbol{\varepsilon}$ as follows:

$$\boldsymbol{\sigma} = D\boldsymbol{\varepsilon} = DB_e(x,y,z)\boldsymbol{s_e} \quad (5.3)$$

where:

- D is the constitutive tensor

The principle of FEA considers boundary conditions, such as forces, interactions, and constraints, along with equilibrium equations, which balance the opposing forces or actions, and constitutive equations. The process is divided into three steps: pre-process, process and post-process.

During the pre-process phase, the geometry is generated or imported. It represents the mathematical domain of PDEs underlying the problem. The user selects the analysis type (e.g. structural static analysis, electromagnetic…), the material properties, the type of constraints to be applied, the interactions between the bodies in the model, the boundary conditions, and the loads applied. Moreover, the user defines the element type to crate the mesh, connecting the elements by the nodes.

The second step is the process, when the processor performs the analysis; this step may require a long time to complete, according to the complexity of the structure. It provides an output file where the results are computed at the nodes.

The postprocess is the review of the results like deformations, temperature, time history, stress, strain. It provides a graphical representation of the results, using the shape functions chosen for the finite elements. As mentioned before, these functions interpolate the results computed at the nodes to determine an approximate solution distributed along the whole geometry of the model. The reliability of the results depends on the settings given when assigning material properties, interaction types, constraints, imposed deformation laws, and mesh sizes.

Using FEA has relevant advantages, such as the safe simulation of potentially threatening or destructive load conditions and failure modes, allowing to simulate the physical response under many conditions [Brush, 2019].

4.2 Some Finite Element Models of human head in literature

During the last three decades, a number of finite element models of a human head have been developed. A short description of the most significant is given below [Samaka et al., 2013].

4.2.1 EEVC WG17 FE model [European enhanced vehicle safety committee, 1991]

This type of impactor consists of a set of concentrical aluminium spheres covered with a layer of vinyl to mimic the skin. In the numerical model, the aluminium parts are assigned as the rigid parts of the human head with specific mass and inertia properties (fig. 4.1).

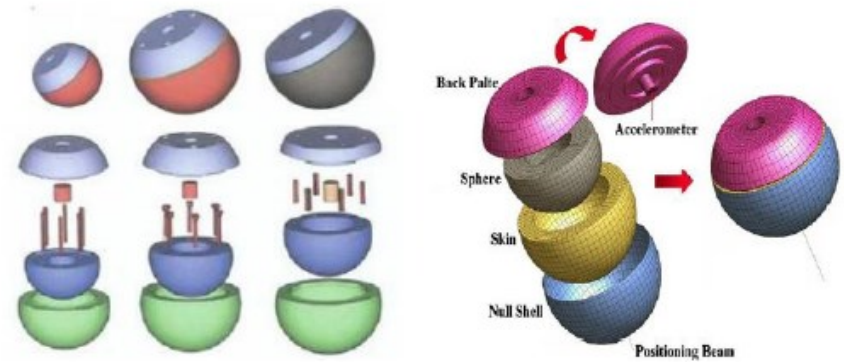


Figure 4.1 - EEVC WG17 headform and numerical model [Samaka et al., 2013]

4.2.2 ULP FEM of the human head, 1999

This model is based on other anatomical designs of the human head; it was developed at the University of Louis Pasteur in Strasbourg. It allows to calculate HIC and internal brain pressure. This model weighs 4.8 kg, and consists of 13208 elements, 10395 brick elements and 2813 shell elements. The properties of the materials are summarized in table 4.1.

ULP FEM of the human head				
Part	*Material Model*	$\rho\ [kg/m^3]$	$E\ [Mpa]$	υ
Falx Cerebri	Lin. Elastic	1140	31.5	0.45
Tentorium Cereb.	Lin. Elastic	1140	31.5	0.45
Brain/Skull int.	Lin. Elastic	1040	0.012	0.49
Brain and Cereb.	Viscoel.	1040	-	-
Skull-Cortical	Elas-Plas. Britt.	1900	15000	0.21
Skull-Trabecular	Elas-Plas. Britt.	1500	4600	0.05
Face	Lin. Elastic	2500	5000	0.23
Skin	Lin. Elastic	1000	16.7	0.42
	$K\ [MPa]$	$\beta\ [s^{-1}]$	$G_0\ [MPa]$	$G_{inf}\ [MPa]$
Brain and Cereb.	1125	145	0.049	0.0167
Skull-Cortical	6200	-	-	-
Skull-Trabecular	2300	-	-	-

Table 4.1 – Material properties of ULP FEM [Samaka et al., 2013]

4.2.3 KTH Model (Kleiven, 2000)

In 2000, Kleiven developed a parametric detailed FE model of an adult human head, including the three layers of bone of the skull, facial bones, scalp, cerebrum, cerebellum, spinal cord, dura mater, tentorium and falx (fig. 4.2) [Kleiven, 2000]. A simplified neck was also modelled, along with the extension of the brain stem to the spinal cord, dura mater, vertebrae and muscular tissue. The compact bone, the facial bones and the skin were modelled with 4-node shell elements, while for trabecular bone and the soft tissues of brain and spinal cord 8-node brick elements were used. Meninges, falx and tentorium were modelled with 4-node membrane elements. To handle the large elastic deformations, a Mooney-Rivlin hyperelastic constitutive law was applied for the nervous tissues. FE model was validated with the experiments of Nahum et al. (1977).

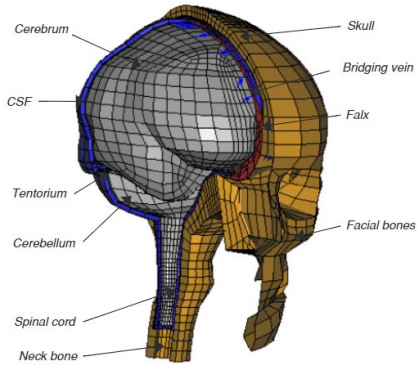


Figure 4.2 – section of Kleiven KTH Model [Kleiven, 2000]

4.2.4 Wayne State University (WSU) Head (Brain) Injury Model (WSUHIM, 2001)

The WSU developed a group of FEMs to study the human head and brain injury. The first prototype was improved until the final version, developed by Zhang, Hardy, Omori, Yang, and King in 2001, where the number of elements reached 245000. The model considers different materials such as the gray and white matter, increasing the accuracy of predicting the occurrence of diffuse axonal injury (DAI) in the areas of contact between grey and white matter. This model was further developed for a better accuracy and a more detailed simulation of the sliding between the brain surface and cerebrospinal fluid (CSF). This model is commonly used in the medical field because it can determine the pressure inside the cranium (fig. 4.3).

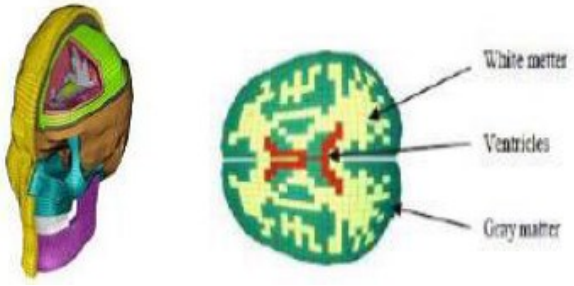


Figure 4.3 – The Wayne State University (WSU) Head (Brain) Injury Model (WSUHIM) [Samaka et al., 2013]

4.2.5 Politecnico di Torino University FEM of the human head

This model was built based on CT and MRI images of the adult human head to build the internal and external surfaces of the cranium, and the facial bones (fig. 4.4). The model consists of 2600 nodes and 55246 elements. The scalp is represented by brick elements with a 6 mm thickness. The cranial bones are modeled with three layers, two for the external compact bone and one for the cancellous bone. The dura mater, falx, and tentorium membranes are represented by four-node shell elements. CSF is described by eightnode brick elements, while brain tissues and ventricles are represented by tetrahedral elements.

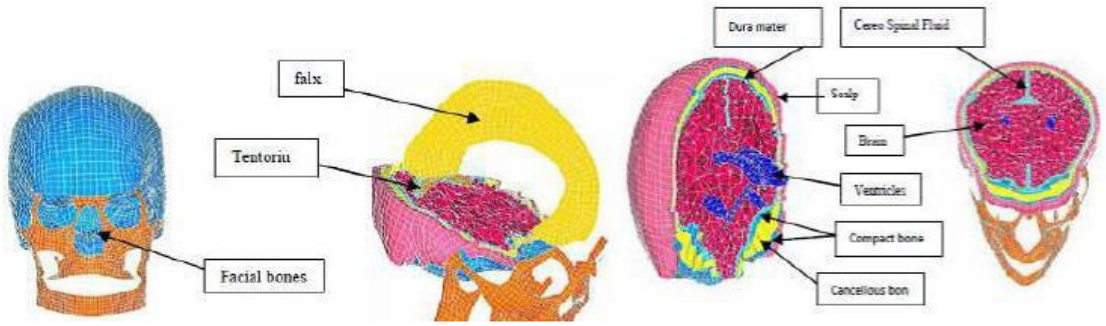


Figure 4.4 – Politecnico di Torino University FEM of the human head [Samaka et al., 2013]

4.2.6 University College Dublin Brain Trauma Model (UCDBTM, 2003)

Six types of 3D FE model were built (the Baseline Model, Sliding Boundary Model, Grey-White-Ventricular matter model (GWV model), three-element CSF model, projection mesh model, and morphed model), all based on data provided by the physiological and anatomical details of the human head. In particular, the Baseline Model consists of the cerebrum, cerebellum and brainstem, falx and tentorium, meninges, CSF, a three-layered skull (cortical and trabecular bone layers) with varying thickness, scalp, and the facial bone. The brain consists of 7318 hexahedral elements, while the CSF layer is made of 2874 hexahedral elements, with one element through the thickness. Earlier FEMs of the brain used linear elastic material, more recently a linear viscoelastic material was adopted. The remaining materials of the model are the same as in previous studies. Table 4.2 shows the mechanical specifications of materials used in the model. The model weight is 4.01 kg and the brain weight is 1.422 kg.

UCDBTM			
Part	$\rho\ [kg/m^3]$	$E\ [MPa]$	υ
Scalp	1000	16.7	0.42
Cortical Bone	2000	15000	0.22
Trabecular Bone	1300	1000	0.44
Dura Mater	1130	31.5	0.45
Pia Mater	1130	11.5	0.45
Falx and Tentorium	1130	31.5	0.45
Brain	1040	Hyperelastic	0.499981
Facial Bone	2100	5000	0.23

Table 4.2 - Material properties of UCDBTM [Samaka et al., 2013]

4.2.7 HEAD-BRAIN FE Model [Masami Imawoto et al., 2007]

This model consists of three main parts: skull, brain, and skin (fig. 4.5). The skull is divided into cortical bone, represented by solid elements, and the cancellous bone, represented by shell elements. Hexagonal solid elements are used to represent brain, cerebellum, brain stem, grey matter, white matter, and CSF. Meninges, falx, and tentorium are modeled by shell elements. The whole model weighs 4.39 kg. The CSF is represented by hexagonal elements. The model contains 25200 shells, 49700 elements, and 24100 solids. The representation of the skull utilizes an elastic-plastic material with failure, while a non-compressible viscoelastic material model is assigned to the brain.

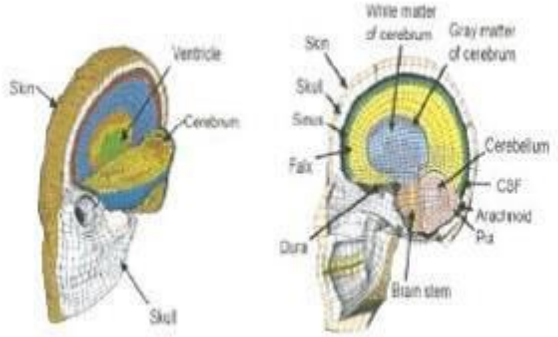


Figure 4.5 – HEAD-BRAIN FE Model [Masami Imawoto et al., 2007]

4.2.8 Yang et al. 2008 human head FE model

This model was designed based on the brain anatomy of a human body according to the specifications of each part of the physical brain, including the cerebellum, bone, and skull. The HIC value, angular head acceleration, and spinal fluid pressure inside the cranium can be determined by this model. This model represents all features of the 50th percentile of a male head. This was the most complex model in terms of the number of layers, simulant materials for the brain, and number of elements to calculate the intracranial pressure, ventricular pressure, and HIC (fig. 4.6).

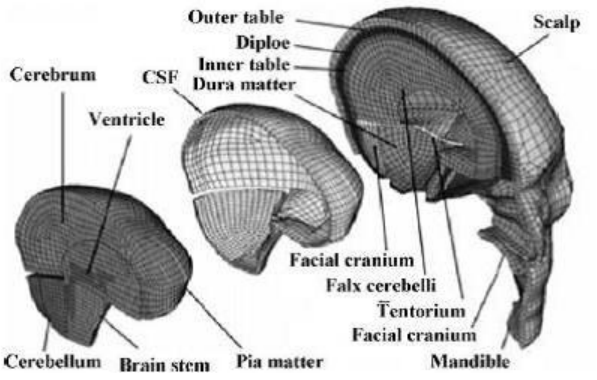


Figure 4.6 - The human head FEM of Yang et al. (2008) [Samaka et al., 2013]

4.2.9 Harvard Medical School FEM, 2008

This model was developed at Harvard School in collaboration with the Bioengineering Laboratory of the University of Salerno, Italy, using MRI images of the brain available in the atlas of the Harvard Medical School to mesh the model (fig. 4.6). The model weighs 1.4 kg[2], the brain size is 1508 cm^3 including CSF, and the skull size is 678 cm^3 with a mass of 0.8 kg. The model was simulated with 39047 tetrahedral composite elements. This model represents different portions of the brain tissue with viscoelastic properties.

4.2.10 TNO Head FE Model, 2009

This model consists of 22 parts, 13868 elements, and 15637 nodes. All parts of the model (cranium, dura mater, falx, and tentorium) were represented by homogeneous isotropic linear elastic material, where for the brain, the brain stem, and the cerebellum it were used the same viscoelastic parameters to simplify the model and the analytical study of the mechanical responses of the brain by mitigating shear strain. The material properties are shown in table 4.3.

Part	Material Properties			
	Material model	**Density [kg/m^3]**	**Elastic modulus [MPa]**	**Poisson's Ratio []**
Cranium	Linear elastic	1800	6500	0.21
Dura mater	Linear elastic	1133	31.5	0.45
Falx cerebri	Linear elastic	1133	31.5	0.45
Tentorium cerebelli	Linear elastic	1133	31.5	0.45

Table 4.3 – Mechanical properties assigned to the materials in TNO Model [Samaka et al., 2013]

The simulation results give an assessment of the distribution of intracranial stresses, the growth of stress waves, and changes in intracranial pressure of the brain at the point of collision.

4.2.11 Unipd FE Model (Pavan et al. 2022)

This model was developed from MRI images of volunteers and is declined into three versions: a 32 yrs adult female (3.61 kg, 3765375 elements), a 35 yrs adult male (3.97 kg, 4180634 elements), and a 16 yrs young male (3.47 kg, 3542819 elements) [Pavan et al., 2022]. The validation of the models was performed against experimental data on human subject post-mortem from literature. The parameters for the validation were the brain tissue displacement relative to the cranium, hydrostatic intracranial pressure, and acceleration of the head. Fig. 4.7 shows the reconstruction of the anatomical regions. As for materials, dura, tentorium and falx were modeled with isotropic linear elastic constitutive parameters; visco-hyperelastic behaviour was assigned to brain tissue, while skin and skull were modeled as rigid bodies, as reported in table 4.4.

[2] The mass appears to be too low respect to the other components. This might be a transcription mistake in the reference

CSF was treated as hyperelastic with an Ogden model with one set of parameters ($\alpha_1 = 2$, $\mu_1 = 0.02$ MPa, $D_1 = 0.1$ MPa^{-1}).

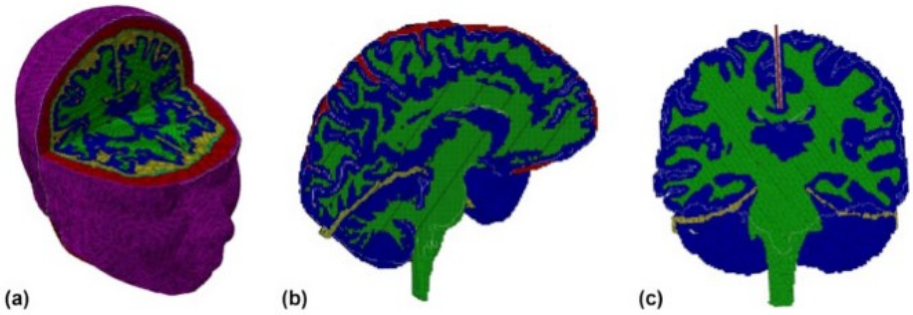


Fig. 4.7 – the anatomic districts modeled in the Unipd 2022 FE model [Pavan et al., 2022]

Constitutive models and some material parameters of head tissues.

Tissue	Constitutive model	Density [kg/m^3]	Young's modulus [MPa]	Poisson's ratio
Skin	Rigid body			
Skull	Rigid body			
CSF	Hyperelastic	1.0	–	–
White matter Gray matter	Visco-hyperelastic*	1.04	–	–
Tentorium Falx cerebri Dura mater	Linear elastic	1.13	31.5	0.45

Constitutive parameters for the hyperelastic response of white and gray matter

μ_1[MPa]	α_1	μ_2[MPa]	α_2	D_1[MPa^{-1}]	D_2[MPa^{-1}]
4.57×10^{-4}	10.684	1.63×10^{-3}	−12.619	8.75	2.45

Constitutive parameters for the viscoelastic response of white and gray matter

Viscoelastic branch	Shear relaxation moduli g_i	Relaxation time constants t_i [s]
1	7.66×10^{-1}	1.25×10^{-5}
2	9.48×10^{-2}	1.4×10^{-3}
3	1.50×10^{-2}	3.26×10^{-1}
4	2.30×10^{-4}	2.37
5	7.38×10^{-3}	5.14

Table 4.4 – Constitutive parameters of the Unipd FE model [Pavan et. al., 2022]

4.3 Development of the finite element model of the UniPD Human Head Surrogate

4.3.1 Pre-processing

4.3.1.1 Parts

Brain, falx – tentorium, arachnoid trabeculae – CSF, skull, skin, grub screws, and flange solid models (.SAT files) were imported in Abaqus software as *Parts*.

A floor was then created as a 3D Discrete Rigid *Part* and it was assigned a *Reference Point.*

4.3.1.2 Materials and Sections

Results from the constitutive analysis (see chapter 2) were needed to define the *Materials* for each district of the head in Abaqus. Moreover, each *Part* was assigned a density [t/mm^3], which was required to simulate a drop test.

Brain surrogate (PlatSil Gel-OO 1A:1B:1D)

As shown in fig. 4.8 A, the density of the silicone rubber was established considering the mass of the physical surrogate (1111.3 g = 1111.3·10^{-6} t) and the volume occupied by the instance (961295 mm^3). Visco-hyperelastic behaviour was defined by the hyperelastic (fig. 4.8 B) and viscoelastic (fig. 4.8 C) constitutive parameters identified in par. 2.2.2 (see table 2.16).

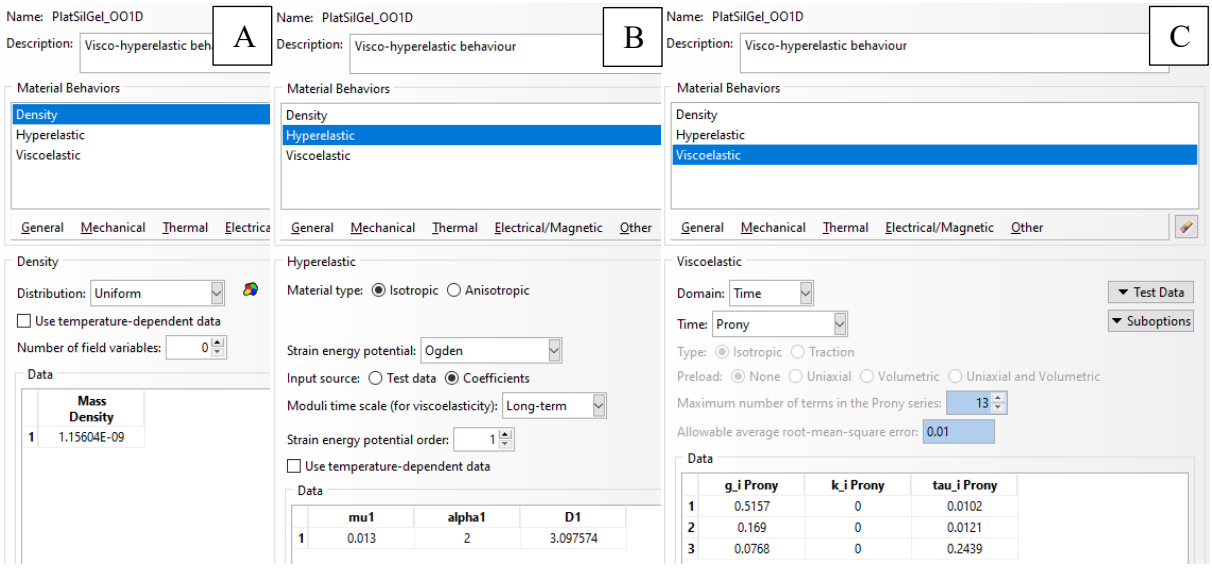


Figure 4.8 – Brain surrogate material properties: (A) density, (B) hyperelastic behaviour, (C) viscoelastic behaviour

Arachnoid trabeculae – CSF surrogate (foam – distilled water)

Water density was assigned as shown in fig. 4.9 A. Hyperelastic behaviour was defined by the hyperelastic constitutive parameters (fig. 4.9 B) identified in par. 2.3.2 (see table 2.17).

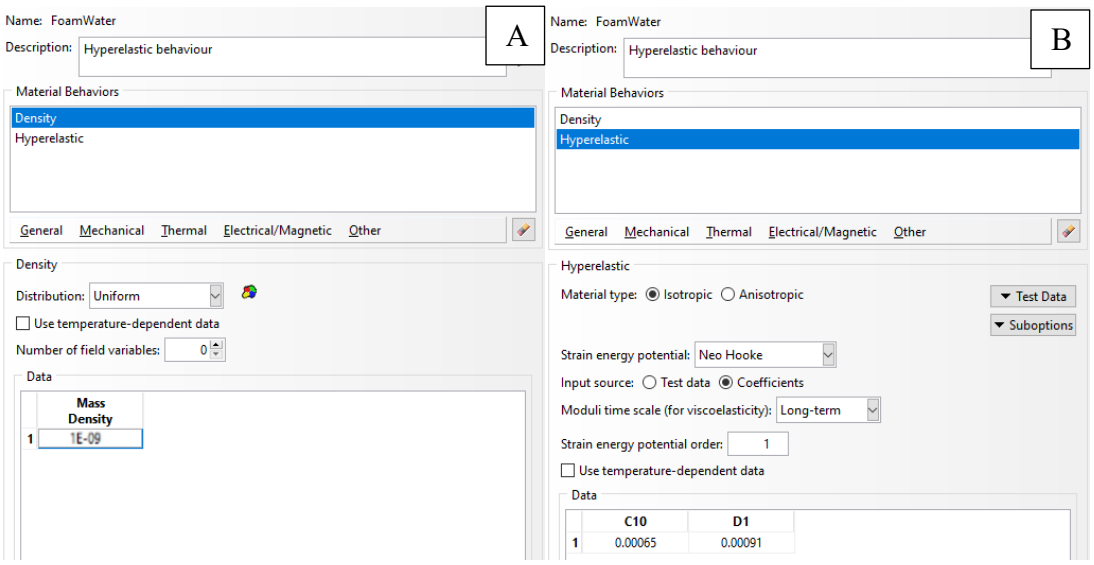


Figure 4.9 – Arachnoid trabeculae-CSF surrogate material properties: (A) density, (B) hyperelastic behaviour

Falx – tentorium surrogate (TPU)

The density (fig. 4.10 A) was established considering the mass of the physical surrogate (33.6 g = $33.6 \cdot 10^{-6}$ t) and the volume occupied by the instance (31283.24 mm^3). Elastic behaviour was defined by the elastic parameters (fig. 4.10 B) identified as explained in par. 2.6.2 (see table 2.20).

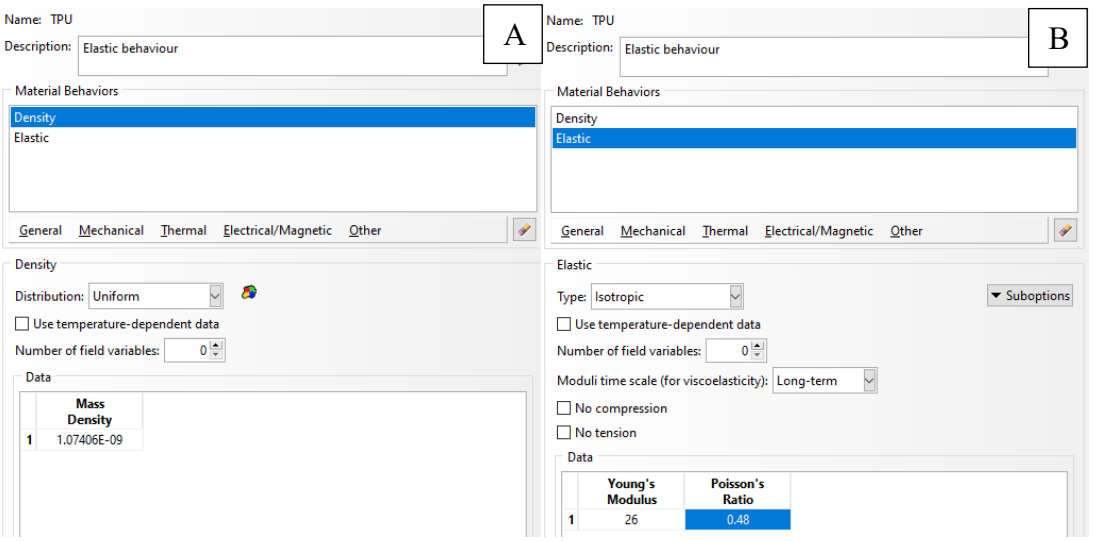


Figure 4.10 – Falx-tentorium surrogate material properties: (A) density, (B) elastic behaviour

Top skull and bottom skull- jaw surrogates (Polyamide PA12)

The density (fig. 4.11 A) of the skull surrogate was established considering the total mass of the two components (817 g = $817 \cdot 10^{-6}$ t) and the volume occupied by the two instances (939326.75 mm^3). The resulting value ($8.69772 \cdot 10^{-10}$ t/mm^3) is close to the one stated in the technical datasheet (0.9 – 0.95 g/cm^3). Elasto-plastic behaviour was defined by the elastic (fig. 4.11 B) and plastic (fig. 4.11 C) constitutive parameters identified in par. 2.5.2 (see table 2.19).

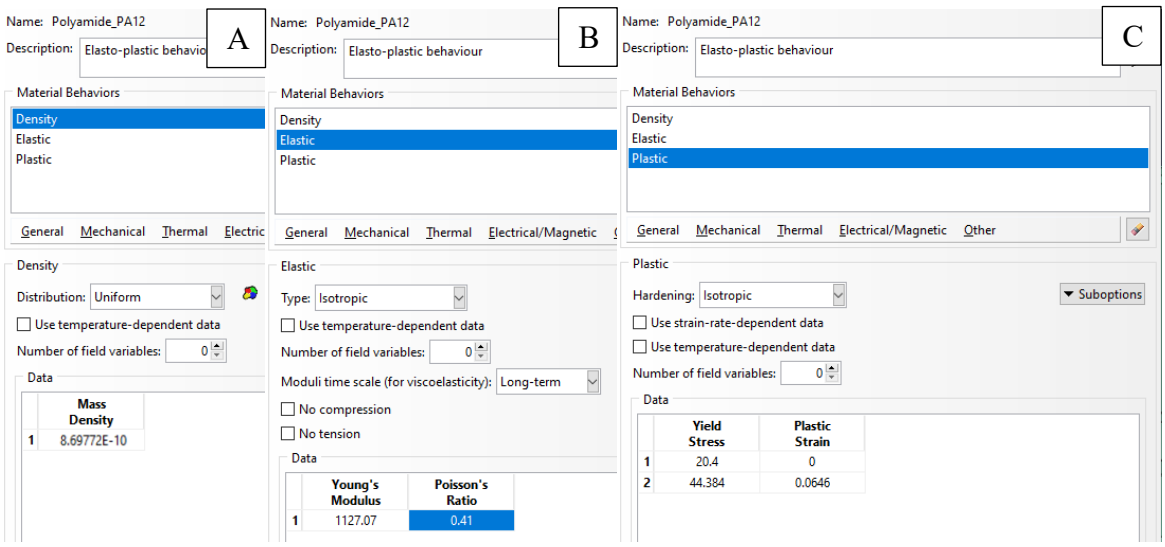


Figure 4.11- Skull surrogate material properties: (A) density, (B) elastic behaviour, (C) plastic behaviour

Skin surrogate (PlatSil Gel-10 1A:1B)

As shown in fig. 4.12 A, the density of the silicone rubber was established considering the mass of the physical surrogate (950.5 g = $950.5 \cdot 10^{-6}$ t) and the volume occupied by the instance (874216.06 mm^3). Visco-hyperelastic behaviour was defined by the hyperelastic (fig. 4.12 B) and viscoelastic (fig. 4.12 C) constitutive parameters identified in par. 2.4.2 (see table 2.18).

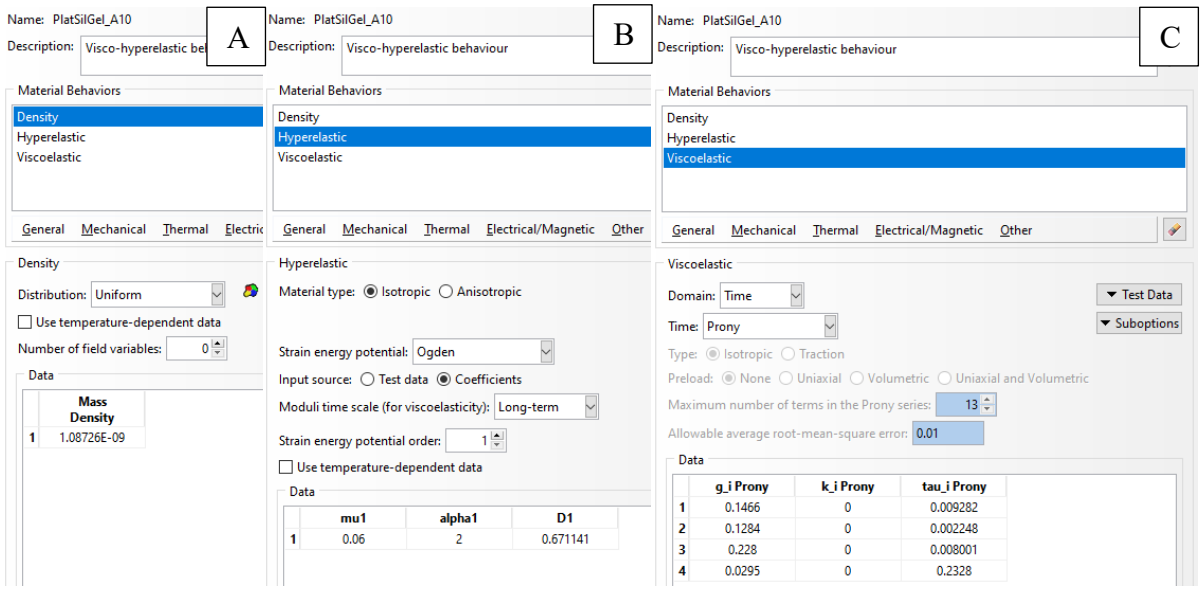


Figure 4.12 - Skin surrogate material properties: (A) density, (B) hyperelastic behaviour, (C) viscoelastic behaviour

Connection components

As mentioned in par. 3.2.2, it were modeled 14 grub screws to simulate the connections between the two components of the skull and the bottom skull and flange. Since the volume of the real screws is higher, due to the heads, the resulting material density was adjusted to obtain the same mass of the physical screws with the lower volume of the grub screws (fig. 4.13 A). Young modulus and Poisson's ratio were obtained form the technical datasheet of steel (fig. 4.13 B).

In the prototype there are sensors housed in a box under the skull, with a mass of approximately 55 g. In order to simplify the model, this mass was added to that of the adjacent flange (about 15 g) and, consequently, the density value of the resulting material was modified (fig. 4.13 C). Elastic modulus and Poisson's ratio of the aluminium constituting the flange were taken from the datasheet (fig. 4.13 D).

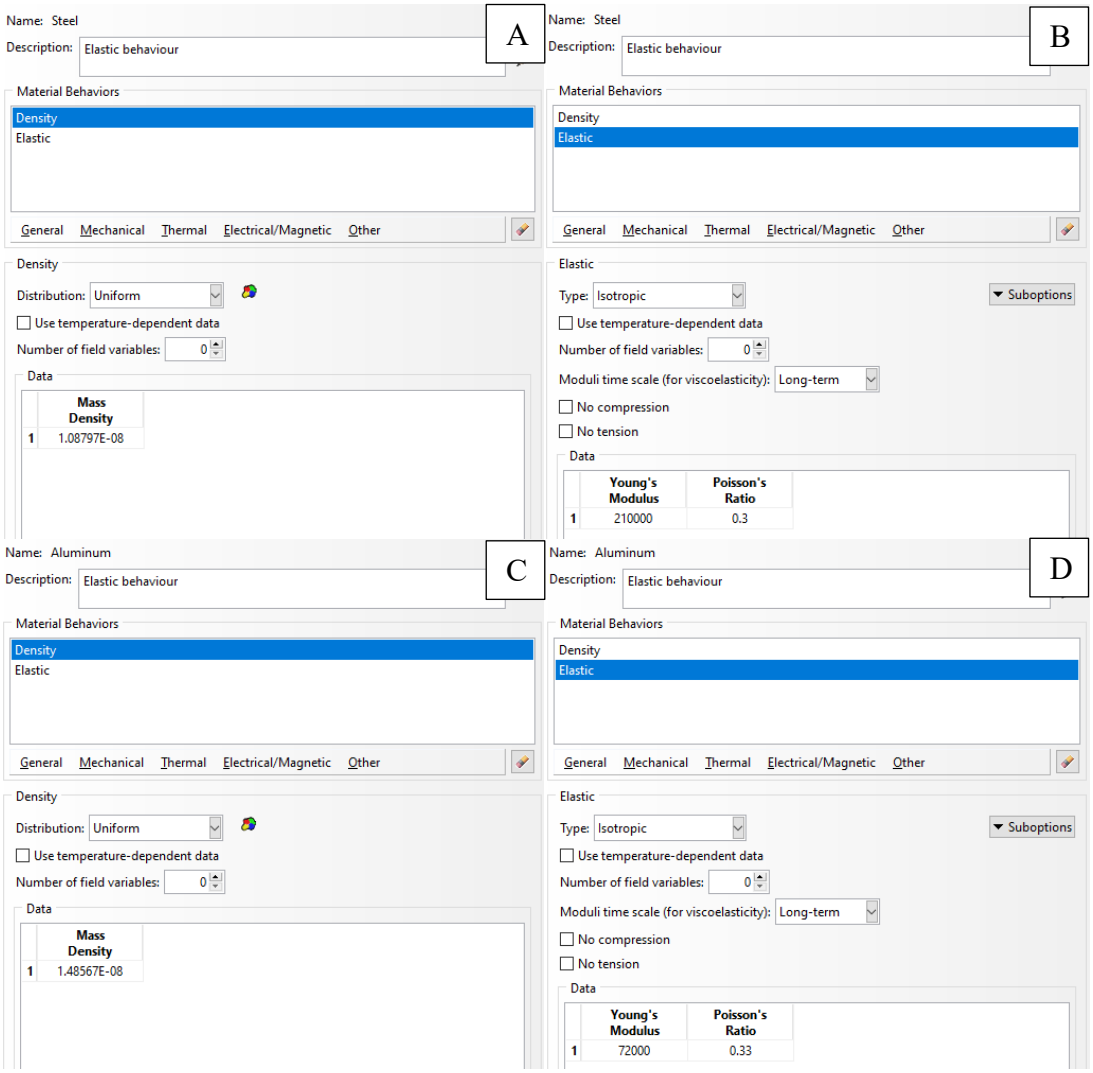


Figure 4.13 – Grub screws surrogate material properties: (A) density, (B) elastic behaviour. Flange – box surrogate material properties: (C) density, (D) elastic behaviour

Finally, *Sections* have been created and assigned to the respective *Parts*.

4.3.1.3 Assembly

Head instances were created in the *Assembly* module and made independent. The instances were rotated 90° CCW about y-axis to get x-axis as sagittal and 90° CCW about x-axis to get z-axis as longitudinal. Fig. 4.14 shows a section of the head in sagittal (A), coronal (B) and transverse (C) views according to the materials.

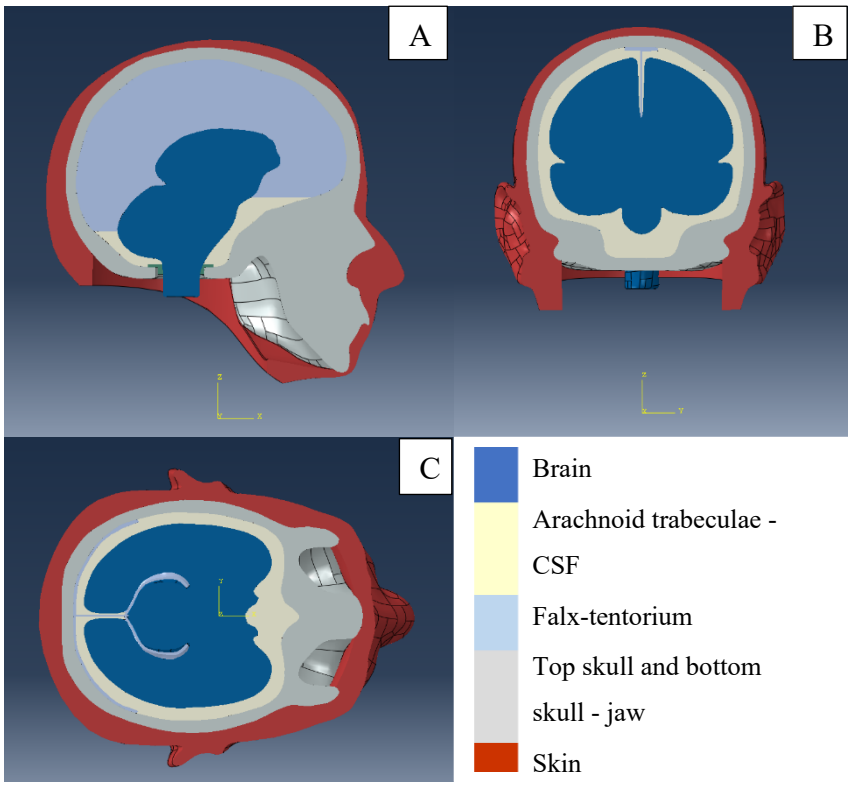


Figure 4.14 – (A) Sagittal, (B) coronal, and (C) transverse sections of the head instances according to the materials

Fig. 4.15 better highlights the head internal instances of the *Assembly*.

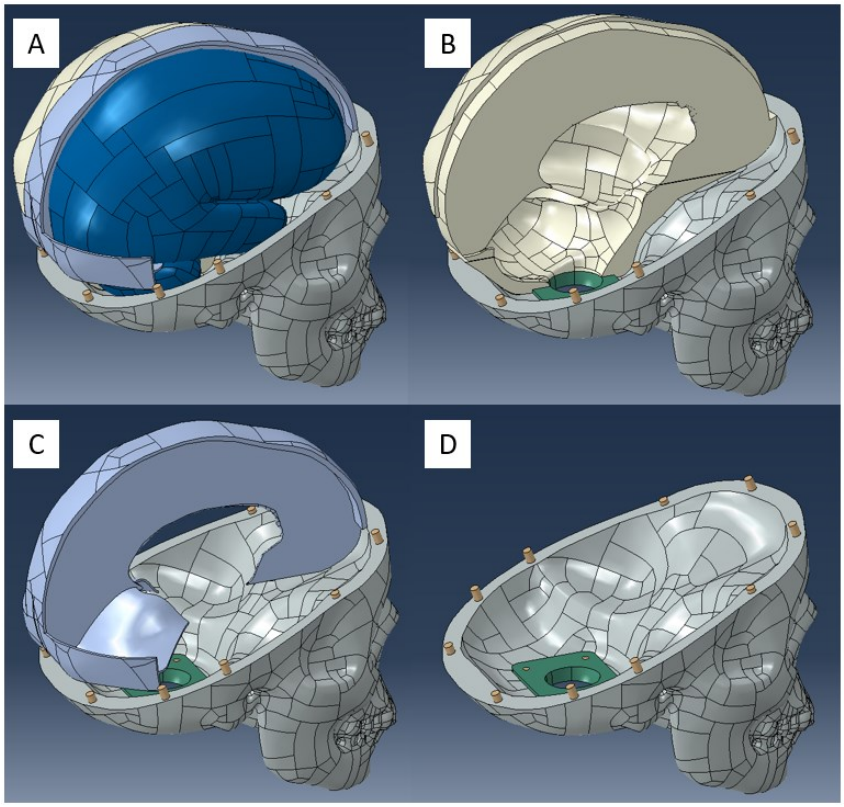


Figure 4.15 – Details of (A) brain, (B) left arachnoid trabeculae – CSF, (C) falx – tentorium, and (D) flange and grub screws

The floor instance was then created in the module *Assembly* (fig. 4.16).

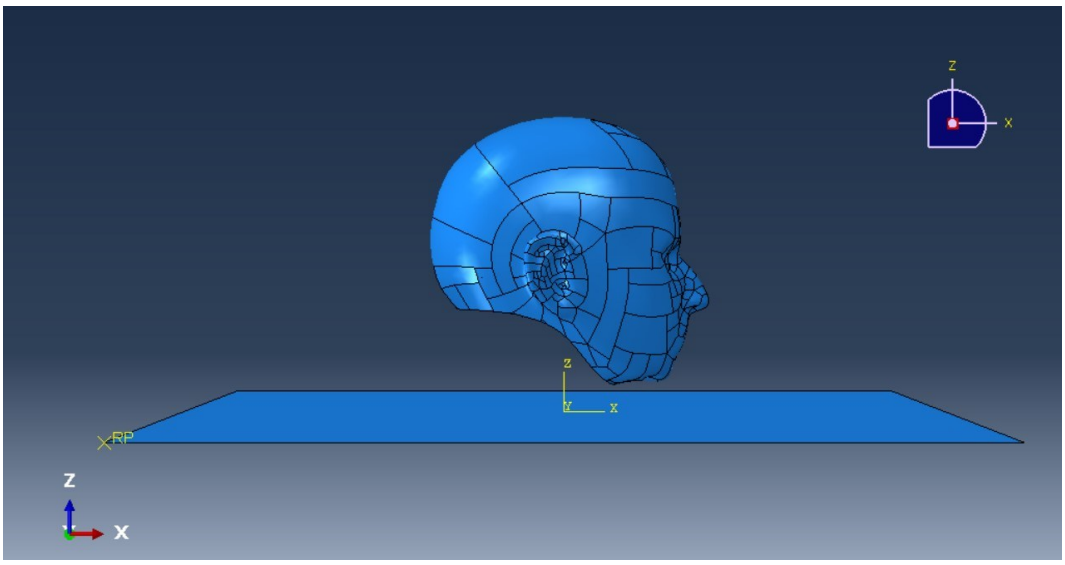


Figure 4.16 – Floor and head instances with default Assembly visualization

Subsequently, the head instances were rotated upside down (fig. 4.17) to simulate the drop test.

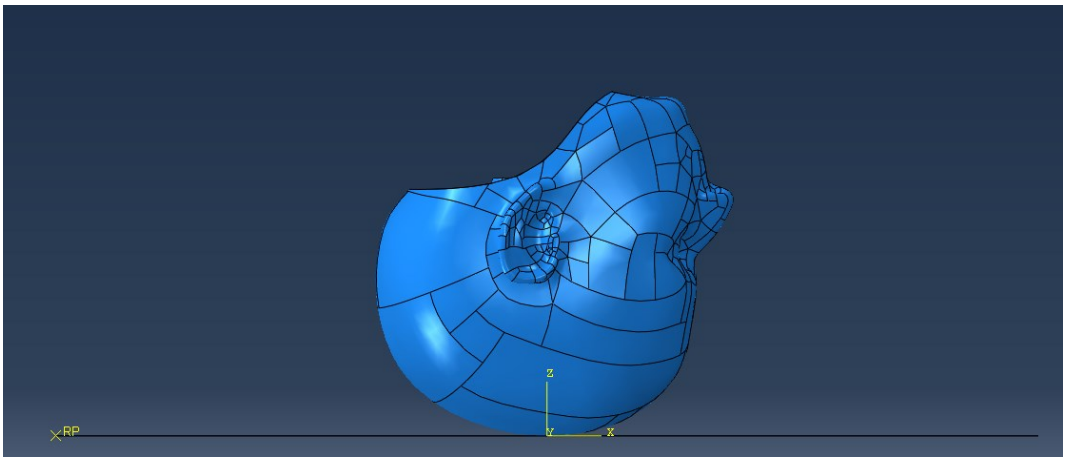


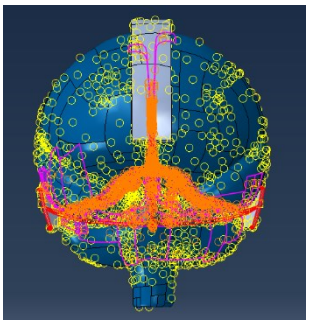
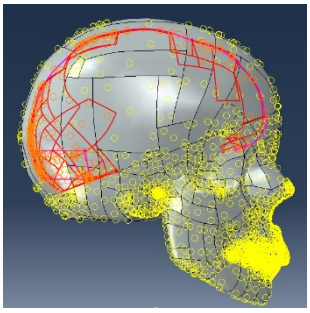
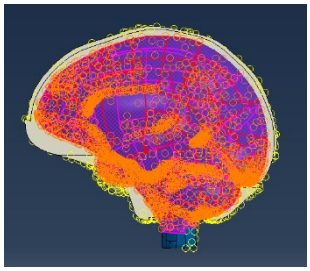
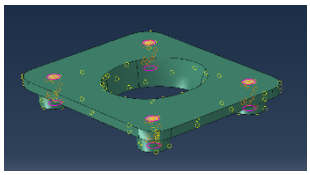
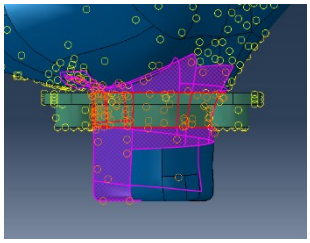
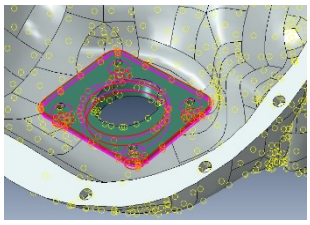
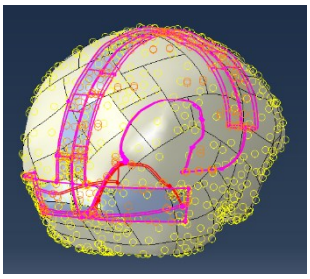
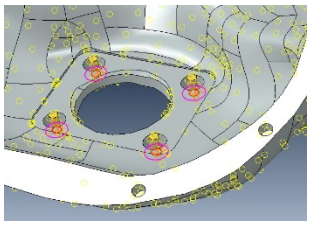
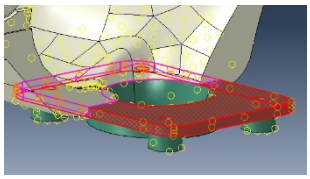
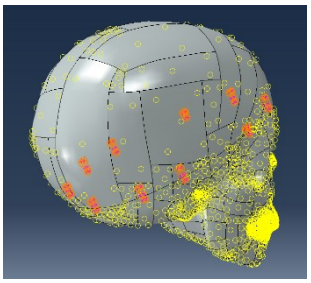
Figure 4.17 – The head rotated upside down

4.3.1.4 Step

A dynamic explicit *Step* was created to simulate the drop test, with a time period of 0,02 s.

4.3.1.5 Constraints and Interactions

The way the head instances are constrained to each other was then specified imposing Tie *Constraints* between couples of master (red) and slave (purple) surfaces belonging to the instances in table 4.5. Orange markers in the figures denote the Tie constraint imposed to simulate gluing among the respective surfaces of the couple.

Master surface	Slave surface	Figure	Master surface	Slave surface	Figure
Falx-tentorium	Brain		Top skull and bottom skull-jaw	Falx-tentorium	
Right and left arachnoid trabeculae-CSF	Brain		Flange grub screws	Flange	
Flange	Brain		Flange	Bottom skull-jaw	
Falx-tentorium	Right and left arachnoid trabeculae-CSF		Flange grub screws	Bottom skull-jaw	
Flange and grub screws	Right and left arachnoid trabeculae-CSF		Skull grub screws	Top skull and Bottom skull-jaw	

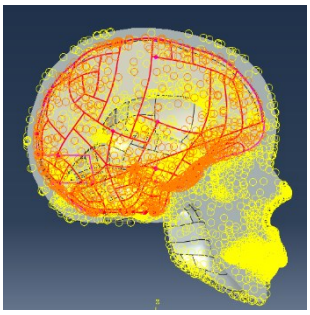
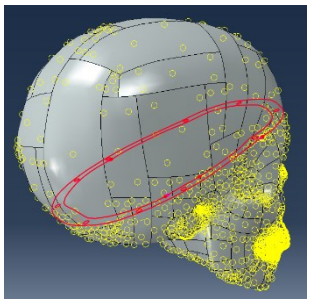
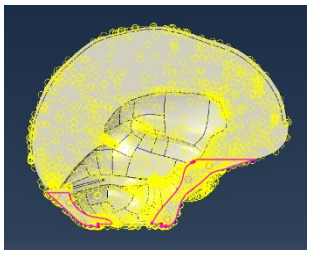
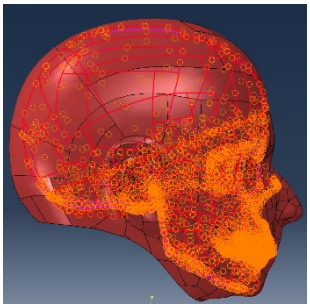
Top skull and Bottom skull-jaw	Right and left arachnoid trabeculae-CSF		Top skull	Bottom skull-jaw	
Right arachnoid trabeculae-CSF	Left arachnoid trabeculae-CSF		Top skull and Bottom skull-jaw	Skin	

Table 4.5 – Tie Constraints definition

To define the mechanism of the interaction between the scalp and the floor during the contact, a Contact *Interaction Property* with Tangential (Penalty) and Normal Behavior was created. This was required to specify a friction coefficient (0.45) and to prevent interpenetration between the scalp and the floor. A General contact (Explicit) *Interaction* was then created to define the Contact domain (selected surface pairs in fig. 4.18) and to assign the *Interaction Property* previously created.

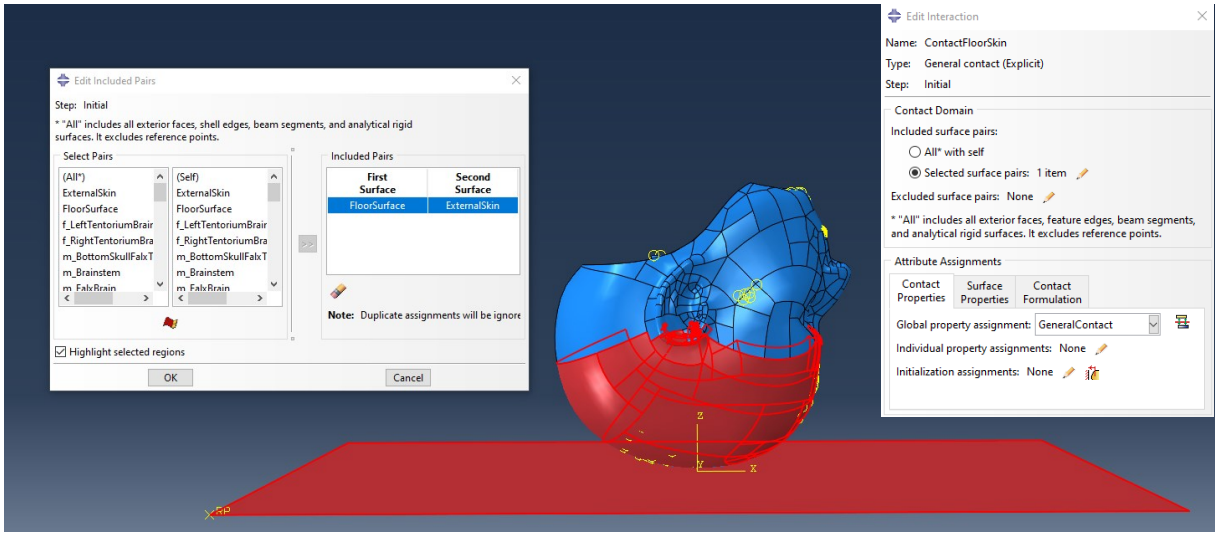


Figure 4.18 – General contact (Explicit) Interaction between scalp and floor surfaces

4.3.1.6 Boundary conditions (*BCs*)

An ENCASTRE was imposed on the floor Reference Point to lock it in position since the Initial step, as shown in fig. 4.19.

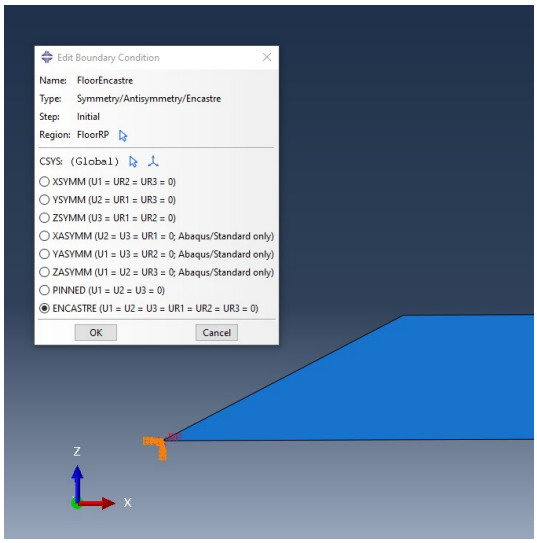


Figure 4.19 – ENCASTRE imposed on the floor Reference Point

4.3.1.7 Mesh

The *Mesh* of the head instances was created using tetrahedral explicit linear elements (C3D4: *4-node linear tetrahedron*), with the only execption for incompressible instances, for which it was used hybrid formulation (C3D4H elements). For this first simulation, it was chosen to assign a Global Seed of 5 mm. For future refinements of the model, this will possibly be locally modified (using a Local Seed) where the number of finite elements should be imposed according to edges thickness and radius of curvature.

The floor was meshed using quad-dominated explicit discrete rigid linear elements (R3D4: *4-node 3-D bilinear rigid quadrilateral*) with a Global Seed of 20 mm.

Table 4.6 reports the total number of nodes and elements in the whole *Assembly*, specifying the element types and their count.

Mesh Statistics

Summary

Total number of nodes: 71778

Total number of elements: 309648

Details

By Instance | By Element Type

	Element Type	Element Shape	Geometric Order	Elements
1	C3D4H	tetrahedral	linear	224558
2	C3D4	tetrahedral	linear	84190
3	R3D4	quadrilateral	linear	900

Table 4.6 – Report of the nodes and element number in the model

Fig. 4.20 A shows the head and the floor mesh, while fig. 4.20 B/C/D presents some internal views.

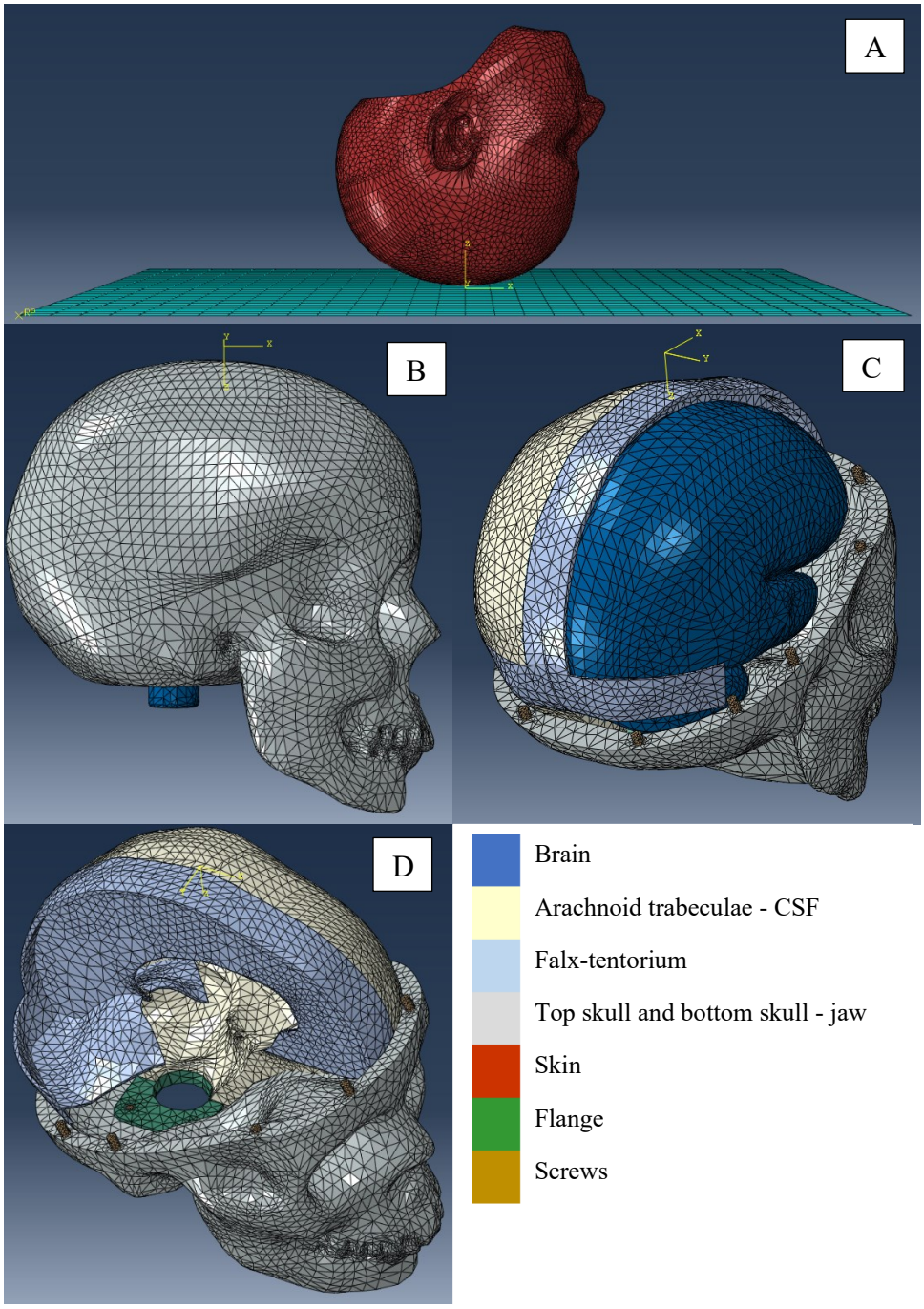


Figure 4.20 - Details of (A) skin and floor, (B) top skull and bottom skull – jaw, (C) internal instances after removing the top skull, (D) falx – tentorium, left arachnoid trabeculae – CSF, flange and grub screws mesh

4.3.1.8 Predefined Field

It was chosen to simulate a drop test from a height of 0.2 m. To reduce the time for the analysis, the simulation was relative only to the last 2.5 mm of free fall. For this reason, the head was translated along the vertical z-axis by 2.5 mm and a velocity was set in the initial step. This initial velocity was determined by considering the initial fall height $h = 0.2\ m$ and the height $h_0 = 0.0025\ m$ to which the beginning of the simulation corresponds, resulting in an already

$h - h_0$ travelled distance in free fall. Hence, a Velocity *Predefined Field* was created with a component along the z-axis equal to:

$$V3 = -\sqrt{2g(h - h_0)} = -\sqrt{2 \cdot 9.81 \cdot (0.2 - 0.0025)}\ ^{m}/_{s} = -1.96849\ ^{m}/_{s} = -1968.49\ ^{mm}/_{s}$$

This initial velocity was assigned to the head nodes as shown in fig. 4.21.

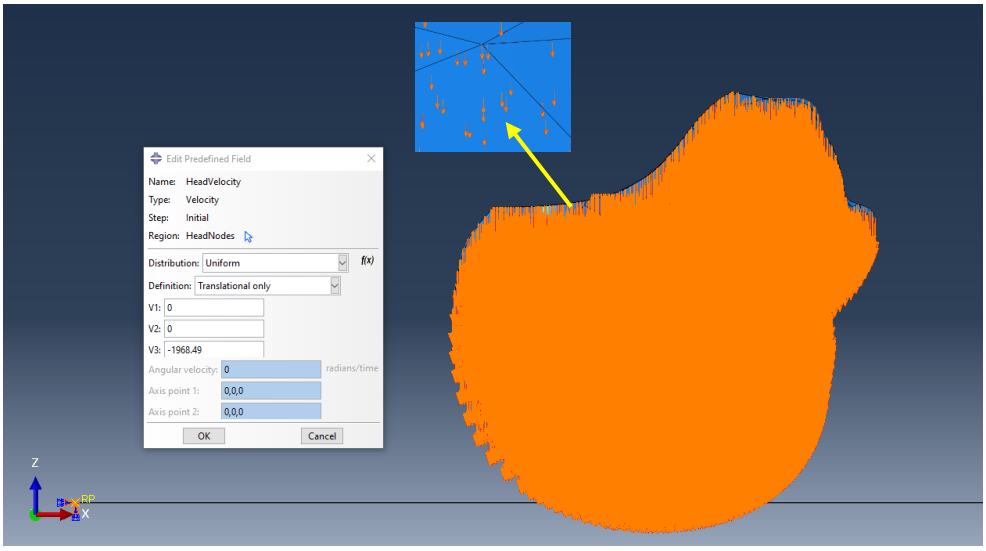


Figure 4.21 – Predefined field definition with orange arrows indicating the velocity vectors assigned to each node of the head, called HeadNodes in the Edit panel

4.3.1.9 Loads

A Gravity acceleration of -9810 mm/s^2 was then applied at the Dynamic step, as shown in fig. 4.22.

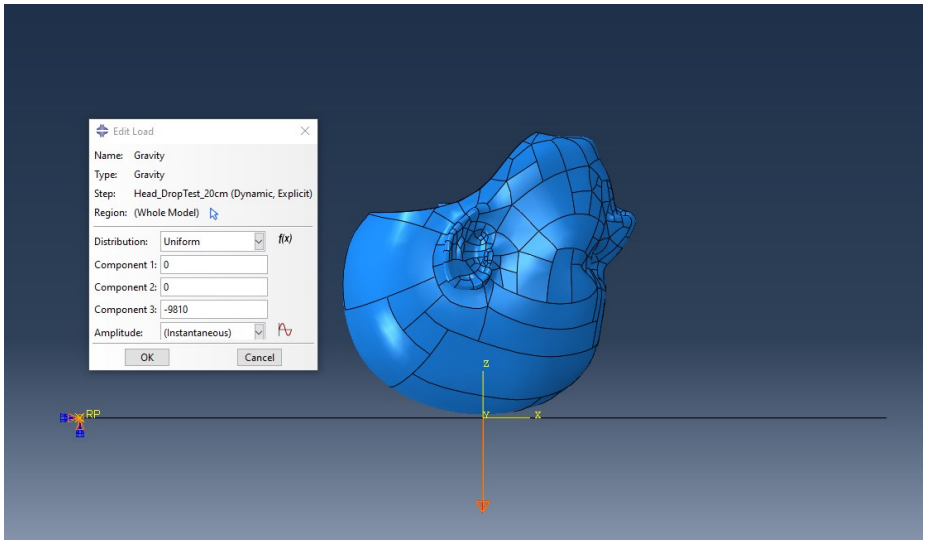


Figure 4.22 – Gravity acceleration definition

4.3.1.10 Summary of mass properties

A local reference system was created with the origin in the right external acoustic meatus (EAM), having the x-axis lying forward in the Frankfurt plane[3], the z-axis normal to the Frankfurt plane directed upwards with respect to the head (opposite to the global z-axis), and the y-axis lying in the Frankfurt plane according to the right-hand rule. Fig. 4.23 shows the skull with the local reference system.

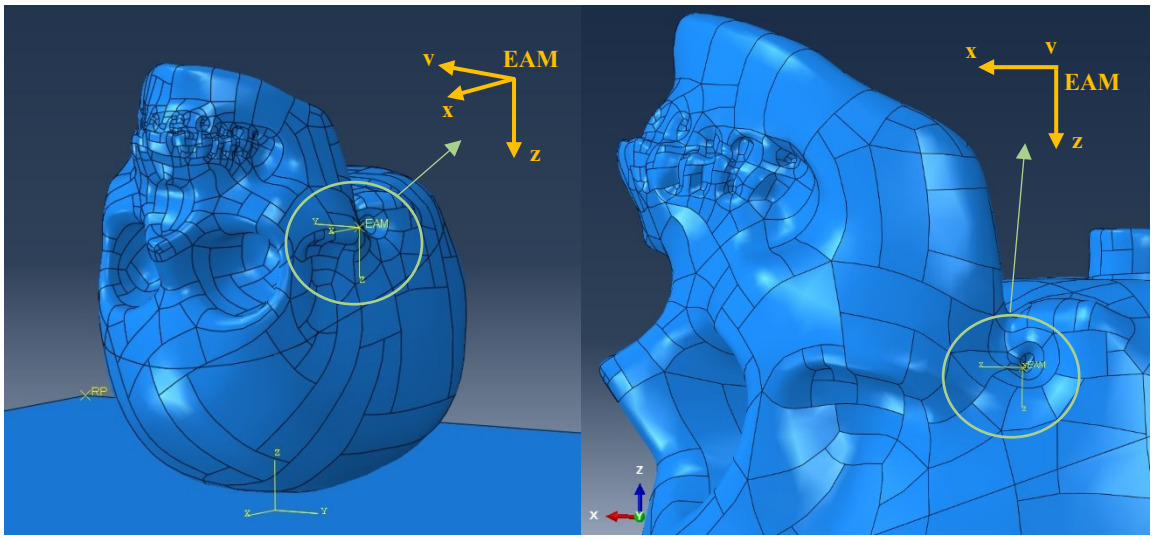


Figure 4.23 – Local reference system with the origin in the EAM

Table 4.7 reports the mass, the density and the position of the center of mass (CoM) of each anatomical district with respect to the local reference system.

Surrogate	**Mass [t]**	**Density [t/mm^3]**	**CoM coordinates (x, y, z) [mm]**
Brain	0.00111	1.15604E-09	(-15.46, 47.50, 50.88)
Right and left trabeculae-CSF	3.96E-04	1E-09	(-12.34, 46.41, 49.02)
Falx-tentorium	3.36E-05	1.07406E-09	(-22.83, 47.08, 62.24)
Top-Bottom skull	8.17E-04	8.69772E-10	(10.11, 47.11, 24.86)
Skin	9.51E-04	1.08726E-09	(-13.72E-03, 43.94, 19.04)

Table 4.7 – Summary of mass properties of each anatomical surrogate

Figure 4.24 shows the CoM of the anatomical surrogates and the CoM of the whole model, including also the connection components.

[3] Frankfurt plane: it is a plane passing through the highest point of the upper margin of the openings of the external auditory canals (external acoustic meati) and the lowest point of the lower margin of the left orbit. In a healthy individual in an upright position this plane is normally horizontal

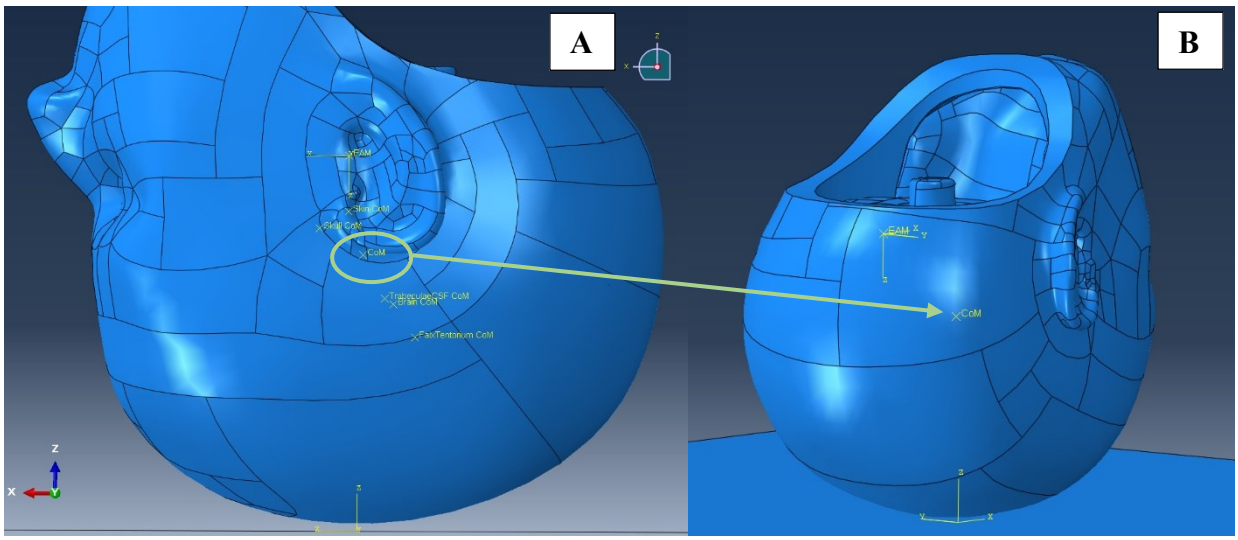


Figure 4.24 – (A) CoM of the anatomical surrogates and CoM of the whole model; (B) detail of the CoM of the whole model

Table 4.8 reports the position of the whole model CoM with respect to the local reference system with the origin in the EAM, along with the mass and the moment of inertia about the EAM.

Mass [t]	**CoM coordinates (x, y, z) [mm]**	**Moment of inertia about the EAM (Ixx, Iyy, Izz, Ixy, Iyz, Izx) [kg·m^2]**
0.00339	(-4.87, 46.28, 34.13)	(30.50E-03, 26.93E-03, 19.38E-03, 0.478E-03, 9.27E-03, -1.97E-03)

Table 4.8 – Inertial properties of the whole model

As shown in table 4.8, the whole head surrogate weights 3.39 kg. This value differs by:

- 25.71% with respect to HEAD-BRAIN FE Model
- 34.43% with respect to ULP FEM
- 16.76% with respect to UCDBTM
- 15.76% with respect to UNIPD adult male model
- 6.29% with respect to UNIPD adult female model
- 2.33% with respect to UNIPD young male model

4.3.1.11 Job

It was then generated the input file to be submitted for analysis.

4.3.2 Processing

The .inp file was sent to the processor for analysis, with the contribution of CAPRI ("Calcolo ad Alte Prestazioni per la Ricerca e l'Innovazione" of the University of Padua). To reduce the time required for the analysis, it was chosen to perform a preliminary drop test of the right half of the head surrogate, described in the next chapter.

Future developments will include the simulation of the drop test of the whole head.

Chapter 5: Drop test simulations

Considering the complexity of the head surrogate model, it was decided to perform some preliminary drop test simulations by simplifying the geometry of the various parts composing the prototype.

5.1 PlatSil Gel-10 (skin simulant material) ball drop test simulation

As seen in par. 2.4.2, for the silicone rubber used to make the skin of the head prototype (PlatSil Gel-10 1A:1B), no DMA simulations were carried out in Abaqus. The viscoelastic constitutive parameters (see table 2.13) were chosen only on the basis of the fit of the shear storage and loss moduli as function of the frequency with respect to the experimental curves (see fig. 2.53 and fig. 2.54). Therefore, a sphere of PlatSil Gel-10 1A:1B with a diameter of 69 mm was cast and a triaxial accelerometer (Analog Devices ADXL377, full-scale range of ±200 g) was embedded in its centre of mass (fig. 5.1 A/B). This sphere was then used to perform some drop tests from different heights (20, 30, 40, 50 and 60 cm) on a force platform equipped with a uniaxial load cell (Futek LCF455 FSH 04320, full-scale range of 44.4822 kN) shown in fig. 5.1 C.

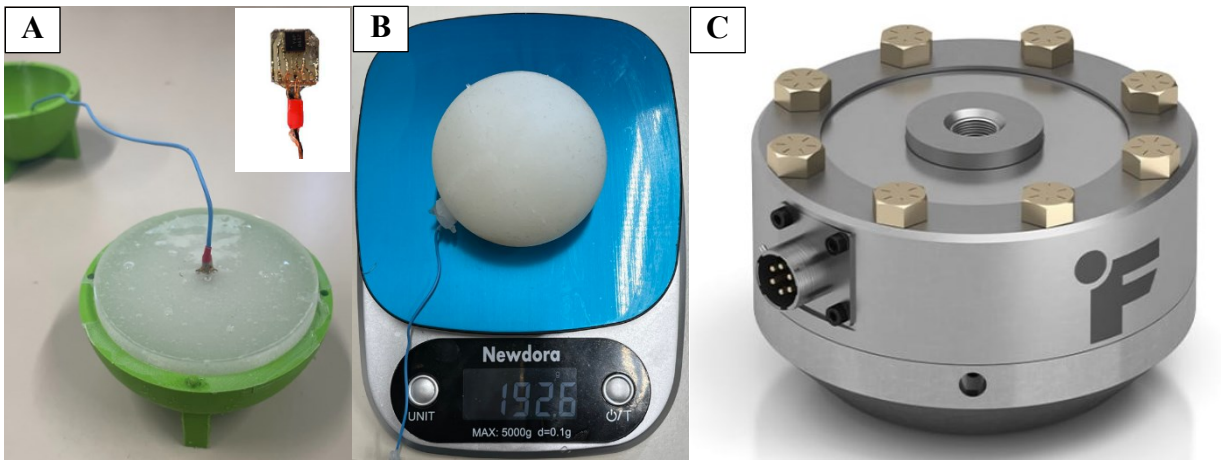


Figure 5.1 – (A) PlatSil Gel-10 ball during the casting process with the embedded accelerometer, (B) weighing of the ball, (C) load cell

Among the tests, the analysis and the numerical simulation of the 30 cm fall is described below. The accelerometer and the load cell output signals were analysed to compute the following values (fig. 5.2 and table 5.1):

- peak of the resultant acceleration in the CoM
- peak of the contact force
- contact time

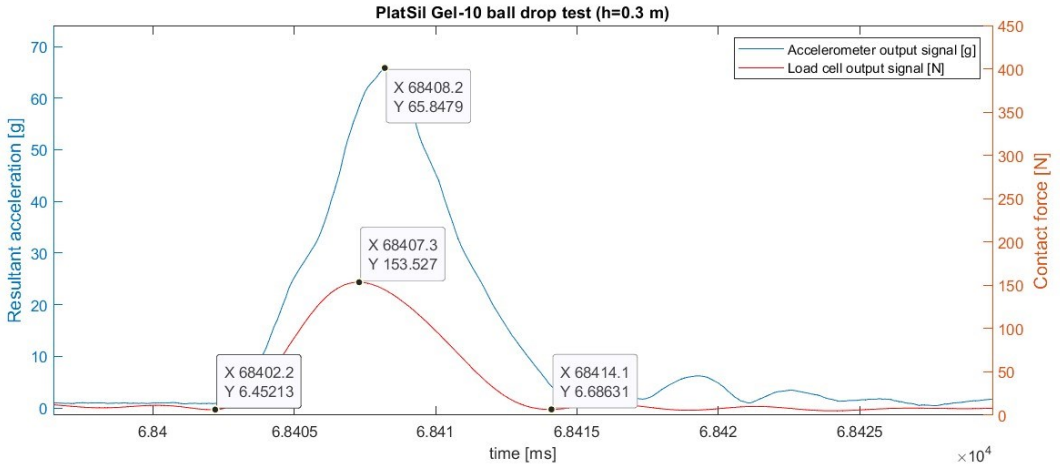


Figure 5.2 – Output of accelerometer and load cell

Peak of the resultant acceleration [g]	Peak of the contact force [N]	Contact time [ms]
65.8479	153.527	11.9

Table 5.1 – Experimental results computed from the accelerometer and load cell output signals: peak of the resultant acceleration, peak of the contact force, and contact time

Fig. 5.3 shows the first contact, the ball reaching the maximum lateral deformation, and the last contact before bouncing.

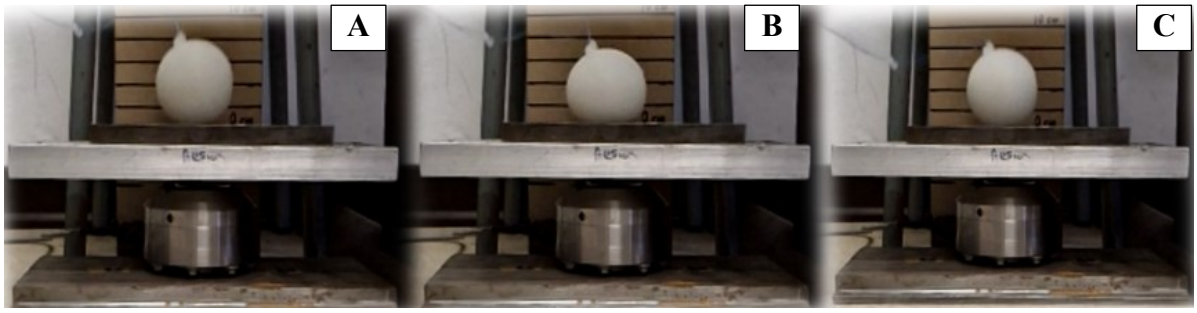


Figure 5.3 – PlatSil Gel-10 ball drop test: (A) first contact, (B) maximum lateral deformation, (C) last contact

This drop test was then simulated in Abaqus to verify the suitability of the viscoelastic constitutive parameters in table 2.18 by comparing the computed peak of the resultant acceleration in the CoM, the computed peak of the contact force and the computed contact time with the experimental results.

5.1.1 Pre-processing

Parts

A deformable *Part* representing a section of the ball was created using Abaqus Axisymmetric modeling space to reduce analysis time. The section was then partitioned (fig. 5.4 A) to vary the mesh seed along it. A floor was then created as Axisymmetric Discrete Rigid *Part* and it was assigned a Reference Point (fig. 5.4 B).

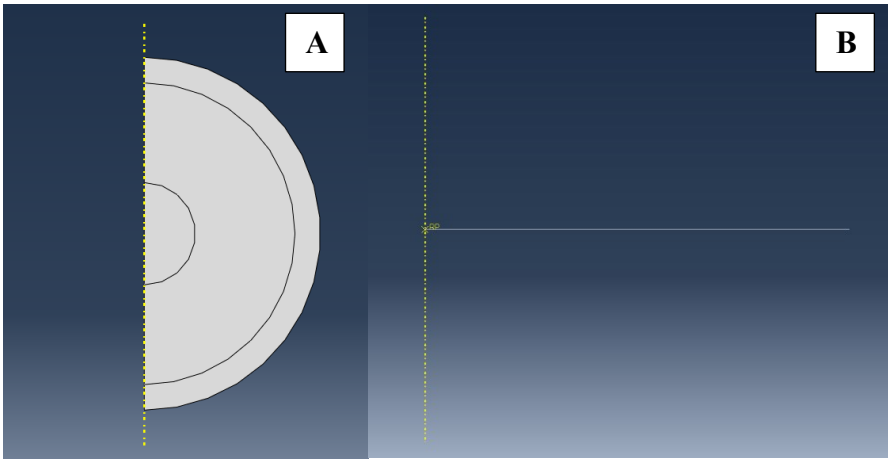


Figure 5.4 – (A) Partition of the ball Part section, (B) Floor Part with the Reference Point

Material and Section

As shown in fig. 5.5 A, the density of the silicone rubber was established considering the mass (192.6 g = $192.6 \cdot 10^{-6}$ t) and the volume ($0.000172 \cdot 10^{9}$ mm^3) of the physical surrogate. Visco-hyperelastic behaviour (fig. 5.5 B/C) was defined by the hyperelastic and viscoelastic (see table 2.18) constitutive parameters identified in par. 2.4.2 for the skin simulant material.

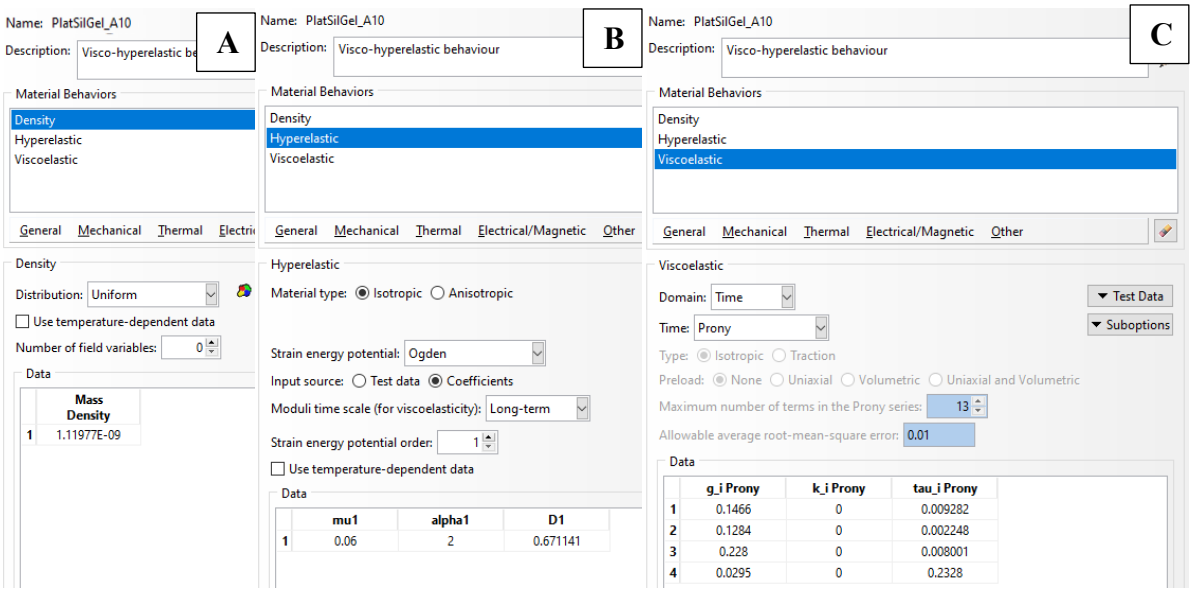


Figure 5.5 - Skin simulant material properties: (A) density, (B) hyperelastic behaviour, (C) viscoelastic behaviour

The *Section* was then created and assigned to the ball *Part*.

Assembly

Ball (made of the skin simulant material) and floor instances were then created in the *Assembly* module. To reduce the time for the analysis, as for the head drop test simulation described in par. 4.3.1, the simulation was relative only to the last 2.5 mm of free fall. For this reason, the ball was translated along the vertical y-axis by 2.5 mm (fig. 5.6).

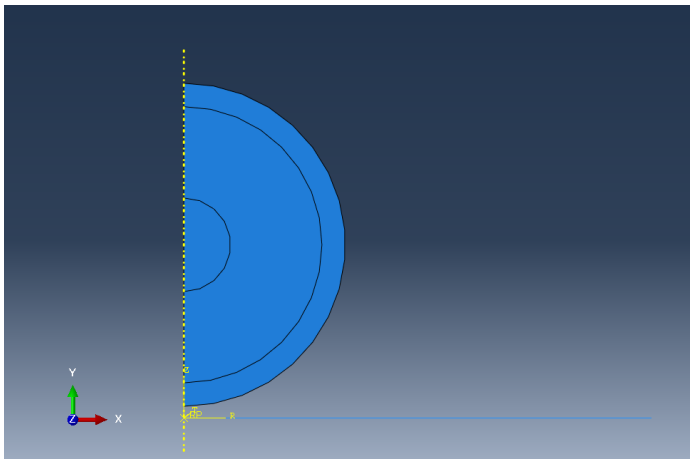


Figure 5.6 – Assembly module: Ball and floor instances after the translation of the ball instance along the vertical y-axis by 2.5 mm

Step

A dynamic explicit step was created to simulate the drop test, with a time period of 0.02 s.

Interaction

To define the mechanism of the interaction between the ball and the floor during the contact, a Contact *Interaction Property* with Tangential (Penalty) and Normal Behavior was created. This was required to specify a friction coefficient (0.45) and to prevent interpenetration between the ball and the floor. A General contact (Explicit) *Interaction* was then created to define the Contact domain (selected surface pairs in fig. 5.7) and to assign the *Interaction Property* previously created.

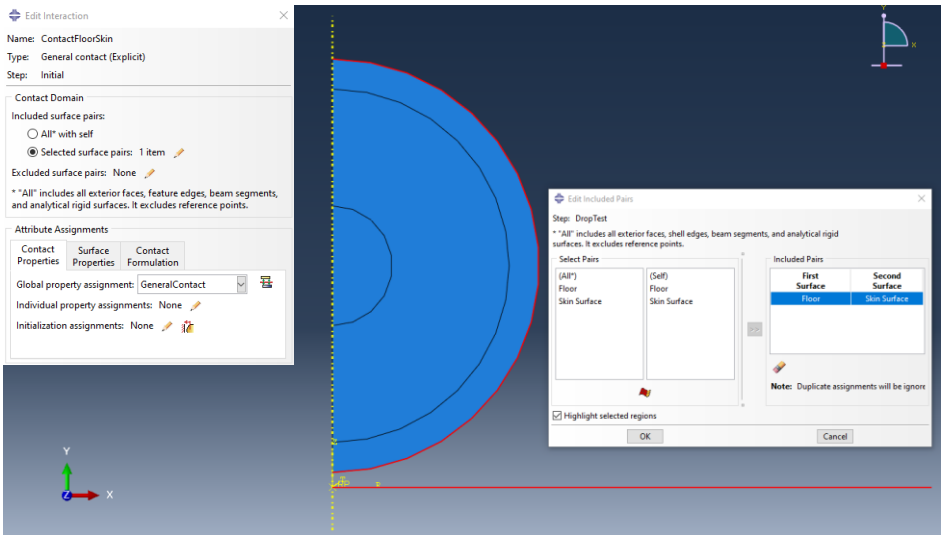


Figure 5.7 - General contact (Explicit) Interaction between ball (skin) and floor surfaces

Boundary conditions (BCs)

An ENCASTRE was imposed on the floor Reference Point to lock it in position since the Initial step, as shown in fig. 5.8.

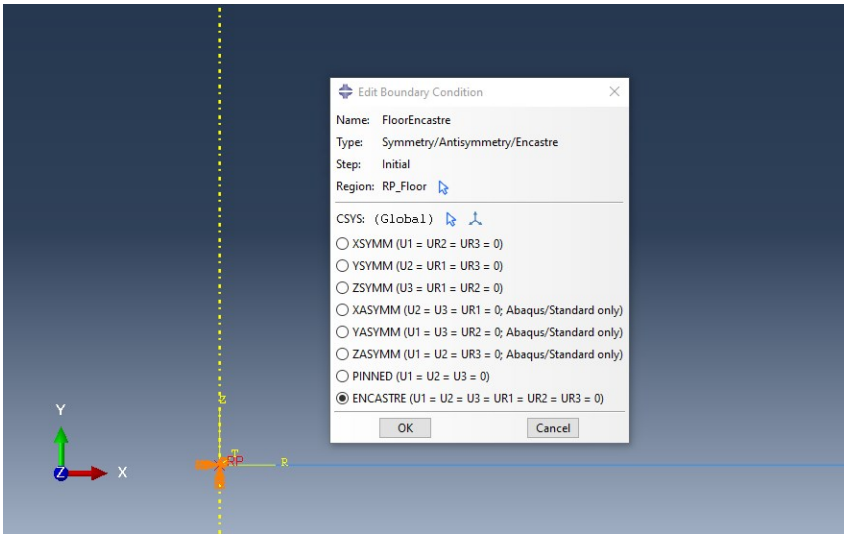


Figure 5.8 - ENCASTRE imposed on the floor Reference Point

Moreover, a *Symmetry* (XSYMM) was imposed on the ball (skin) red edges in figure 5.9 to lock the movement along x-axis.

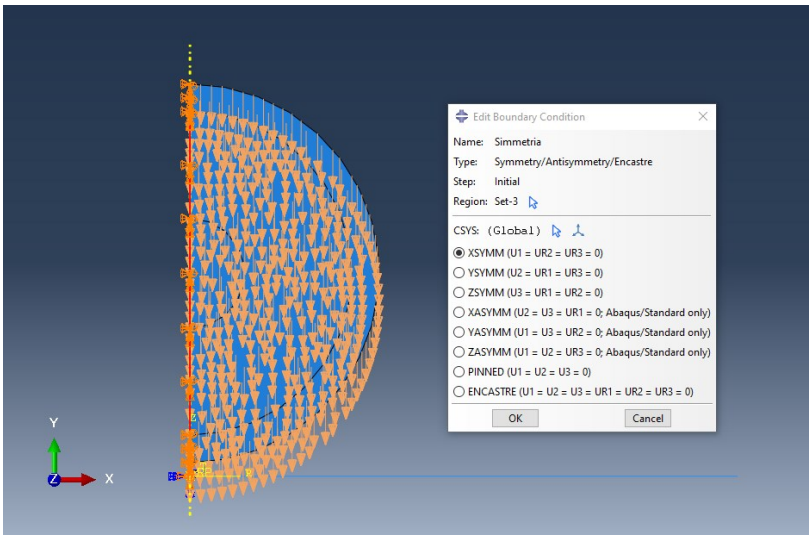


Figure 5.9 – Symmetry (XSYMM) imposed on the ball section edges along the vertical y-axis (red in figure)

Mesh

The *Mesh* of the ball (skin) section (fig. 5.10 A) was created using Axisymmetric Explicit Linear Quad elements (CAX4R*: 4-node bilinear axisymmetric quadrilateral, reduced integration*). It was imposed a mesh seed on edges (*by number*), increasing the number of elements:

- in the outer area, in part involved in the contact with the floor
- in the central area, where the accelerometer is placed in the physical ball

The floor (fig. 5.10 B) was meshed using Explicit Discrete Rigid Linear elements (RAX2: *2-node linear axisymmetric rigid link*) with a Global Seed of 10 mm.

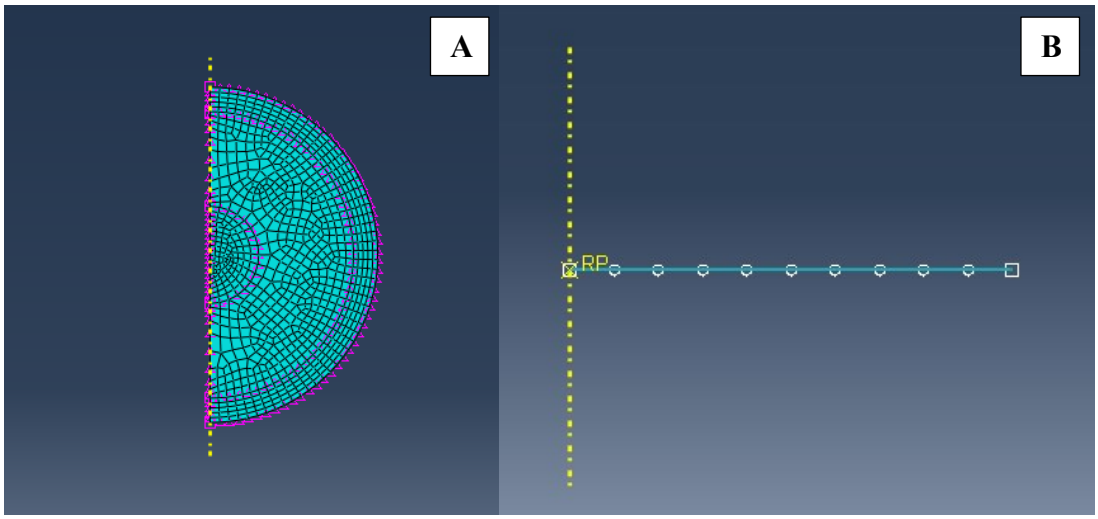


Figure 5.10 – (A) Ball (skin) mesh seed, (B) floor mesh seed

Table 5.2 reports the total number of nodes and elements in the whole *Assembly*, specifying the element types and their count.

Mesh Statistics

Summary

Total number of nodes: 894

Total number of elements: 839

Details

By Instance | By Element Type

	Element Type	Element Shape	Geometric Order	Elements
1	RAX2	line	linear	10
2	CAX4R	quadrilateral	linear	829

Table 5.2 - Report of the nodes and elements number in the model

Predefined Fields

As mentioned above, the simulation was relative only to the last 2.5 mm of free fall. To impose the correct initial velocity, the recorded video of the actual drop test was analysed to quantify the exact initial fall height, that was $h = 28.96\ cm = 0.2896\ m$. As for the whole head model, a velocity was set in the initial step. This initial velocity was determined by considering the initial fall height $h = 0.2896\ m$ and the height $h_0 = 0.0025\ m$ to which the beginning of the simulation corresponds, resulting in an already $h - h_0$ travelled distance in free fall. Hence, a Velocity *Predefined Field* was created with a component along the y-axis equal to:

$$V2 = -\sqrt{2g(h - h_0)} = -\sqrt{2 \cdot 9.81 \cdot (0.2896 - 0.0025)}\ {}^{m}/_{s} = -2.37337\ {}^{m}/_{s} = -2373.37\ {}^{mm}/_{s}$$

This initial velocity was assigned to the ball section nodes as shown in fig. 5.11.

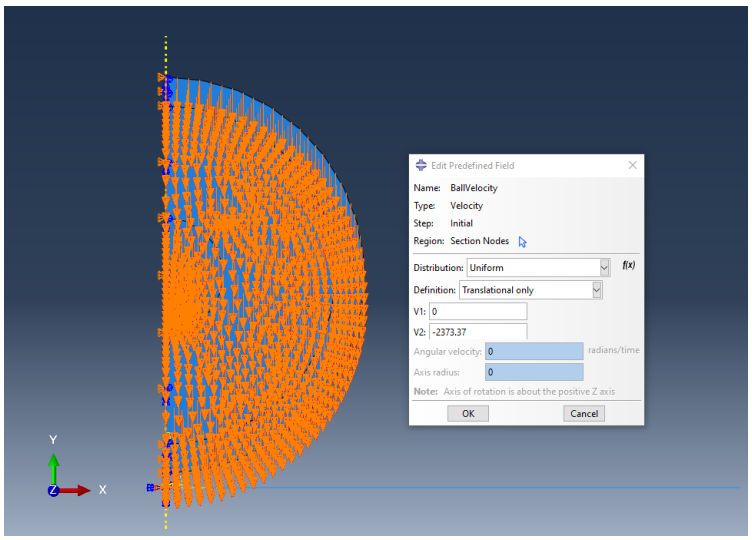


Figure 5.11 - Predefined field definition with orange arrows indicating the velocity vectors assigned to each node of the ball section, called Section Nodes in the Edit panel

Loads

A Gravity acceleration of -9810 mm/s^2 was then applied at the Dynamic step, as shown in fig. 5.12.

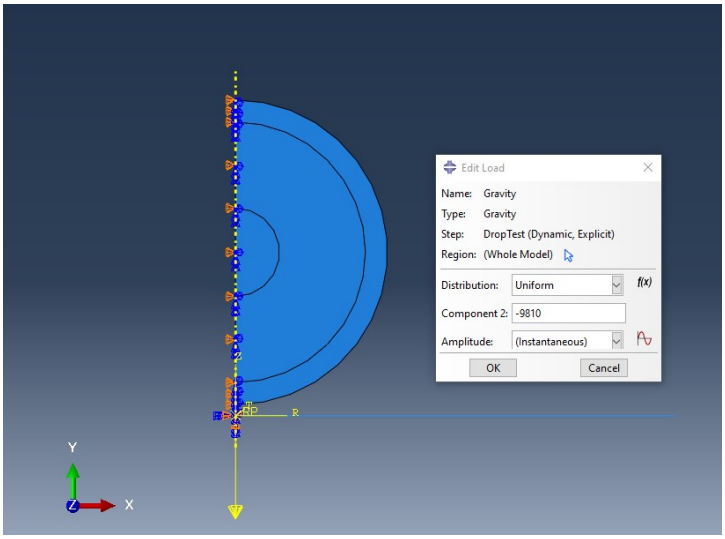


Figure 5.12 - Gravity acceleration assignment

Job

It was then generated the input file to be submitted for analysis.

5.1.2 Processing

The input file (.inp) was sent to the processor for analysis.

5.1.3 Post-processing

The .odb file was then opened to analyse the results. Fig. 5.13 shows the ball in its initial position (2.5 mm far from the floor). Figure 5.14 shows the first contact, the ball reaching the maximum lateral deformation, and the last contact before bouncing in the simulation.

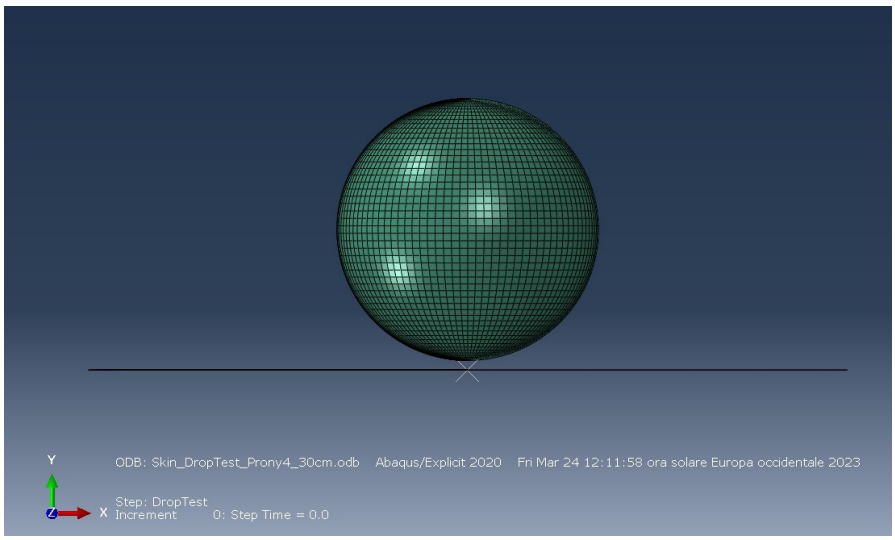


Figure 5.13 – Ball (PlatSil Gel-10) at the beginning of the simulation: 2.5 mm far from the floor

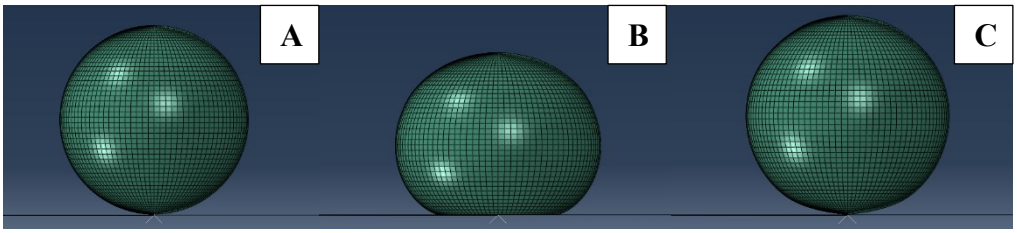


Figure 5.14 - PlatSil Gel-10 ball drop test: (A) first contact, (B) maximum lateral deformation, (C) last contact

The contact force was computed and the raw signal was filtered (fig. 5.15). The raw acceleration along the vertical axis (y) in the ball centre of mass was then computed. This raw signal was then filtered (fig. 5.16), obtaining the only non-zero component of the resultant acceleration (the symmetry boundary condition and the axysimmetry in the model prevent every lateral movement of the falling ball).

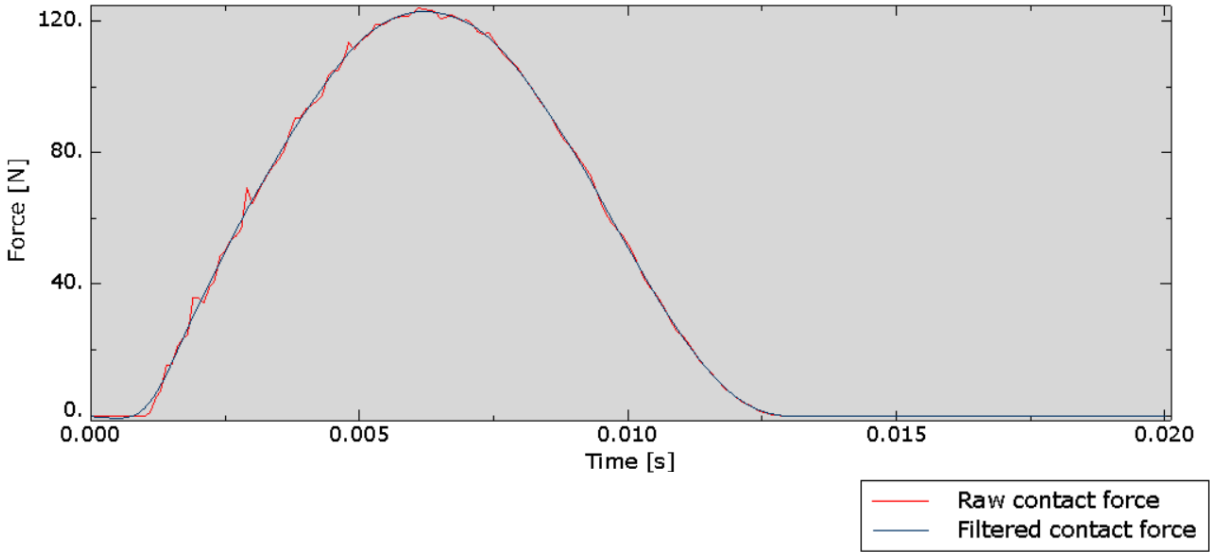


Figure 5.15 – Raw and filtered contact force from the simulation

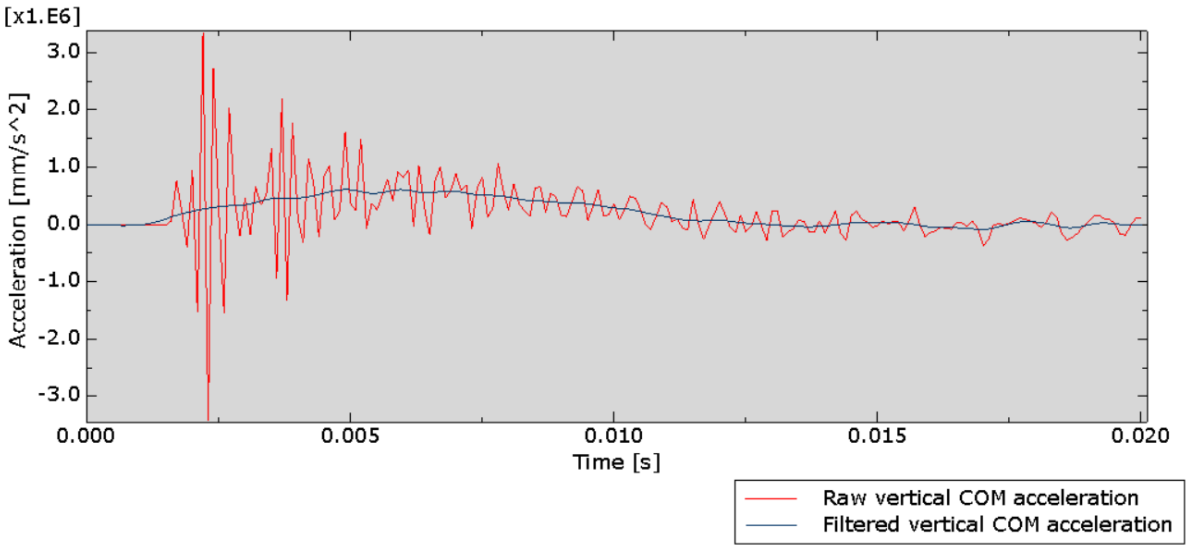


Figure 5.16 – Raw and filtered vertical acceleration of CoM from the simulation

Fig. 5.17 shows the plots of the filtered signals, related to the contact force and to the acceleration of the CoM respectively.

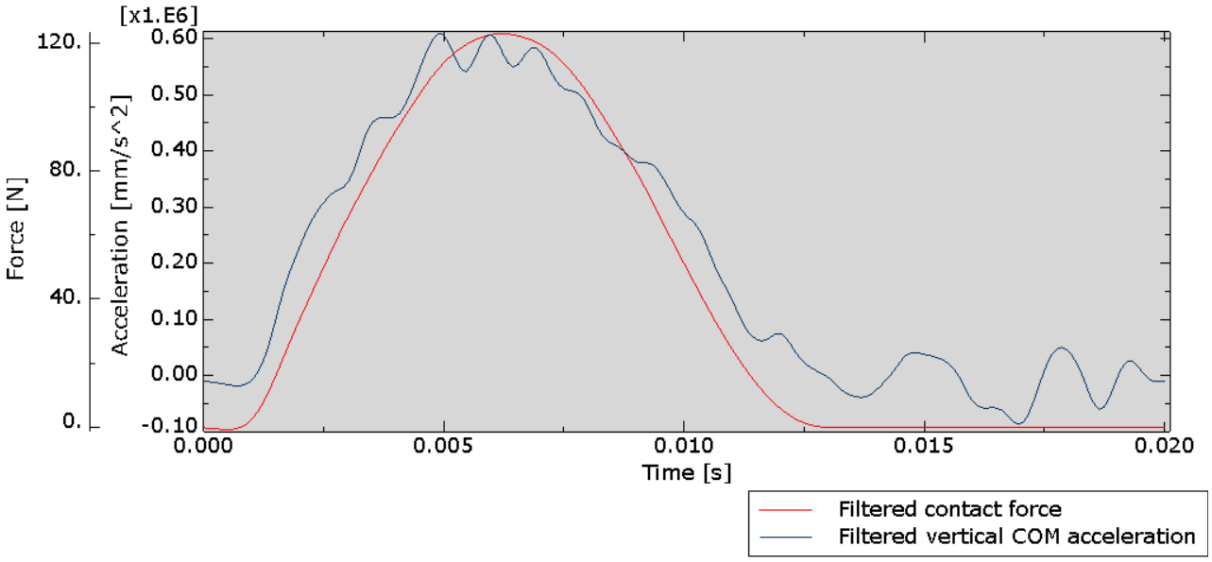


Figure 5.17 – Plots of filtered signals of contact force and simulated CoM acceleration

A comparison between experimental data and the results of the numerical simulation is given in table 5.3.

	Experimental	Numerical	Percentage change
Contact time	11.900 ms	11.798 ms	-0.86%
Peak of the contact force	153.527 N	122.870 N	-19.97%
Peak of the CoM acceleration	65.848 g	60.955 g	-7.43%

Table 5.3 – Experimental vs computed contact time, peak of the contact force and peak of the CoM acceleration with the respective percentage change

As shown in table 5.3, the load cell output is almost equal to the simulation finding in terms of contact time, while the computed contact force underestimates the actual value measured by

the force platform by -19.97%. Moreover, the acceleration in the CoM resulting from the numerical analysis is close to the experimental data recorded by the triaxial accelerometer, showing a percentage decrease of 7.43 %.

5.2 Drop test simulations of a simplified head surrogate

In parallel, numerical simulations of drop tests from different heights (0.2 and 0.5 m) were carried out, modeling a set of concentric hollow spheres representing the main districts of the head surrogate (brain, arachnoid trabeculae-CSF, skull, skin) to simplify the complex geometry of the prototype.

The aim of these trials was to get some preliminary information about the behaviour of the different materials when they interact, preparing a simplified model in view to test the physical prototype model.

5.2.1 Preliminary simulations to optimize the mesh

Initially, three drop tests from 0.5 m height were simulated varying the number of elements along the thickness of the hollow spheres to optimize the mesh. The three scenarios considered:

- 1 finite element along the thickness
- 2 finite elements along the thickness
- 4 finite elements along the thickness

In general, a more accurate solution is produced using a finer mesh. Despite this, the analysis time required in the processing phase increases when a mesh is refined. In order to balance the accuracy and the processing resources, it's possible to start performing a first analysis generating a mesh using less elements as possible. Then, these results can be compared to the findings of a second analysis performed increasing the number of elements to densify their distribution. Further analyses can be performed while densifying the mesh till the results reasonably converge [Autodesk documentation]. In this case, three analyses were performed.

For these early trials, only the contribution of the trabeculae in the subarachnoid space was considered, neglecting the cerebrospinal fluid.

5.2.1.1 Pre-processing

Parts, Materials and Sections

Brain, arachnoid trabeculae, skull and skin deformable *Parts* were created using Abaqus Axisymmetric modeling space to reduce analysis time. A floor was then created as Axisymmetric Discrete Rigid Part and it was assigned a Reference Point. The brain sphere section was partitioned to vary the mesh seed along it. Each half sphere section was assigned a *Section* with material parameters obtained from the mechanical characterization of the materials used in the physical head prototype. For detailed specs of the *Materials* refer to par. 4.3.1. The

only difference regards the subarachnoid space simulant material: as mentioned before, for these first analyses it was chosen to simulate the open-cell polymer foam 30 PPI, neglecting the CSF. Hence, stress-strain curves obtained from uniaxial compression and normal traction tests (see fig. 2.53 B/D in par. 2.3.1) were inserted as test data to define the Hyperfoam behaviour in Abaqus (fig. 5.18 A). *Evaluate* option was used to identify constitutive parameters defining the foam behaviour, and stability was satisfied for all strains (fig. 5.18 B). Fig. 5.19 reports the density of the foam [t/mm^3] and the constitutive parameters resulting from *Evaluate* option.

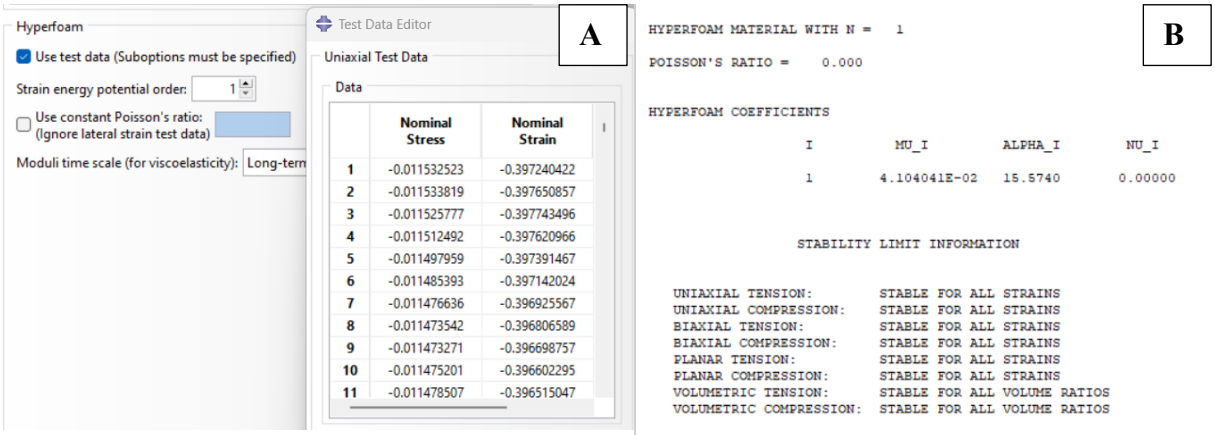


Fig. 5.18 – 30 PPI open-cell foam behaviour: (A) quasi-static compressive and normal traction uniaxial Test Data obtained from the mechanical characterization; (B) hyperfoam constitutive parameters resulting from Evaluate option

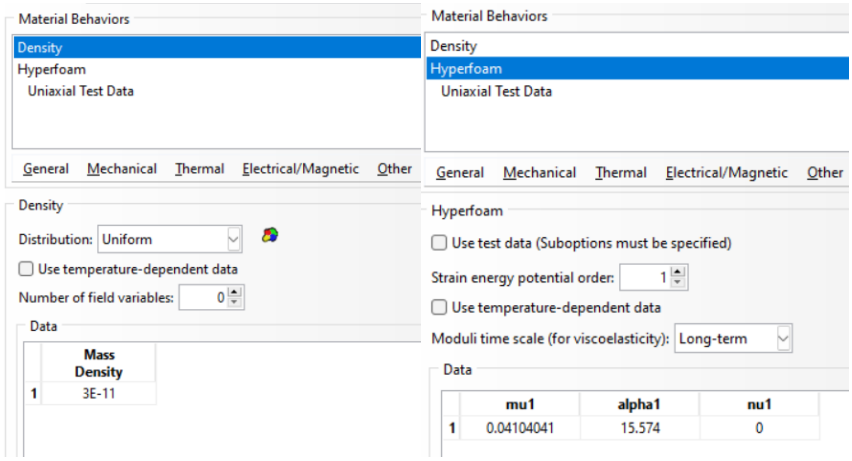


Figure 5.19 – Open-cell foam Material definition

Assembly

Instances were then created in the *Assembly* module. To reduce the time for the analysis, as for the head drop test simulation described in par. 4.3.1, the simulation was relative only to the last 2.5 mm of free fall. For this reason, the spheres representing brain, arachnoid trabeculae, skull, and skin were translated along the vertical y-axis by 2.5 mm (fig. 5.20).

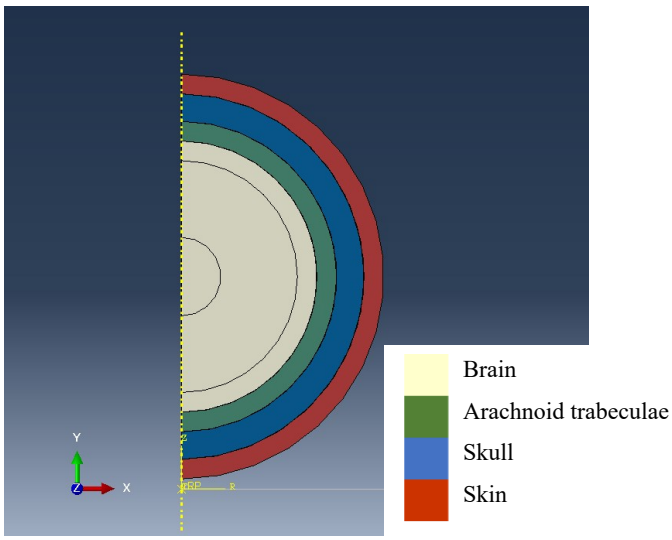


Figure 5.20 – Assembly module after the translation of the sphere instances along the vertical y-axis by 2.5 mm

Step

A dynamic explicit step was created to simulate the drop test, with a time period of 0,02 s.

Constraints and interaction

A Tie Constraint was created to simulate gluing between brain and arachnoid trabeculae, arachnoid trabeculae and skull, and skull and skin instances (fig. 5.21).

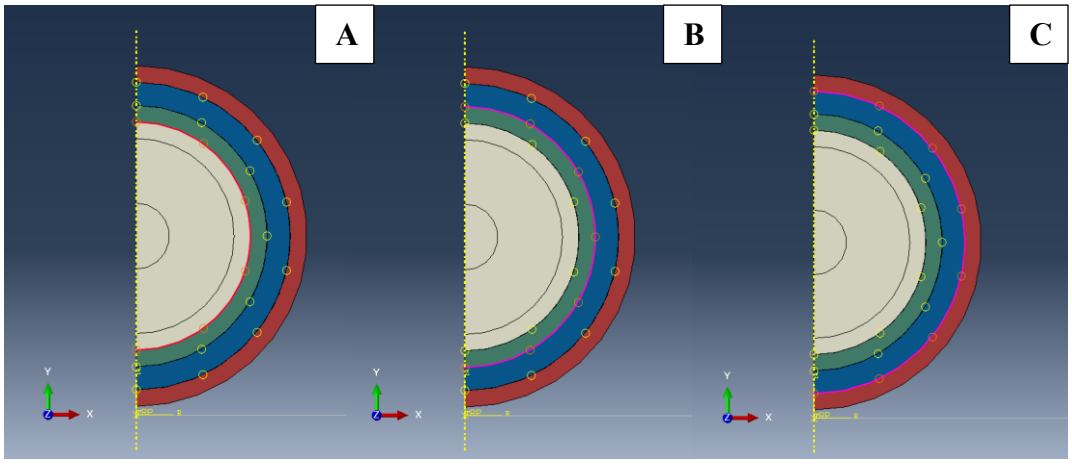


Figure 5.21 – Tie Constraints definition: (A) arachnoid trabeculae-brain, (B) skull-arachnoid trabeculae, (C) skull-skin

To define the mechanism of the interaction between the skin and the floor during the contact, a Contact *Interaction Property* with Tangential (Penalty) and Normal Behavior was created. This was required to specify a friction coefficient (0.45) and to prevent interpenetration between the skin and the floor. A General contact (Explicit) *Interaction* was then created to define the Contact domain (selected surface pairs in fig. 5.22) and to assign the *Interaction Property* previously created.

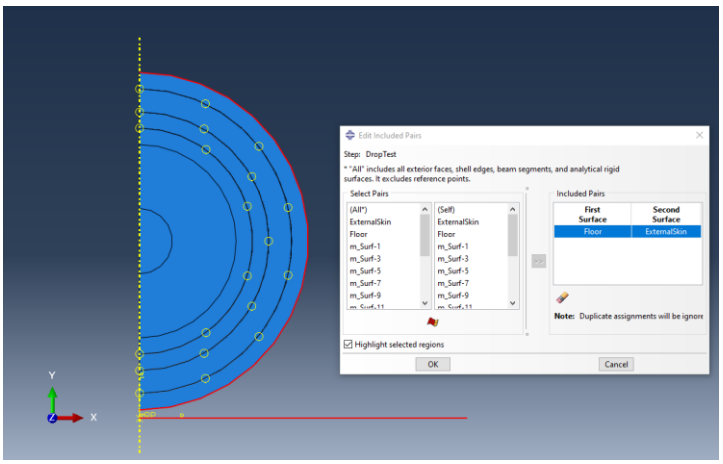


Figure 5.22 - General contact (Explicit) Interaction between floor and external skin surfaces

Boundary conditions (BCs)

An ENCASTRE was imposed on the floor Reference Point to lock it in position since the Initial step, as shown in fig. 5.23.

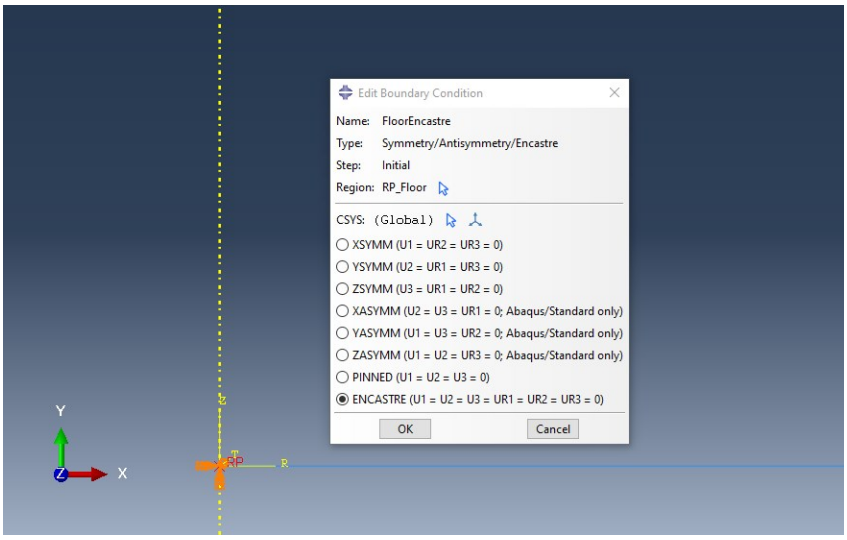


Figure 5.23 - ENCASTRE imposed on the floor Reference Point

Moreover, a *Symmetry* (XSYMM) was imposed on the red edges in figure 5.24 to lock the movement along x-axis.

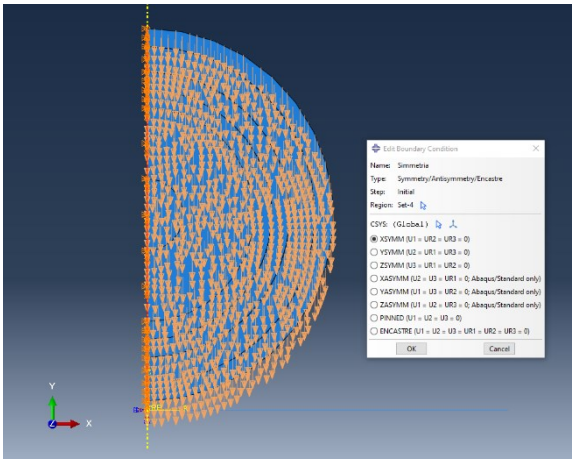


Figure 5.24 – Symmetry (XSYMM) imposed on the whole ball section edges along the vertical y-axis (red in figure)

Mesh

Each sphere/hollow sphere section was meshed with Axisymmetric Explicit Linear Quad elements (CAX4R*: 4-node bilinear axisymmetric quadrilateral, reduced integration*), imposing a mesh seed on edges (*by number*), with 1, 2, and 4 elements along the thickness of hollow spheres sections in the three cases (fig. 5.25). The rigid floor was meshed using Explicit Discrete Rigid Linear elements (RAX2: *2-node linear axisymmetric rigid link*) with a Global Seed of 10 mm.

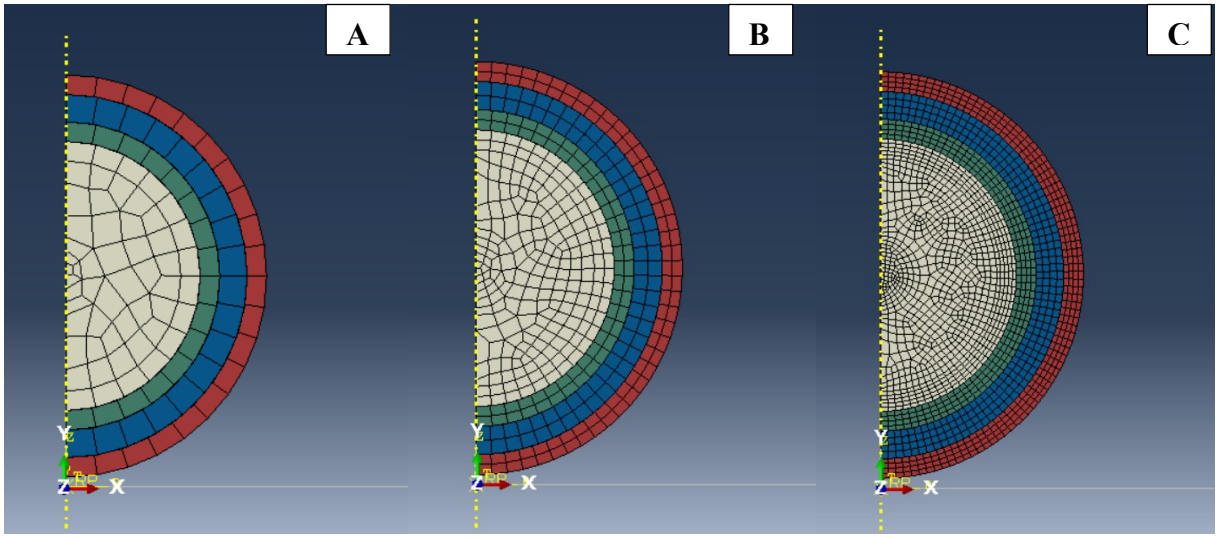


Figure 5.25 – Mesh: (A) 1 element, (B) 2 elements, (C) 4 elements along the hollow spheres thickness

Table 5.4 reports the total number of nodes and elements in the whole *Assembly*, specifying the element types and their count for the three scenarios.

A

Summary

Total number of nodes: 194

Total number of elements: 118

Details

By Instance | By Element Type

	Element Type	Element Shape	Geometric Order	Elements
1	CAX4R	quadrilateral	linear	108
2	RAX2	line	linear	10

B

Summary

Total number of nodes: 579

Total number of elements: 433

Details

By Instance | By Element Type

	Element Type	Element Shape	Geometric Order	Elements
1	CAX4R	quadrilateral	linear	423
2	RAX2	line	linear	10

C

Summary

Total number of nodes: 1989

Total number of elements: 1703

Details

By Instance | By Element Type

	Element Type	Element Shape	Geometric Order	Elements
1	CAX4R	quadrilateral	linear	1693
2	RAX2	line	linear	10

Table 5.4 - Report of the nodes and elements number in the model: model with (A) 1 element, (B) 2 elements, (C) 4 elements along hollow spheres thickness

Predefined Field

As mentioned above, the simulation was relative only to the last 2.5 mm of free fall. As for the whole head model, a velocity was set in the initial step. This initial velocity was determined by considering the initial fall height of $h = 0.5\,m$ and the height $h_0 = 0.0025\,m$ to which the beginning of the simulation corresponds, resulting in an already $h - h_0$ travelled distance in free fall. Hence, a Velocity *Predefined Field* was created with a component along the y-axis equal to:

$$V2 = -\sqrt{2g(h - h_0)} = -\sqrt{2 \cdot 9.81 \cdot (0.5 - 0.0025)}\,{}^{m}/_{s} = -3.12425\ {}^{m}/_{s} = -3124.25\,{}^{mm}/_{s}$$

This initial velocity was assigned to the ball section nodes as shown in fig. 5.26.

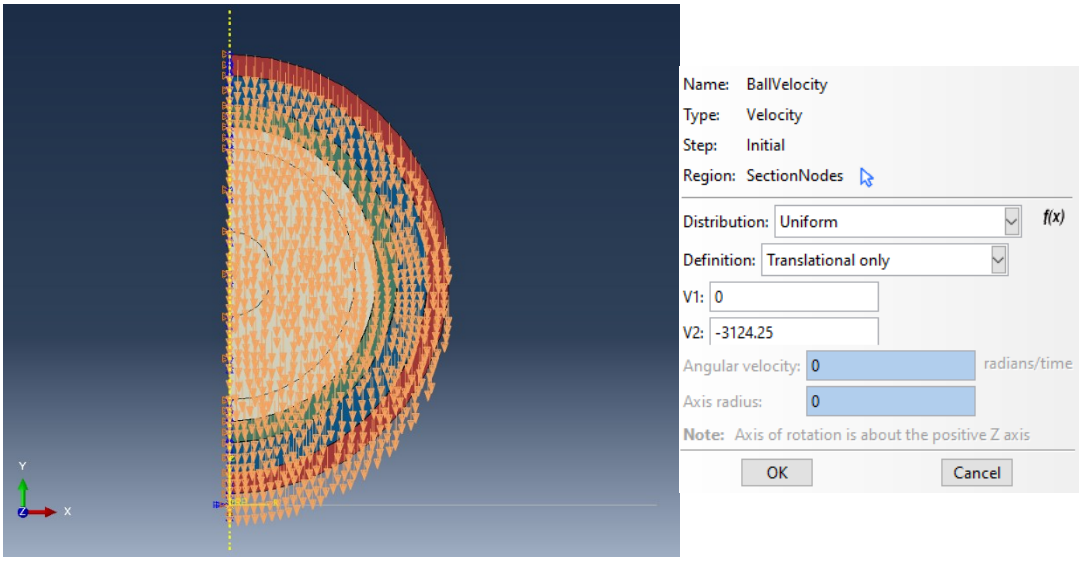


Figure 5.26 - Predefined field definition with orange arrows indicating the velocity vectors assigned to each node of the ball section, called SectionNodes in the Edit panel

Loads

A Gravity acceleration of -9810 mm/s^2 was then applied at the Dynamic step, as shown in fig. 5.27.

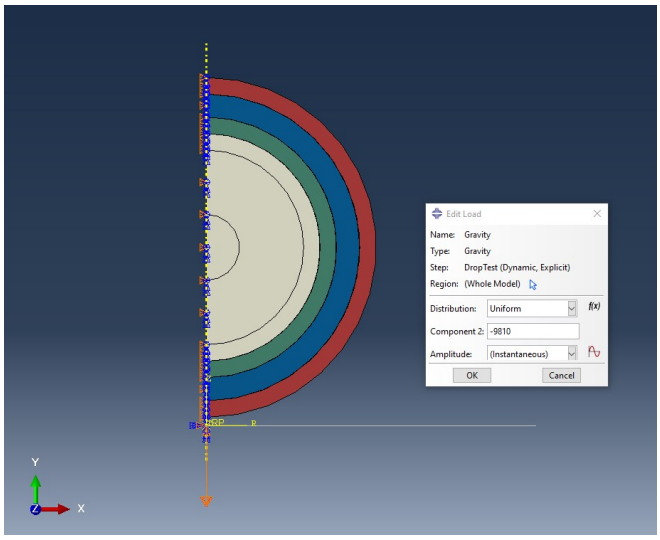


Figure 5.27 - Gravity acceleration definition

Job

The three input files were then generated to be submitted for analyses.

5.2.1.2 Processing

The three input files (.inp) were sent to the processor for analyses.

5.2.1.3 Post-processing

For simplicity, models will hereafter be named as follows:

- Quarter seed → 1 element along the thickness
- Half seed → 2 elements along the thickness
- Full seed → 4 elements along the thickness

Since the physical prototype is equipped with an accelerometer and a multiaxial pressure sensor in the centre of mass, the vertical acceleration in the centre of mass and the Von Mises stress in the centroid of an element having the CoM among its nodes were computed.

As shown in fig. 5.28, despite an initial similar behaviour, the full seed model reaches higher vertical acceleration peaks in the CoM with respect to the other two models. In particular, the maximum and minimum peak values in the three scenarios are reported in table 5.5.

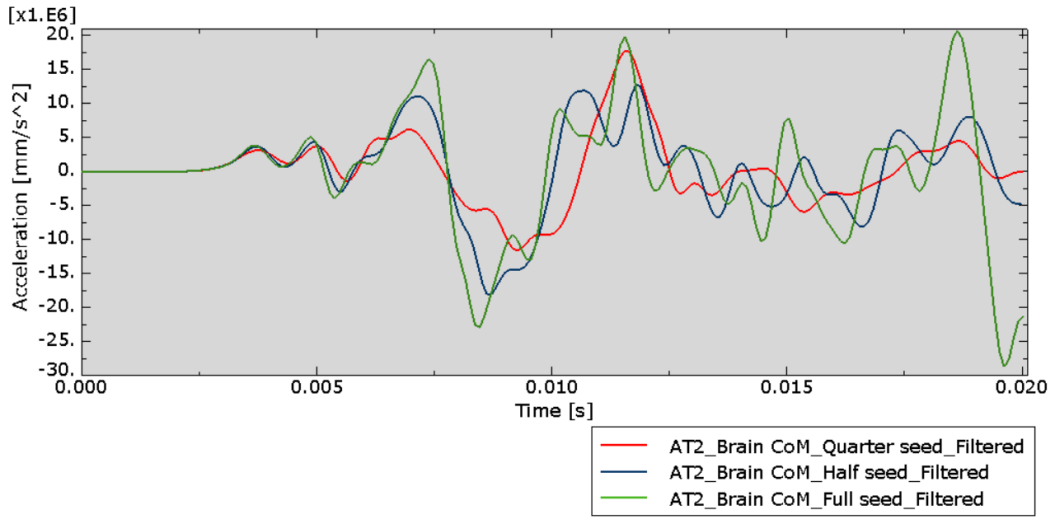


Figure 5.28 – Comparison of the vertical acceleration AT2 in the CoM

	Quarter seed model	Half seed model	Full seed model
Max AT2 [g]	1767.59	1276.32	2067.06
Min AT2 [g]	-1164.51	-1812.42	-2877.32

Table 5.5 – Peaks of vertical acceleration AT2 in the three models

As shown in fig. 5.29, the Von Mises stress computed in the centroid of an element having the CoM among its nodes shows a quite similar behaviour for the half and full model. In particular, for these two models there is a percentage change of 8.75% between the peak values of 0.164 MPa (half model) and 0.179 MPa (full model). The quarter seed model reaches a peak Von

Mises stress of 0.101 MPa, showing a percentage decrease of 47.55% with respect to the half model and of 55.71% with respect to the full model. Decreasing the number of elements along the thickness till 1, the Von Mises stress curve shows an important percentage difference with respect to the others.

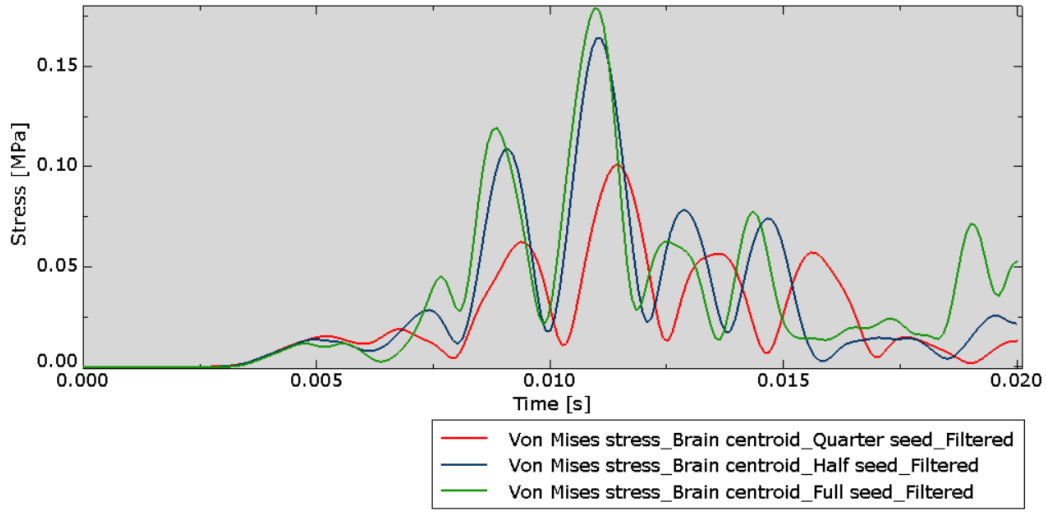


Figure 5.29 – Comparison of the Von Mises stress in the centroid of an element of the brain having the CoM among its nodes

Since the maximum principal strain (MPS) is an important and widely used indicator for mild TBI, it was analysed also the nominal maximum principal strain close to the brain CoM. As shown in fig. 5.30, the quarter seed model reaches a peak of nominal MPS of about 56%, while the half and full seed model show a MPS of 78% and 80% respectively.

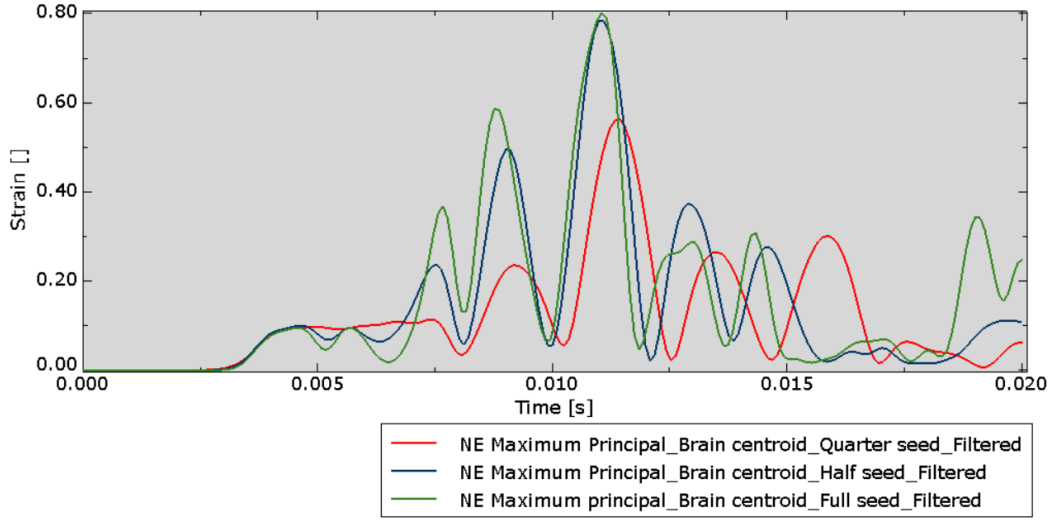


Figure 5.30 – Comparison of the nominal MPS in the centroid of an element having the CoM among its nodes

As shown in fig. 5.31, it was then evaluated the vertical acceleration in a lateral point of the skull (thickness midpoint for the full and half seed models, internal node for the quarter seed model). This value was considered because the physical prototype has an accelerometer placed under the mouth palate, that's aside with respect to the contact zone. The three models reach a peak value of about 290g, 295g, and 311g for the quarter, half, and full seed models

respectively. As can be observed, the signal shows less vibrations in the two cases with denser mesh, converging to a quite similar behaviour.

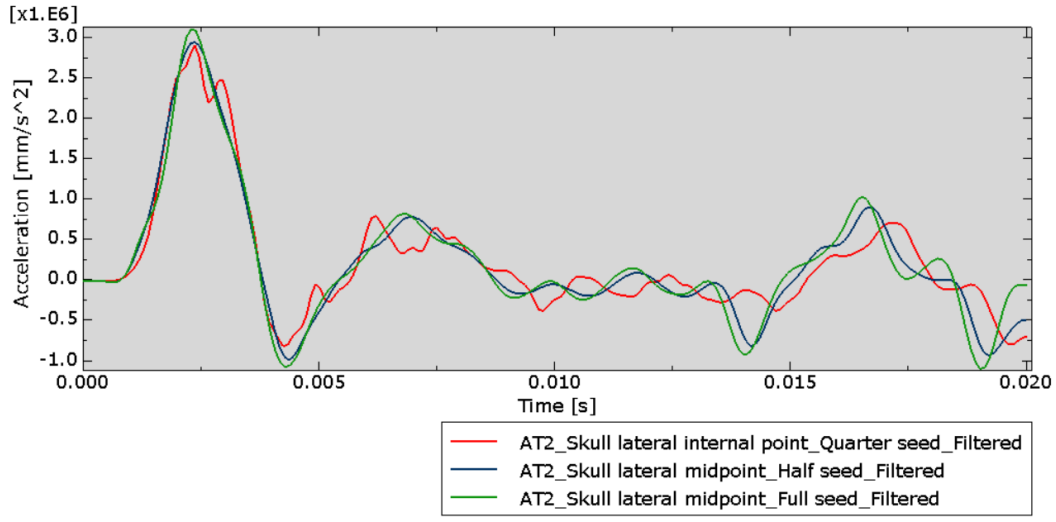


Figure 5.31 – Comparison of the vertical acceleration AT2 in the lateral zone of the skull hollow sphere

Finally, it was computed the contact force, as shown in figure 5.32.

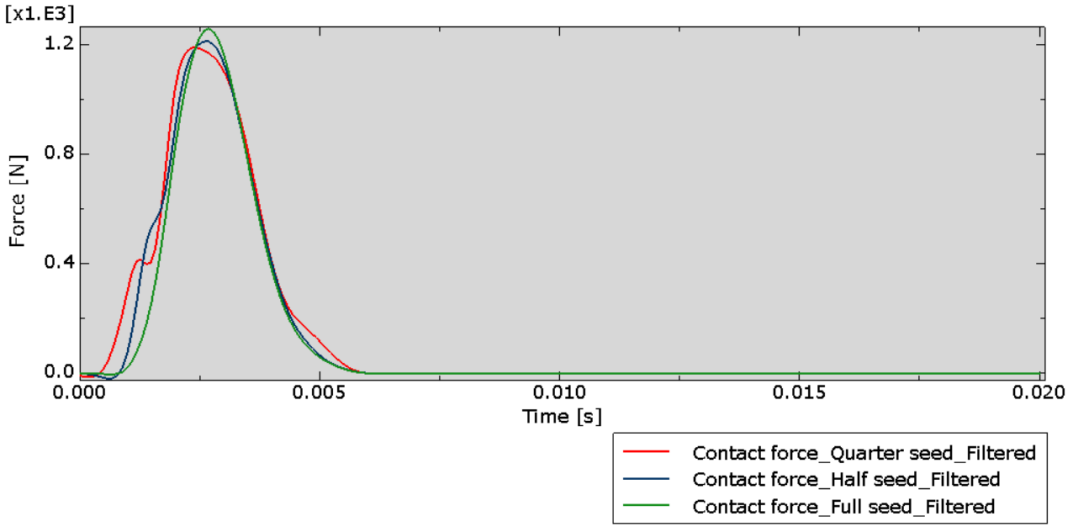


Figure 5.32 – Comparison of contact force

In conclusion, the denser mesh generated by the smaller seed allows the elements near the centre of the brain sphere a greater possibility of movement, due to the mutual dislocation of the elements that occurs during impact. While the elements of the sphere with the larger mesh interfere with each other, exerting an overall damping action, the smaller elements move with greater freedom. This allows the material in the centre to keep falling for a longer time after the contact of the ball surface with the ground has occurred. As a result, the material close to the surface at the top is stretched more, while the elements at the bottom are compressed. At the same time, the central core of the sphere rebounds, reverses the direction of motion and moves upwards. The result of this mode of movement is a wave moving within the material, which

justifies the greater amplitude of acceleration found in the case of the denser mesh. Fig. 5.33 highlights the CoM displacement in the quarter and full seed models.

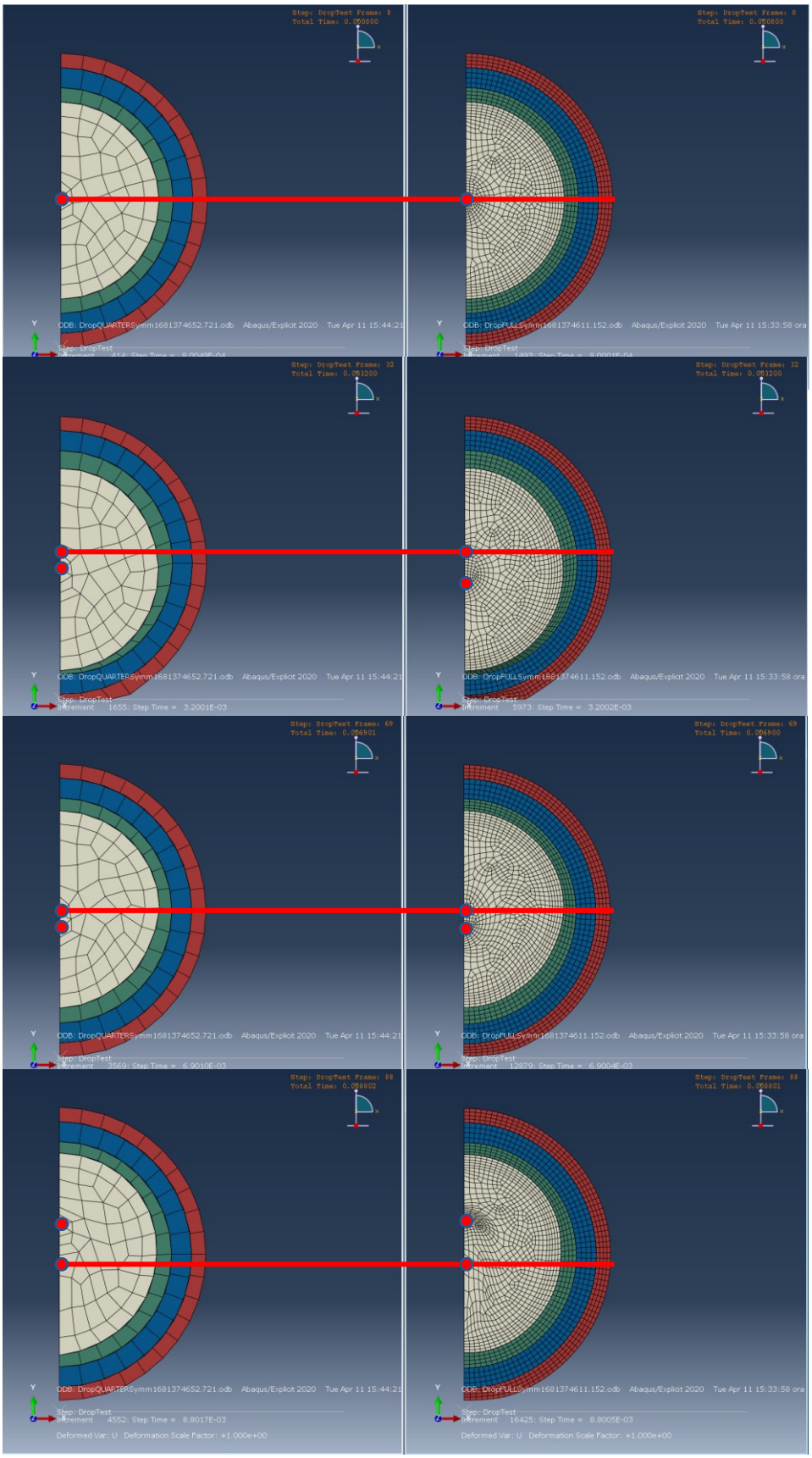


Figure 5.33 – CoM displacement in the quarter and full seed models: (A) first contact, (B) maximum lateral deformation, (C) last contact, (D) maximum upper displacement of CoM while bouncing

Moreover, in general it can be noticed that, for the first 18 ms, the computed signals converge to a quite similar behaviour when increasing the mesh seed, so in the half and full seed models. Hence, for the subsequent analyses it was chosen to use the full seed model mesh.

5.2.2 Preliminary simulations from different heights

The following analyses were performed to simulate a drop test of the simplified surrogate composed by concentric spheres from 0.2 m and 0.5 m, with the aim to get some preliminary information about the behaviour of the different materials when they interact, preparing a simplified model in view to test the physical prototype model. To this purpose, the subarachnoid space was here defined by the hyperelastic constitutive parameters reported in table 2.17, that were identified to simulate the action of the distilled water in conjunction with the damping effect of the open-cell foam.

5.2.2.1 Pre-processing

To generate the .inp file it was adopted the procedure explained in 5.2.1.1, with the only differences described below for the specified Abaqus modules.

Parts, Materials and Sections

The subarachnoid space material was defined as described for the real head surrogate, assigning water density (1E-09 t/mm^3] and Neo-hookean constitutive parameters defined in table 2.17 (also see fig. 4.9).

Mesh

It was adopted the same mesh of the full seed model created in par. 5.2.1.1 (see fig. 5.22 C), with 4 elements along the hollow spheres thickness. Fig. 5.34 reports the instances mesh for clarity.

Table 5.6 reports the total number of nodes and elements in the whole *Assembly*, specifying the element types and their count.

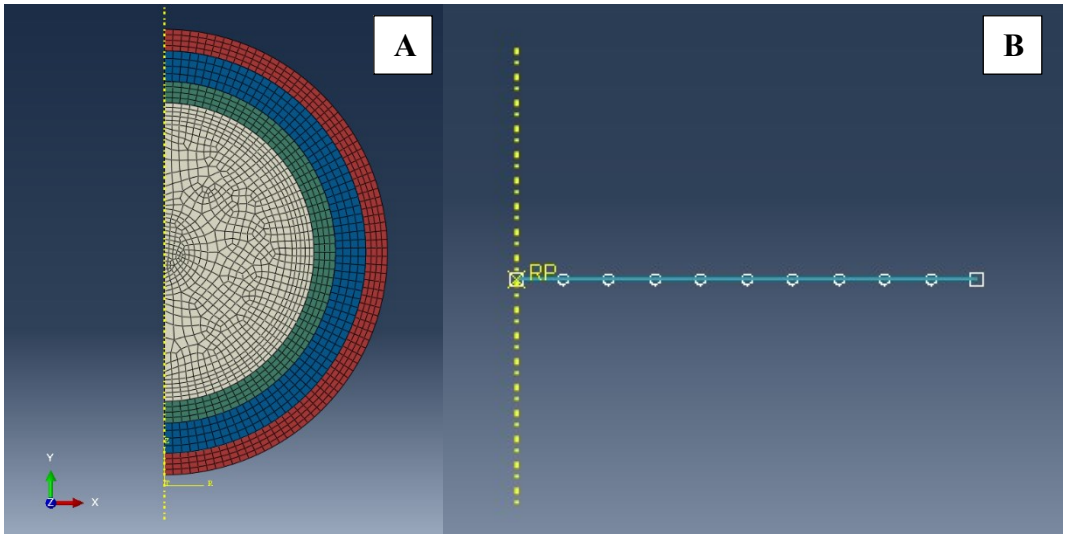


Figure 5.34 - Mesh: (A) brain, arachnoid trabeculae-CSF, skull, and skin; (B) floor

Mesh Statistics

Summary

Total number of nodes: 1989

Total number of elements: 1703

Details

By Instance | By Element Type

	Element Type	Element Shape	Geometric Order	Elements
1	CAX4R	quadrilateral	linear	1693
2	RAX2	line	linear	10

Table 5.6 - Report of the nodes and elements number in the model

Predefined Field

As mentioned above, the simulation was relative only to the last 2.5 mm of free fall. As for the whole head model, a velocity was set in the initial step. This initial velocity was determined by considering the two initial fall heights of $h = 0.2\ m$ and $h = 0.5\ m$, as mentioned before, and the height $h_0 = 0.0025\ m$ to which the beginning of the simulation corresponds, resulting in an already $h - h_0$ travelled distance in free fall. Hence, a Velocity *Predefined Field* was created with a component along the y-axis equal to, respectively for 0.2 and 0.5 m initial heights:

$$V2 = -\sqrt{2g(h - h_0)} = -\sqrt{2 \cdot 9.81 \cdot (0.2 - 0.0025)}\ {}^{m}/_{s} = -1.96849\ {}^{m}/_{s} = -1968.49\ {}^{mm}/_{s}$$

$$V2 = -\sqrt{2g(h - h_0)} = -\sqrt{2 \cdot 9.81 \cdot (0.5 - 0.0025)}\ {}^{m}/_{s} = -3.12425\ {}^{m}/_{s} = -3124.25\ {}^{mm}/_{s}$$

This initial velocity was assigned to the ball section nodes as shown in fig. 5.35.

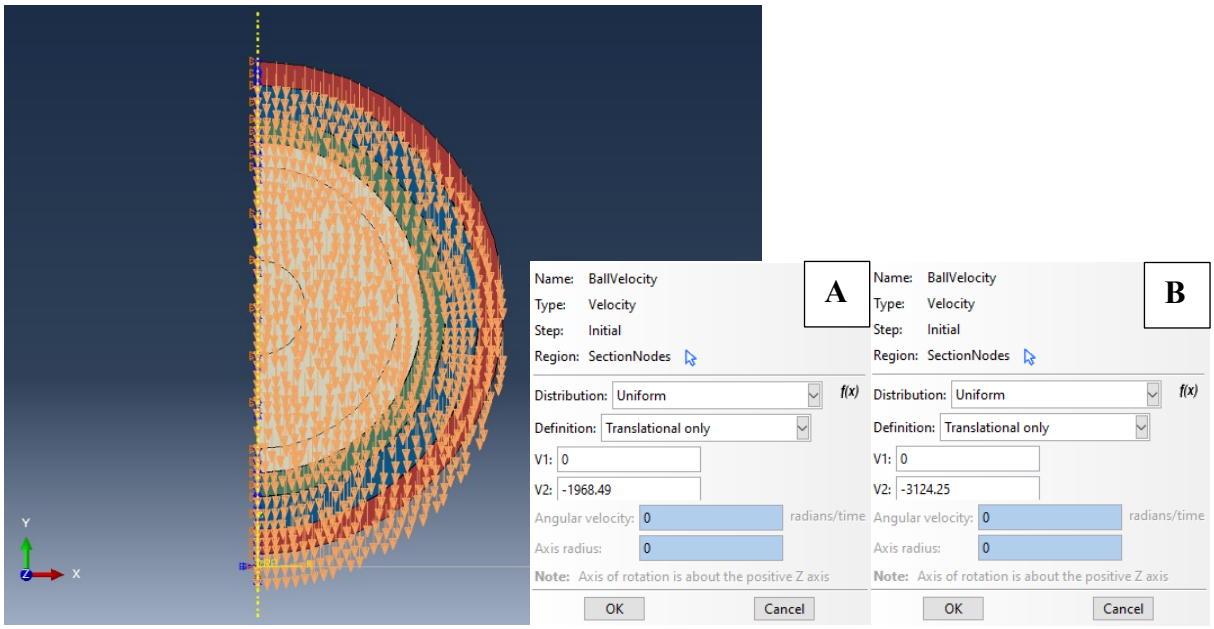


Figure 5.35 - Predefined field definition with orange arrows indicating the velocity vectors assigned to each node of the ball section, called SectionNodes in the Edit panel for the drop test from: (A) 0.2 m, (B) 0.5 m

Job

The input files were then generated to be submitted for analyses.

5.2.2.2 Processing

The input files (.inp) were sent to the processor for analyses.

5.2.2.3 Post-processing

As mentioned for the previous analyses, since the physical prototype is equipped with an accelerometer and a multiaxial pressure sensor in the centre of mass, the vertical acceleration in the centre of mass and the Von Mises stress in the centroid of an element having the CoM among its nodes were computed.

As shown in fig. 5.36, the maximum and minimum peaks of the vertical acceleration in the CoM reach higher values in the simulation of the drop test from 50 cm with respect to the free fall from 20 cm. In particular, the maximum and minimum peak values in the two scenarios are reported in table 5.7.

	Drop test from 20 cm	Drop test from 50 cm
Max AT2 [g]	293.84	622.98
Min AT2 [g]	-249.67	-707.56

Table 5.7 - Peaks of vertical acceleration AT2 in the two models

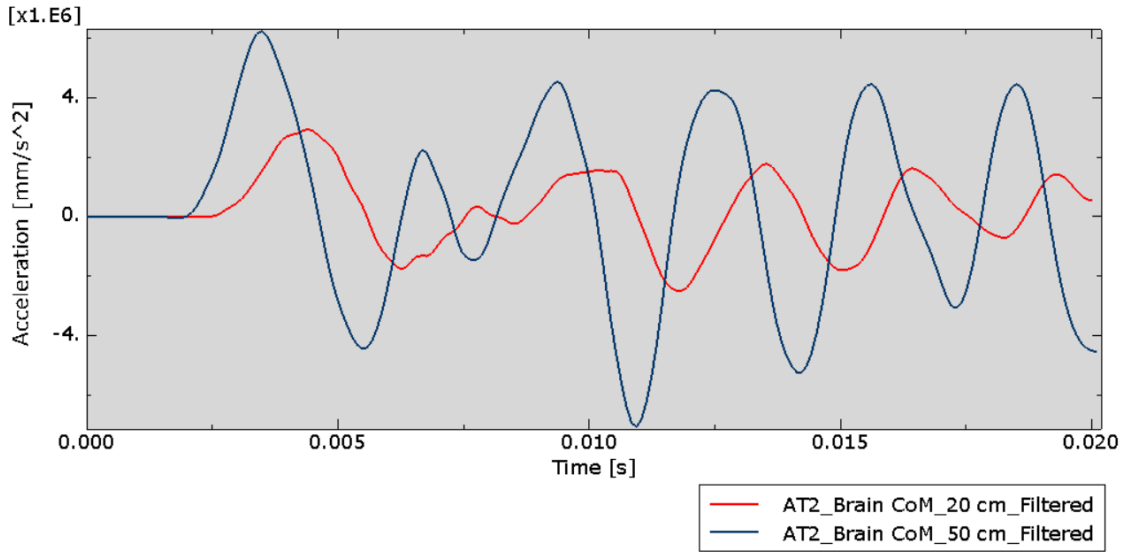


Figure 5.36 - Comparison of the vertical acceleration AT2 in the CoM in the two models

As shown in tables 5.5 and 5.7, considering the two drop test simulations from 50 cm, it can be observed that there is a percentage change of 107.37% between the maximum peak values of the vertical acceleration in brain CoM and a percentage change of 121.051% between the minimum peak values of the vertical acceleration in brain CoM. The two models are different only for the subarachnoid space material definition: considering the presence of the distilled water simulating CSF, it can be observed an important reduction in the peak acceleration values, confirming that the fluid helps damping the brain while impacting with the ground.

As shown in fig. 5.37, there is a percentage change of 115.044% between the peak values of the Von Mises stress computed in the centroid of an element having the CoM among its nodes in the two simulations. In fact, when falling from 20 cm the signal reaches a peak value of 0.0039 MPa (3.90 kPa), while in the simulation of free fall from 50 cm the Von Mises stress reaches 0.01447 MPa (14.47 kPa).

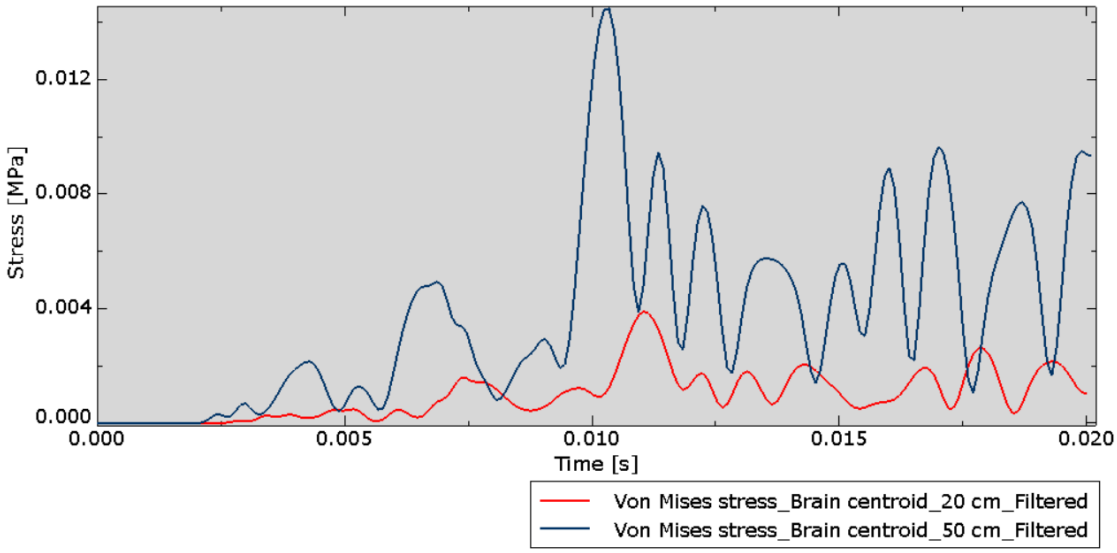


Figure 5.37 – Comparison of the Von Mises stress in the centroid of an element of the brain having the CoM among its nodes in the two simulations

Fig. 5.38 shows the nominal MPS in the two scenarios. The set of concentric spheres falling from 20 cm reaches a peak value of nominal MPS 1.44%, while simulating the drop test from 50 cm the peak increases to 6.30%. Hence, increasing the initial fall height, the MPS close to the CoM increases.

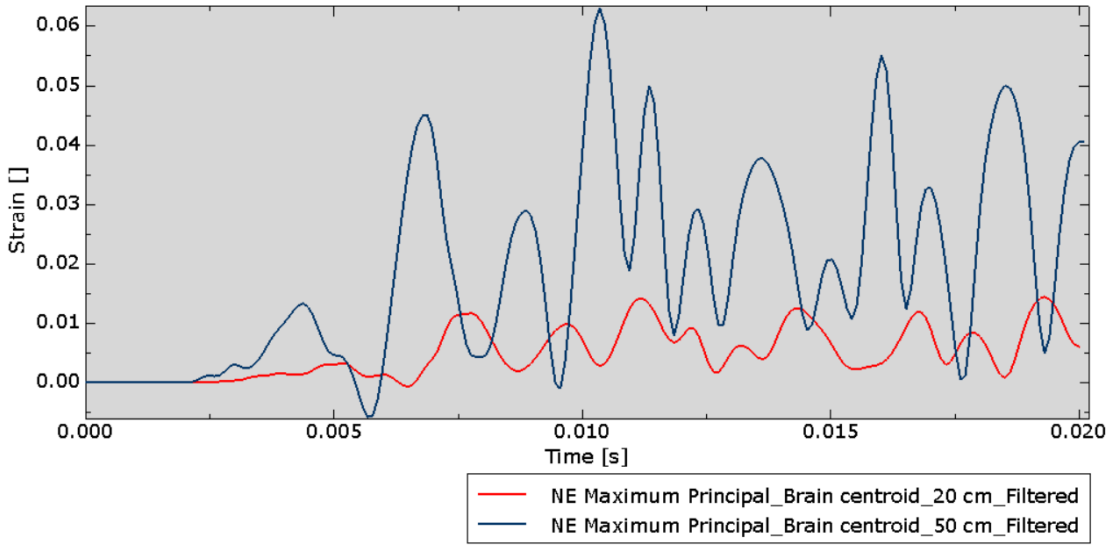


Figure 5.38 – Comparison of the nominal MPS in the centroid of an element having the CoM among its nodes in the two scenarios

The physical skull surrogate is equipped with 12 pressure sensors, to acquire data about the CSF pressure. Thus, pressure distribution along the modeled subarachnoid district was then computed in the lower (close to the contact area), upper and lateral zones of the simulated arachnoid trabeculae-CSF district in the two scenarios.

Figures 5.39 shows the comparison of the pressure computed in the centroid of an element placed in the lower (fig. 5.39 A), upper (fig. 5.39 B), and lateral (fig. 5.39 C) zones of the instance. As evinced by the plots, there is a delay in the initial propagation of the pressure while decreasing the initial height of free fall. Moreover, it can be noticed that the maximum and minimum values of the signals recorded in the free fall from 20 cm are lower than their respective signal peaks in the drop test simulation from 50 cm. Table 5.8 summarizes the maximum and minimum peaks of pressure in the three zones for the two scenarios.

Furthermore, considering each simulation separately, it can be observed an initial depression in the upper zone of the SAS, while the first (and maximum) peak value in the lower zone is positive and almost equal in absolute value to the first (and minimum) negative peak in the upper zone. Moreover, the pressure signal recorded in the lateral zone is always intermediate with respect to the upper and lower ones.

	Drop test from 20 cm	Drop test from 50 cm
Max pressure in the lower zone [MPa]	0.0814	0.1443
Min pressure in the lower zone [MPa]	-0.0261	-0.0860
Max pressure in the upper zone [MPa]	0.0292	0.0805
Min pressure in the upper zone [MPa]	-0.0808	-0.1504
Max pressure in the lateral zone [MPa]	0.0027	0.0109
Min pressure in the lateral zone [MPa]	-0.0046	-0.0141

Table 5.8 – Maximum and minimum peaks of the pressure in the lower, upper, and lateral SAS zones for the two tests

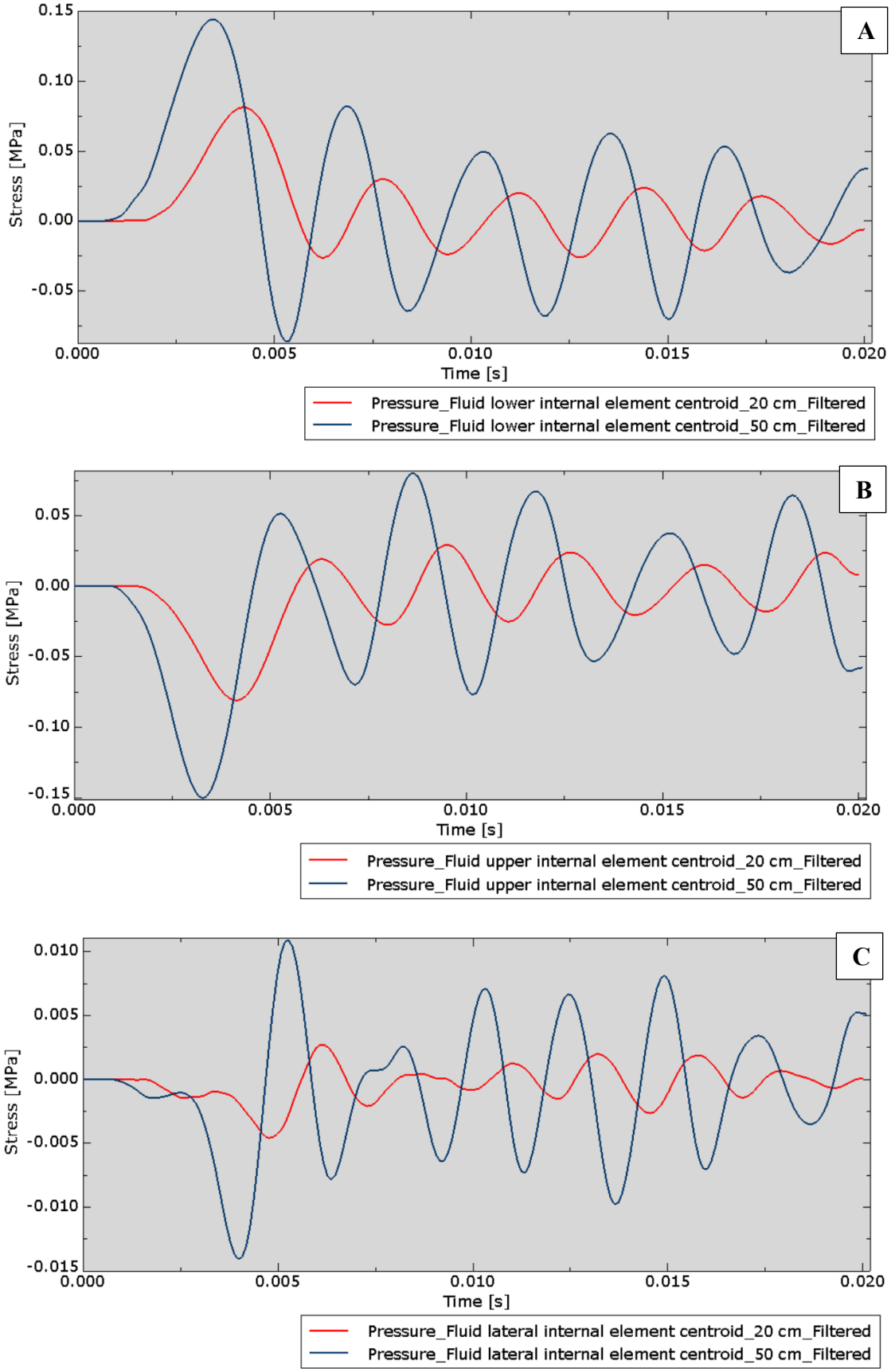


Fig. 5.39 - Comparison of the pressure in the centroid of an element in the (A) lower, (B) upper, and (C) lateral zones of the SAS in the two cases

As shown in fig. 5.40, it was then evaluated the vertical acceleration in the lateral midpoint of the skull thickness. As mentioned for the preliminary analyses evaluating the influence of the mesh seed, this value was considered because the physical prototype has an accelerometer placed under the mouth palate, that's aside with respect to the contact zone. The two models reach a peak value of about 138.46g (drop test simulation from 20 cm) and 267.59g (drop test simulation from 50 cm).

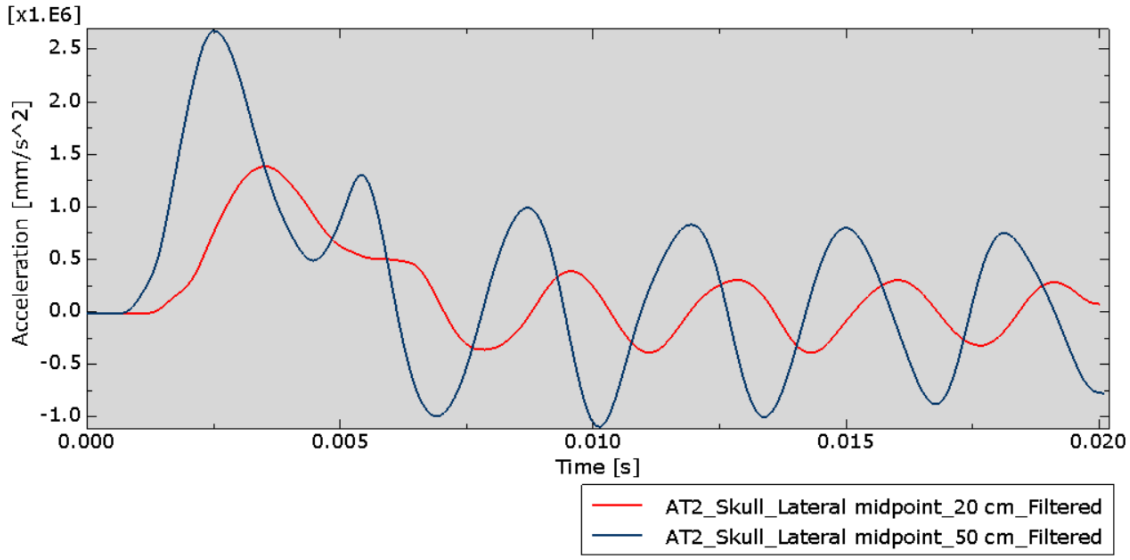


Figure 5.40 – Comparison of the vertical acceleration AT2 in the lateral zone of the skull hollow sphere in the two scenarios

Finally, it was computed the contact force, as shown in figure 5.41.

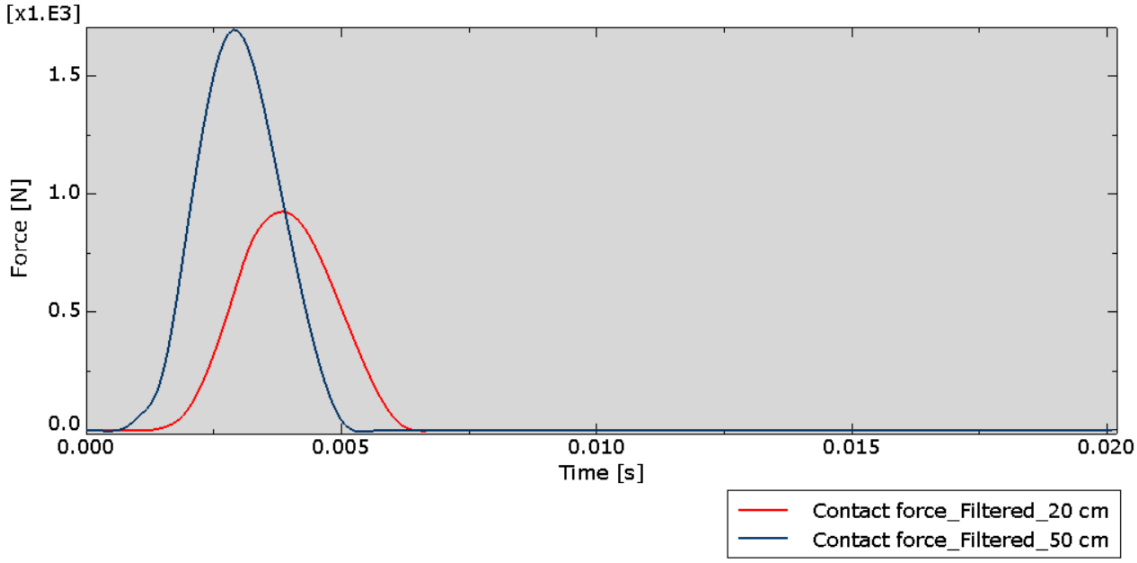


Figure 5.41 – Comparison of contact force

Table 5.9 summarizes the peak contact force and the contact time in the two simulations.

	Peak of the contact force [N]	Contact time [ms]
Drop test from 20 cm	925.77	4.8
Drop test from 50 cm	1696.61	4.1

Table 5.9 - Peak of the contact force and contact time comparison

As evinced by the table, for the drop test from an initial height of 50 cm the peak value of the contact force increases, and the contact time decreases with respect to the drop test from 20 cm findings.

Figures 5.42 and 5.43 report the contact force and the vertical acceleration in the CoM in the two simulations. The initial contact is followed by further vibrations of the CoM in both cases.

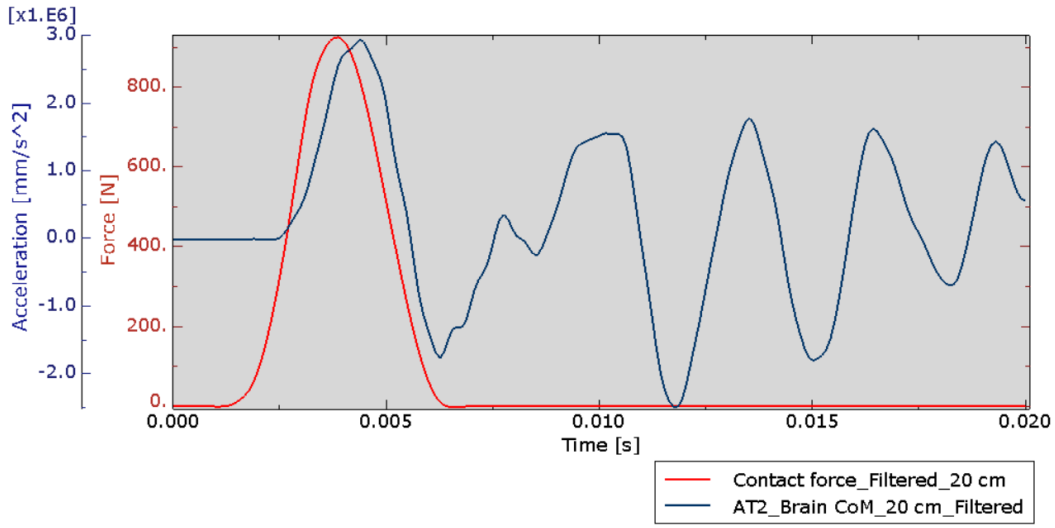


Figure 5.42 – Contact force and vertical CoM acceleration computed for the drop test simulation from 20 cm

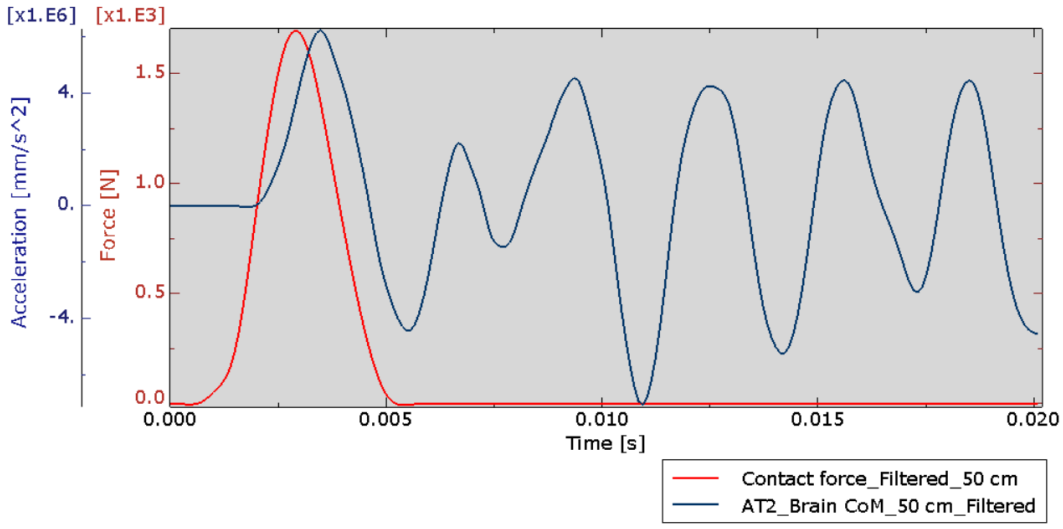


Figure 5.43 - Contact force and vertical CoM acceleration computed for the drop test simulation from 50 cm

These preliminary simulations were needed to simplify the geometry of the physical surrogate and get some information about the computed signals in conjunction with the behaviour of the instances during the impact. Due to lack of time and materials, no experimental drop tests were carried out to validate this simplified model.

5.3 Drop test simulation of the right half head surrogate

As mentioned before, to reduce the time required for the analysis, it was chosen to perform a preliminary drop test of the right half of the head surrogate.

5.3.1 Pre-processing

The pre-process phase was the same described for the whole model of the head, with the only differences regarding the imported *Parts*, the position of the global reference system, and the symmetry BC to prevent the lateral movement of the head while falling.

In fact, the solid models of the head prototype (brain, SAS, falx-tentorium, top skull, bottom skull-jaw, skin, and flange) were divided into two halves in Fusion 360, and the only right components were imported in Abaqus as *Parts*, along with the two grub screws joining the flange and the five grub screws connecting right top-bottom skull. Figure 5.44 shows the Assembly module of the half model.

The instances were oriented to have the global z-axis passing through the EAM. In this case it wasn't created a local reference system in the EAM itself, and the coordinates of the CoM of the whole head with respect to the global reference system are reported in table 5.10.

	CoM coordinates (x, y, z)
x [mm]	-4.87
y [mm]	46.28
z [mm]	94.77

Table 5.10 – Whole head CoM coordinates with respect to the global system

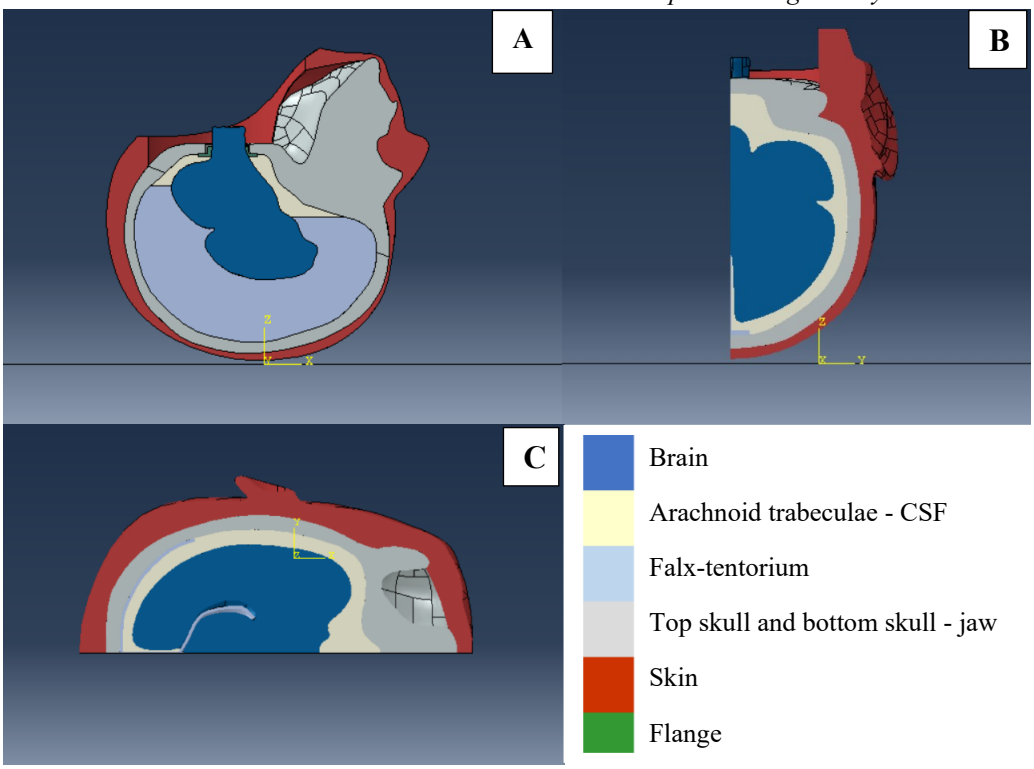


Figure 5.44 – (A) Sagittal, (B) coronal, and (C) transverse sections of the half head instances according to the materials

A boundary condition was then imposed on the faces of the sagittal section of the half head instances to lock the movement along y-axis, as shown in fig. 5.45.

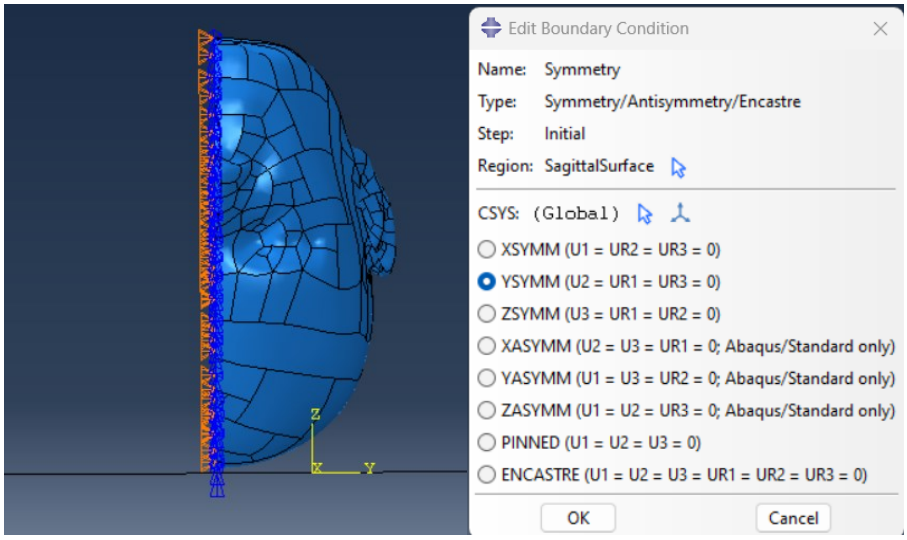


Figure 5.45 - Symmetry (YSYMM) imposed to prevent the lateral movement of the half head

5.3.2 Processing

The .inp file was then sent to the processor for analysis, with the contribution of CAPRI ("Calcolo ad Alte Prestazioni per la Ricerca e l'Innovazione" of the University of Padua).

5.3.3 Post-processing

As mentioned for the previous analyses, since the physical prototype is equipped with an accelerometer and a multiaxial pressure sensor in the centre of mass, the vertical acceleration in the whole head model CoM (fig. 5.46) and the Von Mises stress in the centroid of an element having the CoM among its nodes (fig. 5.47) were computed. Table 5.11 reports the peak values of the vertical acceleration, which reaches a first peak value of 127g (during contact) and a minimum value of -57.3g during the vibrations that follow the contact. The computed peak of von Mises stress during contact is 0.00868 MPa (8.68 kPa), while a maximum peak value of 0.0117 MPa (11.7 kPa) is reached after the contact, still having vibrations. These findings have not been validated against the laboratory drop test, as the experimental data are missing due to hardware malfunctioning. The window shown in all the figures identifies the contact time.

Max AT3 [g]	127
Min AT3 [g]	-57.3

Table 5.11 - Peaks of vertical acceleration AT3 in the CoM of the whole head

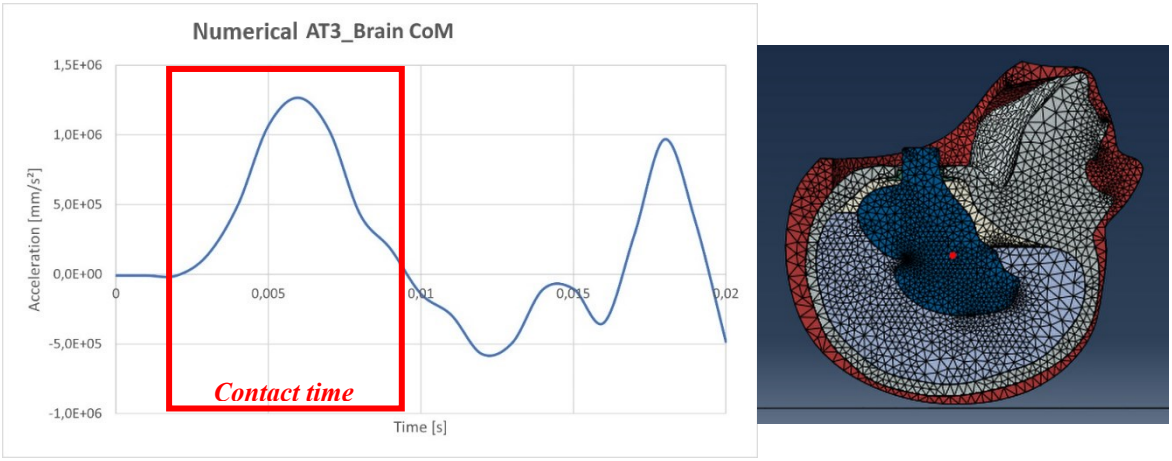


Figure 5.46 – Numerical vertical acceleration AT3 in the CoM of the whole model

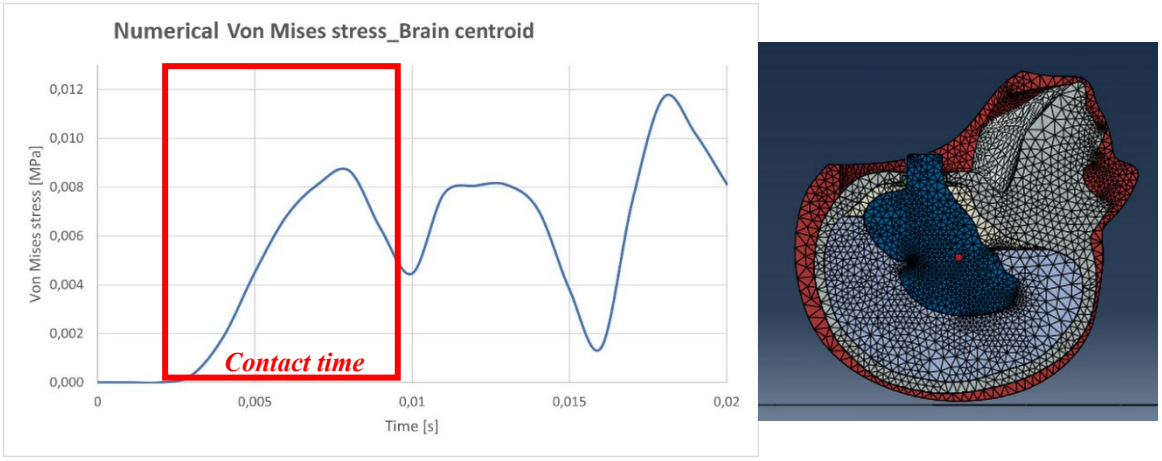


Figure 5.47 – Numerical Von Mises stress in the centroid of an element of the brain having the whole head CoM among its nodes

Fig. 5.48 shows the nominal Maximum Principal Strain (MPS) in the centroid of an element having the whole model CoM among its nodes. The half head falling from 20 cm reaches a first peak value of 4.39% nominal MPS, while after the contact the maximum nominal MPS is about 7.38%, that's still below the 15% threshold indicated in the MPS criterion.

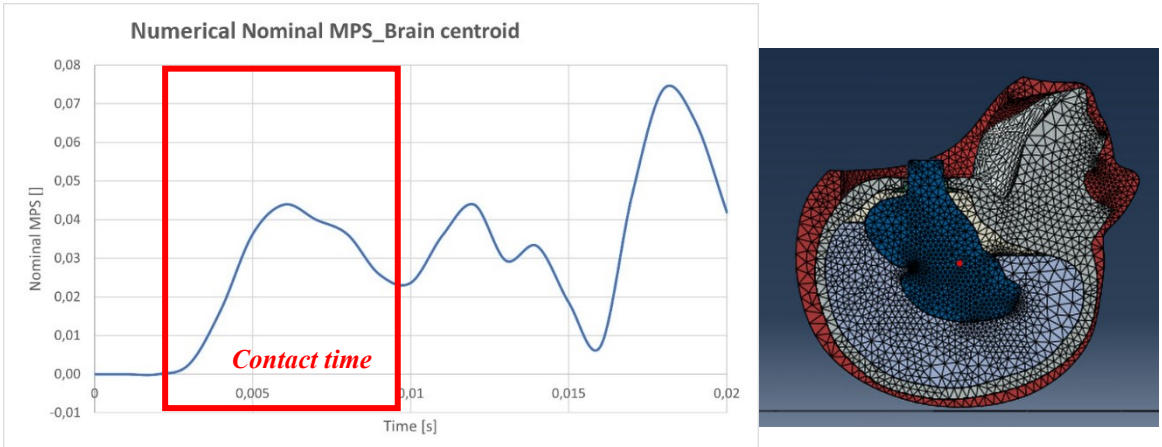


Figure 5.48 – Numerical nominal MPS in the centroid of an element having the whole head CoM among its nodes

The physical skull surrogate is equipped with 12 pressure sensors, to acquire data about the CSF pressure. Thus, pressure distribution along the modeled subarachnoid district was then computed in 4 out of the 6 zones corresponding to the position of the 6 pressure sensors on the right half of the top skull physical surrogate. Figure 5.49 A shows the comparison of the pressures computed in the centroid of an element placed in the frontal (fig. 5.49 C), temporal (fig. 5.49 D), occipital (fig. 5.49 E), and top (fig. 5.49 F) zones of the modeled SAS. It can be observed that the zone of the CSF simulant that impacts (top zone) reaches a first peak of 0.2287 MPa (228.7 kPa). Fig. 5.49 B highlights the elements studied in the four zones. These findings have not been validated against the laboratory drop test, as the pressure sensors didn't acquire data in this first experiment.

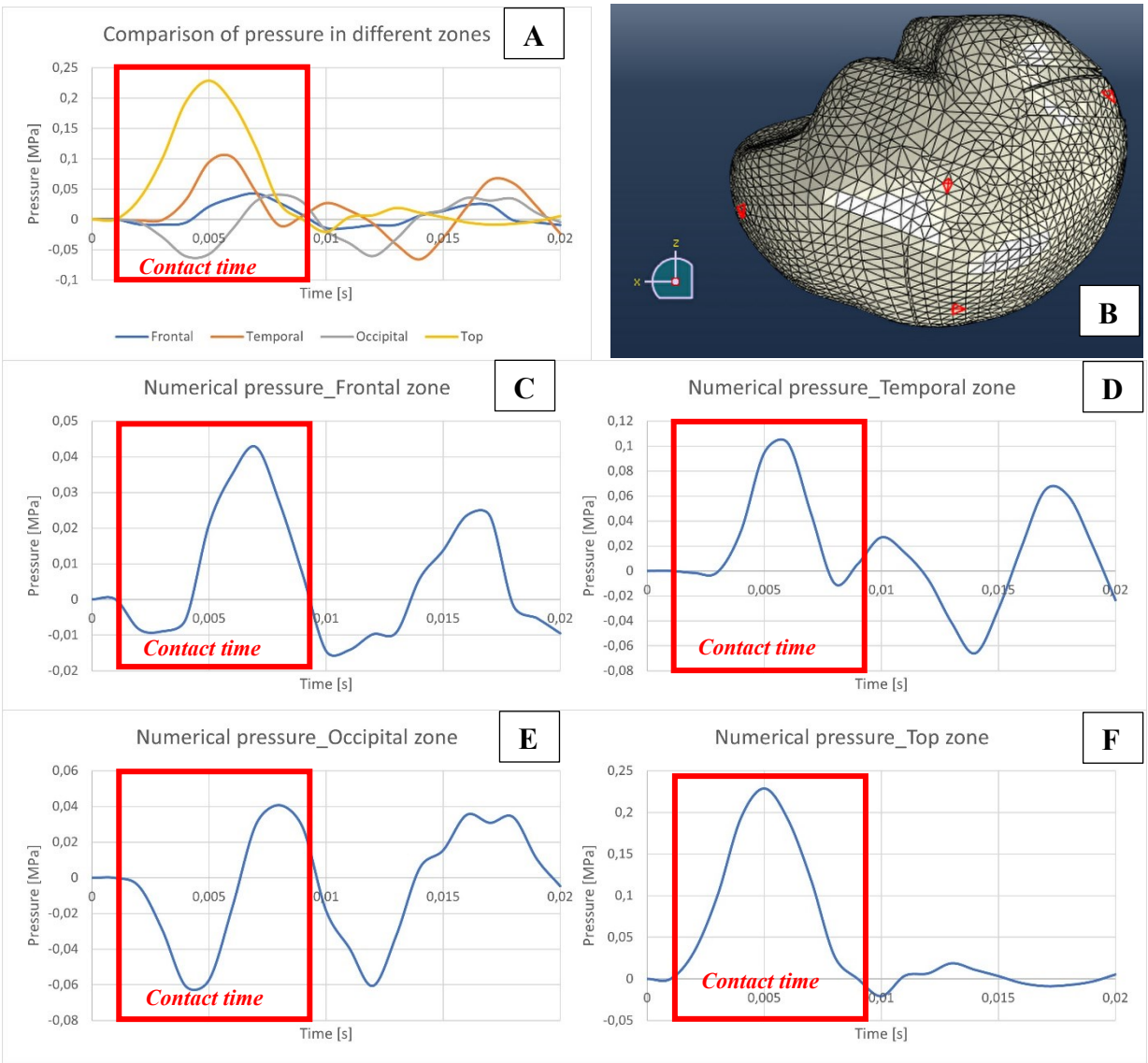


Figure 5.49 – Comparison of the numerical pressure (A) computed in the centroid of the elements highlighted (B): (C) frontal, (D) temporal, (E) occipital, and (F) top zones of the CSF simulant

As mentioned before, the physical prototype has a triaxial accelerometer placed under the mouth floor of the skull (palate). Hence, as shown in fig. 5.50, it was evaluated the vertical acceleration in a node placed in that zone of the half skull model, which reaches a peak value of 91.9g. The signal was then compared with the vertical component of the accelerometer output to evaluate the first peak values in the two cases (see par. 5.3.4).



Figure 5.50 - Numerical vertical acceleration AT3 in the mouth floor of the skull

Finally, fig. 5.51 shows the computed contact force along with the vertical acceleration calculated in the whole head CoM. As observed, the force signal reaches the maximum value of 1750 N and the contact time lasts 7 ms. This force value was duplicated to find the contact force value to be compared with the experimental finding from the whole head drop test (see par. 5.3.4).

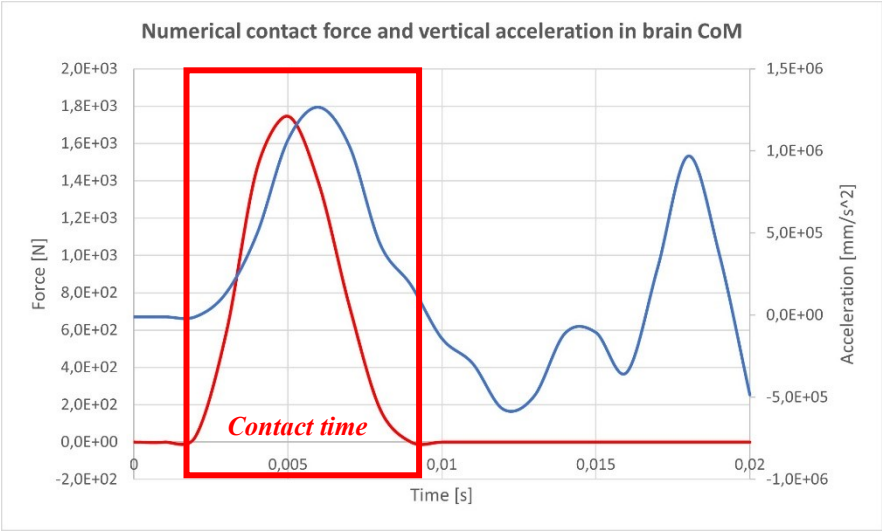


Figure 5.51 - Numerical contact force and vertical acceleration in the whole head CoM

A preliminary experimental drop test was performed to acquire data and validate the numerical model, as described in the next paragraph.

5.3.4 Experimental preliminary tests for model validation

A preliminary drop test was performed using the drop tower shown in fig. 5.52. The head surrogate was dropped from 20 cm, kept in trajectory by means of a sliding collar, and it impacted on a flat anvil, as shown in fig. 5.53.

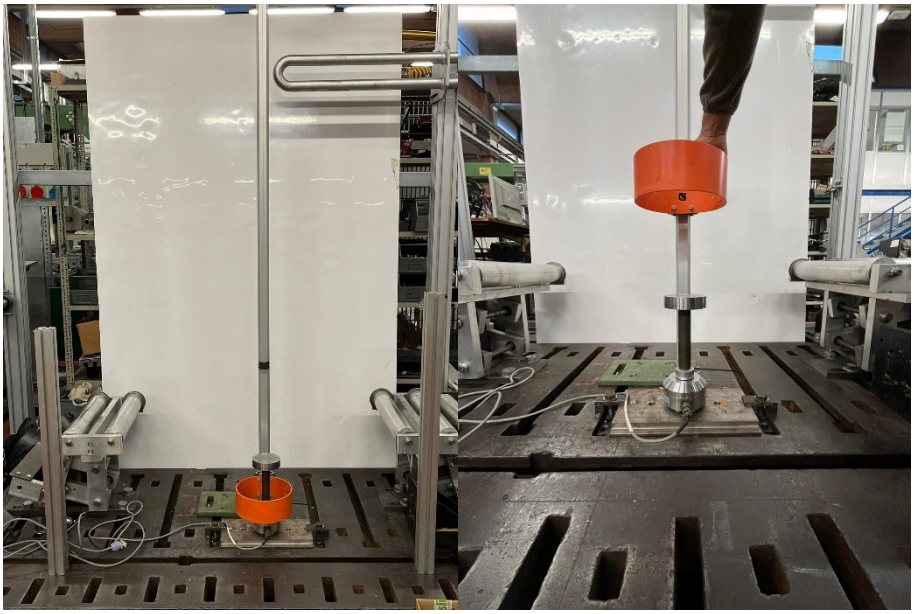


Figure 5.52 – Drop tower with the flat anvil and the orange sliding collar

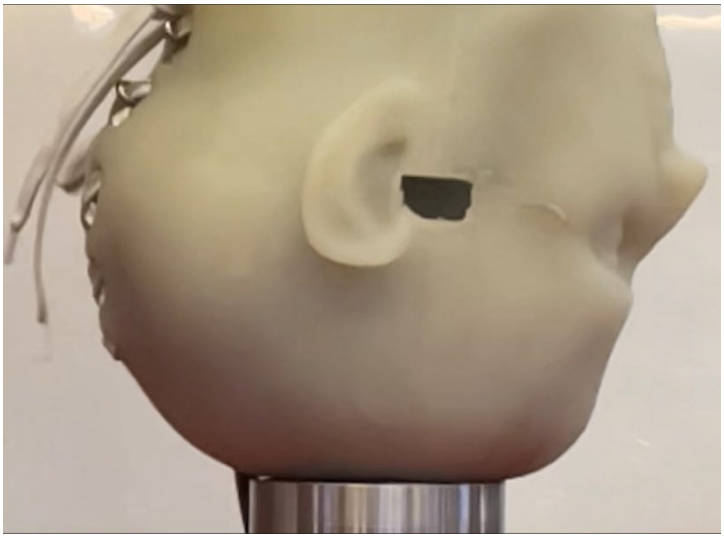


Fig. 5.53 – Head impact on the flat anvil

The only signals that were correctly acquired were the acceleration under the mouth floor of the skull, the contact force, and the contact time.

Fig. 5.54 A shows the three components of the acceleration acquired by the triaxial accelerometer placed under mouth floor of the skull (palate). The first peak of the vertical component was compared to the first peak of the numerical output (see fig. 5.50), to evaluate the maximum vertical acceleration reached during contact in both cases.

The load cell output signal (fig. 5.54 B) was analysed to compute the following values:

- peak of the contact force
- contact time

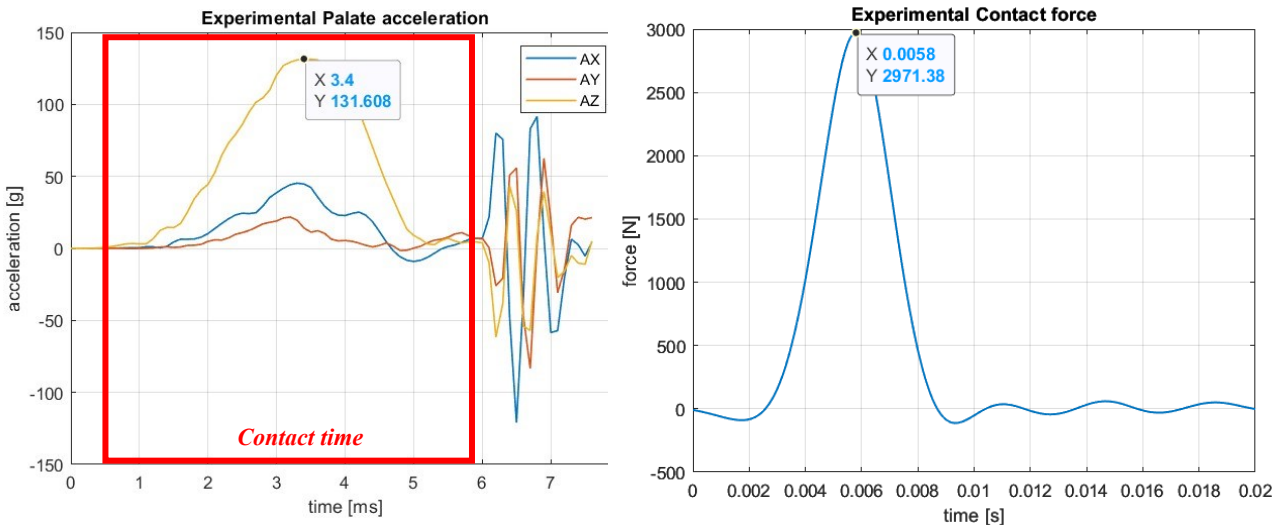


Figure 5.54 – Experimental (A) acceleration components in the mouth floor of the skull and (B) contact force

As underlined in table 5.12, the numerical finding in the palate underestimates the actual value measured by the accelerometer, showing a 30.17% percentage decrease. On the other hand, the contact force and the contact time estimated by the numerical simulation are higher with respect to the load cell outputs, showing a percentage increase of 17.79% and 25% respectively.

	Experimental	Numerical	Percentage change
Peak of the vertical acceleration [g]	131.61	91.90	-30.17%
Contact force [N]	2971.38	3500	17.79%
Contact time [ms]	5.6	7	25%

Table 5.12 – Comparison of experimental vs numerical first peak of vertical acceleration under the mouth floor, contact force, and contact time

Further experimental tests will be necessary to acquire the missing data, thus being able to continue with the validation of this first model. In this way it will be possible to eventually modify the required material specs and to generate a finer mesh till the validation will be satisfied.

5.4 Discussion of preliminary results and conclusions

In drawing the final considerations on the work described so far, it should be mentioned that it is part of a complex long-term project, very important for the topic addressed, i.e. the social impact of the consequences of head injuries. The project led to the realisation of different evolutions of the replica of the human head, instrumented with different types of sensors (accelerometers, gyroscopes and pressure sensors) for the acquisition of data obtained from impact tests.

The main difficulty in the realisation of this type of headform is the achievement of satisfactory bio-fidelity, due to the complexity of the anatomical structures. The first problem is the choice of materials: biological tissues, in fact, exhibit peculiar physical and mechanical properties, which entail the continuous research and testing of improving solutions.

To contribute to this topic, it was decided to develop a numerical finite element model of the latest evolution of the human head surrogate, which would be useful both for improving the surrogate itself and for all the applications involving its use (e.g. helmet design).

The work presented here represents the first step towards the complete FEM modelling of the replica. The constitutive analysis carried out, including laboratory tests on the materials constituting the simulated anatomical parts (brain, space occupied by the arachnoid trabeculae and the CSF, falx and tentorium, skull, and skin), allowed the identification of the corresponding constitutive parameters. The geometrical analysis allowed to obtain the solid models of the districts to be imported in Abaqus software, which was used to create the finite element model of the physical prototype.

For an initial validation, it was decided to focus on more simplified geometries in order to optimise the mesh parameters of the model. In fact, since the model does not derive from the composition of parametric geometries, but from the segmentation of medical diagnostic images, the surfaces delimiting the various components of the solid are complex and irregular, which entails a large number of finite elements in the model, as well as a high probability of having distorted elements in the mesh. This leads to analysis time that can be very long and with a high probability of analysis failure. To this purpose, an initial series of simulations was carried out on a simplified model, consisting of a set of concentric spheres constructed with an axisymmetric model, which allows for faster analysis.

In particular, three preliminary analyses were performed while densifying the mesh to identify the best seed to be applied in the following simulations. The model composed by the set of concentric hollow spheres having 4 elements along the thickness was chosen to perform the following analyses, since the results reasonably started to converge. Thus, the full seed model was used to simulate two drop tests from different heights, with the aim to get some preliminary

information about the behaviour of the different materials when they interact, preparing a simplified model in view to test the physical prototype model. It was observed an important reduction in the peak acceleration values considering the presence of the distilled water simulating CSF, thus confirming that the fluid helps damping the brain while impacting with the ground. In general, it was noticed that the maximum and minimum values of the signals recorded in the free fall from 20 cm are lower than their respective signal peaks in the drop test simulation from 50 cm.

Due to the unavailability of materials, it was only possible to conduct a drop test on a force platform of a sphere instrumented with an accelerometer cast with skin-simulating gel. The drop test showed a good match of the data acquired by the instruments with that predicted by the model, however further experiments are required to confirm this correspondence.

In the meantime, again with the intent to reduce computation time, at this early stage of model development, it was carried out a simulation of the free fall of the right half of the head model only. This made it possible to check the presence of critical elements in the mesh and evaluate the output signals. In parallel, the physical head surrogate was dropped using a drop tower; the accelerometer placed under the mouth floor of the skull and the load cell correctly acquired data. A preliminary validation of the half head model was performed comparing the numerical findings with the experimental results, keeping in mind that the mass was halved. The results obtained in this first phase of the model's development appear promising for the next developments, which include the refinement of the model for the optimisation of the mesh, which will be followed by analyses on the complete model for its validation. Further testing will include free fall trials on inclined anvil to assess the rotational effects.

REFERENCES

1. Abel, J., Gennarelli, T., Segawa, H., (1978). Incidence and severity of cerebral concussion in the rhesus monkey following sagittal plane angular acceleration. In: Proceedings of the 22nd Stapp Car Crash Conference, pp. 33–53.
2. Anastasi G. (2010). Trattato di Anatomia umana vol 3
3. Benko, N., Luke, E., Alsanea, Y., & Coats, B. (2021). Mechanical characterization of the human pia-arachnoid complex. Journal of the mechanical behavior of biomedical materials, 120, 104579. https://doi.org/10.1016/j.jmbbm.2021.104579
4. Betts, J (2017). Anatomy & Physiology – OpenStax, in https://openstax.org/books/anatomy-and-physiology-2e/pages/6-3-bone-structure
5. Bhattacharya S. (2018). Death by Staircase
6. Bien-aimé, L.K.M., Blaise, B.B. & Beda, T. Characterization of hyperelastic deformation behavior of rubber-like materials. SN Appl. Sci. 2, 648 (2020). https://doi.org/10.1007/s42452-020-2355-6
7. Bilston, L.E. (2019). Brain Tissue Mechanical Properties. *In: Miller, K. (eds) Biomechanics of the Brain. Biological and Medical Physics, Biomedical Engineering.* Springer, Cham. https://doi.org/10.1007/978-3-030-04996-6_4
8. Bray, M. (2018). Examining Causes and Consequences of Mental Health Disorders in Chronic Traumatic Brain Injury. Thesis for MSc
9. Brush K, online in https://www.techtarget.com/searchsoftwarequality/definition/finite-element-analysis-FEA (2023)
10. Budday, S., Ovaert, T.C., Holzapfel, G.A. et al (2020). Fifty Shades of Brain: A Review on the Mechanical Testing and Modeling of Brain Tissue. *Arch Computat Methods Eng* 27, 1187–1230. https://doi.org/10.1007/s11831-019-09352-w
11. Carraro, G. (2016) Development of a sensorized human head prototype for studying traumatic brain injury mechanisms prototype for studying traumatic brain injury, Master Thesis in University of Padua, MidSweden University, 2016.
12. Contento, S (2019) Mechanical characterization of surrogate materials for the validation of an instrumented human head physical model. Master Thesis in University of Padua
13. Dall'aqua, F, Lee, N. Prabhu, R. (2020). Compressive behavior of porcine skin and its material modeling. Southern Biomedical Engineering Conference (SBEC) 2020
14. Dewan, M. C., Rattani, A., Gupta, S., Baticulon, R. E., Hung, Y. C., Punchak, M., Agrawal, A., Adeleye, A. O., Shrime, M. G., Rubiano, A. M., Rosenfeld, J. V., & Park, K. B. (2018). Estimating the global incidence of traumatic brain injury. *Journal of Neurosurgery*, 1–18. Advance online publication. https://doi.org/10.3171/2017.10.JNS17352
15. Donatelli, D., Romagnoli, L. (2020). Nonreflecting Boundary Conditions for a CSF Model of Fourth Ventricle: *Spinal SAS Dynamics. Bulletin of Mathematical Biology*. 82. 10.1007/s11538-020-00749-4

16. Faggin A. (2020) Development and construction of an instrumented human head replica for the experimental investigation of traumatic brain injuries mechanisms. Faggin Alberto. Master Thesis in University of Padua

17. Fallenstein G.T, Hulce V.D., Melvin J.W. (1969) Dynamic mechanical properties of human brain tissue. Journal of Biomechanics, Volume 2, Issue 3, Pages 217-226. ISSN 0021-9290, https://doi.org/10.1016/0021-9290(69)90079-7

18. Freitas, C.J., Mathis, J.T., Scott, N., Bigger, R.P., MacKiewicz, J. (2014). Dynamic Response Due to Behind Helmet Blunt Trauma Measured with a Human Head Surrogate. International Journal of Medical Sciences, 11(5), 409-425. https://doi.org/10.7150/ijms.8079

19. Ghaffari, M., Zoghi, M., Rostami, M. Abolfathi, N. (2014). Fluid Structure Interaction of Traumatic Brain Injury: Effects of Material Properties on SAS Trabeculae. International Journal of Modern Engineering. 14. 54-62.

20. Ghannam JY, Al Kharazi KA. Neuroanatomy, Cranial Meninges. [Updated 2022 Jul 25]. *In: StatPearls [Internet]*. Treasure Island (FL): StatPearls Publishing; 2022 Jan-. Available from: https://www.ncbi.nlm.nih.gov/books/NBK539882/

21. Golman, A. J., Wickwire, A. C., Harrigan, T. P., Iwaskiw, A., Armiger, R., & Merkle, A. (2013). Hierarchical model validation of the falx cerebri and tentorium cerebelli. In Proceedings of the forty first international workshop (pp. 41-3).

22. Ho J, Zhou Z, Li X, Kleiven S. (2017). The peculiar properties of the falx and tentorium in brain injury biomechanics, Journal of Biomechanics, Volume 60, Pages 243-247, ISSN 0021-9290, https://doi.org/10.1016/j.jbiomech.2017.06.023

23. Holbourn A.H.S. (1943) Mechanics of head injuries, The Lancet,Volume 242, Issue 6267, Pages 438-441. ISSN 0140-6736, https://doi.org/10.1016/S0140-6736(00)87453-X.

24. Hopkins J. (2023) in https://www.hopkinsmedicine.org/health/conditions-and-diseases/anatomy-of-the-brain

25. Jammes, Y., Viala, M., Dutto, W., Weber, J. P., & Guieu, R. (2017). Skin hardness and epidermal thickness affect the vibration sensitivity of the foot sole. Clin Res Foot Ankle, 5(3), 1-5.

26. Jin, X., Lee, J. B., Leung, L. Y., Zhang, L., Yang, K. H., & King, A. I. (2006). Biomechanical response of the bovine pia-arachnoid complex to tensile loading at varying strain-rates. Stapp car crash journal, 50, 637–649. https://doi.org/10.4271/2006-22-0025

27. Jin, X., Mao, H., Yang, K.H. et al. (2014) Constitutive Modeling of Pia–Arachnoid Complex. Ann Biomed Eng 42, 812–821. https://doi.org/10.1007/s10439-013-0948-6

28. Kleiven, S., & Hardy, W. N. (2002). Correlation of an FE Model of the Human Head with Local Brain Motion : Consequences for Injury Prediction. Stapp Car Crash Journal, 46, 123–144. Retrieved from http://urn.kb.se/resolve?urn=urn:nbn:se:kth:diva-12478

29. Knapp S. (2020) in https://biologydictionary.net/the-skull/

30. Kraus, M.A., Schuster, M., Kuntsche, J. et al. (2017) Parameter identification methods for visco- and hyperelastic material models. Glass Struct Eng 2, 147–167 https://doi.org/10.1007/s40940-017-0042-9

31. Lezak, M. D., (2012). Neuropsychological Assessment. USA: Oxford University Press.
32. Majdan, M., Plancikova, D., Brazinova, A., Rusnak, M., Nieboer, D., Feigin, V., & Maas, A. (2016). Epidemiology of traumatic brain injuries in Europe: a cross-sectional analysis. *The Lancet. Public health*, 1(2), e76–e83. https://doi.org/10.1016/S2468-2667(16)30017-2
33. Mao G. Traumatic Brain Injury https://www.msdmanuals.com/professional/injuries-poisoning/traumatic-brain-injury-tbi/traumatic-brain-injury-tbi Online, latest review Feb 2023
34. Margulies, S. S., & Thibault, L. E. (1992). A proposed tolerance criterion for diffuse axonal injury in man. Journal of biomechanics, 25(8), 917–923. https://doi.org/10.1016/0021-9290(92)90231-o
35. Menon, D.K., Schwab, K., Wright, D.W., et al. (2010). Position statement: Definition of traumatic brain injury. *Archives of Physical Medicine and Rehabilitation*, 91, 1637–1640.
36. Meyers M.A., Chawla K.K., (1999) "Mechanical behavior of materials" Prentice-Hall, Inc., USA, p. 644.
37. Miller K, Chinzei K, (1997) Constitutive modelling of brain tissue: Experiment and theory, Journal of Biomechanics, Volume 30, Issues 11–12, Pages 1115-1121, ISSN 0021-9290, https://doi.org/10.1016/S0021-9290(97)00092-4.
38. Miller-Keane Encyclopedia and Dictionary of Medicine, Nursing, and Allied Health, Seventh Edition. (2003). Retrieved April 3 2023 from https://medical-dictionary.thefreedictionary.com/encephalon
39. Nabi D. (2018) Brain Hemorrage. In https://www.myupchar.com/en/disease/brain-hemorrhage
40. Nahum, A., Smith, R., and Ward, C., (1977) "Intracranial Pressure Dynamics During Head Impact," SAE Technical Paper 770922, https://doi.org/10.4271/770922.
41. Paar A. (2023) in https://wiki.anton-paar.com/it-it/basics-of-dynamic-mechanical-analysis-dma/
42. Paulsen F, Böckers T, Waschke J (2019). Sobotta Anatomy Textbook. Elsevier
43. Pavan, P. G., Nasim, M., Brasco, V., Spadoni, S., Paoloni, F., d'Avella, D., Khosroshahi, S. F., de Cesare, N., Gupta, K., & Galvanetto, U. (2022). Development of detailed finite element models for in silico analyses of brain impact dynamics. Computer methods and programs in biomedicine, 227, 107225. https://doi.org/10.1016/j.cmpb.2022.107225
44. Periyasamy, R., Mishra, A., Anand, S., & Ammini, A. C. (2012). Foot pressure distribution variation in pre-obese and non-obese adult subject while standing. Foot (Edinburgh, Scotland), 22(4), 276–282. https://doi.org/10.1016/j.foot.2012.08.009
45. Petrone, N., Carraro, G., Castello, S. D., Broggio, L., Koptyug, A., & Bäckström, M. (2018, February). A novel instrumented human head surrogate for the impact evaluation of helmets. In Proceedings (Vol. 2, No. 6, p. 269). MDPI.
46. Petrone, N., Candiotto, G., Marzella, E., Uriati, F., Carraro, G., Bäckström, M., & Koptyug, A. (2019). Feasibility of using a novel instrumented human head surrogate to measure helmet, head and brain kinematics and intracranial pressure during

multidirectional impact tests. Journal of science and medicine in sport, 22 Suppl 1, S78–S84. https://doi.org/10.1016/j.jsams.2019.05.015

47. Post, A. (2013) The Influence of Dynamic Response Characteristics on Traumatic Brain Injury. Thesis for PhD
48. Rashid, B., Destrade, M., & Gilchrist, M. D. (2013). Influence of preservation temperature on the measured mechanical properties of brain tissue. Journal of biomechanics, 46(7), 1276–1281. https://doi.org/10.1016/j.jbiomech.2013.02.014
49. Saboori P, Sadegh A, (2011) Material modeling of the head's subarachnoid space, Scientia Iranica, Volume 18, Issue 6, Pages 1492-1499, ISSN 1026-3098, https://doi.org/10.1016/j.scient.2011.11.032.
50. Saboori, P., Sadegh, A. (2014). On the properties of brain sub arachnoid space and biomechanics of head impacts leading to traumatic brain injury. Advances in Biomechanics and Applications, 1(4), 253–267. https://doi.org/10.12989/ABA.2014.1.4.253
51. Samaka, Hatam & Tarlochan, Faris. (2013). Finite Element (FE) Human Head Models - Literature Review. International Journal of Scientific & Technology Research. VOLUME 2. 17-31.
52. Silvestroni A. L. (2020) Mechanical characterization of a biofidelic sensorized human head replica during impact tests. Master Thesis in University of Padua
53. Standring, S., Borley, N. R., & Gray, H. (2008). Gray's anatomy: the anatomical basis of clinical practice. 40th ed., Churchill Livingstone/Elsevier.
54. Steinmann, P., Hossain, M. & Possart, G. Hyperelastic models for rubber-like materials: consistent tangent operators and suitability for Treloar's data. Arch Appl Mech 82, 1183–1217 (2012). https://doi.org/10.1007/s00419-012-0610-z
55. Stone B, Mitchell S, Miyazaki Y, Peirce N, Harland A. A destructible headform for the assessment of sports impacts (2017). Proceedings of the Institution of Mechanical Engineers, Part P: Journal of Sports Engineering and Technology. 2023;237(1):7-18. doi:10.1177/17543371211055905
56. Takhounts, E. G., Ridella, S. A., Hasija, V., Tannous, R. E., Campbell, J. Q., Malone, D., Danelson, K., Stitzel, J., Rowson, S., & Duma, S. (2008). Investigation of traumatic brain injuries using the next generation of simulated injury monitor (SIMon) finite element head model. Stapp car crash journal, 52, 1–31. https://doi.org/10.4271/2008-22-0001
57. Takhounts, E. G., Craig, M. J., Moorhouse, K., McFadden, J., & Hasija, V. (2013). Development of brain injury criteria (BrIC). Stapp car crash journal, 57, 243–266. https://doi.org/10.4271/2013-22-0010
58. Tajran J, Gosman AA. Anatomy, Head and Neck, Scalp. [Updated 2022 Jul 25]. In: StatPearls [Internet]. Treasure Island (FL): StatPearls Publishing; 2023 Jan-. Available from: https://www.ncbi.nlm.nih.gov/books/NBK551565/
59. Tapia Romero, M. A., Gomez, M, Lugo, L. (2020). Prony series calculation for viscoelastic behavior modeling of structural adhesives from DMA data. Ingeniería Investigación y Tecnología. 21. 1-10. 10.22201/fi.25940732e.2020.21n2.014.
60. Vaughn, P. (2016) Anatomy and Physiology Made Easy: A Concise Learning Guide to Master the Fundamentals. Createspace Independent Pub.

61. Versace, J. (1971) A Review of the Severity Index, SAE Technical Paper 710881, 1971, https://doi.org/10.4271/710881.
62. Uriati, F. (2018) Development of a sensorized physical model of the human head for the innovation of helmet safety tests. Master Thesis in University of Padua, Mid Sweden University
63. van Noort, R., Martin, T. R., Black, M. M., Barker, A. T., & Montero, C. G. (1981). The mechanical properties of human dura mater and the effects of storage media. Clinical physics and physiological measurement : an official journal of the Hospital Physicists' Association, Deutsche Gesellschaft fur Medizinische Physik and the European Federation of Organisations for Medical Physics, 2(3), 197–203. https://doi.org/10.1088/0143-0815/2/3/003
64. Wiechert, E (1889); "Ueber elastische Nachwirkung", Dissertation, Königsberg University, Germany
65. Wiechert, E (1893); "Gesetze der elastischen Nachwirkung für constante Temperatur", Annalen der Physik, Vol. 286, issue 10, p. 335–348 and issue 11, p. 546–570
66. Xin Jin, Feng Zhu, Haojie Mao, Ming Shen, King H. Yang, A comprehensive experimental study on material properties of human brain tissue, Journal of Biomechanics, Volume 46, Issue 16, 2013,
67. Zhan, X., Liu, Y., Raymond, S.J., Alizadeh, H.V., Domel, A.G., Gevaert, O., Zeineh, M.M., Grant, G., & Camarillo, D.B. (2020). Deep Learning Head Model for Real-time Estimation of Entire Brain Deformation in Concussion. ArXiv, abs/2010.08527.
68. Zhang, X. A., Qi, S. T., Huang, G. L., Long, H., Fan, J., & Peng, J. X. (2012). Anatomical and histological study of Liliequist's membrane: with emphasis on its nature and lateral attachments. Child's nervous system : ChNS : official journal of the International Society for Pediatric Neurosurgery, 28(1), 65–72. https://doi.org/10.1007/s00381-011-1599-2
69. Zullo G, Silvestroni AL, Candiotto G, Koptyug A, Petrone N. (2021). A Novel Multi-Axial Pressure Sensor Probe for Measuring Triaxial Stress States Inside Soft Materials. Sensors. 2021; 21(10):3487. https://doi.org/10.3390/s21103487
70. International Testing Standard BS EN ISO 527-2:2012
71. https://www.humaneticsgroup.com/products/anthropomorphic-test-devices (2023)
72. https://www.shponline.co.uk/common-workplace-hazards/understanding-the-risk-of-rotational-head-injury/ (2021)
73. https://www.therapistaid.com/therapy-worksheet/the-human-brain-diagram (2023)
74. https://www.mayoclinic.org/diseases-conditions/traumatic-brain-injury/symptoms-causes/syc-20378557 (2023)
75. http://www.weerg.com/it/guide/file-formato-stl (2021)
76. Abaqus 6.14 Online Documentation, Dassault Systèmes, 2014
77. Meshmixer Online Documentation (Autodesk)